Three-dimensional wake dynamics of curved cylinders

Anthi Miliou

Department of Aeronautics

Imperial College London

Prince Consort Road

London SW7 2BY

A thesis submitted for the degree of Doctor of Philosophy of the University of London

February 2004

Abstract

Three-dimensional computations have been performed in order to study the fundamental mechanisms of vortex shedding past curved circular cylinders in directions normal and parallel to the plane of curvature at Reynolds numbers of 100 and 500. The basic shape upon which all the geometries were built was that of a quarter ring. The spatial discretization of the three-dimensional Navier-Stokes algorithm was based on the spectral/*hp* element method.

For the cases where the flow was normal to the plane of curvature, a quarter ring geometry and a curved cylinder ending semi-buried in the ground were studied. Different flow conditions were applied including a uniform or sheared velocity profile and a slip or a no-slip wall. The effect of a sheared velocity profile was found to be dominant to that of the wall boundary and resulted in vortex linking and lack of correlation along the span.

For the cases where the flow was parallel to the plane of curvature, different configurations were investigated with respect to the leading edge orientation. When the flow was directed onto the outside of the bend, three-dimensional shedding was observed not governed by the variation of local normal Reynolds numbers considered by a sectional approach. With the free-stream aligned onto the inside of the bend, however, no conventional shedding was detected. The axial flow directed towards the top of the geometry and the production of streamwise vorticity played a key role in stabilizing the wake. The steady wake features persisted on the whole even when a straight cylinder extension was added on top of the curved body. The feeding of the axial flow, stemming from the curved part, into the straight cylinder extension, weakened the shedding process expected from a straight cylinder at these

Reynolds numbers. Maximum w velocity components of the order of the free-stream at $Re = 500$ were located in the wakes of these bodies. Experimental work was also conducted alongside. The towing tank flow visualizations were found to be in qualitative agreement with the computational findings.

Overall, the importance of investigating these curved cylinder flows with a fully three-dimensional approach has been demonstrated, especially for the second set of computations.

Acknowledgements

Hoping that I won't forget anyone, I would like to take the chance here and thank some people who made this colourful journey possible, with all its good and bad moments, with all the frustrations, disappointments, happiness and enthusiasm together.

On the academic side, I would like to express my gratitude and thank first both of my supervisors for their support and this learning experience; Dr. Spencer Sherwin for his enthusiasm and encouragement and Professor Mike Graham for his valuable guidance. I would also like to extend my thanks to Professor Peter Bearman for his genuine interest in the work.

In terms of computational resources, I would like to acknowledge the Imperial College Parallel Computing facilities (Fujitsu AP3000) and the Computer Services for Academic Research (CSAR) at the University of Manchester (EPSRC grant number GR/R64957). For the experimental part of the work, my most sincere thanks go to John Owen and Christine Lear for the towing tank flow visualizations.

On the social side, some friends I made in the Department. Richard, Rupad, and John for exposing me to the world of cylinder flows my first year. Christine for roaring the boat together from the start of this journey, including the intensive moments of the last year. Sergio for all those tasteless espressi that made us famous in the common room. Masa and Barney who made all the coffee and chocolate breaks enjoyable. I would also like to thank Iain, Sylvaine and Fabien among other officemates during the past four years.

Away from Imperial, my thanks go to some of flatmates and friends in London, George, Eri, Maria, and Teresa, for the drinks, the gatherings and the late night discussions. Lele for the entertaining italian lessons. Thanks also to Elena and

Alex for becoming the old "Small World" friends in London, and away from the UK, to Yannis for all the transatlantic dreams of the return home.

Some of my oldest friends from home, Pia, from a high-school friendship to knowing everything that happened especially the years that she was here, Anna, for being the constant link to home, at happy and difficult times, Nadia and Stathis.

Finally, some special thanks to my uncle Panagiotis and my sister. Natalia, I think that all the years of us being in separate countries, if anything, bonded us more than we both expected. Last but not least, the biggest thank you goes to my parents, to whom this thesis is dedicated, for their unconditional support not only through my years at Imperial, but also throughout all my years abroad. As words are not enough, I just hope that somehow in the future I will prove worthwhile all the sacrifices especially at times when they questioned I would ever come back.

Στους γονείς μου,
Γιώργο και Βασιλική

To my parents

Contents

Abstract 1

Acknowledgements 3

Table of Contents 5

Nomenclature 8

List of Figures 11

List of Tables 20

1 Introduction 22

1.1 Marine riser pipes and motivation 22

1.2 Aims and objectives of this study 23

1.3 Problem definition 25

1.4 Synopsis 30

2 Literature Review 32

2.1 Background on bluff body flows 32

2.2 Straight circular cylinders under uniform flow 36

2.2.1 Flow regimes for the circular cylinder 36

2.2.2 Shedding configurations in the laminar regime 39

2.2.3 Experimental and computational studies of the flow structures in the wake transition regime 42

2.2.4 Dislocations and their relation to the wake transition 48

2.3 Straight cylinders under shear flow 51
2.4 Oblique cylinders 55
2.5 Tapered cylinders 56
2.6 The effect of curvature: the ring geometry 57
2.7 Flow past a straight circular cylinder in proximity to a wall boundary 60

3 Computational method 62
3.1 Mesh generation 63
3.2 Navier-Stokes algorithm 63
3.3 Basics of the spectral/*hp* element formulation 69
3.4 Details of the three-dimensional simulations 81
3.5 Utilities 84
3.5.1 The λ_2 criterion for vortex core identification 84
3.5.2 Enstrophy and cut-off analysis of vortical structure identification 86
3.5.3 Sectional force coefficients 92

4 Three-dimensional computations with the flow normal to the plane of curvature 94
4.1 Reynolds number 100: Results and discussion 95
4.1.1 Flow past body A 95
4.1.2 Flow past body B with a no-slip wall and a sheared velocity profile (case I) 104
4.1.3 Flow past body B with a slip wall and a sheared velocity profile (case II) 112
4.1.4 Flow past body B with a slip wall and a uniform velocity profile (case III) 117
4.2 Reynolds number 500: Flow past body A 119
4.3 Conclusions of this chapter 121

5 Three-dimensional computations with the flow parallel to the plane of curvature 125
5.1 Reynolds number 100: Results and discussion 126

5.1.1 Flow past body C 126
5.1.2 Flow past body D 143
5.1.3 Flow past body D with a six-diameter straight cylinder vertical addition 153
5.2 Reynolds number 500: Results and discussion 167
5.2.1 Flow past body C 167
5.2.2 Flow past body D 174
5.2.3 Flow past body D with a six-diameter straight cylinder vertical addition 181
5.3 Conclusions of this chapter 191

6 Conclusions and further work **194**
6.1 Conclusions 194
6.1.1 Flow normal to the plane of curvature 194
6.1.2 Flow parallel to the plane of curvature 196
6.2 Further work 199

Bibliography **201**

Nomenclature

x, y, z	Cartesian coordinates
u, v, w	three-dimensional velocity components
w_x, w_y, w_z	three-dimensional vorticity components
C_{Fx}, C_{Fy}, C_{Fz}	force coefficients in the three Cartesian directions
R	radius of rotation
d	cross-section diameter
AR	aspect ratio
K	non-dimensional curvature
S	arc length along the curved cylinder
Re	Reynolds number
St	Strouhal number
f	vortex shedding frequency
ρ	fluid density
ν	kinematic viscosity
U_∞	free-stream velocity

p_∞	pressure at free-stream
p_b	base pressure
C_{pb}	base pressure coefficient
St^*	universal Strouhal number
U_s	velocity at separation
θ	yaw angle (or angle between horizontal and plane of each cross section)
Re_l	local normal Reynolds number
β	shear parameter
$\mathbf{G}$	gap distance
Δt	time step
$\mathbf{h}$	characteristic size of an element
$\mathbf{P}$	polynomial order
λ	Helmholtz constant
Ω	computational domain
N_{dof}	number of degrees of freedom
$\mathbf{Q}$	number of quadrature points
ψ_p	modal expansion basis
ε	error estimate
$\mathbf{Z}$	enstrophy
λ_2	second largest eigenvalue of velocity gradient tensor

2D	two-dimensional
3D	three-dimensional
rms	root-mean-square
IP	Independence Principle
FPSO	Floating Production Storage and Offloading
TTR	Top Tensioned Riser
SCR	Steel Catenary Riser
CFL	Courant-Friedrichs-Lewy
ALE	Arbitrary-Lagrangian-Eulerian

List of Figures

1.1 Non-dimensional radius of curvature, $R/d = 12.5$, for an example curved circular cylinder 26

1.2 (a) Definition of body A, $R/d = 12.5$; (b) Definition of body B, $R/d = 12.5$. Artificial blend applied on sections of the body that correspond to angles larger than 63° from the horizontal. 28

1.3 (a) Definition of body C, $R/d = 12.5$. A ten diameter horizontal extension is included; (b) Definition of body D, $R/d = 12.5$ 29

2.1 Variation of the base suction coefficient, $-C_{pb}$, with Reynolds number (data from several sources (Roshko 1993)) 37

2.2 Variation of Strouhal vs. Reynolds number in the laminar and wake transition regimes (Williamson 1992a). The two discontinuities attributed to Mode A and B instabilities are depicted in this curve. . . 43

2.3 (a) Deformation of spanwise vortices and formation of streamwise vortex loops for Mode A; (b) Finer scale streamwise vortex pairs for Mode B (Williamson 1992a) 44

2.4 Schematic drawing of the vortex structures for Mode A and B instabilities (Brede *et al.* 1996). The shape of "tongues" from the deformation of spanwise vortices for Mode A and the in-line arrangement for Mode B are illustrated. 45

2.5 Vorticity fields from the numerical simulations of Henderson (1998) at: (a) $Re = 195$, Mode A instability, (b) $Re = 265$, Mode B instability. Red and blue contours highlighting the positive and negative extremes in streamwise vorticity components. 47

2.6 Comparison of: (a) one-sided, and (b) two-sided vortex dislocations. Flow is from left to right (Williamson 1992a). 50
2.7 Dislocations occurring naturally in the wake transition regime, Re=210 (Williamson 1992a) 50
2.8 Vortex splitting in the wake of bluff bodies with a blunt trailing edge (Bearman 1998) 52
2.9 Description of parameters for shear flows past various bluff bodies (Griffin 1985) 53
2.10 Flow visualizations depicting the sequence of the vortex splitting process for a tapered cylinder (Piccirillo & Van Atta 1993) 57
2.11 Vortex rings developed in the wake of a ring of aspect ratio 76.2 at $Re = 105$ (Leweke & Provansal 1995). Flow is from right to left. . . . 59

3.1 Unstructured hybrid mesh for body C (only half of the mesh is shown in the y-direction) 64
3.2 (a) Surface triangulation; (b) Structured layer around the solid boundary 64
3.3 Shape of expansion modes for a polynomial order of $P = 5$ (Karniadakis & Sherwin 1999) 74
3.4 h-convergence of the solution $u = \sin(\pi x)$ in the one-dimensional Helmholtz equation in a log-log axis, $P = 4$ 79
3.5 P- and h- convergence of the solution $u = \sin(\pi x)$ in the one-dimensional Helmholtz equation in a semi-log axis: ∇ p-convergence in 2 elements; ◯ p-convergence in 20 elements; □ h-convergence at $P = 4$ 80
3.6 (a) Normalized enstrophy, Z/Z_{tot}, versus λ_2 for the flow past Body C at $Re = 100$, (b) log-log axis 89
3.7 Isocontours of λ_2 at: (a) λ_2 = -0.0001, (b) λ_2 = -0.005, (c) λ_2 = -0.02, (d) λ_2 = -0.1, (e) λ_2 = -0.2, (f) λ_2= -1.5 91
3.8 Variation of sectional C_{F_y} for Body C, $Re = 100$. To illustrate the orientation of the planes along the cylinder's span two sample sections are also shown. 93

4.1 Computational boundaries (not to scale) for body A in a plane normal to the free-stream vector 95
4.2 (a) Integrated force coefficients for the flow past Body A at $Re = 100$, x- and z- are the horizontal and vertical component of the transverse force respectively, y- is the direction of the drag; (b) A shorter section of the force history at sixth and eighth polynomial orders 97
4.3 Power spectra density of the integrated forces in the x-, y- and z-directions for the flow past body A at $Re = 100$ 98
4.4 (a) Pressure contours on planes normal to the cylinder axis for the flow past body A at $Re = 100$, $\frac{tU_\infty}{d} \approx 435$, C_{Fx} maximum; (b) 3D pressure isocontours for body A, $Re = 100$, $\frac{tU_\infty}{d} \approx 435$, C_{Fx} maximum: (1) 3D view, $C_p = -0.78$, (2) top view, $C_p = -0.98$ 101
4.5 Wake topology for the flow past body A, $Re = 100$, $\lambda_2 = -0.1$, $\frac{tU_\infty}{d} \approx 435$, C_{Fx} maximum 102
4.6 Variation of the forcing in two-dimensional sections normal to the axis of body A, $Re = 100$: (a) Sectional C_{Fx}, (b) Cartesian x-component force coefficient, (c) Cartesian z-component force coefficient 103
4.7 Integrated force coefficients at $P = 6$ for the flow past body A, $Re = 100$, using a second mesh of larger computational domain size 104
4.8 Computational boundaries (not to scale) for body B in a plane normal to the free-stream vector 105
4.9 Force history for the flow past body B, case I, at $Re = 100$, x- and z- are the horizontal and vertical component of the transverse force respectively, y- is the direction of the drag 106
4.10 Normalized enstrophy, Z/Z_{tot}, versus λ_2 for the flow past Body B, case I, at $Re = 100$ 107
4.11 Isocontours of λ_2 at: (a) λ_2 = -0.001, (b) λ_2 = -0.03, (c) λ_2 = -0.1, (d) λ_2 = -0.3, (e) λ_2 = -1.5. Normalized enstrophy isocontour at the average value, 0.363, of the flow in the domain (f). 109
4.12 Pressure contours on planes normal to the cylinder axis for the flow past body B, case I, at $Re = 100$ 110

4.13 (a) Variation of sectional C_{Fx} along the length of Body B, case I, at $Re = 100$; (b) Arc length definition followed in describing the sectional forces for body B 111
4.14 (a) Force history for the flow past body B at $Re = 100$, case II, x- and z- are the horizontal and vertical component of the transverse force respectively, y- is the direction of the drag; (b) A shorter section of the force history marking the sectors that correspond to Figures 4.15 and 4.16 113
4.15 (a) Variation of sectional C_{Fx} for body B, case II, at $Re = 100$ from $\frac{tU_\infty}{d} \approx 943$ to $\frac{tU_\infty}{d} \approx 984$; (b) Wake topology extracted at the specified times $t_1^* \approx 949$, $t_2^* \approx 957$, $t_3^* \approx 970$, and $t_4^* \approx 978$, $\lambda_2 = -0.1$. 115
4.16 (a) Variation of sectional C_{Fx} for body B, case II, at $Re = 100$ from $\frac{tU_\infty}{d} \approx 999$ to $\frac{tU_\infty}{d} \approx 1178$; (b) Wake topology extracted at the specified times $t_5^* \approx 1009$, $t_6^* \approx 1027$, $t_7^* \approx 1040$, and $t_8^* \approx 1054$, $\lambda_2 = -0.1$ 116
4.17 (a) Force history for the flow past body B, case III, at $Re = 100$, x- and z- are the horizontal and vertical component of the transverse force respectively, y- is the direction of the drag; (b) A more detailed section of the force history from $\frac{tU_\infty}{d} = 375$ to $\frac{tU_\infty}{d} = 738$ 118
4.18 Variation of sectional C_{Fx} along the length of Body B, case III, at $Re = 100$ 119
4.19 Pressure contours at planes normal to the axis of body B, case III, at $Re = 100$, $\frac{tU_\infty}{d} \approx 756$ (C_{Fx} maximum) 120
4.20 Vortex cores in the wake of body B, case III, at $Re = 100$, $\lambda_2 = -0.1$, $\frac{tU_\infty}{d} \approx 756$ (C_{Fx} maximum) 120
4.21 (a) Force history for the flow past Body A at $Re = 500$, x- and z- are the horizontal and vertical component of the transverse force respectively, y- is the direction of the drag; (b) A more detailed section of the integrated force coefficients at sixth polynomial order 122
4.22 3D pressure isocontours for body A, $Re = 500$, $C_p = -0.74$: (a) $\frac{tU_\infty}{d} \approx 627$, (b) $\frac{tU_\infty}{d} \approx 656$ 123

4.23 Variation of sectional C_{Fx} along the length of Body A, $Re = 500$ . . . 123

5.1 Computational boundaries (not to scale) for body C in a plane including the free-stream vector 126

5.2 (a) Integrated force coefficients for the flow past Body C at $Re = 100$, x- is the direction of the drag, y- is the horizontal component of the transverse force and z- is the vertical one; (b) Snapshot in time for the integrated force coefficients from $\frac{t|U_\infty|}{d} = 305$ to $\frac{t|U_\infty|}{d} = 625$, part of $P = 4$ to $P = 8$ 127

5.3 Power spectra density of the integrated forces in the x-, y- and z-directions for the flow past body C at $Re = 100$ 129

5.4 Vortex cores in the wake of body C at $Re = 100$, $\lambda_2 = -0.1$: (a) 3D view extracted at a minimum of the integrated C_{Fy}, $\frac{t|U_\infty|}{d} \approx 524$, (b) 3D view extracted at a maximum of the integrated C_{Fy}, $\frac{t|U_\infty|}{d} \approx 532$, (c) View from the top 132

5.5 Variation of sectional C_{Fy} along the length of the quarter ring part of body C, $Re = 100$ (t^* represents non-dimensional time, $\frac{t|U_\infty|}{d}$; $t_1^* \approx 524$ and $t_2^* \approx 532$) 133

5.6 Three planes normal to the axis of body C intersecting the wake structures extracted at the time of a C_{Fy} minimum, $\frac{t|U_\infty|}{d} \approx 524$; two different views 135

5.7 (a) A 3D view of the vortex core intersections at the three planes A, B, C; (b) Planar views of these cross-sections 135

5.8 Spanwise vorticity component at the A, B, C planes extracted at the time of a C_{Fy} minimum, $\frac{t|U_\infty|}{d} \approx 524$ 136

5.9 Centreplane streamlines ($y = 0$) overlaid on pressure contours for the flow past body C, $Re = 100$ 137

5.10 Pressure contours on planes normal to the cylinder axis for the flow past body C at $Re = 100$ at: (a) a minimum in the integrated C_{Fy}, $\frac{t|U_\infty|}{d} \approx 524$, (b) a maximum in the integrated C_{Fy}, $\frac{t|U_\infty|}{d} \approx 532$ 138

5.11 Variation of pressure and velocity along the span of body C, Re = 100, $\frac{t|U_\infty|}{d} \approx 524$: (a) Base pressure and stagnation pressure, (b) u and w velocity components extracted 0.3 diameters upstream of the curved cylinder, (c) Normal $((u\cos\theta - w\sin\theta)/|U_\infty|)$ and axial $((w\cos\theta + u\sin\theta)/|U_\infty|)$ components computed from the 3D simulation 0.3 diameters upstream of the curved cylinder 139

5.12 Streamwise vorticity component on vertical planes five and seven diameters upstream of the end of the quarter ring shape ($x/d = 5$ and $x/d = 7$) for the flow past body C at $Re = 100$ at a minimum in the integrated C_{Fy}, $\frac{t|U_\infty|}{d} \approx 524$ 140

5.13 Two different views of the curved cylinder model used for the towing tank flow visualizations 141

5.14 Towing tank flow visualization for body C, $Re = 100$ 142

5.15 Wake topology for the flow past body C at $Re = 100$, $\lambda_2 = -0.03$ . . 142

5.16 Computational boundaries (not to scale) for body D in a plane including the free-stream vector 143

5.17 Force history for the flow past body D at $Re = 100$, x- is the direction of the drag, y- is the horizontal component of the transverse force and z- is the vertical one 144

5.18 Centreplane streamlines ($y = 0$) overlaid on pressure contours for the flow past body D at $Re = 100$. The insets show u velocity contours at horizontal slices which are located at the top plane, and two, five and eight diameters vertically below. 146

5.19 (a) Streamwise vorticity on a vertical plane five diameters downstream of body D, $Re = 100$; (b) Spanwise vorticity on horizontal planes two and five diameters vertically below the top surface for body D, $Re = 100$ 147

5.20 Two different views of the wake topology for the flow past body D at $Re = 100$, $\lambda_2 = -0.01$ 149

5.21 Sectional C_{Fy} along the length of body D, $Re = 100$ 150

5.22 Variation of pressure and velocity along the span of body D, $Re = 100$: (a) Base pressure and stagnation pressure, (b) u and w velocity components extracted 0.3 diameters upstream of the curved cylinder, (c) w velocity component extracted 0.3, 0.6 and 1.5 diameters downstream of the curved cylinder, (d) Normal $((u\cos\theta - w\sin\theta)/U_\infty)$ and axial $((w\cos\theta + u\sin\theta)/U_\infty)$ components computed from the 3D simulation 0.3 diameters upstream of body D 151

5.23 Computational boundaries (not to scale) in a plane including the free-stream vector for body D with a straight cylinder addition of six diameters vertically 153

5.24 Integrated forces for the flow past body D with six diameters vertical addition at $Re = 100$, x- is the direction of the drag, y- is the horizontal component of the transverse force and z- is the vertical one 154

5.25 Centreplane streamlines ($y = 0$) overlaid on pressure contours for the flow past body D with a vertical extension of six diameters, $Re = 100$, $\frac{tU_\infty}{d} = 414$ (C_{Fy} maximum). The insets depict u velocity contours at four horizontal slices along the span. 156

5.26 Wake topology for body D with a six-diameter vertical extension at $Re = 100$, $\lambda_2 = -0.01$: (a) extracted at a C_{Fy} maximum, $\frac{tU_\infty}{d} = 414$, (b) extracted at a C_{Fy} minimum, $\frac{tU_\infty}{d} \approx 427$ 157

5.27 (a) Variation of sectional C_{Fy} for body D with a six-diameter straight cylinder extension vertically, $Re = 100$; (b) Variation of C_{Fy} with time at the specified locations of $S/d = 1$, $S/d = 3$, and $S/d = 6$ . . . 159

5.28 Vortex core intersections at three horizontal planes: $S/d = 1$ (plane A), $S/d = 3$ (plane B) and $S/d = 6$ (plane C) for the flow past body D with a six-diameter straight cylinder extension on top 160

5.29 Vortex core intersections at six planes for the flow past body D with a vertical extension of six diameters, $Re = 100$: (a) $\frac{tU_\infty}{d} = 414$, C_{Fy} maximum, (b) $\frac{tU_\infty}{d} \approx 427$, C_{Fy} minimum 161

5.30 Spanwise vorticity contours for body D with a straight cylinder extension of six diameters at $Re = 100$: (a) $\frac{tU_\infty}{d} = 414$, C_{Fy} maximum, (b) $\frac{tU_\infty}{d} \approx 427$, C_{Fy} minimum 162
5.31 Streamwise vorticity on a vertical plane five diameters downstream of body D with a straight cylinder extension of six diameters, $Re = 100$, at a C_{Fy} maximum, $\frac{tU_\infty}{d} = 414$ 163
5.32 Variation of pressure and velocity along the span of body D with a six-diameter straight cylinder extension, $Re = 100$: (a) Base pressure and stagnation pressure, (b) u and w velocity components extracted 0.3 diameters upstream of the curved cylinder, (c) w velocity component extracted 0.3, 0.6 and 1.5 diameters downstream of the curved cylinder, (d) Normal $((u\cos\theta - w\sin\theta)/U_\infty)$ and axial $((w\cos\theta + u\sin\theta)/U_\infty)$ components computed from the 3D simulation 0.3 diameters upstream of the geometry 164
5.33 Production of streamwise vorticity on body D with a vertical extension of six diameters, $Re = 100$ 165
5.34 (a) Force history for Body C at Reynolds number of 500; (b) A more detailed section of the integrated force coefficients at sixth polynomial order 168
5.35 (a) Normalized enstrophy, Z/Z_{tot}, versus λ_2 for the flow past Body C at $Re = 500$, (b) log-log axis 169
5.36 Isocontours of λ_2 at: (a) λ_2 = -0.005, (b) λ_2 = -0.3, (c) λ_2 = -0.6, (d) λ_2 = -0.8, (e) λ_2 = -1.3, (f) λ_2= -5.0 170
5.37 Sectional C_{Fy} variation along the length of the quarter ring part of body C, $Re = 500$ 171
5.38 Vortex cores in the wake of body C at $Re = 500$, $\lambda_2 = -0.8$, $\frac{t|U_\infty|}{d} \approx$ 652: (a) 3D view, (b) View from the top 172
5.39 Towing tank flow visualization for body C, $Re = 500$ 173
5.40 Pressure contours on planes normal to the cylinder axis for the flow past body C at $Re = 500$, $\frac{t|U_\infty|}{d} \approx 652$ 173

5.41 Variation of pressure and velocity along the span of body C, $Re = 500$: (a) Base pressure and stagnation pressure, (b) u and w velocity components extracted 0.3 diameters upstream of the curved cylinder, (c) Normal ($u\cos\theta - w\sin\theta/|U_\infty|$) and axial ($w\cos\theta + u\sin\theta/|U_\infty|$) components computed from the 3D simulation 0.3 diameters upstream of the curved cylinder 175

5.42 Integrated force coefficients for body D, $Re = 500$ 176

5.43 (a) Variation of sectional C_{Fy} along the length of body D, $Re = 500$; (b) Variation of C_{Fy} with time at the specified locations of $S/d = 2$, $S/d = 4$, $S/d = 5$, and $S/d = 7.5$ 177

5.44 Spanwise vorticity contours at planes normal to the cylinder axis for body D at $Re = 500$, $\frac{tU_\infty}{d} \approx 616$ (C_{Fy} maximum) 178

5.45 Wake topology for body D at $Re = 500$, $\lambda_2 = -0.4$, $\frac{tU_\infty}{d} \approx 616$ (C_{Fy} maximum) 179

5.46 Towing tank flow visualization for body D, $Re = 500$ 179

5.47 Variation of pressure and velocity along the span of body D, $Re = 500$: (a) Base pressure and stagnation pressure, (b) u and w velocity components extracted 0.3 diameters upstream of the curved cylinder, (c) w velocity component extracted 0.3, 0.6 and 1.5 diameters downstream of the curved cylinder, (d) Normal ($(u\cos\theta - w\sin\theta)/U_\infty$) and axial ($(w\cos\theta + u\sin\theta)/U_\infty$) components extracted from the 3D computation 0.3 diameters upstream of the curved cylinder 180

5.48 Integrated force coefficients for the flow past body D with a six-diameter vertical addition, $Re = 500$ 181

5.49 (a) Variation of sectional C_{Fy} for body D with a six-diameter straight cylinder extension vertically, $Re = 500$; (b) Variation of C_{Fy} with time at the specified locations of $S/d = 1$, $S/d = 3$, $S/d = 6$, $S/d = 8$, $S/d = 10$, and $S/d = 13.5$ 182

5.50 Spanwise vorticity contours for body D with a vertical addition of a six-diameter long cylinder, $Re = 500$: (a) $\frac{tU_\infty}{d} \approx 432$, C_{Fy} maximum, (b) $\frac{tU_\infty}{d} \approx 436$, C_{Fy} minimum 184

5.51 Wake topology for body D with a six-diameter straight cylinder extension vertically at $Re = 500$, $\lambda_2 = -0.6$, $\frac{tU_\infty}{d} \approx 432$, C_{Fy} maximum 185
5.52 Towing tank flow visualization at two different time instants for body D with a vertical addition of 6 diameters, $Re = 500$ 186
5.53 Variation of pressure and velocity along the span of body D with a six-diameter straight cylinder extension, $Re = 500$: (a) Base pressure and stagnation pressure, (b) u and w velocity components extracted 0.3 diameters upstream of the curved cylinder, (c) w velocity component extracted 0.3, 0.6 and 1.5 diameters downstream, (d) Normal $((u\cos\theta - w\sin\theta)/U_\infty)$ and axial $((w\cos\theta + u\sin\theta)/U_\infty)$ components computed from the 3D simulation 0.3 diameters upstream of the curved cylinder 188
5.54 Production of streamwise vorticity on body D with a vertical extension of six diameters, $Re = 500$ 189
5.55 (a) Streamlines in 3D at the rear of body D with a vertical extension of six diameters, $Re = 500$, (b) Enlarged view 190
5.56 Presumed regimes in the wake of body D with a long straight cylinder vertical extension, $Re = 500$ 191

List of Tables

3.1 Coefficients of the splitting scheme (Karniadakis *et al.* 1991) 67

4.1 Frequencies along with mean and rms values for the integrated force coefficients for the flow past body A at $Re = 100$ computed at $P = 8$ with first order time integration 99

4.2 Statistics for the flow past body A at $Re = 100$ computed with first order time integration at $P = 6$ for three different time steps 100

5.1 Frequencies along with mean and rms values for the integrated force coefficients for the flow past body C at $Re = 100$ computed at $P = 8$ with first order time integration 130

5.2 Statistics for the flow past body C at $Re = 100$ computed with first order time integration at $P = 6$ for three different time steps 131

5.3 Mean values for the integrated force coefficients for the flow past body D at $Re = 100$ computed at different polynomial orders 145

5.4 Mean values for the integrated force coefficients and rms values for the fluctuating component of C_{F_y} for the flow past body D with six diameters vertical addition at $Re = 100$ computed at $P = 4$ and $P = 6$ 155

5.5 Location and magnitude of the maximum w velocity component upstream and downstream of the curved bodies for the different cases . 192

Chapter 1

Introduction

1.1 Marine riser pipes and motivation

As the need to develop deep-water reservoirs for the exploitation of hydrocarbons below the sea has been increasing, floating offshore platforms and production vessels are now required to operate in depths up to 2000m. The transport of the well fluids and the provision of the reservoir support in offshore engineering applications is accomplished by riser pipes.

On average, marine riser pipes have a diameter up to approximately $0.5m$ and they are often found in groups of 20 for example when passing through the turret of an FPSO. Risers typically operate in currents up to $2m/s$ at Reynolds numbers of the order of 10^6. Two types of deployment are used: top tensioned risers (TTRs) which are substantially vertical and catenary risers which are effectively curved riser pipes. The latter are increasingly preferred over the vertical risers for deep-water reservoirs as they can accommodate larger motions of the floating vessel. While steel catenary risers (SCRs) are normally associated with large radii of curvature, flexible catenary risers can have quite drastic localized deformation. A catenary riser is subject to fluid dynamic loading from a combination of waves and current and, being a compliant structure, may be subject to vortex-induced-vibrations especially in such large depths.

A catenary riser may be in tangential contact with the seabed while part of its

length, that can be up to $2000m$, lies near horizontal to the ground being partially- or even fully- buried. In the industrial sector considerable conservatism is applied in the modelling of complex areas of a riser such as the touch down point where the riser is in contact with the seabed. This is a very sensitive region for the structure particularly when the riser is continuously being lifted off and dropped back onto the seabed as a result of vessel motion. With the touch down point being usually the weak spot structurally, a riser can be susceptible to fatigue failure posing problems for the offshore industry.

Finally, another area of concern which applies to both vertical and curved riser pipes is the clashing or collision of individual risers in riser arrays. Especially for deep sea riser systems, a small difference in static deflection may lead to mechanical contact between risers; hence various practical solutions are sought in offshore designs (Huse & Kleiven 2000).

All the above points comprise the practical problems presented by the marine industry for catenary riser pipes. Understanding the unsteady flow pattern developed behind a catenary riser pipe is a problem that would appear to require investigation in three dimensions. The majority of the methods employed by the industry use empirical hydrodynamic force coefficients based on data sets from fundamental experiments. Moreover, different assumptions apply for the various models (Larsen 2000) resulting frequently in different response predictions. A sectional approach that assumes locally two-dimensional flow for a curved pipe may not be suitable for the analysis of such a three-dimensional problem. For the cases where the free-stream velocity vector is not normal to the centreline of the body at all the sections, a two-dimensional sectional model may fail where the vortices are not necessarily shed normal to the axis of the body.

1.2 Aims and objectives of this study

A curved circular cylinder can be considered as a generic shape for a catenary riser pipe. Within the bluff body flow community, there is an extensive amount of past literature on various aspects of the flow past a straight cylinder. For exam-

ple, the different flow regimes occurring at increasing Reynolds numbers have been broadly studied (the initiation of vortex shedding, the wake transition to three-dimensionality etc.). Moreover, straight rigid cylinders under shear flow and vortex-induced-vibrations of flexible cylinders have also been widely investigated. In comparison, the wake of curved cylinders has received much less attention. No extensive studies have been performed for the flow past curved cylinders especially under a combination of different boundary conditions and orientations.

Therefore, with the motivation stemming from the offshore industry, the focus of this work is identified as studying the wake topology and the vortex shedding patterns of curved cylinders. This study is restricted to low Reynolds numbers; hence, it does not represent an effort to model the fluid dynamic loading past practical catenary riser pipes. Such a study for catenary risers in their natural environment would require higher aspect ratios and Reynolds numbers, as well as incorporating the structural dynamics and the feedback process implied in vortex-induced-vibrations. Investigating the practical catenary riser pipe problem under a combination of all these factors would be too complicated for a first study and with too many parameters. It is thus more important at an initial stage to gain an understanding of the fundamental flow physics past a generic shape, that of the curved cylinder, before developing the modelling of the full scale three-dimensional catenary riser problem. The aim of this work is therefore to computationally investigate the fundamental fluid mechanics past fixed curved circular cylinders at a set of different orientations and boundary conditions. This subject has not been broadly investigated previously with a fully three-dimensional approach.

With the increasing computing power and the advances in the Computational Fluid Dynamics area, the study of fully three-dimensional large scale problems has become increasingly feasible recently. The current work has been performed with a three-dimensional spectral/*hp* element code, *NεκTar* (Karniadakis & Sherwin 1999). Numerical investigations have thus been performed at Reynolds numbers of 100 and 500 in order to study the fundamental mechanisms of vortex shedding and the 3D flow structures past curved circular cylinders at low Reynolds numbers in distinction to a sectional approach. In addition to the computations, experiments have

been conducted alongside in order to qualitatively validate the numerical results.

The challenges inherently connected with this study are related to the three-dimensional nature of the problem under investigation and the large size computational domains involved. Considerable computational expense is required by a three-dimensional unsteady fluid dynamics solver for such a large scale problem.

1.3 Problem definition

When considering a three-dimensional body, a range of flow orientations are possible. A quarter ring with a vertical or a horizontal extension has been considered as a generic shape for a catenary riser. The possible configurations can be divided primarily into two categories: the ones where the flow is normal to the plane of curvature and the ones where the flow is parallel to the plane of curvature. For the flow in the normal direction, different flow conditions are applied. Evaluating the results of this part of the study, the emphasis was then placed more on different orientations rather than different inflow profiles. For the flow in the parallel direction, therefore, the incident profiles are all uniform and different orientations of the leading edge are investigated.

The main part of all the three-dimensional body configurations considered in this study was a curved circular cylinder, which effectively is a quarter of a ring (torus) geometry. The first characteristic to specify this curved body is, hence, the radius of curvature.

The non-dimensional radius of curvature is defined as the ratio of the radius, R, of the curved axis of the centres of the cross-sections to the cross-section diameter, d, of the cylinder. In all the numerical investigations performed in this work, the curved circular cylinder had a non-dimensional radius of curvature, R/d, of 12.5 as Figure 1.1 depicts.

In past literature, the term aspect ratio has been used interchangeably with the non-dimensional curvature when referring to the complete ring geometry (Leweke 1994). For a ring of outer diameter D and cross-section diameter d, the aspect ratio was then defined as $AR = \frac{\pi D}{d}$ and the non-dimensional curvature as $K = \frac{2d}{D}$.

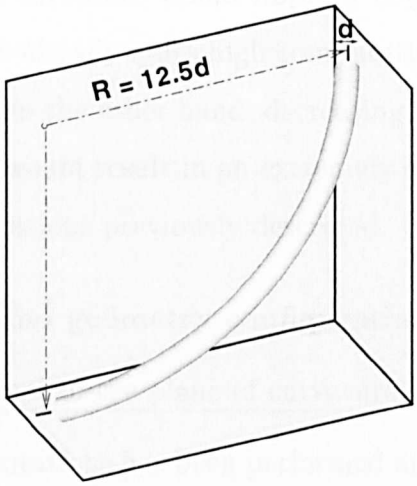


Figure 1.1: Non-dimensional radius of curvature, $R/d = 12.5$, for an example curved circular cylinder

To compare the non-dimensional radius of curvature for the curved cylinders of this study with the aspect ratio for complete rings, the aspect ratio is calculated as if the geometry were a whole ring. With the cross-section diameter being equal to one, the aspect ratio for the present case is found to be equal to $AR = \frac{(2)(\pi)(13)}{(1)} = 81.7$. A ring with large aspect ratio is effectively one with small curvature. At really high values of aspect ratio the body can be considered locally as a straight body, hence the wake patterns produced should approximate those of a straight circular cylinder.

The non-dimensional radius of curvature used throughout this work may, to some extent, even be considered as a lower limit for the local deformation of the most flexible catenary riser pipes (i.e. the geometries of this study are the upper limit of how curved locally the bodies in the marine industry can be). Steel catenary riser pipes, on the other hand, typically have much larger radii of curvature. In terms of the radius of curvature, the results for the current work may have more relevance to flexible riser pipes, where the three-dimensional effects are stronger, as opposed to the steel catenary riser pipes.

In the course of this research, after evaluating the results of Chapter 4, it became apparent that any configuration with larger radius of curvature than the one originally selected would probably not demonstrate any significant qualitative difference for the cases where the flow is normal to the plane of curvature. Moreover, a larger

non-dimensional radius of curvature would imply a larger computational domain; hence it would increase the already quite high computational cost of the fully three-dimensional simulations. On the other hand, decreasing the non-dimensional radius of curvature even further, would result in an extremely curved body not relevant to the marine industry applications previously described.

- **Inflow directions and geometry configurations**

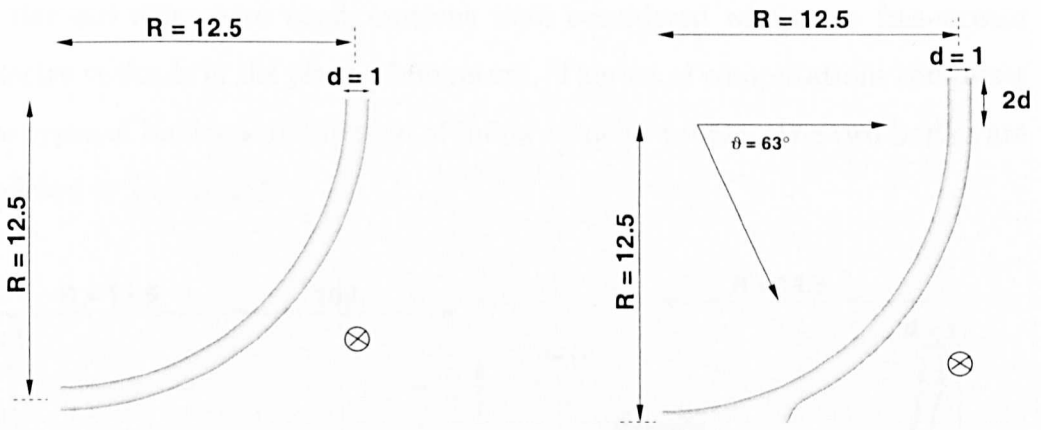
  ▷ Set one: Flow normal to the plane of curvature

  The first set of computations has been performed at a Reynolds number, based on the cylinder diameter, d, of 100 and includes cases where the free-stream flow vector is normal to the plane of curvature. These computations include cases of a quarter ring and a deformed quarter ring with a vertical extension, subject to either uniform or sheared flow in contact with either a no-slip or a slip wall. Effectively, this set of computations incorporates two body geometries and four combinations of boundary conditions.

  The two bodies are depicted in Figure 1.2. Body A is a curved cylinder, effectively a quarter ring. Body B has the same non-dimensional radius of curvature down to an angle of 63° to the horizontal, but is then semi-buried into a solid boundary using an artificial blend on the outer side. This body also includes a vertical addition of a straight cylinder of two diameters length at the upper end. The artificial blending applied, and the reasons behind it, are discussed in Chapter 4.

  The different boundary conditions considered can be distinguished as follows. Body A has been studied under uniform velocity profile at the inlet. Body B ends in a wall boundary in all the cases, and has been studied under the following combination of boundary conditions:

  - shear velocity inlet profile and no-slip wall
  - shear velocity inlet profile and slip wall
  - uniform velocity inlet profile and slip wall



(a) (b)

Figure 1.2: (a) Definition of body A, $R/d = 12.5$; (b) Definition of body B, $R/d = 12.5$. Artificial blend applied on sections of the body that correspond to angles larger than 63° from the horizontal.

In all these cases, the flow is into the page as Figure 1.2 is viewed. The specific boundary conditions and the type of sheared velocity profile applied will be discussed in Chapter 4.

This set of computations has aimed at investigating the effects of curvature compared to a straight cylinder and the effects of the interaction with the seabed as well as a sheared current profile.

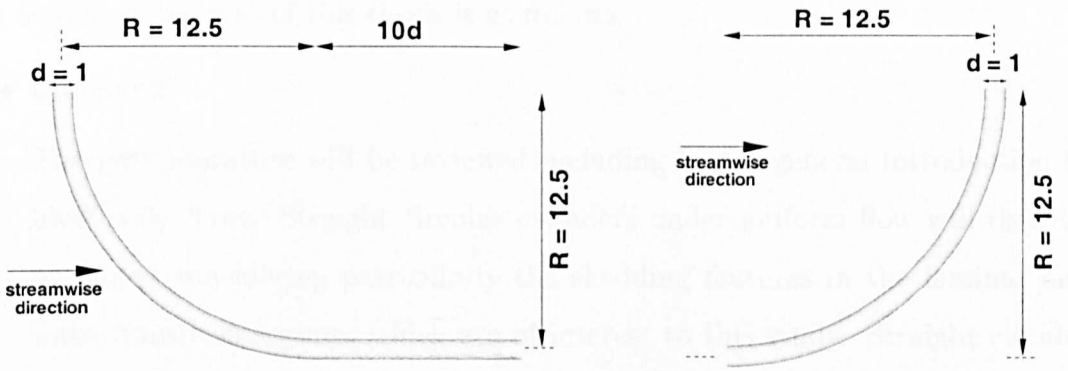
Since this work was intended to be a fundamental study, a low Reynolds number of 100 was first chosen. At such a low Reynolds number the detailed flow structures can be captured using direct numerical simulation without any additional modelling. Also the basic case of the flow past a straight 2D cylinder is two-dimensional at this Reynolds number.

Furthermore, computations have also been performed at a higher Reynolds number of 500, above the onset of three-dimensionality in the wake of a straight 2D cylinder. From this set of computations, body A has been studied at $Re = 500$ under uniform velocity profile.

▷ Set two: Flow parallel to the plane of curvature

The second set of computations has been performed at Reynolds numbers

of 100 and 500. Two configurations were considered where the free-stream velocity vector is in the plane of curvature. This set of computations comprises two types of bodies and one type of inflow velocity profile. The two bodies are depicted in Figure 1.3.



(a) (b)

Figure 1.3: (a) Definition of body C, $R/d = 12.5$. A ten diameter horizontal extension is included; (b) Definition of body D, $R/d = 12.5$

Body C is the quarter ring of body A, which is now aligned to the flow and has a horizontal addition of ten diameters. A uniform flow parallel to the plane of curvature has been applied onto the outside of the bend. Body D is identical to body A, or can be considered as the quarter ring part of body C after 180° rotation with respect to the z-axis. A uniform flow parallel to the plane of curvature has been applied on the inside of the bend for body D. Hence body D is distinguished from body A where the flow is normal to the plane of curvature. Symmetry boundary conditions were assigned to the top plane boundary of intersection with the curved cylinder. The specific boundary conditions for this set will be discussed in Chapter 5. Furthermore, the flow past body D with a vertical addition of a straight cylinder six diameters long on the upper end has also been investigated.

The emphasis on this set of computations is to study the effect of these two different leading edge orientations on the vortex shedding patterns of the curved cylinders under a uniform flow in the plane of curvature.

1.4 Synopsis

The motivation behind this research has now been presented and the aims and objectives of this work have been identified. The problem definition has been outlined including a combination of different body shapes and inflow cases for this study. The format of the rest of this thesis is as follows:

- Chapter 2

  The past literature will be reviewed including first a general introduction to bluff body flows. Straight circular cylinders under uniform flow will then be presented considering particularly the shedding features in the laminar and wake transition regimes which are of interest to this study. Straight circular cylinders subjected to sheared inflow will subsequently be examined and the flow past oblique and tapered cylinders will be discussed. Finally, the flow past the ring, a geometry without ends but which introduces the effect of curvature on the straight circular cylinder, will be presented. This chapter will conclude with a short section on straight cylinders in proximity to the ground.

- Chapter 3

  The computational method employed is presented in this chapter. The mesh generation procedure will be first overviewed. The Navier-Stokes algorithm and its temporal discretization will then be discussed. Subsequently, the solution in one-dimension to a Helmholtz problem will be presented along with the spectral/*hp* element formulation for spatial discretization. The details of the three-dimensional computations will then be summarized. Finally, the post-processing utilities employed to analyse the computational results will be discussed.

- Chapter 4

  The first set of results, where the flow is normal to the plane of curvature, will be presented in this chapter. A combination of different inflow and wall boundary conditions have been applied and the corresponding results compared.

- Chapter 5

  This chapter will present the computational cases where the flow is parallel to the plane of curvature. The differences in the flow features observed for the two alternative configurations will be discussed. Moreover, the computational results will be qualitatively compared with the experimental flow-visualizations.

- Chapter 6

  Finally, the conclusions from this work are drawn in Chapter 6 and recommendations for further work are put forward.

Chapter 2

Literature Review

2.1 Background on bluff body flows

In order to properly introduce the past literature conducted in this field, it is necessary first to define what a bluff body is. A bluff body is one that is associated with a high degree of separation when flow is introduced around it ("extensive regions of flow separation" (Bearman 1998)). The boundary layers developed around the bluff body, as a result of the no-slip condition on the body's surface, separate as they cannot support the adverse pressure gradient. This flow separation occurs usually for bluff bodies at positions where the velocity at the edge of the boundary layer is larger than the free-stream's (Bearman 1998). Once the boundary layers separate, they then become free shear layers. When a critical Reynolds number is reached, which is body-dependent (see next section for circular cylinder), the process of vortex shedding is initiated.

As Gerrard (1966) discussed, a growing vortex is fed by circulation from the shear layer. When the vortex becomes strong enough, it draws fluid from the opposite side of the wake which eventually follows three pathways depicted by Gerrard (1966): part of it is entrained in the growing vortex, part of it is entrained by the shear layer of the corresponding growing vortex and finally a small part of it advances in the interior of the formation region in a reversed flow. When the feeding of opposite sign vorticity becomes large enough, the supply of circulation to the growing

vortex stops; hence the vortex detaches from the corresponding shear layer. This continuous process of the shear layers interacting and rolling up resulting in the alternate shedding (asymmetric instability is necessary) of vortices of opposite sign in a staggered array in two rows in the wake is termed vortex shedding. The alternate shedding of vortices can cause unsteady forces of high amplitude, primarily in the lift direction, which under some circumstances can cause structural failures.

With vortex shedding being a periodic phenomenon, a non-dimensional way to express its frequency is required, and that is named the Strouhal number, St, defined as:

$$St = \frac{fd}{U_\infty} \tag{2.1}$$

where f is the vortex shedding frequency, d is the characteristic length of the bluff body, and U_∞ is the free-stream velocity. Note that in Chapters 4 and 5 the terms St_{Fx}, St_{Fy}, and St_{Fz} will be employed to denote the frequencies in each of the three Cartesian directions.

This Strouhal number is however body-dependent. In an effort to describe the shedding phenomenon irrespectively of the actual body that caused it, Roshko (1955) defined a "universal" Strouhal number, St^*, based on wake parameters as follows:

$$St^* = \frac{fd'}{U_s} \tag{2.2}$$

where d' is the wake width and U_s is the velocity at separation. Bearman (1967b) also devised a universal wake Strouhal number using as the characteristic length the lateral displacement between the vortex rows.

Roshko (1955) noted that the decisive region for the flow features of a bluff body is the vortex formation region in the first four-to-five diameters behind the body. Placing an interference element, such as a splitter plate, in the near wake increases the base pressure and decreases the drag and shedding frequency as the shear layers are not allowed to interact and roll up in the critical region in the immediate vicinity of the rear of the cylinder (a downstream shift of the vortex formation region). For a specific bluff body shape, a decrease in drag is associated with an increase in wake

width and a decrease in shedding frequency. Comparing among different bluff body shapes though, the bluffer the body is, the larger the wake width and drag are, and the lower the Strouhal number.

The process of vortex shedding creates a pressure deficit in the wake, as the pressure at the rear of the bluff body does not recover the value of the stagnation pressure. This brings about a resultant pressure drag that for bluff bodies is the most significant component of the total drag. A non-dimensional way to represent the pressure at the rear of the bluff body, which is also a very receptive indicator of the vortex formation process, is the base pressure coefficient, C_{pb}, defined as:

$$C_{pb} = \frac{p_b - p_\infty}{\frac{1}{2}\rho {U_\infty}^2} \tag{2.3}$$

where p_b is the base pressure (180° from the front stagnation point), p_∞ is the pressure at the free-stream and ρ is the density of the fluid. Note that the term base suction coefficient is often encountered in the literature and refers to the negative of the base pressure coefficient ($-C_{pb}$).

Both the Strouhal number and the base pressure coefficient vary with Reynolds number ($Re = \frac{U_\infty d}{\nu}$, where ν is the kinematic viscosity of the fluid and the rest of the terms are as above). The curves of St vs. Re and of C_{pb} vs. Re for the circular cylinder required the work of many researchers (with considerable scientific debate in some cases) and are often representative of the cylinder's vortex shedding stage as will be discussed in the next section.

Before proceeding with the past literature on various cylinder and flow configurations, two remarks should be made within the scope of the computational work conducted in this study. For cylinders whose axis does not make a 90° angle with the free-stream, a sectional two-dimensional argument considers the local normal Reynolds number, Re_l, based on the cosine law (similarly to what we will see below for the case of oblique cylinders):

$$Re_l = Re \cos\theta \tag{2.4}$$

where θ is the angle between the horizontal plane and the plane of the corresponding

cross-section. In Chapters 4 and 5 the applicability of this argument, employed by a lot of the empirical methods, will be discussed in relation to the findings of the three-dimensional computations performed in this work.

Moreover, two-dimensional computations for circular cylinders at Reynolds numbers above 200 have been shown in past literature to considerably overpredict the force coefficients compared to experimental findings. Graham (1992) presented a compilation of data from various two-dimensional codes and compared with a three-dimensional computation and experimental results. He found that two-dimensional simulations exhibit the wrong trend for the force coefficients, most remarkably for the lift coefficient. Szepessy & Bearman (1992) also reported on the differences, between two-dimensional flow computations and experiments, in measured data of the fluctuating lift coefficient at high Reynolds numbers. The three-dimensionalities present even in the straight cylinder wake above a certain Reynolds number as will be seen below dictate a three-dimensional treatment of the flow in computational approaches.

In this chapter hence the past literature on the uniform flow past straight cylinders will be presented first in section 2.2. After discussing the intrinsic three-dimensionalities of such a uniform flow past a uniform 2D geometry, flows where three-dimensionalities are introduced either in their upstream profile or in the actual geometry of the body will be described. Shear flows past straight cylinders will thus be considered in section 2.3. The uniform flow past oblique cylinders will then be discussed in section 2.4, in particular the effect of the yaw angle by which the straight cylinder is inclined into the flow. The literature on tapered cylinders will subsequently be overviewed in section 2.5. Furthermore, with the flow past curved cylinders being the subject of this thesis, the effect of curvature will be considered. The past literature on the shedding patterns in the wake of the ring geometry is hence presented in section 2.6. Finally, the flow past a straight cylinder in proximity to a wall boundary will be briefly discussed in section 2.7.

2.2 Straight circular cylinders under uniform flow

Among the various bluff bodies, the flow past the straight circular cylinder has received most attention over the past century. The number of practical engineering applications that the circular cylinder shape has along with the fascinating nature of the fluid mechanics developed even when such a simple geometry is placed in a fluid at a range of Reynolds numbers has initiated a vast amount of studies. Various reviews over the past years have been devoted to the study and description of the phenomenon of vortex shedding. In one of the earlier ones, Berger & Wille (1972) presented, as their introduction to periodic flow phenomena, the vortex trails resembling the von Kármán street behind islands.

In this section we will first examine the flow regimes of the circular cylinder with increasing Reynolds number. The features of the laminar and the wake transition regime will then be described in more detail as they are of interest to the findings of this study. In the laminar regime the parallel and the oblique shedding modes will be presented in relation to the Strouhal-Reynolds number curve. The influence of end effects will be discussed and ways to promote parallel shedding will be overviewed. In the wake transition regime the three-dimensional modes of instability will be presented through experimental but also through computational studies performed mostly in the past decade in the literature.

2.2.1 Flow regimes for the circular cylinder

The circular cylinder has been found to exhibit different flow regimes with increasing Reynolds number. These regimes are manifested in the curve of the base suction coefficient vs. Reynolds number, Figure 2.1, produced from several sources by Roshko (1993). While mostly the regimes covering up to the maximum Reynolds number of this study ($Re = 500$) will be overviewed in this section, the key Reynolds numbers for the flow past the circular cylinder from that point onwards will be identified. A full description of the flow regimes can be found by Roshko (1993) and a review of the various studies in each one of them is presented by Williamson (1996).

For very low Reynolds numbers, the flow is still attached to the cylinder's surface.

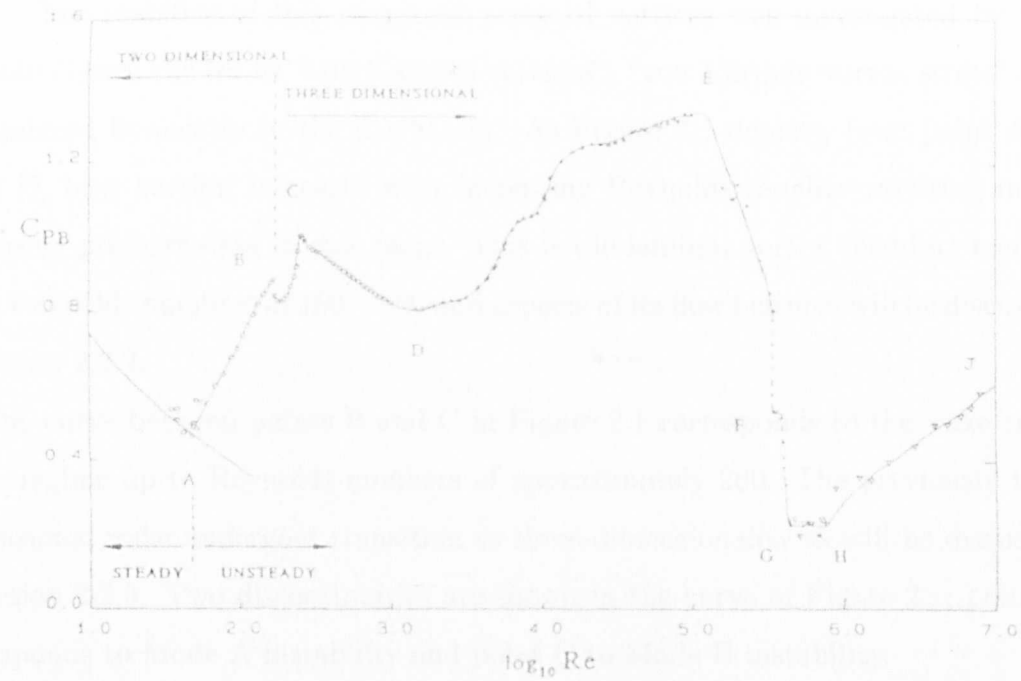


Figure 2.1: Variation of the base suction coefficient, $-C_{pb}$, with Reynolds number (data from several sources (Roshko 1993))

Increasing the Reynolds number, the flow starts separating and a recirculation region is formed consisting of two vortices positioned symmetrically with respect to the wake centreline.

The initiation of vortex shedding, represented by point A in Figure 2.1, has been found to occur at Reynolds numbers between 47 and 49 and is demarcated by a Hopf bifurcation in a transition that is not hysteretic (primary instability). The flow past the cylinder has now become unstable to any perturbations. Henderson (1995) performed a numerical study at the onset of vortex shedding using a spectral element method in two-dimensions. Starting his first simulation at a Reynolds number of 25, and incrementing at intervals of 5 the Reynolds numbers of his simulations, he found the critical Reynolds number to fall between 45 and 50. No steady state solution could be achieved after this range as any infinitesimal perturbation will grow too quickly, resulting in the periodic solution of laminar vortex shedding. Henderson (1995) showed the distinct change from a steady to an unsteady wake to be marked by a sharp transition in the drag and base pressure coefficient curves.

An anti-symmetric configuration of vortices develops in what is now an unsteady

wake. The stability of this staggered array of vortices was investigated by von Kármán (hence the terms "von Kármán vortices", "von Kármán vortex street" etc. encountered frequently in the literature). As Figure 2.1 depicts, from point A to point B, base suction increases with increasing Reynolds number resulting in an increasing pressure drag in this range. This is the laminar vortex shedding regime, up to Reynolds numbers of $160-194$, and aspects of its flow features will be discussed in section 2.2.2.

The curve between points B and C in Figure 2.1 corresponds to the wake transition regime up to Reynolds numbers of approximately 260. The previously two-dimensional wake undergoes transition to three-dimensionality as will be discussed in section 2.2.3. Two discontinuities are shown in the curve of Figure 2.1; point B corresponds to Mode A instability and point C to Mode B instability.

As the Reynolds number is increased from point C in Figure 2.1 the base suction is found to decrease hence resulting in a pressure drag reduction. An increasing disorder in the fine-scale three-dimensionality appears (Williamson 1996).

Finally, at a Reynolds number of approximately $1,000$, point D in Figure 2.1, shear layer transition occurs. The turbulent transition point in the separating shear layers moves upstream (Roshko 1993). At a Reynolds number of approximately $200,000$, point E in the curve of Figure 2.1, a drastic decrease in base suction and drag occurs. A separation reattachment bubble causes the boundary layer to separate further downstream on the cylinder (at approximately 140°) (Roshko 1993). Eventually, in regime H-J transition takes place in the actual boundary layer before separation.

Bearman (1998), pointing out that the transition to turbulence occurs in an upstream route, first in the wake, then in the shear layers and finally in the boundary layers, outlined the key-Reynolds numbers for the flow past a circular cylinder as follows:

- **Re $\approx$ 47** : onset of vortex shedding (primary instability)
- **Re $\approx$ 160**: intrinsic three-dimensionality in the wake first appears (secondary instability)

- **Re $\approx$ 1,000**: transition starts to appear within the shear layers separating from the cylinder
- **Re $\approx$ 200,000**: transitional effects in the boundary layer first affect the flow

2.2.2 Shedding configurations in the laminar regime

Discontinuity in the Strouhal-Reynolds number curve and oblique shedding

In 1972 Berger & Wille had discussed the presence of a parallel and a slantwise (oblique) pattern of vortex shedding, where the vortices shed are inclined with respect to the cylinder axis. Related to the issue of oblique shedding, in one of the first investigations, Tritton (1959) had observed a discontinuity in his plot of the Strouhal vs. Reynolds number curve. He identified a "low-speed" mode and a "high-speed" mode with the transition between them occurring at a Reynolds number of approximately 90. He associated the origin of the former mode with an instability of the wake, whereas that of the latter with an instability directly close from the cylinder. While in general he observed angles of up to 30° between the vortices and the cylinder axis, smaller angles, less than 10°, were more frequently encountered in the low-speed mode rather than the high-speed one.

The source of this discontinuity became the point of discussion for many investigations later on in relation to whether it is an intrinsic phenomenon or it is associated with the condition of the flow upstream. Thirty years later, Williamson (1989) distinguished two modes for oblique vortex shedding and linked the discontinuity of the Strouhal-Reynolds number curve to the transition between those two oblique modes. The first mode, found for Reynolds numbers larger than 64, forms the so called chevron pattern. The slantwise appearance of the vortices is initiated from the end effects discussed in a subsequent section. Without considering the end cells (which correspond to a lower frequency), the entire rest of the span is shedding at one frequency. The second oblique shedding mode, found for Reynolds numbers smaller than 64, pertains to a central cell of higher frequency bound by two cells of

lower frequency, on each side of the midspan, and finally the end cells. This oblique shedding pattern is associated with the presence of vortex dislocations as a result of cells of different frequency becoming out of phase with each other. The phenomenon of vortex splitting or dislocation refers to a vortex dividing and connecting with two other vortices of the same sign at the other cell as will be further discussed in a later subsection.

In answer to Tritton's interpretation of the discontinuity in the Strouhal vs. Reynolds number curve, Williamson (1989) claimed that the discontinuity was brought about probably by the same transition of modes, even though it occurred at higher Reynolds number. Furthermore, Williamson (1989) deduced a shedding angle of $12 - 14°$ for the transition between modes for Tritton's data, whereas for his experiments a critical angle of 19° was found. Once parallel shedding was induced, however, a continuous Strouhal-Reynolds number curve could be attained as was also found by Hammache & Gharib (1989).

König *et al.* (1990) also attributed the discontinuity of the Strouhal-Reynolds number curve to the end conditions established at the cylinder boundaries. A continuous curve was observed once parallel shedding was achieved using hollow cylinders at the two ends as will be discussed below. Once the hollow cylinders were removed, discontinuities appeared in the Strouhal-Reynolds number curve with the first one occurring at a Reynolds number of approximately 65 as in Williamson (1989). The largest shedding frequencies were measured with the parallel shedding mode. For oblique shedding they found smaller shedding frequencies with largest values of approximately 23° for the oblique shedding angle.

The influence of end effects

In general end effects can refer either to a free end of the cylinder or an endplate attached at the cylinder span. Frequently in experimental investigations endplates are used to isolate the flow on the cylinder span from the wind tunnel wall boundary layers. As mentioned before, Williamson (1989) attributed the phenomenon of oblique vortex shedding to end effects. In a towing tank experiment, the parallel mode is often encountered initially, until the end effects are felt throughout the

span resulting in an oblique shedding mode. The parallel mode was considered as the most unstable one, whereas from the two oblique shedding modes mentioned previously, the second one was conjectured to be more unstable. Overall, the end effects were found to have a direct influence for a spanlength of approximately ten diameters and an indirect effect for the rest of the span.

In their experiments with a cylinder towed in a water tank, Slaouti & Gerrard (1981) observed a "suppression of the vortex shedding" behind the bottom free end of the cylinder with an inclination of the vortices and bowing towards the bottom cylinder end. Gerich & Eckelmann (1982) conducted an experimental study in a wind tunnel on the influence of end effects in the circular cylinder wake. They found that end effects result in the regions close to them having a lower frequency, approximately $10 - 15\%$ less than the shedding frequency of the main cylinder part. A beat phenomenon is then observed as a result of the difference frequency between the main cylinder part and the region directly influenced by the end effects. Similar modulations have been observed at higher Reynolds numbers also in the experimental study of Szepessy & Bearman (1992) where moveable end plates were used for different cylinder aspect ratios.

Promoting two-dimensionality

Various methods can be found in past literature for inducing parallel shedding past a circular cylinder. Angling inwards the leading edge of the endplates was found by Williamson (1989) to promote two-dimensionality. On the other hand, end suction control allowed the continuous variation of the end boundary conditions also achieving parallel shedding (Williamson 1992b). Miller & Williamson (1994) placed two suction tubes towards the cylinder boundaries at a downstream distance of ten diameters from the cylinder. They found that an increase of the local incident velocity at the cylinder ends only by $1.5 - 2\%$ above free-stream was adequate to promote parallel vortex shedding.

Eisenlohr & Eckelmann (1989) placed short hollow cylinders of slightly larger outer diameter (approximately 1.8 to 2.2 cylinder diameters) on the test cylinder ends, near both endplates, and found parallel, two-dimensional shedding to be pro-

moted. Hammache & Gharib (1989, 1991) positioned two control cylinders transverse to the test cylinder and upstream in order to promote two-dimensionality. They found that parallel shedding could be achieved when the two control cylinders were both placed at the same distance upstream of the test cylinder equal to a specific optimum value that the vortices in the controlled region remain straight and parallel to the cylinder axis. This optimum value is a function only of the diameter of the control cylinders. In their experimental study of the parallel and oblique vortex shedding modes, Hammache & Gharib (1991) demonstrated that oblique shedding is a result of a pressure gradient at the rear of the cylinder. In order to achieve parallel vortex shedding, the pressure distribution imposed has to be uniform over the centre span of the cylinder; and placing the control cylinders upstream of the test cylinder is one way to achieve this. On the other hand, a spanwise velocity component is associated with the oblique shedding mode as a result of the pressure difference between the cylinder ends.

An illustration of the parallel shedding patterns achieved by all the above techniques can be found in the review by Williamson (1996).

2.2.3 Experimental and computational studies of the flow structures in the wake transition regime

Williamson (1988) showed that the transition to three-dimensionality for the circular cylinder wake involves two stages that manifest themselves also as discontinuities in the Strouhal-Reynolds number curve depicted in Figure 2.2. The wake can no longer preserve a two-dimensional state even with control of the spanwise end conditions in this transition regime. The first discontinuity occurs at a Reynolds number of approximately 180 (a range of $180 - 194$ has been reported in the past depending on experimental conditions (Williamson 1996)) in a transition that is hysteretic. It has been named Mode A and involves the deformation of the spanwise vortices in a wavy fashion and the formation of streamwise vortex loops, depicted in Figure 2.3(a), whose two ends constitute effectively a pair of counter-rotating streamwise vortices. This procedure is self-sustaining with the vortex loops forming at the

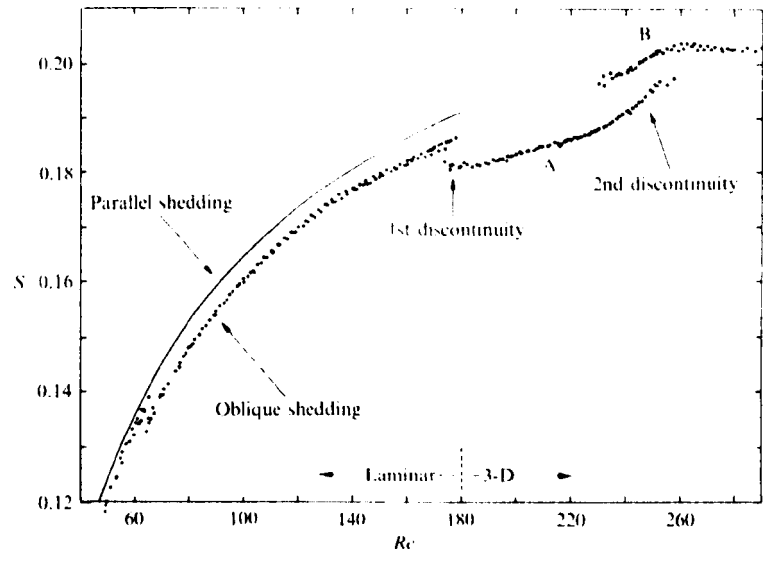


Figure 2.2: Variation of Strouhal vs. Reynolds number in the laminar and wake transition regimes (Williamson 1992a). The two discontinuities attributed to Mode A and B instabilities are depicted in this curve.

same spanwise locations over the shedding cycles. The second discontinuity occurs at Reynolds numbers between 230 and 260 and is not hysteretic. It has been named Mode B and entails finer-scale streamwise vortices, as can be observed in Figure 2.3(b). A gradual transfer of energy from the lower-frequency mode of shedding to the upper one is apparent in the spectra of velocity fluctuations at these Reynolds numbers (this corresponds to a transfer of energy from frequencies related to curve A of Figure 2.2 to frequencies related to curve B).

It should be noted that Figure 2.2 demonstrates also the discontinuity at $Re = 64$ attributed to the two different oblique shedding modes in section 2.2.2. The higher shedding frequencies associated with parallel shedding compared to the oblique shedding ones are also depicted.

In his experimental study of the flow past circular cylinders, Norberg (1994) also found the two modes of instability observed by Williamson while his data for base suction indicated a relatively weak influence of the cylinder's aspect ratio in this regime.

Williamson (1996) reviewed the findings on Mode A and B and showed the symmetries that each mode accounts for: Mode A involves a staggered arrangement

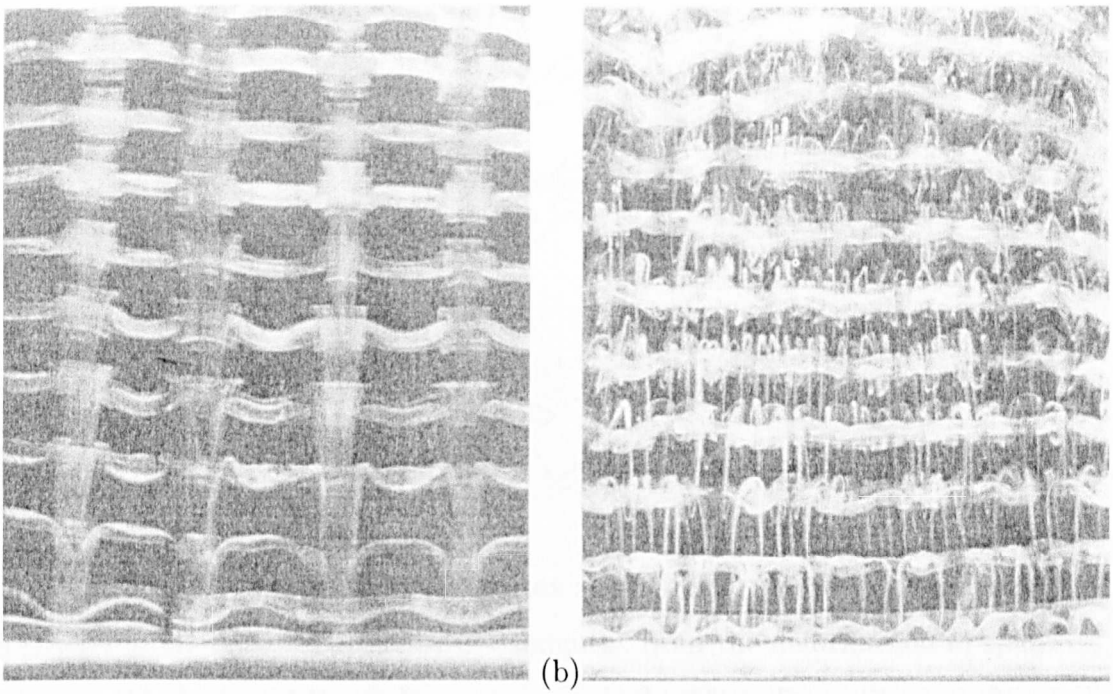


Figure 2.3: (a) Deformation of spanwise vortices and formation of streamwise vortex loops for Mode A; (b) Finer scale streamwise vortex pairs for Mode B (Williamson 1992a)

of streamwise vortices from one braid to the next one with a spanwise wavelength of approximately 4 diameters, whereas Mode B involves an in-line arrangement with a spanwise wavelength of about 1 diameter.

Brede *et al.* (1996) performed an experimental study of the wake of a circular cylinder at Reynolds numbers between 160 and 500. They recognized Mode A with a spanwise wavelength of 4.5 diameters at Reynolds numbers from 160 to 240 and Mode B with a spanwise wavelength of 1 diameter at Reynolds numbers larger than 240. In agreement with the staggered arrangement described by Williamson for Mode A, they also observed regions of positive and negative streamwise vorticity alternating in the spanwise direction and in time as the sign of ω_x changes twice every Kármán cycle. The staggered arrangement is formed by each primary vortex pulling out a new spanwise row of secondary (streamwise) vortices in what they called a shape of "tongues", shown in Figure 2.4. Mode A is therefore related to the deformation of primary vortices. As these vortex "tongues" stem from counter-rotating spanwise vortices, with increasing time they have opposite sense of rotation.

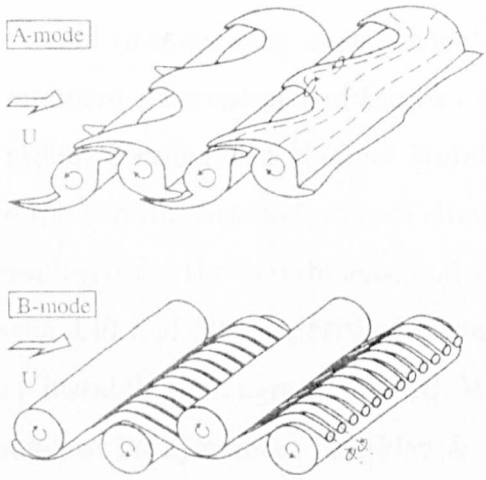


Figure 2.4: Schematic drawing of the vortex structures for Mode A and B instabilities (Brede *et al.* 1996). The shape of "tongues" from the deformation of spanwise vortices for Mode A and the in-line arrangement for Mode B are illustrated.

For Mode B, however, Brede *et al.* (1996) observed an in-line arrangement with a spanwise change in the sign of w_x but no change in time of the sign of streamwise vorticity at a specific spanwise location. Therefore they too concluded that, unlike Mode A, these secondary vortices are not related to any deformation of the primary vortices. The vortex pair structure of Mode B was also visualized in the particle-image-velocimetry measurements of Wu *et al.* (1994).

On the computational side now, only during the past 10-13 years has it been feasible to study the 3D wake transition regime with computational methods as a result of the increasing computing power. Some of the studies that have been performed to investigate whether agreement with experiments is achieved or not are presented below.

Thompson *et al.* (1995, 1996) employing a high-order spectral element method with the Fourier extension in the spanwise direction investigated the transition of the circular cylinder wake to three-dimensionality. In agreement with the previous findings, they found streamwise vortex structures with a spanwise wavelength of $3-4$ cylinder diameters for their numerical simulation at $Re = 210$. The spanwise vortex rollers are connected by streamwise vortex loops. At a Reynolds number of 250,

they visualized Mode B with a spanwise wavelength for the streamwise structures of one diameter. Mode B was found to occur only once Mode A was established, and for intermediate Reynolds numbers a coexistance of the two modes was suggested.

Henderson & Barkley (1996) conducted a Floquet stability analysis of three-dimensional disturbances to the two-dimensional wake of circular cylinders. A spectral element method was employed for the two-dimensional simulations at a range of Reynolds numbers between 140 and 300. A critical Reynolds number of 188.5 was found for this secondary instability. In agreement with Williamson (1988), this mode of instability was found to be hysteretic. Barkley & Henderson (1996) reported a critical spanwise wavelength of 3.96 diameters for this critical Reynolds number corresponding to previous findings for Mode A. A second critical Reynolds number, corresponding to Mode B transition, was found to be that of 259 with a wavelength of 0.822 diameters. They also discussed, in agreement with the stability analysis of Thompson *et al.* (1996) and the experimental findings of Williamson (1988), the coexistance of the two modes at this range of Reynolds numbers; even at Reynolds numbers where Mode B is dominant, the wake of the circular cylinder could physically amount to a mixture of both modes. The two-dimensional wake at the second critical Reynolds number is already unstable to the longer wavelength perturbations corresponding to Mode A. In answer to the question how can Mode B be apparent at Reynolds numbers lower than the second critical, something that is not explained by this stability analysis, Barkley & Henderson (1996) pointed out that the transition from Mode A to Mode B would be bound by the stability analysis of Mode A and not the stability of the two-dimensional vortex street. The non-linear interaction of the two modes and the destabilizing effect of Mode A was subsequently considered by Barkley *et al.* (2000) who found the mixed-mode state to terminate at $Re \approx 265$, above which only the pure Mode B state was detected. Finally, the outcome of a critical Reynolds number of 170 with a spanwise wavelength of 1.8 diameters in the Floquet stability analysis of Noack *et al.* (1993) has been attributed to the low-dimensional method employed (10^2 as opposed to 10^4 spatial degrees of freedom used by Barkley & Henderson (1996)). Recently, critical Reynolds numbers of 190 and 261 with unstable wavelengths of 3.96 and 0.825 diameters respectively

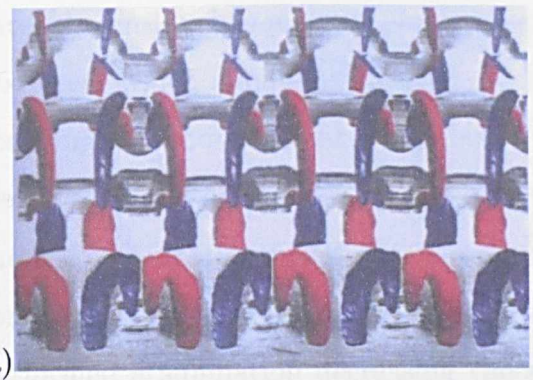
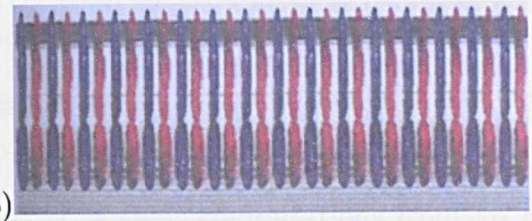
(a)  (b) 

Figure 2.5: Vorticity fields from the numerical simulations of Henderson (1998) at: (a) $Re = 195$, Mode A instability, (b) $Re = 265$, Mode B instability. Red and blue contours highlighting the positive and negative extremes in streamwise vorticity components.

for Mode A and Mode B were determined by the stability analysis of Posdziech & Grundmann (2001) in confirmation to the findings of Barkley & Henderson (1996).

Henderson (1998) suggested that the relatively long wavelength (approximately 4 diameters) of Mode A can be related to the primary instability of the wake scaling to the von Kármán vortex spacing. On the other hand, Mode B has a much shorter wavelength that he conjectured to scale on the thickness of the separating shear layer. Henderson (1998), in agreement with the experimental findings of Williamson (1996) and Brede *et al.* (1996), visualized in his computations also the two symmetries, shown in Figure 2.5: a staggered array of streamwise vortices for Mode A and an inline array of streamwise vortices for Mode B. It should be drawn to attention that in nature a mixture of Mode A and Mode B would be found at the intermediate Reynolds numbers 230−260 as opposed to the computer simulations where the initial conditions correspond to the 2D base flow perturbed with the exact eigenmode for the instability.

In one of the earliest computational studies of the three-dimensionality of the cylinder wake, Karniadakis & Triantafyllou (1992) had investigated numerically the transition of the cylinder wake from two-dimensionality to turbulence. They employed a spectral element technique and performed three-dimensional simulations in a range of Reynolds numbers up to 500. They found that the wake becomes

three-dimensional as a result of a secondary instability of the two-dimensional vortex street which manifests itself at a Reynolds number of approximately 200. The spanlength of most of their computations was π, however the diameter of the cylinders was 2 non-dimensional units. They claimed that the route to turbulence in the wake of circular cylinders is through the period-doubling mechanism. Thompson *et al.* (1995), in answer to this finding of Karniadakis & Triantafyllou (1992), performed a simulation decreasing the spansize of their computations from πd to $\pi d/2$. They found the period-doubling to appear only for the shorter spansize simulation, hence highlighting the fact that simulations with spanlenghts smaller than the critical wavelength for the secondary instability may introduce spurious effects.

Closing up this section on the wake transition, a note should be made on an interesting phenomenon occurring towards the end of this regime. Prasad & Williamson (1997) showed that at a Reynolds number of 260, point C in Figure 2.1, parallel shedding conditions can be induced again. The base suction coefficient reaches a local maximum and periodic vortex shedding patterns suggestive of those in the laminar shedding regime can then be observed.

2.2.4 Dislocations and their relation to the wake transition

Eisenlohr & Eckelmann (1989) described the vortex splitting process "in which neighbouring vortex filaments of one core split apart, to merge into the offset cores of other vortices". As a result of varying shedding frequency along the span of the body, the vortex axes start either becoming curved or changing their angle with respect to the cylinder axis. When this oblique angle becomes too large or the axes become too curved, they found that vortex splitting takes place. The presence of characteristic envelope profiles in the velocity signals or force measurements is often associated with this procedure of vortex splitting.

Williamson (1992a) studied the formation of dislocations in the cylinder wake. In order to investigate whether the presence of dislocations is a natural phenomenon of the transition of the cylinder wake to three-dimensionality, he conducted an experimental investigation forcing dislocations to occur at the span of the cylinder.

The experiments were performed at a Reynolds number of 120, which is lower than the onset of the transition regime. This way it would be clearer to track down the evolution of the dislocation features in an otherwise two-dimensional wake in principle at such a Reynolds number. In order to force the dislocations to occur, Williamson (1992a) placed a ring of diameter equal to 1.5 cylinder diameters and height (spanlength) equal to half of a cylinder diameter at a specific spanwise location.

A dislocation is thus defined to occur when the spanwise vortices fall out of phase with each other and then split and connect with vortices of the same sign at the boundary of the cells of different frequency. The dislocations were divided in the following three categories in terms of their nature: (a) one-sided, where the dislocation develops at the boundary between two cells of different frequency, Figure 2.6(a), and (b) two-sided, where a local phase variation exists within a larger shedding cell which would otherwise be of constant phase, Figure 2.6(b). The latter type of dislocations can be found in a stable or in an unstable (transient) arrangement. The one-sided dislocation is usually an asymmetric configuration whereas the two-sided dislocation in its stable form is usually a symmetric configuration.

Williamson (1992a) found similarities, such as the streamwise bending of the vortices at the dislocation sides and the spanwise spreading of this phenomenon, between the structures of forced dislocations and dislocations occurring naturally during the transition of the wake to three-dimensionality. However, the external forcing (as in this case with the ring disturbance) initiates a sequence of periodic dislocations whereas the transition to three-dimensionality is associated with the growth of intermittent dislocations mirrored in irregular velocity signals.

He concluded that the dislocations are indeed an inherent characteristic of the wake transition regime of the circular cylinder with its three-dimensional vortex dynamics. In this regime is usually the symmetric two-sided configuration encountered more often or the one-sided configuration when a coexistance of Mode A and Mode B takes place. Finally, it should be noted that dislocations have also been found to occur in the laminar shedding regime associated with the end effects at the cylinder boundaries (one-sided dislocations).

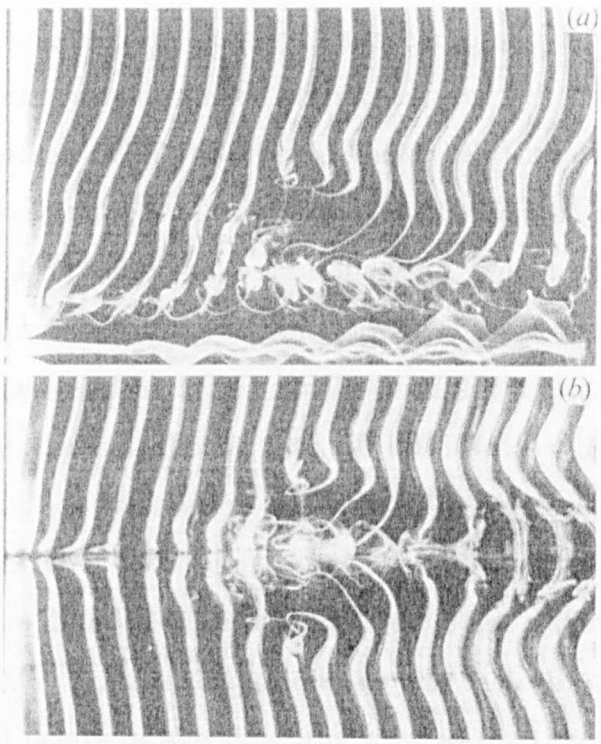


Figure 2.6: Comparison of: (a) one-sided, and (b) two-sided vortex dislocations. Flow is from left to right (Williamson 1992a).

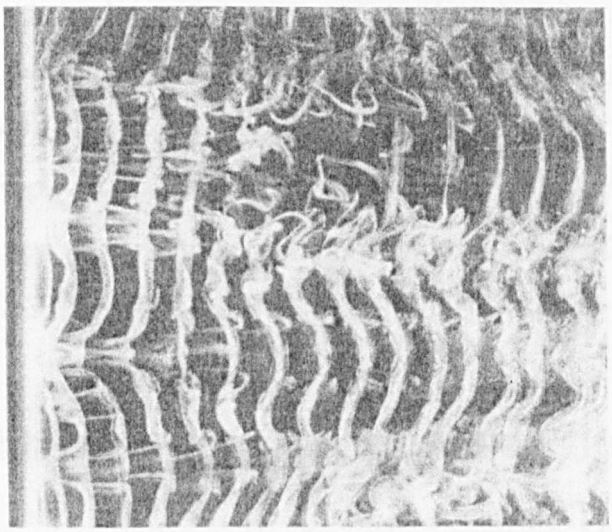


Figure 2.7: Dislocations occurring naturally in the wake transition regime, Re=210 (Williamson 1992a)

As will be described in sections 2.3 and 2.5 dislocations (mostly one-sided) are also encountered for non-uniform flows, such as shear, past cylinders and for uniform flows past non-uniform cylinder shapes, such as tapered cylinders.

Tombazis & Bearman (1997) investigated how the dislocations they previously observed in the wake of bluff bodies with a blunt trailing edge would be affected by applying a wavy deformation at the trailing edge. Such a dislocation is also depicted in Figure 2.8, extracted from Bearman (1998). Wind tunnel and water flume experiments were performed at high Reynolds numbers using a half-ellipse model with a blunt trailing edge and showed that the introduction of this mild geometric disturbance fixed the positions where the dislocations appeared. The presence of dislocations was associated with the bowing of the vortices backwards towards the body to adapt to the difference in shedding time of the different locations in the cylinder span. Specifically, if in one shedding cycle the cell at the peak (furthest downstream section) delays its shedding, the vortices from the valley (furthest upstream section) will bend further back. As described also by Eisenlohr & Eckelmann (1989), a vortex split is then found to occur when this bowing angle becomes too large; a vortex from the peak would connect at that time with two vortices from the adjacent valley. Finally, Tombazis & Bearman (1997) showed that the introduction of the waviness at the trailing edge resulted, along with fixing the dislocation positions, in an increase in formation length and base pressure and a decrease in the drag when compared to the straight model.

In conclusion of this section on straight cylinders, recent reviews for further information on the flow past circular cylinders comprise those of Williamson (1996), Bearman (1997), Bearman (1998) and Norberg (2003).

2.3 Straight cylinders under shear flow

Proceeding now with a non-uniform velocity profile upstream, Maull & Young (1973) showed that the shedding pattern developed for shear flows past bluff bodies occurs in spanwise cells. They noted that when the Strouhal number was based on the midspan velocity, it was found to be constant along each cell. The cell boundaries

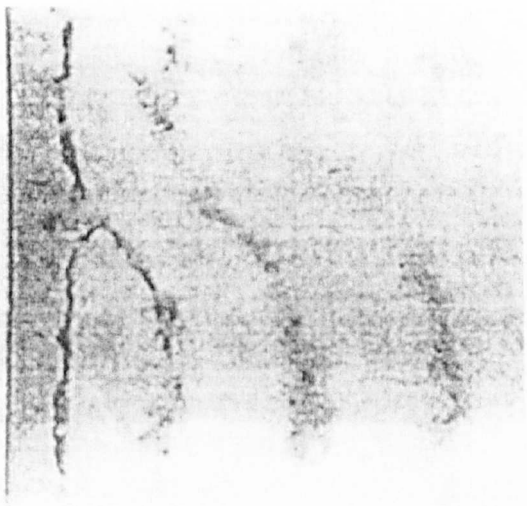


Figure 2.8: Vortex splitting in the wake of bluff bodies with a blunt trailing edge (Bearman 1998)

were also apparent from the changes in the slope of the base pressure coefficient curve. Moreover, they associated the divisions between spanwise cells of different frequencies with the presence of longitudinal vortices at the cell boundaries.

Mair & Stansby (1975) also conducted experiments on cylinders of various cross-sections and aspect ratios. A number of cells were observed along the span of the cylinders from measurements of the vortex shedding frequency. They suggested that there is perhaps an upper limit to the spanwise length of the cells, and they reported greatest cell lengths in the range of $4-6$ diameters.

In a review paper, Griffin (1985) summarized the key-findings from experiments performed over the years with circular, rectangular and D-section cylinders under shear flows. Each shear flow profile is characterized in terms of a "steepness or shear parameter", $\overline{\beta}$, defined for circular cylinders as follows:

$$\overline{\beta} = \frac{D}{\overline{V}_{REF}} \frac{d\overline{V}}{d\overline{z}} \tag{2.5}$$

where in this case D is the cylinder diameter, $\overline{V}_{REF}$ is the midspan incident velocity and $\frac{d\overline{V}}{d\overline{z}}$ is the velocity gradient. Shear parameters of $0.01-0.015$ describe in principle a moderate shear level. Figure 2.9 depicts the key-terms used in equation (2.5) to describe a shear flow past a bluff body.

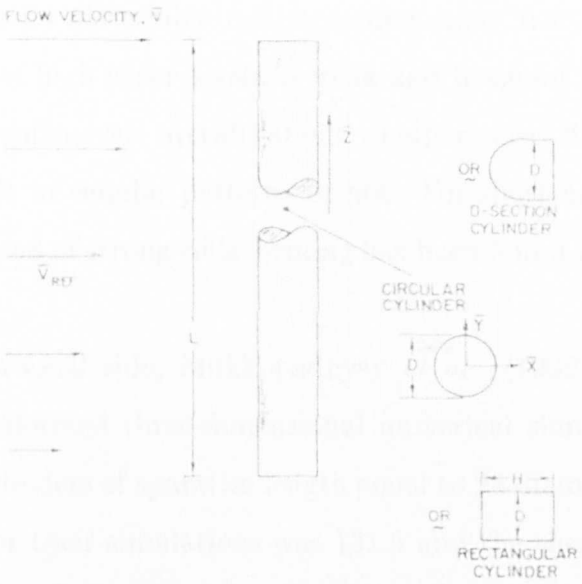


Figure 2.9: Description of parameters for shear flows past various bluff bodies (Griffin 1985)

The points reviewed by Griffin (1985) on linear shear flows past circular cylinders are briefly summarized below:

- A cellular vortex shedding pattern has been found to develop in the wake of a circular cylinder under shear flow. The number of spanwise cells and the base pressure and drag variation along the cylinder rely upon its aspect ratio, and are highly sensitive to end conditions.

- From experiments with relatively high values for the shear parameter, it has been concluded that when the shear flow is highly turbulent, the critical Reynolds number decreases by a factor of ten compared to that for an incident uniform smooth flow on the circular cylinder. Note that the critical Reynolds number refers to the onset of the drag-crisis and is of the order of 10^5 for a smooth circular cylinder in uniform flow.

- Surface-roughened circular cylinders in shear flow have also been found to exhibit the characteristic cellular vortex shedding pattern.

Finally, in his review, Griffin (1985) reported that shear flows past high aspect ratio cylinders (L/D = 20 to 50 and larger) at subcritical Reynolds numbers have

been found to form no discernible cell structures away from the end boundaries or, in the presence of high shear levels, a weak and irregular cell structure. There seems to be some controversy, overall, about whether shear flows past high aspect ratio cylinders result in cellular patterns or not. For short aspect ratio cylinders, however, the likelihood of strong cells forming has been found to be strongest at the boundaries.

On the computational side, Mukhopadhyay *et al.* (1999), employing a finite volume method, performed three-dimensional numerical simulations of a sheared flow past circular cylinders of spanwise length equal to 24 diameters first. The mean Reynolds number for their simulations was 131.5 and the shear parameter, β, was 0.02. The cellular shedding pattern reported above was observed in this study also where five cells of constant frequency were discerned. The cells varied in length between three and seven diameters, and in each one of them, the Strouhal number based on the mean velocity was constant whereas the one based on the local velocity was found to vary linearly exhibiting discontinuities at the cell boundaries. Their computational results also showed the presence of dislocations in the wake.

More recently, Mukhopadhyay *et al.* (2002), extended their computational study to cylinders of spanwise length equal to 48 diameters. Along with the cylinder aspect ratio, they evaluated the effects of spanwise grid resolution. Any instantaneous base pressure distribution along the span of the cylinder, both for the 24- and the 48-diameter cylinder, was found to exhibit a number of slope changes, which in general coincide with the cell boundaries, in agreement with the findings of Maull & Young (1973). The 48-diameter cylinder however resulted in multiple dislocations along the span, rather than just a dislocation at the higher velocity end observed for the 24-diameter cylinder. The frequencies of the cells for the 48-diameter cylinder were found to be lower than the frequencies observed for the 24-diameter cylinder, and overall in both cases they were lower than the corresponding two-dimensional cases (parallel shedding) with uniform flow.

In conclusion to this description of shear flows, it must be noted that if the Independence Principle (see next section) is to hold, there may be some similarity between straight cylinders in shear and curved cylinders.

2.4 Oblique cylinders

Ramberg (1983) investigated the flow past yawed circular cylinders in a range of yaw angles from 0 to 60°, where the yaw angle is measured between the cylinder axis and the normal to the free-stream direction. He compared his findings with the Independence Principle according to which the flow over a yawed cylinder is described in terms of the component of the free-stream that is normal to the cylinder axis. Accordingly, for a yawed cylinder the characteristic velocity used is $U_N = U_\infty \cos\theta$, where U_∞ represents the free-stream velocity and θ the yaw angle. For the stationary yawed cylinders he noted an interdependence between shedding angle and shedding frequency and the Independence Principle not to hold: the shedding frequency was greater than the one predicted while the shedding angle, the vortex-formation length, the wake width and the base pressure were all found to be less than expected. However, it is not clear where the lower limits in terms of yaw angle are for this principle not to hold. In an earlier study, Van Atta (1968) had found that for yaw angles up to 35° the shedding frequency decreases nearly with the cosine law, whereas for angles above this value the decrease in frequency with increasing yaw angle is slower than the cosine law.

Recently, Lucor & Karniadakis (2002) performed computations of the flow past yawed fixed circular cylinders at large angles of attack and Reynolds number of 1000 employing the Fourier version of *NekTar* discussed in section 3.2. Their findings confirmed those by Ramberg (1983) in that the base pressure on the yawed cylinder was found to be lower than the value predicted by the Independence Principle. The computational flow visualizations were also in agreement with Ramberg (1983) showing the shedding angle to be smaller than the yaw angle.

Finally, oblique cylinders with a cone attached on top have been discussed by Thomson & Morrison (1971). While no wake exists close to the nose of the body, a symmetric pattern of vortices develops further downstream. For large angles of attack (i.e. small yaw angles), an unsteady flow regime can develop similar to that evolving past a two-dimensional cylinder. Therefore, while at moderate angles of attack the symmetrical wake configuration prevails, at large angles, this

pattern shrinks towards the nose of the body and the asymmetric wake configuration becomes more extensive.

In conclusion, an extensive review on this subject can be found in Zdravkovich (2003).

2.5 Tapered cylinders

Tapered cylinders have many similarities to cylinders in shear flows and will thus be reviewed briefly below.

Gaster (1969) performed experiments on cones of taper ratio (cylinder length by diameter difference between narrow and wide cylinder end) of 36:1 and 18:1. He found a modulated signal for both cylinders at all the locations along the span. This low frequency modulation was found to persist at almost the same value along the length of the model (independent of any physical length of the model) while the shedding frequency at a specific position was found to be a function of the local diameter. The shedding frequencies of these linearly tapered cylinders were found to be slightly lower than those of the corresponding uniform parallel cylinders. In a later paper, Gaster (1971) discussed the flow past a more mildly tapered cylinder, with taper ratio of 120:1. He found vortex shedding to occur still in cells with jumps in frequency between them.

Piccirillo & Van Atta (1993) conducted experiments on linearly tapered cylinders, with taper ratios varying from 50:1 to 100:1, in the range of laminar vortex shedding for a non-tapered cylinder. They verified that the flow past tapered cylinders consists of distinct shedding cells each with a constant frequency. The number of cells was shown to be a linear function of the cylinder aspect ratio and of the inverse of the taper ratio. The modulation frequencies were found to be constant along the span in accordance with the findings of Gaster (1969). Piccirillo & Van Atta (1993) found dislocations or vortex splits, depicted in Figure 2.10, to be associated with these flow patterns. They presented the time sequence of this phenomenon with the vortex lines starting to steepen and vortex splitting beginning near the small-diameter end of the cylinder. These vortex splits were shown to follow one another

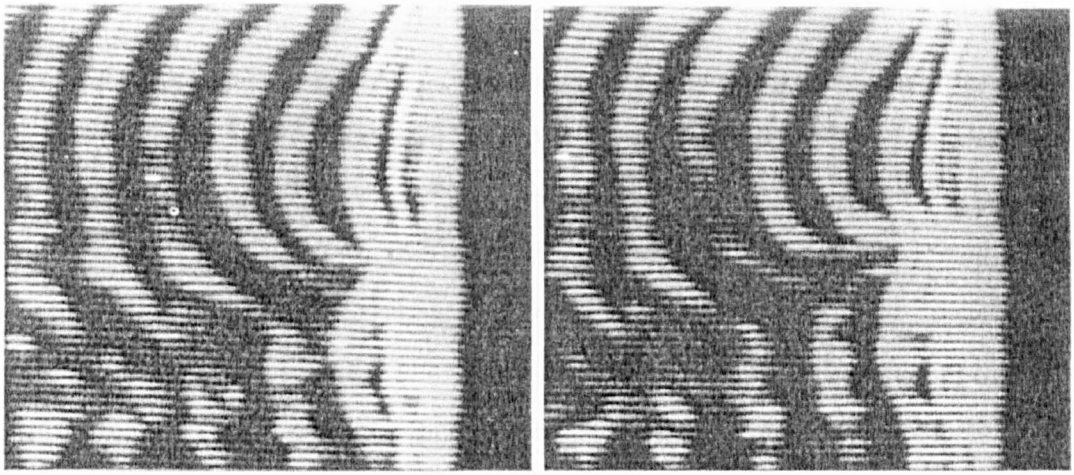


Figure 2.10: Flow visualizations depicting the sequence of the vortex splitting process for a tapered cylinder (Piccirillo & Van Atta 1993)

in sequence. Note the similarities in the flow structures for the vortex dislocations of tapered cylinders and those of the straight circular cylinders presented in section 2.2.4.

2.6 The effect of curvature: the ring geometry

As discussed in section 1.3, the possible flow orientations for a curved body can be represented by the two canonical cases: the ones where the flow is normal to the plane of curvature and the ones where the flow is parallel to the plane of curvature. The flow past the ring geometry belongs to the former category and has been studied in past literature.

Takamoto & Izumi (1981) reported on the stable arrangement of vortex rings developed in experiments behind an axisymmetric ring at low Reynolds numbers (the Reynolds number was based on the ring width -effectively the cylinder's cross-section diameter). They visualized an axisymmetrical row of a pair of vortex rings rotating opposite to each other.

Bearman & Takamoto (1988) investigated the wake structures developed past rings and discs in a wind tunnel where the models were suspended normal to the free-stream at Reynolds numbers of the order of 10^4. The curvature of these bluff bodies is described by the non-dimensional parameter $\frac{d}{w} = \frac{d_o+d_i}{d_o-d_i}$, where d is the

mean diameter, w is the ring width, and d_o and d_i are the outer and inner diameters respectively. When $\frac{d}{w}$ is equal to one, the bluff body is effectively a solid disc-like geometry, whereas when $\frac{d}{w}$ tends to infinity, the body is effectively a two-dimensional bluff body. Bearman & Takamoto (1988) found a critical value for $\frac{d}{w}$ to be 5: for rings of $\frac{d}{w}$ larger than 5, the wake consists of vortex rings shed in a regular, periodic manner whereas for rings below this critical value a shedding of weaker vortex structures is observed. The base pressure and drag coefficient curves indeed exhibited considerable changes for $\frac{d}{w}$ values between 4 and 6. Finally, the results presented for a ring with $\frac{d}{w} = 6$ showed that the larger diameter outer vortices were found to travel more slowly than the inner ones, but under no circumstances did the inner vortices pass the outer ones. The convection velocity of the vortex rings was found to be less than the free-stream velocity.

Leweke & Provansal (1995) studied the wake of high aspect ratio rings at low Reynolds numbers, based on the diameter, d, of the circular cross-section. The motivation for their study stemmed from the fact that the ring geometry offers in essence a geometry without ends. Hence, the three-dimensionality attributed to the end effects of typical cylinder configurations can be eliminated in the wake of a ring, so that only the phenomena inherent to the wake of such a bluff body can be studied. Leweke & Provansal (1995) expected and then confirmed that for sufficiently large aspect ratios the additional effects of body curvature should be small; the wake should behave similarly to the wake of a straight infinite circular cylinder subject to periodic boundary conditions in the spanwise direction.

In the Reynolds number range between 50 and 200 they found that, depending on the initial conditions, different modes of vortex shedding could occur. Specifically, for a ring of aspect ratio equal to 76.2 at a Reynolds number of 105 they visualized four different possible configurations: vortex rings parallel to the body, and single, double or triple helixes. Figure 2.11 depicts the first configuration, where vortex rings are shed parallel to the ring geometry. Leweke & Provansal (1995) explained that when the oscillatory state was reached from smooth initial conditions the parallel mode dominated in the run. The helical modes, on the other hand, were associated with "messy" initial conditions. Each of the modes was found to be per-

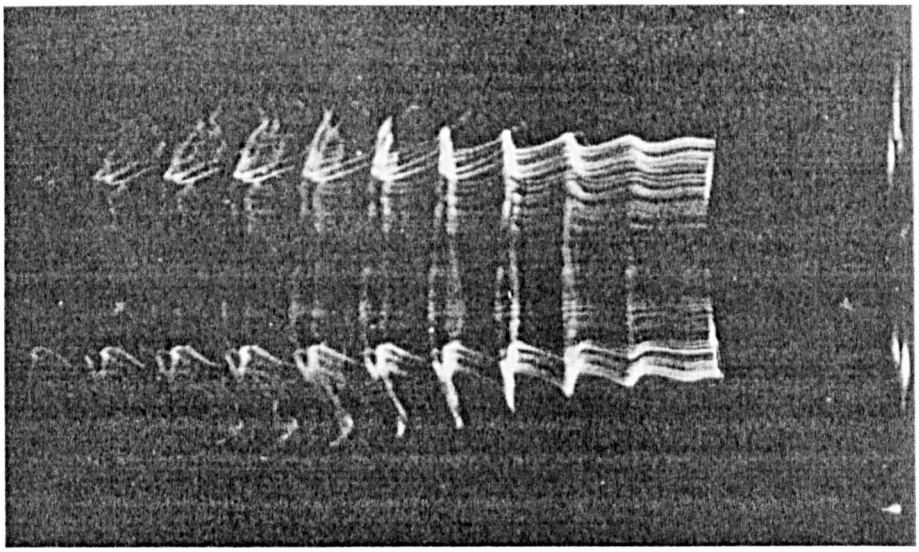


Figure 2.11: Vortex rings developed in the wake of a ring of aspect ratio 76.2 at $Re = 105$ (Leweke & Provansal 1995). Flow is from right to left.

fectly stable. Nevertheless, considering the stability domains of the vortex shedding modes for a ring, the parallel mode was found to be the one with the lowest stability limit. With the upper stability limit demarcating the beginning of the transition range, the higher helix modes were observed to have a tendency to remain stable longer. The different modes of shedding along with their stability limits from this experimental work were first presented in Leweke *et al.* (1993).

The Strouhal-Reynolds number curve was found to be continuous in this range of Reynolds numbers. Moreover, Leweke & Provansal (1995) found that curvature tends to increase the critical Reynolds number for the transition from a steady to an oscillating wake. Interestingly, when extrapolating the data to zero curvature, the critical Reynolds number was identified to be equal to 46.8 and can thus be compared with the critical Reynolds number for long straight cylinders. In addition, the Strouhal frequency was observed to decrease with growing curvature for the parallel shedding mode.

Finally, Leweke & Provansal (1995) performed experiments in a range of Reynolds numbers between 150 and 350. They investigated the transition Reynolds number with respect to increasing curvature for all the different modes developed in a ring wake. The tendency for the higher helix modes to remain stable longer was found

to increase with increasing curvature. Barkley & Henderson (1996) compared their critical Reynolds number, $Re = 188.5$, for the secondary instability of the straight cylinder wake to the measured data of Leweke & Provansal (1995) who reported an upper stability limit at $Re = 190$ for laminar periodic shedding for the various ring aspect ratios.

2.7 Flow past a straight circular cylinder in proximity to a wall boundary

Bearman & Zdravkovich (1978) investigated experimentally the flow past a straight circular cylinder in proximity to a wall boundary as the vertical distance of the cylinder from the plane boundary was varied. Wind tunnel experiments were performed with the cylinder positioned 36 diameters downstream from the leading edge of a plate deployed at the middle of the tunnel. The experiments were conducted at Reynolds numbers of 2.5×10^4 and 4.8×10^4 and at different gap to cylinder diameter ratios (G/d).

For all $G/d < 0.3$ no regular shedding frequency was detected. At all the gap to diameter ratios, the mean force on the cylinder was such as to repel it from the wall while this force was found to fall off very rapidly as the cylinder was moved away from the surface. The base pressure was shown to increase as the ground was approached. Furthermore, with respect to the flow along the plate, the following patterns were discerned. For $G/d = 0$ the pressure minimum on the plate was at the point of contact while its position moved downstream with increasing gap to diameter ratios. At $G/d = 0.4$ the magnitude of the negative peak in C_p was found to reach its maximum which occurred right at the rear of the cylinder (0.5d). The position of this maximum C_p magnitude remained at the same location for all gap to diameter ratios larger than 0.4. Bearman & Zdravkovich (1978) found separation bubbles on the plate upstream and downstream of the cylinder for small gap to diameter ratios, where the vortex shedding was suppressed, whereas no separation bubbles were found at the upper range of G/d. Finally, the pressure distribution

around the cylinder became more symmetric about the front stagnation point as the cylinder was moved away from the wall boundary, reaching near symmetry for $G/d = 0.4$.

A comprehensive review on this subject can be found in Zdravkovich (2003).

Finally, in the offshore technology environment this subject of cylinders in proximity to a wall boundary has relevance to marine pipelines. Jensen *et al.* (1990) investigated the flow around a pipeline placed on an initially flat bed, developing into a trenched ground as a result of the scour process. A negative lift force was then found to occur in contrast to the plane bed case. A model for the flow induced vibrations of pipeline free spans also has been presented by Hansen *et al.* (1999). Further information on these subjects can be found in the book by Sumer & Fredsoe (1999).

Chapter 3

Computational method

For the numerical solution of the Navier-Stokes equations in a given domain, a mesh must be initially constructed to provide the computational grid on which the equations will be solved. The governing equations must then be discretized. A spatial discretization must also be performed in order to numerically solve for the unknown equation variables, in the present case at the specific grid points.

In section 3.1 the mesh generation procedure for all the computational investigations of this study is briefly overviewed. The Navier-Stokes algorithm employed is discussed in section 3.2 and its temporal discretization is presented. To convert the governing partial differential equations to a system of algebraic equations some of the methods available are the finite difference, the finite element, the finite volume, and the spectral methods. In the current work the Navier-Stokes algorithm is discretized using the spectral/*hp* element method which can be considered as an amalgam of the finite element and the spectral method. Hence, in section 3.3 the features of the spectral/*hp* element method are discussed and the basics of this spectral/*hp* formulation are presented through the solution of a one-dimensional Helmholtz equation. Section 3.4 summarizes the details of the computations. Finally, section 3.5 presents the post-processing utilities most frequently employed to analyse the computational results.

3.1 Mesh generation

The mesh generation for all the computational investigations performed in this work has been accomplished by *Felisa* (Peiró *et al.* 1994). A variant of the advancing front method (Peraire *et al.* 1993) is employed for the triangulation of the domain surfaces and the generation of the 3D tetrahedral mesh. For the generation of a boundary layer mesh near the pipe wall regions, a modified advancing layers method (Peiró & Sayma 1995) has also been employed whereby the nodes of the mesh in the neighbourhood of the solid boundaries are generated along lines that are approximately normal to the surface.

For each mesh, the curved cylinder is first geometrically defined in the computational domain. A boundary layer mesh is then constructed consisting of a structured layer of prisms growing in the direction normal to the cylinder surface. In this way improved resolution is allowed in the normal direction and the physical boundary layer developing on the curved cylinder is better captured. All the prisms have one of their two triangular faces attached to the solid boundary. The interior of the computational domain is subsequently filled with tetrahedra hence a hybrid and unstructured 3D mesh is finally built.

As an example, Figure 3.1 depicts the unstructured mesh created for body C. For visualization purposes only half of the mesh in the y-direction is shown. The surface triangulation on the solid boundary is depicted in Figure 3.2(a). A snapshot of Figure 3.1 is shown in Figure 3.2(b) so that the structured layer of prisms around the curved cylinder is highlighted.

3.2 Navier-Stokes algorithm

In section 3.1 we briefly outlined how the meshes were constructed, hence providing the computational grid on which to compute the flow solution past the curved cylinders. The incompressible Navier-Stokes solver then employed to accomplish this task was $\mathcal{N}\varepsilon\kappa\mathcal{T}ar$, originally developed by Sherwin & Karniadakis (Sherwin (1995), Sherwin & Karniadakis (1995)) for unstructured triangular and tetrahedral

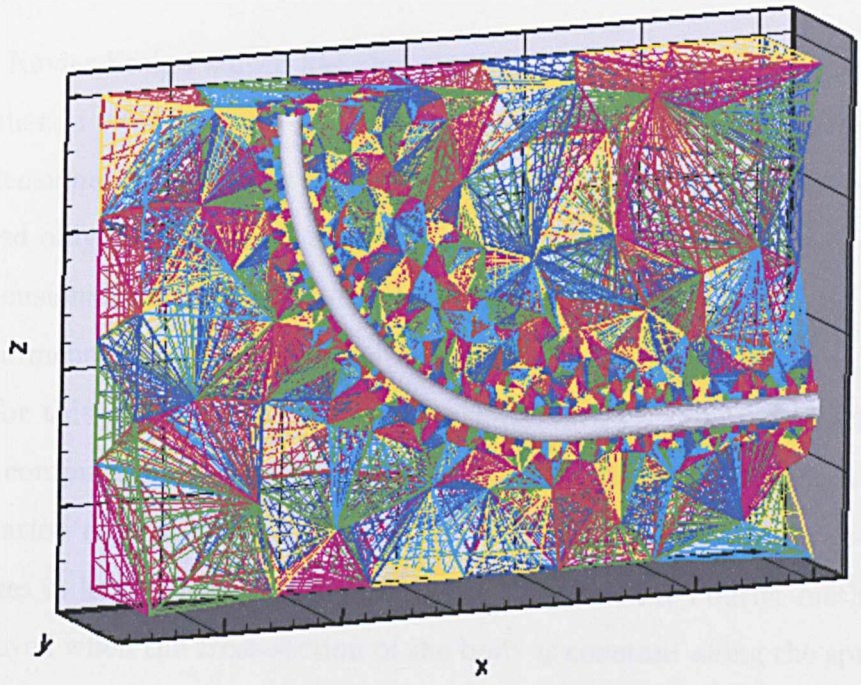


Figure 3.1: Unstructured hybrid mesh for body C (only half of the mesh is shown in the y-direction)

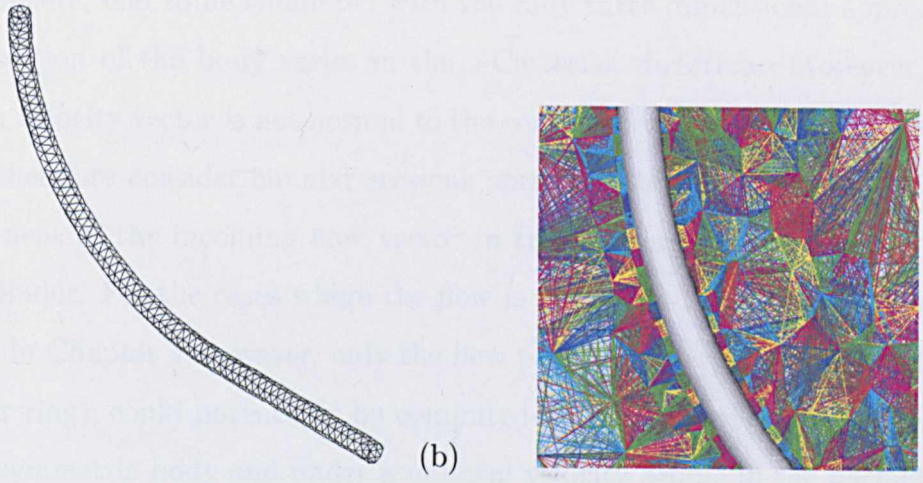


Figure 3.2: (a) Surface triangulation; (b) Structured layer around the solid boundary

elements and extended by Warburton (1998) to hybrid domains. The numerical code was based upon an earlier nodal spectral element code developed by Henderson (1994).

The Navier-Stokes solver has the capability of spectral/*hp* element discretizations either in two- or in three- dimensions. Moreover, a Fourier extension to the two-dimensional code is also available in which spectral element discretization is performed only on two-dimensional planes and a Fourier series is used to link these two-dimensional planes in the third direction. In the past, the Fourier extension to the two-dimensional code has been applied frequently and successfully on bluff body flows. For this method only a two-dimensional mesh is required. Furthermore, in terms of computational cost this approach is preferable to the fully three-dimensional discretization especially for studying three-dimensional flows past two-dimensional geometries in large computational domains. However, the Fourier method can only be employed when the cross-section of the body is constant along the span and when periodic boundary conditions can be imposed in the spanwise direction where the Fourier expansion is applied.

The nature of the current study necessitated full three-dimensional discretizations in all Cartesian directions for all but one of the computational cases. All the computational cases discussed in Chapter 5, where the flow is parallel to the plane of curvature, had to be simulated with the fully three-dimensional approach as the cross-section of the body varies in the z-Cartesian direction. Moreover, the free-stream velocity vector is not normal to the centreline of the body at all the sections. If we therefore consider circular sections normal to the centreline of the body, the component of the incoming flow vector in these planes varies along the length of the cylinder. For the cases where the flow is normal to the plane of curvature, discussed in Chapter 4, however, only the flow past body A (uniform normal flow on a quarter ring), could potentially be computed with the Fourier method. The ring is an axisymmetric body and under a uniform velocity profile in the normal direction it would fulfill the requirements for the Fourier approach. For the remaining of the cases in Chapter 4 still, the Fourier approach would be inappropriate as they involve shear profiles and a wall boundary.

All the computational investigations for this study have therefore been performed with the fully three-dimensional code. In the remaining part of this section, the temporal discretization of the Navier-Stokes algorithm is discussed. The basic principles behind the spatial discretization of the Navier-Stokes equations with spectral/*hp* elements are presented in section 3.3.

Let us first consider the Navier-Stokes equations for incompressible flows:

$$\frac{\partial \mathbf{u}}{\partial t} = -\nabla p + \mathbf{N}(\mathbf{u}) + \nu \mathbf{L}(\mathbf{u}) \tag{3.1}$$

$$\nabla \cdot \mathbf{u} = 0 \tag{3.2}$$

where $\mathbf{u}$ represents the velocity vector, p is the static pressure and ν is the kinematic viscosity. For simplicity we have assumed that the density, ρ, is equal to 1. The non-linear and linear operators, $\mathbf{N}$ and $\mathbf{L}$ respectively for the convective and diffusive terms, represent:

$$\begin{aligned} \mathbf{N}(\mathbf{u}) &= -(\mathbf{u} \cdot \nabla)\mathbf{u} \\ \mathbf{L}(\mathbf{u}) &= \nabla^2 \mathbf{u} \end{aligned} \tag{3.3}$$

where $\mathbf{N}(\mathbf{u})$ is said to be in convective form.

The temporal discretization of the Navier-Stokes equations in ***NεκTαr*** has been achieved by a stiffly stable splitting scheme (Karniadakis *et al.* 1991) that accounts for enhanced stability properties compared to the Adams-family schemes frequently used in other splitting methods. This splitting scheme propagates the velocity and pressure at time t_n over a time step Δt in three substeps in order to determine the fields at t_{n+1}. An important feature of the splitting schemes is that the primitive variables ($\mathbf{u}$, p) can be treated independently: the pressure term is decoupled from the convective and diffusive terms. Efficiency and stability reasons dictate a mixed explicit-implicit discretization for the convective and viscous terms respectively.

Specifically, if we integrate equation (3.1) over one time step Δt, we obtain:

$$\mathbf{u}^{n+1} - \mathbf{u}^n = -\int_{t_n}^{t_{n+1}} \nabla p dt + \int_{t_n}^{t_{n+1}} \mathbf{N}(\mathbf{u}) dt + \nu \int_{t_n}^{t_{n+1}} \mathbf{L}(\mathbf{u}) dt \tag{3.4}$$

The pressure term can be re-written as:

$$\int_{t_n}^{t_{n+1}} \nabla p dt = \Delta t \nabla \overline{p}^{n+1} \tag{3.5}$$

where $\overline{p}$ is a scalar field that ensures that the final velocity field is incompressible at t_{n+1}. If we approximate the time derivative in a general multistep method as $\frac{1}{\Delta t}\left(\gamma_0 \mathbf{u}^{n+1} - \sum_{i=0}^{Je-1} \alpha_i \mathbf{u}^{n-i}\right)$ and discretize all other terms at $n+1$, then equation (3.4) can be written in the following format (Karniadakis *et al.* 1991):

$$\gamma_0 \mathbf{u}^{n+1} - \sum_{q=0}^{Je-1} \alpha_q \mathbf{u}^{n-q} = -\Delta t \nabla \overline{p}^{n+1} + \Delta t \sum_{q=0}^{Je-1} \beta_q \mathbf{N}(\mathbf{u}^{n-q}) + \Delta t \nu \mathbf{L}(\mathbf{u}^{n+1}) \tag{3.6}$$

where Je is the integration order and α_q, γ_0, and β_q are the stiffly stable coefficients shown in Table 3.1 at the different integration orders up to third. We also note that the $\mathbf{N}(\mathbf{u})$ term has essentially been extrapolated to time level $n+1$ from previous time levels.

Coefficient	1st order	2nd order	3rd order
γ_0	1	3/2	11/6
α_0	1	2	3
α_1	0	-1/2	-3/2
α_2	0	0	1/3
β_0	1	2	3
β_1	0	-1	-3
β_2	0	0	1

Table 3.1: Coefficients of the splitting scheme (Karniadakis *et al.* 1991)

The final velocity field, $\mathbf{u}^{n+1}$, will be determined via two intermediate velocity fields, $\hat{\mathbf{u}}$ and $\hat{\hat{\mathbf{u}}}$. The three substeps of this splitting method therefore are:

$$\frac{\hat{\mathbf{u}} - \sum_{q=0}^{Je-1} \alpha_q \mathbf{u}^{n-q}}{\Delta t} = \sum_{q=0}^{Je-1} \beta_q \mathbf{N}(\mathbf{u}^{n-q}) \tag{3.7}$$

$$\frac{\hat{\hat{\mathbf{u}}} - \hat{\mathbf{u}}}{\Delta t} = -\nabla \overline{p}^{n+1} \tag{3.8}$$

$$\frac{\gamma_0 \mathbf{u}^{n+1} - \hat{\hat{\mathbf{u}}}}{\Delta t} = \nu \mathbf{L}(\mathbf{u}^{n+1}) \tag{3.9}$$

Equation (3.7) treats the non-linear terms explicitly. Taking the divergence of the second step, equation (3.8), and enforcing the incompressibility constraint on the second intermediate velocity field (i.e.$\nabla \cdot \hat{\hat{\mathbf{u}}} = 0$), we obtain the Poisson equation for pressure:

$$\nabla^2 \overline{p}^{n+1} = \nabla \cdot \left(\frac{\hat{\hat{\mathbf{u}}}}{\Delta t} \right) \tag{3.10}$$

Finally equation (3.9) treats the linear terms implicitly and we can obtain the final velocity field by a Helmholtz equation of the form: $\nabla^2 \mathbf{u}^{n+1} - \frac{\gamma_0}{\nu \Delta t} \mathbf{u}^{n+1} = -\left(\frac{\hat{\hat{\mathbf{u}}}}{\nu \Delta t} \right)$. Hence, overall a Helmholtz equation is solved for each of the velocity components and a Poisson equation for pressure.

We note that appropriate boundary conditions must be assigned to the pressure Poisson equation in order to minimize splitting errors. Karniadakis *et al.* (1991) presented a high order pressure Neumann boundary condition that alleviates the splitting errors encountered in some of the splitting methods as a result of incorrect boundary conditions.

Further details of this splitting scheme along with examples of Navier-Stokes solutions of model flows can be found in Karniadakis *et al.* (1991).

Recently, Sherwin (2002) presented a high-order splitting scheme for a substepping Navier-Stokes formulation. Since the non-linear terms are treated explicitly, they incur a CFL time step restriction. Sherwin (2002) discussed the two alternative approaches (substepping technique, semi-Lagrangian formulation) encountered in the spectral/*hp* element community for alleviating the problem of overly restrictive time steps with respect to accuracy requirements in some flow problems. He

presented the substepping approach, where the advection terms are advanced using a smaller time step than the rest of the Navier-Stokes solver, in conjunction with a high-order splitting scheme.

3.3 Basics of the spectral/*hp* element formulation

As mentioned before, different discretization methods are available for converting partial differential equations to a system of algebraic equations in a computational domain. The finite element method has been applied to a variety of engineering problems especially in structural mechanics, but also in fluid dynamics. In this method contiguous elemental subdomains are defined within the computational domain and the solution is approximated by given shape functions of low order polynomials defined in a standard finite region. An inherent attribute of the finite element method is the h-convergence where h refers to the characteristic size of an element. As the number of elements in the domain is increased and their size decreases, keeping the polynomial order fixed, the analytical solution is approximated more closely and the error in the numerical solution decays algebraically.

Spectral methods, on the other hand, use higher-order polynomial or trigonometric expansions which are defined globally throughout the whole solution domain (for example trigonometric functions leading to Fourier series). The error in the numerical solution is reduced by keeping the number of elements constant and increasing the order of the expansion basis. For infinitely smooth solutions, the error decays exponentially (exponential or spectral convergence).

Spectral/*hp* element methods combine attributes of both approaches and account for *hp*-convergence. The *hp* extension to the finite element approach refers to this new approach, where one can increase simultaneously the number of elements in the domain, h-refinement, and the order, P, of the polynomial expansions in the elemental domains, p-refinement.

As discussed in the previous section, the Navier-Stokes algorithm involves the solution of a Helmholtz equation for each velocity component and the solution of a Poisson equation for pressure. With this motivation, we describe the solution of

a Helmholtz equation in one dimension. Coding this Helmholtz problem provided some basic understanding of the principles of the spectral/*hp* element method employed for the spatial discretization of the Navier-Stokes solver.

• **Mathematical formulation**

Let us then consider the general form of the Helmholtz equation:

$$\nabla^2 \mathbf{u} - \lambda \mathbf{u} = -\mathbf{f} \tag{3.11}$$

supplemented by compatible Dirichlet or Neumann boundary conditions. In one dimension,

$$\frac{\partial^2 u(x)}{\partial x^2} - \lambda u(x) = -f(x) \tag{3.12}$$

where λ is the Helmholtz constant and f is the forcing function.

In general, for a linear differential equation described by $L(u) = 0$ the substitution of the approximate solution, u^δ, would result in a non-zero residual, R, so that $L(u^\delta) = R(u^\delta)$. The approximate solution can be expressed as (Karniadakis & Sherwin 1999):

$$u^\delta(x,t) = u_0(x,t) + \sum_{i=1}^{N_{dof}} \hat{u}_i(t)\Phi_i(x) \tag{3.13}$$

where $u_0(x,t)$ is known a priori and satisfies the initial and boundary conditions, $\hat{u}_i(t)$ represents the N_{dof} unknown coefficients, and $\Phi_i(x)$ denotes the known analytic functions to be used as expansion functions, or the so called trial functions.

The method of weighted residuals is based on the fact that the inner product of the residual with respect to a weight (or test) function, $v_j(x)$, is equal to zero. We denote the inner product in a domain Ω as:

$$(f,g) = \int_\Omega f(x)g(x)dx \tag{3.14}$$

Hence, for the j^{th} degree of freedom the method of weighted residuals dictates:

$$(v_j(x), R(u^\delta)) = 0 \tag{3.15}$$

Among the different types of test functions used in the method of weighted residuals, the Galerkin method adopted here dictates that $v_j(x) = \Phi_j$. In other words, the test functions are taken to be the same with the expansion functions chosen.

Going back to our original motivation of solving the Helmholtz problem, equation (3.15) for the one-dimensional Helmholtz equation (3.12) becomes:

$$\left(v_j(x), \frac{\partial^2 u^\delta(x)}{\partial x^2} - \lambda u^\delta(x) + f(x)\right) = 0 \tag{3.16}$$

Let us define the domain Ω in which we wish to solve the one-dimensional Helmholtz equation, as $\Omega = \{x | A < x < B\}$. Under equation (3.14) and integrating by parts the second derivative we obtain:

$$\int_A^B \frac{\partial v}{\partial x}\frac{\partial u^\delta}{\partial x}dx + \lambda \int_A^B v u^\delta dx = \int_A^B v f dx + \left[v\frac{\partial u^\delta}{\partial x}\right]_A^B \tag{3.17}$$

The approximate solution, u^δ(x), can be written as:

$$u^\delta(x) = \sum_{i=0}^{N_{dof}-1} \hat{u}_i \Phi_i(x) \tag{3.18}$$

Similarly,

$$v(x) = \sum_{j=0}^{N_{dof}-1} \hat{v}_j \Phi_j(x) \tag{3.19}$$

Substituting equations (3.18) and (3.19) into (3.17) and factoring $\hat{v}_j$, we obtain:

$$\int_A^B \frac{\partial}{\partial x}\sum_{j=0}^{N_{dof}-1} \Phi_j \frac{\partial}{\partial x}\sum_{i=0}^{N_{dof}-1} \Phi_i \hat{u}_i dx + \lambda \int_A^B \sum_{j=0}^{N_{dof}-1} \Phi_j \sum_{i=0}^{N_{dof}-1} \Phi_i \hat{u}_i dx = \int_A^B \sum_{j=0}^{N_{dof}-1} \Phi_j f dx + \left[\sum_{j=0}^{N_{dof}-1} \Phi_j \frac{\partial u^\delta}{\partial x}\right]_A^B \tag{3.20}$$

Defining the entries of a stiffness matrix, $\mathbf{K}$, and of a mass matrix, $\mathbf{M}$, respectively as follows,

$$\begin{aligned} K_{ij} &= \left(\frac{\partial \Phi_i}{\partial x}, \frac{\partial \Phi_j}{\partial x}\right) \\ M_{ij} &= (\Phi_i, \Phi_j) \end{aligned} \tag{3.21}$$

and introducing

$$F_j = (\Phi_j, f) \tag{3.22}$$

equation (3.20) can be written in a general matrix notation format as:

$$(\mathbf{K} + \lambda \mathbf{M})\hat{\mathbf{u}} = \mathbf{F} + \mathbf{BC} \tag{3.23}$$

where the $\mathbf{BC}$ term must be evaluated at the boundaries of the domain.

- **Attributes of the *hp* method**

At this point we need to address two aspects: first, the tessellation of multiple elements in a computational domain, and second, the choice of the expansion bases. As previously mentioned, the benefits of the spectral/*hp* element method rely also on the fact that it entails characteristics both from the *h*-type approach and from the *p*-type approach.

To differentiate between local and global coordinates, let us define the standard element Ω_{str} in one dimension spanning the interval $-1 < \xi < 1$, where ξ is the local coordinate. In a computational domain with multiple non-overlapping elements, we need to define a mapping between the local coordinate ξ in the standard element and the global coordinate x in each elemental domain $\Omega_e = \{x | x_{e-1} < x < x_e\}$. This transformation can be written as (Karniadakis & Sherwin 1999):

$$x = \chi^e(\xi) = \phi_0(\xi) x_{e-1} + \phi_1(\xi) x_e \tag{3.24}$$

introducing a Jacobian, $J = \frac{dx}{d\xi}$. For a linear finite element expansion, where in the standard interval $\phi_0(\xi) = \frac{1-\xi}{2}$ and $\phi_1(\xi) = \frac{1+\xi}{2}$, the Jacobian becomes equal to $\frac{x_e - x_{e-1}}{2}$.

We now introduce the second attribute of the *hp* method, the *p*-type approach, and hence we advance from linear finite elements to higher order polynomial expansions, which can be either nodal or modal. The spectral element method of the current study is associated with the method of weighted residuals and employs the latter type of polynomial expansions. Among the modal expansions available, the one employed in this spectral/*hp* element method is based on Jacobi polynomials, which form an orthogonal set of polynomials.

Jacobi polynomials, expressed as $P_p^{\alpha,\beta}(x)$, represent the family of polynomial solutions to a singular Sturm-Liouville problem which in the region $-1 < x < 1$ is written as (Karniadakis & Sherwin 1999):

$$\frac{d}{dx}\left[(1-x)^{(1+\alpha)}(1+x)^{(1+\beta)}\frac{d}{dx}u_p(x)\right] = \lambda_p(1-x)^{\alpha}(1+x)^{\beta}u_p(x) \tag{3.25}$$

where $u_p(x) = P_p^{\alpha,\beta}(x)$ and $\lambda_p = -p(\alpha+\beta+p+1)$.

This expansion basis is a hierarchical one as the expansion set of polynomial order P is included in the expansion set of order $P+1$. The use of a modal polynomial expansion normally indicates that the expansion basis is hierarchical.

The expansion basis used in the current spectral/*hp* element formulation is formed with symmetric Jacobi polynomials where $\alpha = \beta = 1$ and we represent it as $\psi_p(\xi)$, where in the standard interval Ω_{str} it is defined as (Karniadakis & Sherwin 1999):

$$\psi_p(\xi) = \begin{cases} \frac{1-\xi}{2} & \textit{if} \quad \mathrm{p} = 0 \\ \left(\frac{1-\xi}{2}\right)\left(\frac{1+\xi}{2}\right)P_{p-1}^{1,1}(\xi) & \textit{if} \quad 0 < \mathrm{p} < \mathrm{P} \\ \frac{1+\xi}{2} & \textit{if} \quad \mathrm{p} = \mathrm{P} \end{cases} \tag{3.26}$$

An example of this modal expansion, for a polynomial order, P, of 5 is depicted in Figure 3.3. Out of the six modes displayed, the first and the last, ψ_0 and ψ_5 respectively, correspond to the linear finite element modes.

Going back to our motivation of solving equation (3.20) under the notation of equation (3.23), and using the above mentioned Jacobi polynomials as an expansion

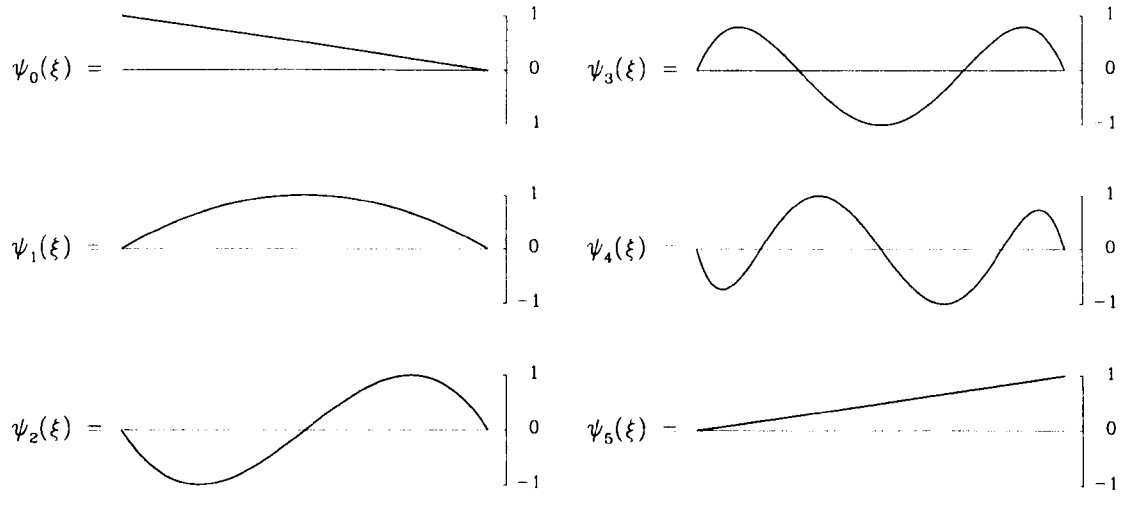


Figure 3.3: Shape of expansion modes for a polynomial order of $P = 5$ (Karniadakis & Sherwin 1999)

basis, the interior entries of the elemental mass matrix, for $0 < p, q < P$ are defined as (Karniadakis & Sherwin 1999):

$$M^e[p][q] = \int_{-1}^{1} \left(\frac{1-\xi}{2}\right)\left(\frac{1+\xi}{2}\right) P_{p-1}^{1,1}(\xi)\psi_q(\xi)d\xi \tag{3.27}$$

Equation (3.27) gives us analytically the entry at the p^{th} row and q^{th} column of the elemental mass matrix. To perform this integration numerically, the Gaussian quadrature rule is employed as follows:

$$M^e[p][q] = \int_{-1}^{1} \psi_p(\xi)\psi_q(\xi)d\xi = \sum_{i=0}^{Q-1} \psi_p(\xi_i)\psi_q(\xi_i)w_i \tag{3.28}$$

where ξ_i are the coordinates of the discrete number of points, Q, in the standard interval, and w_i are the weights. A description of Gaussian quadrature and its various types with respect to the choice of abscissae can be found in Sherwin & Karniadakis (1995, 1996). Finally, exact integration using Gauss-Lobatto-Legendre quadrature in one dimension requires that $Q \geq P + 2$.

Up to now we have considered the standard element Ω_{str} spanning a region (-1,1) in one-dimension. The approximate solution $u^\delta(x)$, recall equation (3.18), for our choice of expansion basis can now be expressed in terms of the number of elements,

N_{elem}, spanning the computational domain as follows:

$$u^{\delta}(x) = \sum_{e=1}^{N_{elem}} \sum_{p=0}^{P} \psi_p^e(\xi) \hat{u}_p^e \tag{3.29}$$

where again, x represents the global coordinate, ξ the local coordinate in the standard interval, and e denotes the elemental domains.

For a computational domain of multiple non-overlapping elements, the number of global degrees of freedom is smaller than the summation of the local degrees of freedom through each of the elements, since the global modes are constrained to be continuous everywhere. This can be enforced in the current expansion by ensuring the end modes have the same expansion coefficient, i.e. $\hat{u}_0^e = \hat{u}_P^{e-1}$. To be able to go from the local degrees of freedom to the global ones, therefore, requires a mapping. We define an array $bmap[e][p]$, where e denotes the local element index and p the local mode index. This mapping array will be explicitly described subsequently when formulating the global mass matrix in the solution of the Helmholtz problem.

Finally, the last issue to be addressed in terms of the formulation before attempting the solution of the Helmholtz equation in one-dimension, is the issue of the boundary conditions. We split the approximate solution into an unknown homogeneous function, u^h, and a known one, u^D. The known function satisfies the Dirichlet boundary conditions whereas the unknown is zero at the Dirichlet boundaries.

• **Solution**

We now go back to equation (3.23) and we will see how all the above aspects of the spectral/*hp* element formulation aggregate to reduce the differential problem into an algebraic one that can be solved with a computer program.

▷ The first step is to determine in the standard interval the coordinates, $\xi[i]$, and the weights, $w[i]$, at the np number of points associated with the Gaussian quadrature. We recall that $np = nm + 1$, where nm represents the number of local modes, $nm = P + 1$.

▷ The second step is to form the matrix of the expansion basis defined in equation

(3.26) at the quadrature points. This matrix is of order $np \times nm$ and contains the values of the expansion basis for each quadrature point i at each $p \leq P+1$ (let us denote each entry as $\psi[i][p]$). Subsequently, the mass matrix is formed following equation (3.28). The mass matrix is a square matrix of order nm, and each entry $mass[p][q]$, where $p,\ q \leq P+1$, is formed by summing the product of $\psi[i][p] \cdot \psi[i][q] \cdot w[i]$ through all the i quadrature points.

▷ The third step is to form the matrix of the derivatives of the expansion basis, and similarly to the mass matrix to now form the stiffness matrix. A detailed description on how differentiation is performed in the current formulation can be found in Sherwin & Karniadakis (1995, 1996).

▷ The fourth step is to proceed from the local formulation in the standard element to the global formulation. For a total number of *nel* elements, the number of global degrees of freedom is: $N_{dof} = nel \cdot (nm-1)+1$. With the Jacobian and a mapping $bmap[e][p] = e \cdot (nm-1)+p$, where $e \leq nel$ and $p \leq P+1$, the global mass matrix can be constructed. The same mapping is also employed for assembling the global stiffness matrix. We recall equation (3.23) and by adding the global stiffness matrix to the product of the global mass matrix times the Helmholtz constant, λ, we produce a square matrix, denoted by $\mathbf{A}$, which is of order N_{dof}.

▷ Now let us work on the first term of the right-hand side of equation (3.23) and this constitutes the fifth step. For a solution of the form $u(x) = \sin(\pi x)$, and with the Helmholtz constant being equal to 1, we obtain $f(x) = (\pi^2+1)\sin(\pi x)$. And let us now denote the matrix of the expansion basis, where as explained above each entry is of the form $\psi[i][p]$, as matrix $\mathbf{G}$. In order to form $\mathbf{F}$, which is a column matrix of order $nm \times 1$, we now perform with the Jacobian the operation $\mathbf{G^T wf}$ where $\mathbf{G}$ is a matrix of order $nm \times np$, $\mathbf{w}$ is a diagonal matrix of order np and includes the weights, and $\mathbf{f}$ is the forcing function column matrix of order $np \times 1$.

▷ For illustrating this model problem, the second term on the right-hand side of equation (3.23) is now considered at the end. Let us assume that the computational domain consists of two elements, where the two global boundaries A, B have coordinates $x_A = -1$ and $x_B = 3$ for example. We apply a Dirichlet boundary condition

on boundary A and a Neumann boundary condition on boundary B; $u(x_A) = -1$ and $\frac{du}{dx}(x_B) = -\pi$. The **BC** column matrix has all its entries as zero except for the very last one which represents the Neumann boundary condition at boundary B. This is equal to the value of the expansion basis at that point multiplied by $(-\pi)$ as described in equation (3.20).

By adding the outcomes of the fifth and sixth step, we have finally formed the right-hand side, and let us call **B** this column matrix of order $N_{dof} \times 1$. Hence, we have now arrived at a matrix equation of the form $\mathbf{A}\hat{\mathbf{u}} = \mathbf{B}$ and we could solve for $\hat{\mathbf{u}}$.

The last thing to take care of is the Dirichlet boundary condition at boundary A. As mentioned earlier the approximate solution, u^δ, can be formed by a known and an unknown part. We can therefore condense the modes that are attached to a Dirichlet boundary out of the system before it is inverted, since these modes are known. We can remove them from the global matrix system by condensing the row and column which represent contributions from these known modes as discussed in Sherwin & Karniadakis (1996). Matrix **A** is thus accordingly reduced to a square matrix of order $N_{dof} - 1$, **B** to a column matrix of order $(N_{dof} - 1) \times 1$ and we can now solve for the $N_{dof} - 1$ unknown coefficients.

Therefore, after splitting the knowns and the unknowns, we have seen how our original differential problem was reduced to an algebraic one where the values of the unknown coefficients could be determined by standard matrix inversion. Recall equation (3.29) and we can now accordingly evaluate the approximate solution to our one-dimensional Helmholtz problem at all the quadrature points.

- **Error analysis**

Finally, we will now consider the error estimates applied to the one-dimensional Helmholtz equation we have solved above, i.e:

$$\frac{\partial^2 u}{\partial x^2} - u = -(\pi^2 + 1)\sin(\pi x) \tag{3.30}$$

As mentioned earlier, the spectral/hp element method employed accounts for expo-

nential convergence. The general error estimate can be written as (Szabo & Babuska 1991):

$$\|\varepsilon\|_E \leq Ch^{\mu-1}P^{-(k-1)}\|u\|_k \tag{3.31}$$

where h is the size of the elements, P is the polynomial order, k is the differentiability of the solution, $\mu = min(k, P+1)$, C is independent of h, P, u, and $\varepsilon = u - u^\delta$. For infinitely differentiable solutions,

$$\varepsilon \propto h^P \tag{3.32}$$

Moreover, as mentioned before, in one dimension the number of degrees of freedom, N_{dof}, are:

$$N_{dof} = nel(nm-1)+1 = (nel)(P)+1 \tag{3.33}$$

where *nel* is the number of elements in the computational domain. Recall that for h-convergence, the polynomial order remains constant. Therefore,

$$h \propto \frac{1}{N_{dof}} \tag{3.34}$$

By taking the natural log of equation (3.32) and combining it with equation (3.34), we obtain the following for h-refinement:

$$\ln\varepsilon \propto -P\ln N_{dof} \tag{3.35}$$

This indicates that for h-convergence the error should vary linearly with N_{dof} on a log-log axis. Considering the L_2 error, where:

$$\varepsilon = \Big(\int (u^\delta - u)^2 dx\Big)^{1/2} \tag{3.36}$$

the h-type convergence at fourth polynomial order for the one-dimensional Helmholtz equation expressed in equation (3.30) is indeed demonstrated in Figure 3.4.

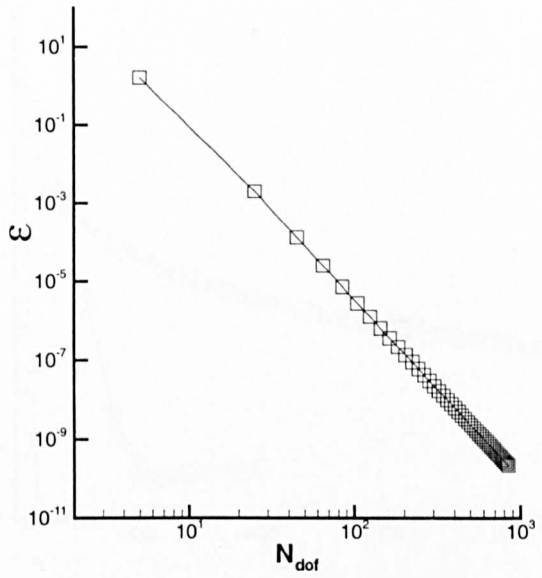


Figure 3.4: h-convergence of the solution $u = \sin(\pi x)$ in the one-dimensional Helmholtz equation in a log-log axis, $P = 4$

Similarly, for polynomial convergence equation (3.32) still holds. However, since h remains constant and P now varies, equation (3.33) suggests:

$$P \propto N_{dof} \tag{3.37}$$

By taking the natural log of equation (3.32) and combining it with equation (3.37), we obtain the following for p-type refinement:

$$\ln \varepsilon \propto N_{dof} \tag{3.38}$$

Figure 3.5 depicts the h- and p- type convergence of the Helmholtz equation expressed in equation (3.30). The fast decay in L_2 error achieved by the p-type approach is shown.

In conclusion, we have seen how the principles of the spectral/hp element formulation have been applied to a Helmholtz equation in one-dimension.

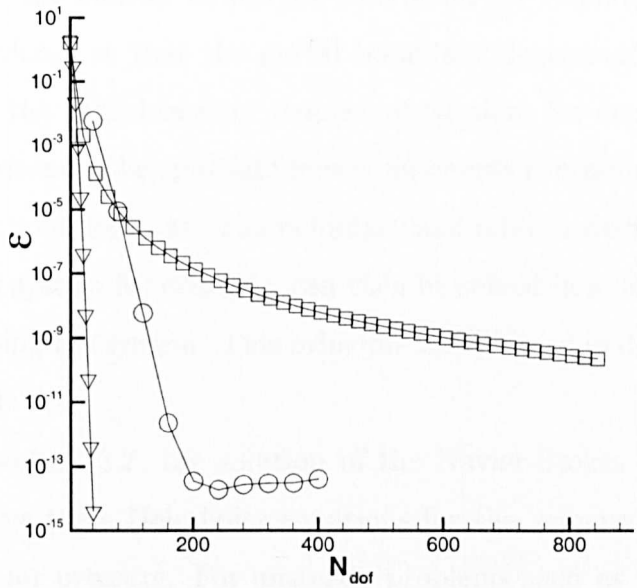


Figure 3.5: P- and h- convergence of the solution $u = \sin(\pi x)$ in the one-dimensional Helmholtz equation in a semi-log axis: $\bigtriangledown$ p-convergence in 2 elements; $\bigcirc$ p-convergence in 20 elements; $\square$ h-convergence at $P = 4$

• **Higher dimensions**

In two- or three- dimensions similar features pertain. Further details about this spectral/*hp* element method along with simulations and comparisons with standard flow cases can be found in Sherwin & Karniadakis (1995, 1996) and Karniadakis & Sherwin (1999). In Sherwin & Karniadakis (1995) the two-dimensional formulation for the Navier-Stokes algorithm is presented with triangular discretizations for complex geometries. In Sherwin & Karniadakis (1996) a new tetrahedral expansion basis is introduced and the formulation and validation of the three-dimensional Navier-Stokes algorithm using this basis are demonstrated.

In three-dimensions the basis can be broken up into four types of modes: vertex, edge, face and interior. An inherent feature of this spectral/*hp* element discretization is the boundary/interior decomposition of the modal expansions. Boundary modes in three-dimensions include the vertex, edge and face modes. The vertex modes have a unit value at one vertex decaying linearly to zero at all other vertices. The edge modes have magnitude along one edge and are zero at all other edges and vertices. The face modes have non-zero contributions in the interior and on one

face only. Finally, the interior modes are zero at all the boundaries. As the global system can be ordered so that the global boundary degrees of freedom are listed first, followed by the global interior degrees of freedom for each element, the elemental mass matrices can be split into four components containing a combination of boundary-interior contributions. The boundary and interior degrees of freedom, in a Helmholtz matrix system for example, can then be solved in a decoupled manner by statically condensing the system. This principle is explained in detail in Karniadakis & Sherwin (1999).

As noted in section 3.2, the solution of the Navier-Stokes equations in three-dimensions involves three Helmholtz equations for the velocity components and a Poisson equation for pressure. For unsteady problems such as the flow past cylinders, the computational cost of the Navier-Stokes solver is mostly dictated by the computational expense of solving these four elliptic problems. Recently, Sherwin & Casarin (2001) presented an efficient preconditioning approach for statically condensed solvers, otherwise known as substructured solvers, by reducing the coupling between the original face mode contributions and the combination of vertex and edge modes in a numerical low-energy basis.

3.4 Details of the three-dimensional simulations

The three-dimensional computations have been performed partially on the Fujitsu AP3000 provided by the Imperial College Parallel Computing Centre and mostly on the CRAY T3E-1200E provided by the Computer Services for Academic Research (CSAR) at the University of Manchester. The simulations on the AP3000 were computed with 16 UltraSPARC 300MHz processors. On the CRAY T3E-1200E the computations were performed with 16 to 96 DEC Alpha 21164 600MHz processors.

The simulations have been performed under the following features:

- **polynomial order**

  In almost all of the simulations, the order of the polynomial expansion has been increased from 2 to 4 and then to 6 (and further to 8 in some of the

computational cases).

- **time integration and time step**

  The time step at each polynomial order has been chosen so that the CFL number for stability reasons is between 0.20 and 0.50. Most of the numerical results presented in this thesis stem from computations at first order time integration. Second order time integration was also successfully attempted. At first order time integration, the effect of the time step level has been investigated for the flow past body A and past body C at different time step values. Specifically, the original time step, Δt, was decreased to $\frac{3}{4}\Delta t$ and then to $\frac{\Delta t}{2}$. In Chapter 4 the statistics for a number of shedding cycles for the flow past body A are hence compared at these different time step levels and in Chapter 5 for the flow past body C. We observe that within the acceptable CFL range the effect of the variation of the time step on the numerical results is indeed negligible.

The individual domain sizes will be considered separately for each case in Chapters 4 and 5. The domain size parameters were investigated only for the flow past body A and as will be discussed in Chapter 4 the same flow features were observed for the smaller and the larger mesh. The numerical results were qualitatively unaffected overall. Because of the large computational requirements of the fully three-dimensional simulations it would be too demanding to do a full mesh resolution study with a set of meshes for each one of the cases. However, a hierarchical p-refinement study was possible. As typically performed in the spectral/hp element method, the solutions were refined by increasing the polynomial order of the expansion functions rather than by increasing the number of elements in the domain. Each element in the mesh of Figure 3.1 accounts for $\frac{(P+1)(P+2)(P+3)}{6}$ local degrees of freedom if it is a tetrahedron, and $\frac{(P+1)^2(P+2)}{2}$ local degrees of freedom if it is a prism. Overall this mesh allows for almost one million local degrees of freedom (993,608) when the solution is computed at sixth polynomial order. As a final comment for the refinement studies, it should be brought to attention that all the numerical results of Chapter 5 have been qualitatively validated successfully by the experimental flow

visualizations.

The boundary conditions that will be encountered in Chapters 4 and 5 are briefly described here:

- A velocity inlet boundary condition has been specified on one or more surfaces of each case. Three Dirichlet boundary conditions for each of the velocity components and a Neumann boundary condition for pressure are applied at this type of boundary condition.

- A wall boundary condition represents no-slip and is the same as the velocity boundary condition with $u = v = w = 0$.

- A symmetry boundary condition corresponds to a Dirichlet boundary condition for the velocity component normal to this symmetry plane and Neumann boundary conditions for all the other velocity components. If, for example, the plane $z = 0$ is assigned a symmetry boundary condition, then $w = 0$, $\frac{du}{dn} \equiv \frac{du}{dz} = 0$ and $\frac{dv}{dn} \equiv \frac{dv}{dz} = 0$. The pressure is set through a Neumann boundary condition.

- Finally, the outflow boundary condition is set by three Neumann boundary conditions for each of the velocity components $\left(\frac{du}{dn} = 0, \frac{dv}{dn} = 0, \frac{dw}{dn} = 0\right)$ and a Dirichlet boundary condition for pressure $(p = 0)$.

In conclusion, a comment should be made about the computational cost and the parallel efficiency of the simulations. As the nature of the problem studied required a fully three-dimensional approach with large computational domains and relatively complex geometries, the computations were relatively intensive in CPU time. Parallel efficiency was observed whereby on average doubling the number of processors from 16 to 32 resulted in a 1.6 speedup, while quadrupling the number of processors from 16 to 64 produced a 2.6 speedup for solutions computed at sixth polynomial order. Considering the complexity of the cases and the high polynomial orders these statistics are encouraging.

3.5 Utilities

A key feature of this work, aiming to study the fundamental mechanisms of vortex shedding past curved cylinders, was the processing and analysis of the computational results. A technique to visualize and study the wake topology and an implementation to extract forces at two-dimensional sections along the length of the curved cylinder were of high-priority among the post-processing tools. The λ_2 identification criterion for vortical structures will be presented in section 3.5.1 along with an analysis of the appropriate cut-off range in section 3.5.2. Finally, in section 3.5.3 we will see how the sectional forces are extracted for two-dimensional slices normal to the cylinder axis.

3.5.1 The λ_2 criterion for vortex core identification

In order to represent the flow structures developed in bluff body flows and study the three-dimensional vortex dynamics and the evolution of a flow-field, a criterion to identify and capture the vortical structures is often necessary. Alternative definitions of what constitutes a vortical structure and how to accurately capture the vortical structures in a flow field have been presented by different researchers over the past years. In this section we limit ourselves to the method proposed by Jeong & Hussain (1995) which stems from the pressure minimum criterion for flow rotation, but in the absence of unsteady or viscous contributions. Taking the gradient of the Navier-Stokes equation and decomposing the acceleration gradient to a symmetric and anti-symmetric part, where the latter is equal to the vorticity-transport equation, Jeong & Hussain (1995) arrived at:

$$\frac{DS_{ij}}{Dt} - \nu S_{ij,kk} + \Omega_{ik}\Omega_{kj} + S_{ik}S_{kj} = -\frac{1}{\rho}p_{,ij} \tag{3.39}$$

The symmetric and anti-symmetric components of the velocity gradient tensor, S_{ij} and Ω_{ij} respectively, are written in tensor notation as follows (where the comma

in subscript indicates partial differentiation):

$$S_{ij} = \frac{1}{2}(u_{i,j} + u_{j,i})$$
$$\Omega_{ij} = \frac{1}{2}(u_{i,j} - u_{j,i}) \tag{3.40}$$

As we will discuss below, the sources of inconsistency between the presence of a pressure minimum and the presence of a vortex core are often the unsteady and viscous effects. Neglecting the first two terms of equation (3.39) and considering the Hessian of pressure which contains information on the local pressure extrema, Jeong & Hussain (1995) developed the following criterion. They defined a vortex core "*as a connected region with two negative eigenvalues of* $\mathbf{S}^2+\mathbf{\Omega}^2$". Since $\mathbf{S}^2+\mathbf{\Omega}^2$ is symmetric and has only real eigenvalues, they postulated that the second largest eigenvalue, λ_2, of $\mathbf{S}^2+\mathbf{\Omega}^2$ must be negative within a vortex core.

Jeong & Hussain (1995) compared their definition to other intuitive definitions, such as the pressure minimum, closed or spiralling streamlines and pathlines, and isovorticity surfaces. They provided examples of types of flows where these criteria prove inadequate in detecting successfully the vortical structures. Specifically, as highlighted in Jeong & Hussain (1995) the presence of unsteady straining can create a pressure minimum even though no vortex core is involved. In addition, in viscous dominated flows vortices can occur without the presence of a pressure minimum. Hence, they concluded that in general, the presence of a local pressure minimum is neither a sufficient nor a necessary condition for the presence of a vortex core when unsteady straining or viscous effects are involved. This provided the reasoning for discarding the first two terms in equation (3.39). Similarly, the criterion of closed or spiralling pathlines and streamlines can be an inappropriate measure as they are not Galilean invariant; if, for example, the reference frame moves faster than any point in the vortex core, the streamlines may as well not be closed or spiralling. Moreover, as a particle may not complete a full revolution around the vortex centre during the lifetime of a vortex, no closed pathlines would be produced. Finally, using vorticity magnitude as the criterion to locate vortical structures can also pose problems in cases of shear flows, as the vortex cores need to be distinguished from other non-rotational shear features in the flow field (presence of vorticity but no

coherent vortical motion).

In all the computational cases presented in this thesis, the vortex cores have been identified in terms of the λ_2 criterion. This technique has been successfully used in the past within the research group for the study of bluff body flows (Darekar 2001).

3.5.2 Enstrophy and cut-off analysis of vortical structure identification

Typically a specific isocontour value, or cut-off, is chosen to identify the coherent structures generally referring to the organized and concentrated rotational patterns within the flow. In numerical practice the cut-off value is varied in order to eliminate numerical noise. The λ_2 criterion outlined in the previous section was now extended a step further in order to determine the optimal cut-off range in the coherent structure identification process and gain a more physical understanding of the cut-off value in terms of the wake features it represents.

Creusé & Mortazavi (2001) compared three different diagnostic methods in order to obtain a better understanding of the flow dynamics downstream of the discontinuity point of a dihedral. The computations on this dihedral plane were performed using a two-dimensional DNS method and the vortex dynamics were studied with instantaneous plots of the entire vorticity field (vorticity isolines), with the vorticity threshold criterion and the Weiss criterion (Weiss 1991).

For their two-dimensional simulations, Creusé & Mortazavi (2001) found that when plotting the proportion of the coherent structure's enstrophy (integral of squared vorticity) to the global flow versus the cut-off value, they observed two different behaviours at the right and left of the optimal cut-off point. They defined the optimal cut-off point as the intersection of the tangents to the curve at zero and infinity (Creusé & Mortazavi 2001). For values smaller than the optimal cut-off point, they claimed that the high variation of the enstrophy value corresponds to contributions from the shear zones of the boundary layer. For values larger than the optimal cut-off point, Creusé & Mortazavi (2001) found the regions captured by the vortex core identification criterion to remain almost unchanged, hence they

argued that these regions correspond to the definition of the coherent structure. The optimal cut-off value was large enough to remove the background flow, but at the same time was small enough to capture the agglomeration of vortical structures in the flow field.

This idea was accordingly adopted in three-dimensions, where apart from the flow past curved cylinders, an internal flow case from the biomedical area was also used as a validation example. Interestingly enough, the curve of the proportion of the coherent structure's enstrophy to the global flow's as a function of the cut-off value exhibited similar trends and the two above-mentioned behaviours were recognized.

The aim of this implementation was therefore to calculate the amount of enstrophy, Z, captured in the coherent structures that correspond to each λ_2 level. All the flow fields obtained by $\mathcal{N}\varepsilon\kappa\mathcal{T}\alpha r$ are solutions to the Navier-Stokes equations using higher order polynomial expansions. The post-processing utilities are however performed with linear shape functions.

Let us consider the sample case of the channel flow in a computational domain where each Cartesian direction spans a length equal to two units (-1,1). With a velocity profile of,

$$u = 1 - z^2 \tag{3.41}$$

we obtain,

$$\omega_y = -2z \tag{3.42}$$

Therefore, the analytical value of ω^2 integrated in the volume of this domain is:

$$Z_{channel} = A_{xy} \int_{-1}^{1} (-2z)^2 dz = \frac{32}{3} \tag{3.43}$$

where A_{xy} is the area on the xy-plane.

Numerically, using linear finite elements, we first decompose each element to a large number of smaller tetrahedra and in each small tetrahedron we perform:

$$Z = \sum_{i=0}^{3} w_i^2 J N_i \tag{3.44}$$

Each vertex shape function contributes 1/3 (i.e. $N_0 = N_1 = N_2 = N_3 = \frac{1}{3}$) while J maps the subtetrahedra to the standard region. In this channel example,

the original mesh consisted of 6 tetrahedra of equal size. If the original element is a tetrahedron, then it can be decomposed to n^3 similar smaller tetrahedra with $n+1$ equispaced interpolating points along each edge of the original element. For example, when evaluating the enstrophy in this channel domain using $n = 4$, each one of the original tetrahedra in the mesh is decomposed into 64 smaller tetrahedra. This allows a better resolution of the non-smooth λ_2 function in space than using a higher order expansion. Assuming w_i to be equal to one, the value of enstrophy in this case is indeed equal to the volume of the domain.

To calculate the enstrophy in this channel case with equation (3.44), the numerical results showed that with $n = 4$, the computed enstrophy was 12. However, as n was increased to 29, the value of enstrophy in this channel domain was found to be equal to 10.692, and as the number of interpolating points was further increased, the numerical results asymptotically approached the analytical solution of $\frac{32}{3} = 10.667$.

Having devised a technique to approximate the amount of enstrophy captured in given volumes, we go back to our original motivation of comparing the amount of enstrophy captured in the coherent structures at each λ_2 level for the flow past the curved cylinders of this study. Figure 3.6(a) shows the normalized enstrophy curve versus λ_2 for the flow past body C at a Reynolds number of 100. The proportion of the enstrophy, Z, captured within the coherent structures using the λ_2 definition has been normalized by the total enstrophy, Z_{tot}, within the global flow domain and is plotted as a function of the cut-off value. The two regimes documented by Creusé & Mortazavi (2001) can be recognized in the results of this three-dimensional case. Figure 3.6(b) depicts this curve in a log-log axis.

In Figure 3.7 the λ_2 structures are shown for the six points (a, b, c, d, e, f) marked along the curve of Figure 3.6 in order to obtain a more physical understanding of the trends of the normalized enstrophy versus λ_2 curve. Specifically, the six positions correspond to cut-off values of: (a)$\lambda_2 = -0.0001$, (b)$\lambda_2 = -0.005$, (c)$\lambda_2 = -0.02$, (d)$\lambda_2 = -0.1$, (e)$\lambda_2 = -0.2$, and (f)$\lambda_2 = -1.5$. We observe that at very low values, as shown in Figure 3.7(a) for $|\lambda_2| = 0.0001$ for example, numerical noise is masking the clear representation of vortex dynamics in the wake. At a higher value of $|\lambda_2| = 0.005$, Figure 3.7(b), the wake topology starts becoming apparent. Extracting

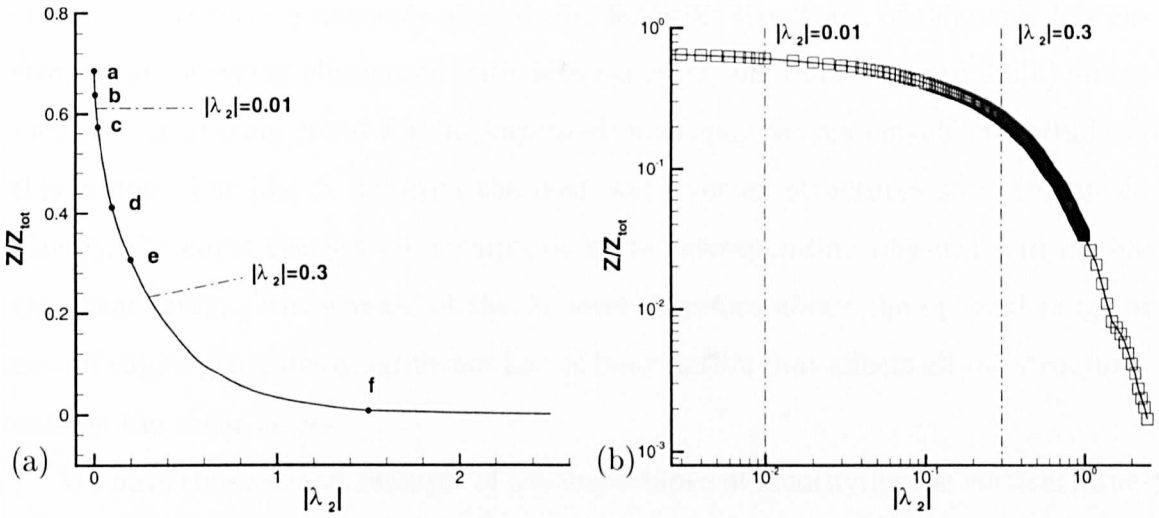


Figure 3.6: (a) Normalized enstrophy, Z/Z_{tot}, versus λ_2 for the flow past Body C at $Re = 100$, (b) log-log axis

at an even higher value of $|\lambda_2| = 0.02$, we can visualize the wake topology and the representative wake dynamics without the presence of numerical noise. Similarly, at $|\lambda_2| = 0.1$ the main vortical structures are still discerned, but we already notice the disappearance of the vortex cores furthest downstream from the body. The difference in the termination of the vortex cores at the horizontal part of the curved cylinder can also be observed. At $|\lambda_2| = 0.2$, Figure 3.7(e), only the higher enstrophy vortex cores, the ones closer to the body, are now apparent. Finally, at $|\lambda_2| = 1.5$ barely the shear layers are captured. Hence, within the range $0.01 \leq |\lambda_2| \leq 0.3$ a more optimal representation of the coherent structures in the wake of body C can be observed. The three-dimensional vortex shedding from the curved cylinder is captured without being obscured by the numerical noise. It is within this range that the vortical structures are not considerably altered hence corresponding to a suitable choice for vortex core extraction.

Going back to Figure 3.6(a), for $|\lambda_2| < 0.01$ there is high variation in the normalized enstrophy for small changes in the λ_2 level and a very large percentage of the total enstrophy is captured. This region corresponds to the numerically noisy vorticity fields as for example shown in Figure 3.7(a). The range $0.01 \leq |\lambda_2| \leq 0.3$ next corresponds to the optimal representation of the coherent structures for the flow past body C as depicted in Figures 3.7(c), (d), (e). The near wake vortical

structures are not significantly altered; the far wake structures of relatively low enstrophy are however eliminated with increasing cut-off value. Figure 3.6(a) shows indeed a decreasing trend for the captured enstrophy versus cut-off magnitude in this region. For $|\lambda_2| > 0.3$ even the near wake vortex structures start to vanish. Finally, the curve reaches an asymptotic state corresponding physically to merely the shear layers. An increase of the λ_2 level therefore above the optimal range of cut-off values generates a significant loss of information that affects all the structures outside the shear layers.

We have thus seen an example of the importance of identifying the vortical structures at the appropriate cut-off range. The asymptote to the curve at zero includes the numerical noise. Extracting at this level therefore would not be desirable since any identification of coherent structures and representation of the wake dynamics would be masked by the numerical noise. The asymptote to the curve at infinity corresponds to the very energetic shear layers; hence extracting at that level would also not be desirable since no information of the wake structures developed would be included. At the optimal cut-off range the λ_2 value is large enough to have eliminated any background noise, but at the same time is small enough not to have missed any information on the wake features. In conclusion, numerical application of the λ_2 identification criterion should be used in conjunction with an analysis of the enstrophy captured in order to determine a valid range of cut-off values.

In Chapters 4 and 5 we will see more examples of the cut-off analysis of coherent vortical structure identification. Specifically, in Chapter 4 we will investigate the enstrophy versus cut-off value trends for the flow past body B at a Reynolds number of 100. This case involves a shear velocity inlet profile and a wall boundary at the bottom of the computational domain where body B ends. It therefore results in complex vortical structures where the difference between the vorticity magnitude criterion and this cut-off analysis of the coherent structures' identification can be highlighted. In Chapter 5 we will see the cut-off analysis for the flow past body C now at a higher Reynolds number of 500.

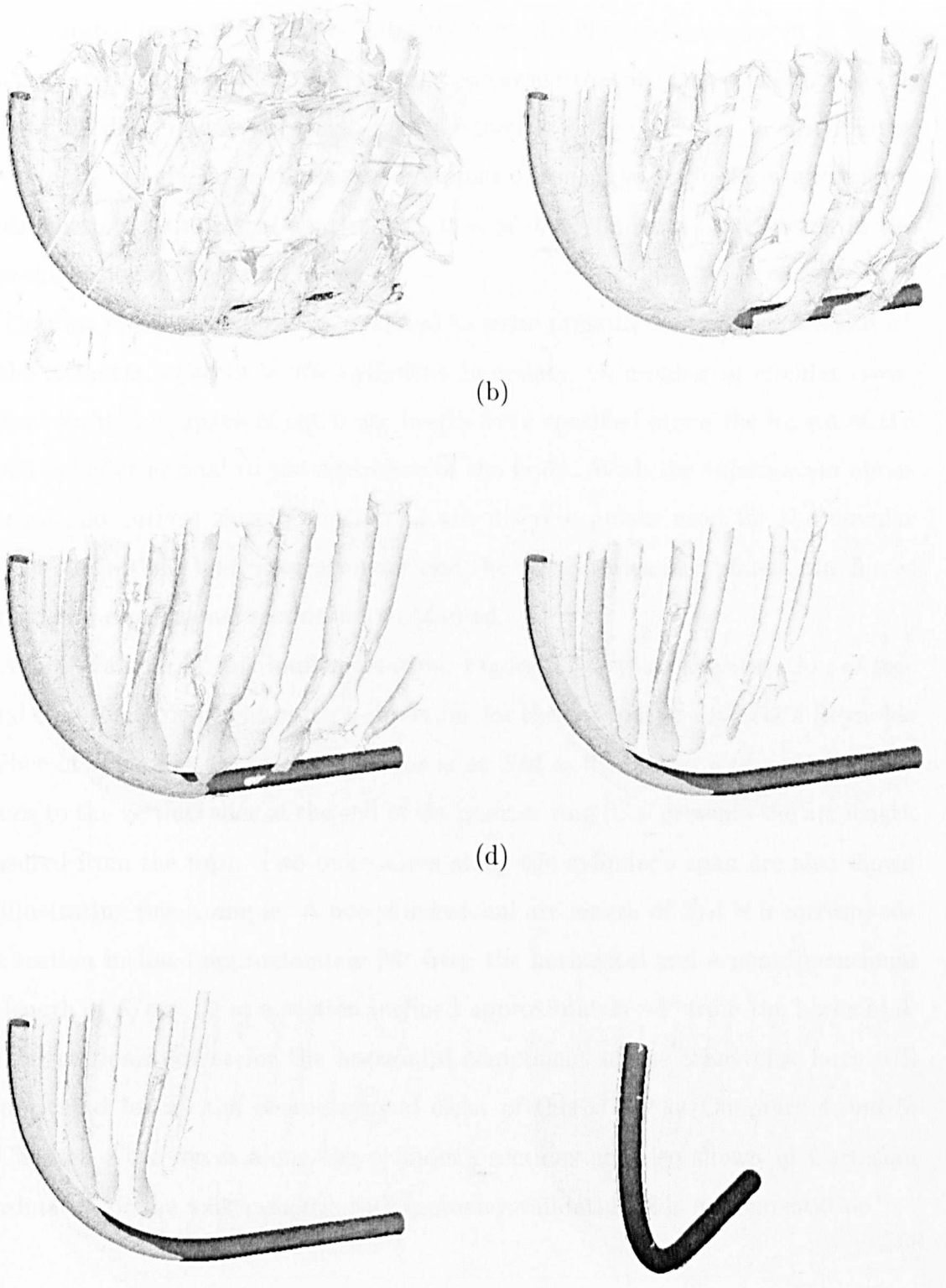


Figure 3.7: Isocontours of λ_2 at: (a) λ_2 = -0.0001, (b) λ_2 = -0.005, (c) λ_2 = -0.02, (d) λ_2 = -0.1, (e) λ_2 = -0.2, (f) λ_2= -1.5

3.5.3 Sectional force coefficients

The integrated forces are extracted directly from the Navier-Stokes solver in three-dimensions. In the course of this research it emerged that valuable insight could be gained from determining the variation of the forcing along the span. Identifying the forces applied at given two-dimensional sections of the curved cylinder would enable the distinction of the extent that each section of the cylinder is contributing to the three-dimensional integrated forces.

The Navier-Stokes solver was modified to write pressure and viscous stresses on all the elements adjacent to the cylinder's boundary. A number of circular cross-sections located at spans of equal arc length were specified along the length of the curved cylinder normal to the centreline of the body. With the information about pressure and surface shear extracted at the discrete points used for the circular sections' definitions and integrating around the two-dimensional planes, the forces on each two-dimensional section were obtained.

As an example of this implementation, Figure 5.5 depicts the variation of sectional C_{Fy}, force coefficient in the y-direction, for the flow past body C at a Reynolds number of 100. The top of the cylinder is at $S/d = 0$ whereas $S/d = 19.6$ corresponds to the vertical slice at the end of the quarter ring (S represents the arc length measured from the top). Two more slices along the cylinder's span are also shown for illustrating this example. A non-dimensional arc length of $S/d = 5$ corresponds to a section inclined approximately 23° from the horizontal and a non-dimensional arc length of $S/d = 10$ to a section inclined approximately 46° from the horizontal.

The sectional forces for the horizontal component of the transverse force will be presented for all the computational cases of this study in Chapters 4 and 5. In Chapter 4 the forces along the cylinder's sections are also shown in Cartesian coordinates for the axisymmetric ring geometry validating this implementation.

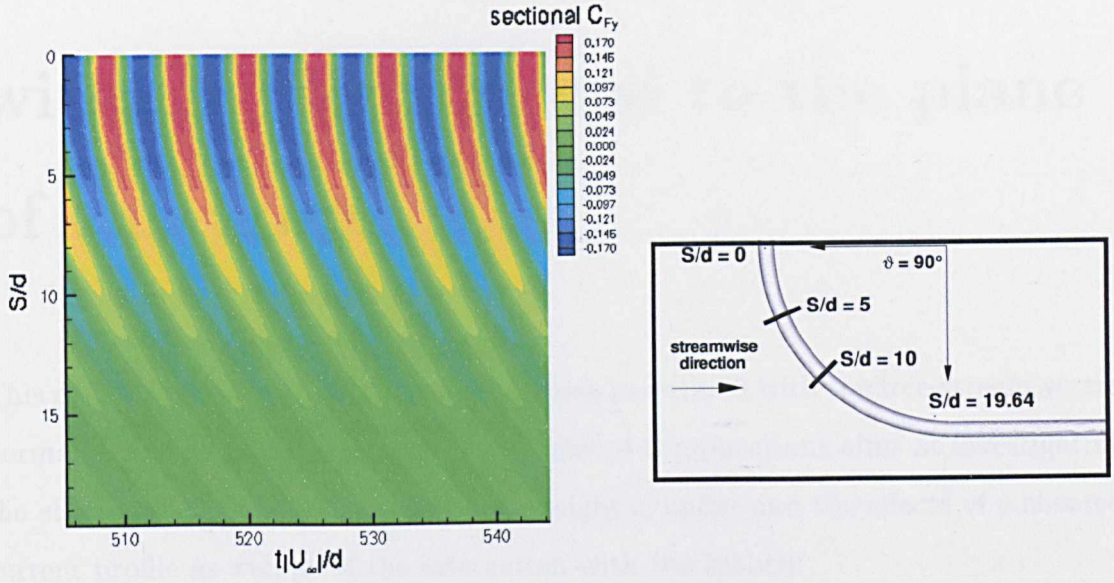


Figure 3.8: Variation of sectional C_{Fy} for Body C, $Re = 100$. To illustrate the orientation of the planes along the cylinder's span two sample sections are also shown.

Chapter 4

Three-dimensional computations with the flow normal to the plane of curvature

This chapter presents the set of computations performed with the free-stream vector normal to the plane of curvature. This series of computations aims at investigating the effects of curvature compared to a straight cylinder and the effects of a sheared current profile as well as of the interaction with the seabed.

The two body configurations employed in this chapter have been discussed in section 1.3 and are depicted in Figure 1.2. In section 4.1.1 the flow past body A at a Reynolds number of 100 will be presented. The flow past body B under the combination of a no-slip wall boundary and a sheared velocity profile at the inlet will be described in section 4.1.2. Section 4.1.3 includes the flow past the same body and sheared velocity profile at the inlet, but with an inviscid wall boundary (slip). Finally, the flow past the same body with a uniform velocity profile and an inviscid wall boundary is presented in section 4.1.4. Furthermore, the flow past body A has also been computed at a higher Reynolds number of 500 and is discussed in section 4.2.

4.1 Reynolds number 100: Results and discussion

4.1.1 Flow past body A

The flow past body A, which is effectively a quarter ring of 12.5 non-dimensional radius of curvature, depicted in Figure 1.2(a), is presented in this section at a Reynolds number of 100.

Figure 4.1 depicts a cut in the computational domain at a plane in the streamwise direction and exhibits symmetry about the diagonal of the region. The flow direction was in the y-direction, effectively into the page and therefore the inlet and outlet planes would be parallel to the page. In the streamwise direction, the distance to the outlet was 15 diameters from the axis of the body and the inlet distance was 5 diameters. Boundaries A and B include an intersection with the curved cylinder and so a symmetry boundary condition was prescribed. Boundaries C and D correspond to free-stream boundaries assigned a uniform velocity boundary condition, U_∞=[0 1 0].

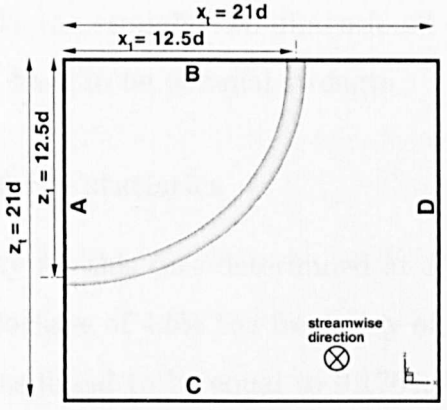


Figure 4.1: Computational boundaries (not to scale) for body A in a plane normal to the free-stream vector

The hybrid mesh created for this computation comprised a total of 7464 elements, out of which 790 were the prismatic boundary layer elements. The computation was performed originally with second order polynomials and was then restarted with polynomials of fourth, sixth and eighth order. At $P = 6$ this mesh accounts for $715,456$ local degrees of freedom, whereas at $P = 8$ it allows for $1,421,160$ local degrees of freedom. Blockage for these computational cases was 4.5%.

Figure 4.2 depicts the integrated force coefficients in the x-, y-, and z- directions. The x- and z- directions represent the horizontal and vertical component of the transverse force respectively and the y- direction is the direction of the drag. Figure 4.2(a) depicts the entire force history whereas Figure 4.2(b) depicts only the sixth to the eighth polynomial order part. The transition from $P = 2$ to $P = 4$ occurs at a non-dimensional time $\frac{tU_\infty}{d} = 200$, from $P = 4$ to $P = 6$ takes place at $\frac{tU_\infty}{d} \approx 403$ and the transition from order 6 to order 8 at $\frac{tU_\infty}{d} \approx 427$.

With this geometry being an axisymmetric body with symmetry boundary conditions, the forces in the x- and z- directions come out to be of equal amplitude and frequency. Unlike the straight cylinder which exhibits a drag force with one frequency equal to twice that of the lift, the curved cylinder, as Figure 4.2 demonstrates, accounts for a second lower amplitude peak in the drag force as an effect of curvature. Note that the lower amplitude peak in the drag force is still apparent even when the polynomial order is increased from 4 to 6 and then to 8. Moreover, the mean in the two components of the transverse force is not zero as is the case for a straight cylinder. Unlike the straight two-dimensional cylinder, the two vortices shed per lift cycle do not have to be of equal strength.

Frequency and mean force statistics

The power spectra density for this case determined at $P = 8$ are shown in Figure 4.3. Under the current blockage of 4.5% the frequency of the horizontal component of the transverse force was found to be equal to 0.1764. As an effect of curvature, the drag was found to exhibit two frequencies as discussed above: one at 0.1764 and one at 0.3527.

- First order time integration, $P = 8$

  Table 4.1 depicts the frequencies, and the mean and rms values of the integrated forces in the three Cartesian directions determined with first order time integration at $P = 8$. Four decimal places will be employed in this section in order to highlight force convergence.

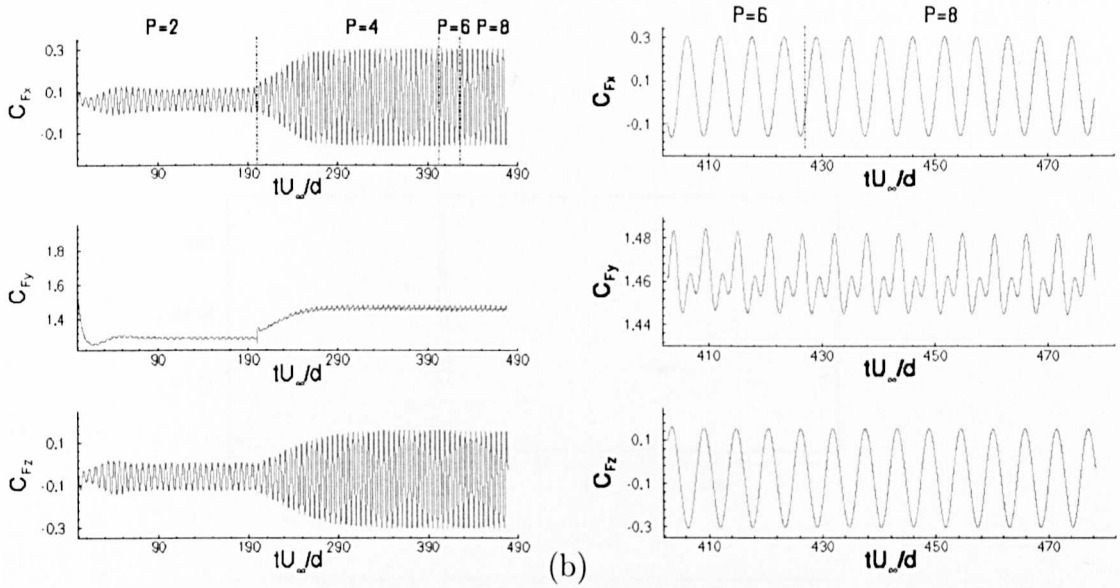


Figure 4.2: (a) Integrated force coefficients for the flow past Body A at $Re = 100$, x- and z- are the horizontal and vertical component of the transverse force respectively, y- is the direction of the drag; (b) A shorter section of the force history at sixth and eighth polynomial orders

- First order time integration, $P = 6$, time step variation

  Table 4.2 shows the frequencies along with the mean and rms values of the integrated force coefficients computed with first order time integration at different time steps, Δt, at $P = 6$. The original time step, $\Delta t = 0.0025$, has been reduced in steps of 1/4 up to $\frac{\Delta t}{2}$.

  As mentioned before, note that the mean in the horizontal and vertical component of the transverse force is not equal to zero, but has a magnitude of 0.0745 on average, exhibiting indeed antisymmetry. That the outer vortex is stronger than the inner one is hence accepted consistent with a positive mean in the x-direction. It should be clarified though that for the full ring geometry no mean forces in any transverse direction would be encountered. The mean forces here are an artefact of the computational domain representing only a quarter of the whole ring geometry as a generic shape for a curved cylinder. Hence only qualitatively can the features of this flow be compared with those of the full ring.

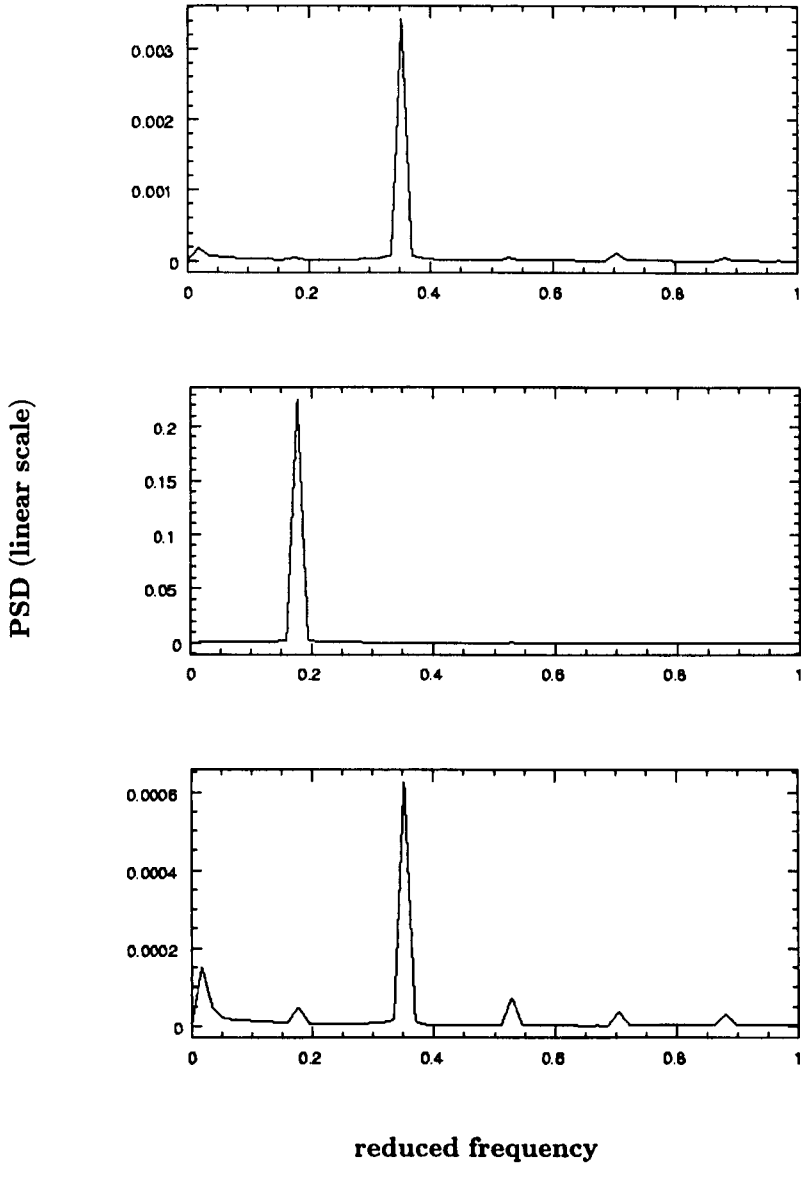


Figure 4.3: Power spectra density of the integrated forces in the x-, y- and z-directions for the flow past body A at $Re = 100$

	P=8
St_{Fx}	0.1764
St_{Fy}	0.1764
	0.3527
St_{Fz}	0.1764
$C_{Fx_{mean}}$	0.0750
$C_{Fx_{rms}}$	0.1614
$C_{Fy_{mean}}$	1.4608
$C_{Fy_{rms}}$	0.0109
$C_{Fz_{mean}}$	-0.0748
$C_{Fz_{rms}}$	0.1609

Table 4.1: Frequencies along with mean and rms values for the integrated force coefficients for the flow past body A at $Re = 100$ computed at $P = 8$ with first order time integration

The frequencies and the mean values for the integrated force coefficients have at most a discrepancy of 0.1% for the different time steps at first order time integration. Moreover, the frequencies and mean values for the force coefficients agree well between $P = 6$ and $P = 8$. With these discrepancies deemed negligible overall, force convergence has been accomplished.

The simulations were also computed with second order time integration and the agreement was in the order of 10^{-3}.

Extraction of pressure contours at slices normal to the axis of the curved cylinder in variable locations along the span indicated in-phase shedding as can be observed from Figure 4.4(a). Extraction of pressure isocontours in three-dimensions verified this as the axis of the vortex was found to be aligned to the axis of the cylinder as Figure 4.4(b) depicts. The ring, being an axisymmetric body, should have indeed been expected to shed in-phase along its length at this Reynolds number. In-phase shedding at this Reynolds number would also be expected from a straight cylinder

P = 6			
	$\Delta t = 0.0025$	$\Delta t = 0.001875$	$\Delta t = 0.00125$
St_{Fx}	0.1763	0.1762	0.1761
St_{Fy}	0.1763	0.1762	0.1761
	0.3526	0.3523	0.3522
St_{Fz}	0.1763	0.1762	0.1761
$C_{Fx_{mean}}$	0.0745	0.0745	0.0744
$C_{Fx_{rms}}$	0.1618	0.1614	0.1610
$C_{Fy_{mean}}$	1.4607	1.4602	1.4598
$C_{Fy_{rms}}$	0.0109	0.0108	0.0108
$C_{Fz_{mean}}$	-0.0744	-0.0744	-0.0743
$C_{Fz_{rms}}$	0.1613	0.1609	0.1605

Table 4.2: Statistics for the flow past body A at $Re = 100$ computed with first order time integration at $P = 6$ for three different time steps

implying that a sectional analysis might still be appropriate for these flow conditions. Even this however would be legitimate only if the difference in circulation shed each side of the wake centreline were negligible (a quasi-2D sectional analysis would not predict the difference in vortex strengths between inner and outer). Figure 4.4(b) (1) shows the extraction of pressure isocontours at a level corresponding to a pressure coefficient of -0.78. Figure 4.4(b) (2), on the other hand, shows the extraction of pressure isocontours at a level corresponding to a pressure coefficient of -0.98, projected onto the xy-plane.

The wake topology for this case, at a λ_2 value of -0.1, is shown in Figure 4.5 at the time of a C_{Fx} maximum, $\frac{tU_\infty}{d} \approx 435$. Recalling that this body is effectively a quarter of the ring geometry, we are essentually visualizing a quarter of the inner and outer vortex rings expected to shed periodically in the wake of an axisymmetric ring.

As mentioned in section 2.6, in their study of the flow past rings at low Reynolds numbers, Leweke & Provansal (1995) visualized vortex rings parallel to the body

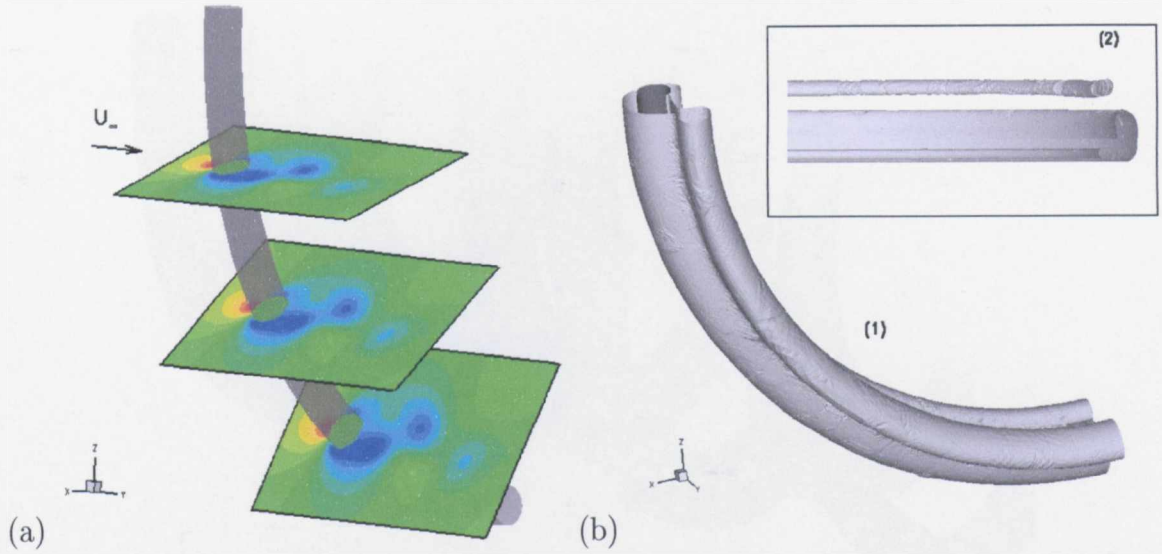


Figure 4.4: (a) Pressure contours on planes normal to the cylinder axis for the flow past body A at $Re = 100$, $\frac{tU_\infty}{d} \approx 435$, C_{Fx} maximum; (b) 3D pressure isocontours for body A, $Re = 100$, $\frac{tU_\infty}{d} \approx 435$, C_{Fx} maximum: (1) 3D view, $C_p = -0.78$, (2) top view, $C_p = -0.98$

for smooth initial conditions for a ring of aspect ratio equal to 76.2 at a Reynolds number of 105 (see Figure 2.11). Note that as mentioned in Chapter 1, body A of this study would correspond to a ring of aspect ratio equal to 81.7.

Finally, it should be noted that the pressure (iso)contours (Figure 4.4) can be used equally well with the λ_2 criterion as indicators of the vortex dynamics for this case as it resembles a 2D flow.

Sectional forces have also been computed at slices normal to the cylinder axis, with S/d designating the non-dimensional arc length measured from the top (the top of the curved cylinder is at $S/d = 0$). Figure 4.6(a) shows a time history of the sectional C_{Fx} which is well correlated with straight bands of alternating sign exhibiting axisymmetric two-dimensional vortex shedding. The regular periodic fluctuations coincide with the maxima and minima in the integrated force coefficients. Figures 4.6(b) and (c) depict the forces along the cylinder in Cartesian coordinates and demonstrate again the antisymmetry between the x- and z- directions as mentioned previously, validating the application of the sectional forces concept. For example, in

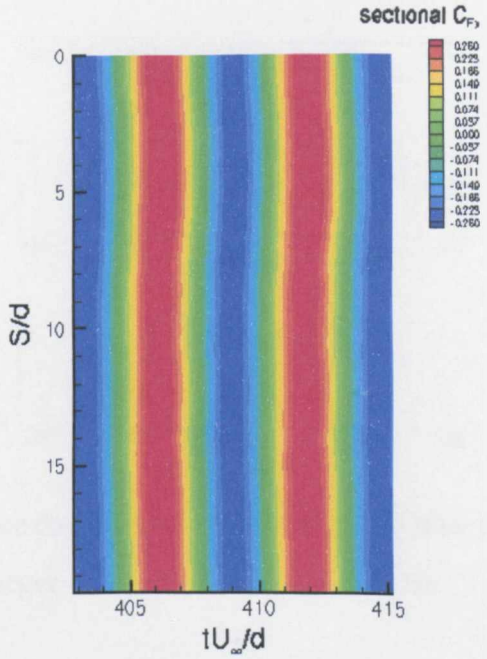


Figure 4.5: Wake topology for the flow past body A, $Re = 100$, $\lambda_2 = -0.1$, $\frac{tU_\infty}{d} \approx 435$, C_{Fx} maximum

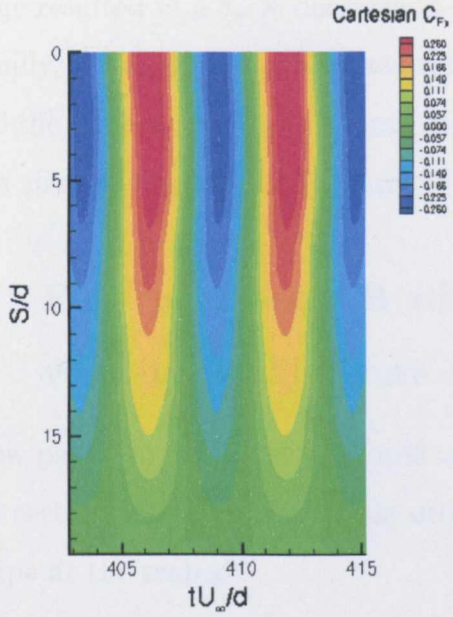
Figure 4.6(b), Cartesian C_{Fx} decays as a result of the geometry becoming aligned to the x-axis, as the horizontal component of the transverse force becomes the vertical one and vice versa.

As mentioned in Chapter 3, the p-refinement attribute of this spectral/hp element method, was taken advantage of in all the cases of this work. In analogy to a hierarchical mesh convergence study, the order of the expansion basis was progressively increased on a fixed mesh of elements. In addition, for this case the domain size parameters were modified to examine the mesh-dependency of the results for the flow past body A. A second mesh was thus constructed, where: (i) boundaries D and C were each moved by another 5 diameters away from the body, and (ii) the inflow and outflow planes were extended to a distance of 10 and 25 diameters, respectively, from the axis of the body. This second mesh comprised $12,526$ elements and at $P = 6$ it accounted for $1,140,664$ local degrees of freedom.

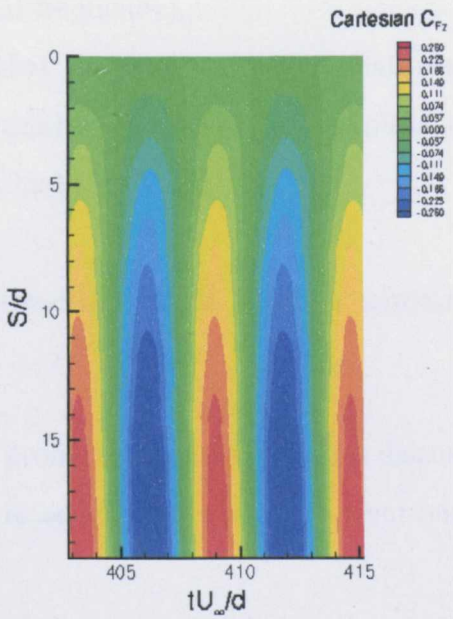
Figure 4.7 depicts the integrated force coefficients for the flow past body A with this larger mesh when the solution was computed at sixth polynomial order and can be compared with Figure 4.2(b). With the computational blockage now reduced to



(a)



(b)



(c)

Figure 4.6: Variation of the forcing in two-dimensional sections normal to the axis of body A, $Re = 100$: (a) Sectional C_{Fx}, (b) Cartesian x-component force coefficient, (c) Cartesian z-component force coefficient

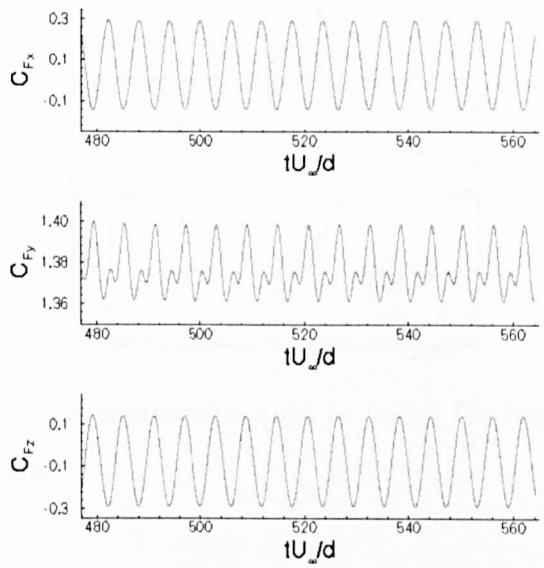


Figure 4.7: Integrated force coefficients at $P = 6$ for the flow past body A, $Re = 100$, using a second mesh of larger computational domain size

2.9%, the Strouhal frequency consistently decreased to 0.1696 (a 35% decrease in blockage resulted in a 3.7% decrease in Strouhal frequency).

Finally, it should be emphasized however that the qualitative flow features remained the same overall for this mesh as for the mesh with the smaller computational domain size used in this study of the flow past body A.

4.1.2 Flow past body B with a no-slip wall and a sheared velocity profile (case I)

The flow past body B under a sheared velocity profile and a no-slip wall is discussed in this section. The geometry was originally intended to represent a semi-buried riser pipe at the seabed.

Figure 4.8 shows a cut in the computational domain at a plane normal to the free-stream. The flow direction is again in the y-direction, into the page, and the inflow and outflow planes are 5 and 15 diameters away from the cylinder axis respectively. Boundaries A and B involve an intersection with the curved cylinder and so a symmetry boundary condition was prescribed. Boundary C was assigned a wall (no-slip) as a boundary condition. Boundary D corresponds to a free-stream

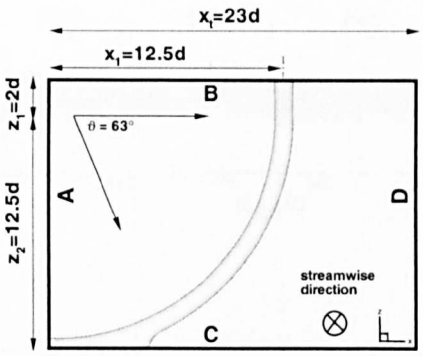


Figure 4.8: Computational boundaries (not to scale) for body B in a plane normal to the free-stream vector

boundary where an exponentially decaying sheared velocity profile was specified. The free-stream velocity boundary condition was U_∞=[0 v 0], where:

$$\mathrm{v} = 1 - e^{-(z+12.5)} \tag{4.1}$$

This shear profile resembles that of a boundary layer developing from the seabed. The velocity is equal to unity at the top of the geometry (expressed as $U_{\infty T} = 1$) and equal to zero at the bottom to conform with the no-slip condition at the wall boundary. The shear profile is such that at 4.6 cylinder diameters from the seabed, the velocity achieves 99% of its maximum value.

As mentioned in section 1.1, artificial blending was applied to body B for sections at angles larger than $63°(0.35\pi)$ to the horizontal and smaller than $68°(0.38\pi)$ where the body ended semi-buried into the solid boundary. The lower half of the geometry was expanded by adding from the centreline a factor of $100(\theta - 0.35\pi)^2$ to the x-coordinates of the originally circular cross-sections.

This artificial blending had to be applied at the point of contact of the body with the seabed in order to alleviate the mesh generation issues resulting from the very small angles developed in the prismatic elements at the intersection of the geometry with the seabed. This artificial expansion is believed not to be significant in altering the flow features. With respect to the offshore industry motivation of this work, finally, the resultant geometry was closer to a catenary riser making tangential

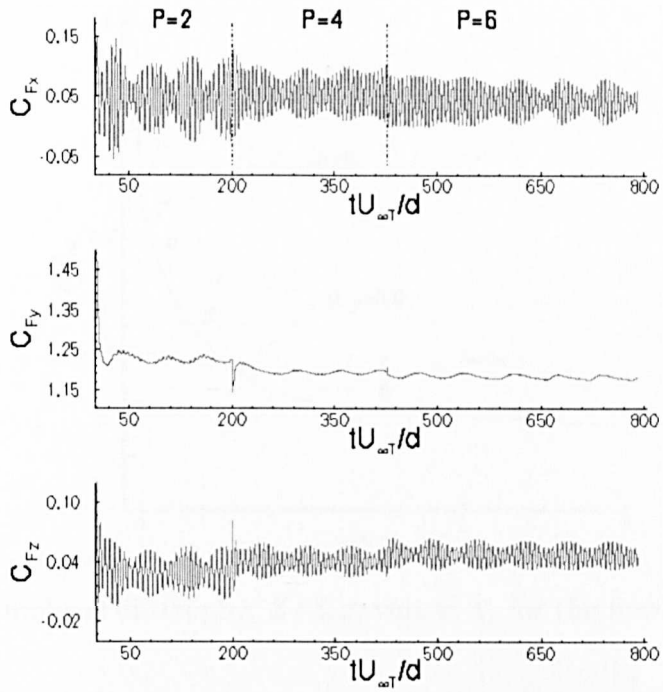


Figure 4.9: Force history for the flow past body B, case I, at $Re = 100$, x- and z- are the horizontal and vertical component of the transverse force respectively, y- is the direction of the drag

contact with the seabed. Risers of this type are often semi-buried in the ground with seabed material adhered over the long run of their lifetime.

The mesh created for this case consisted of 7902 elements, out of which 864 were the prismatic surface elements. The computation was initially performed using second order polynomials and was then restarted at $P = 4$ and $P = 6$. At $P = 6$, this mesh accounted for 760, 536 local degrees of freedom per variable. Blockage for these computational cases was approximately 6%.

Figure 4.9 depicts the force coefficients in the x-, y-, and z- directions, where y- is the direction of the drag and x- and z- are the horizontal and vertical components of the transverse force respectively. Non-dimensional time $\frac{tU_{\infty T}}{d} = 200$ represents the transition from $P = 2$ to $P = 4$ and $\frac{tU_{\infty T}}{d} \approx 426$ corresponds to the transition from $P = 4$ to $P = 6$. These force plots demonstrate a modulation in the horizontal and vertical component of the transverse force with the beating frequency being equal to a tenth of the shedding frequency (indeed from the integrated 3D forces

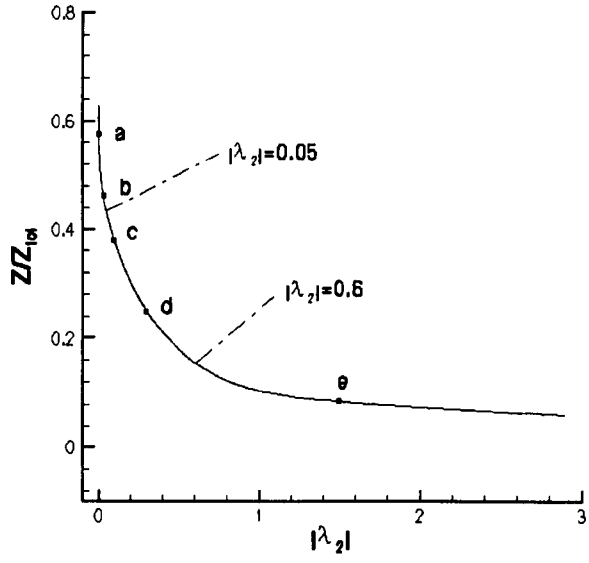


Figure 4.10: Normalized enstrophy, Z/Z_{tot}, versus λ_2 for the flow past Body B, case I, at $Re = 100$

the envelope is repeated every 10 shedding periods).

As mentioned in section 3.5.2, the enstrophy versus λ_2 cut-off value trends for this flow also will be presented in this chapter. Figure 4.10 depicts the enstrophy Z, captured at each λ_2 level, normalized by the total enstrophy, Z_{tot}, as a function of the cut-off value for the flow past body B at $Re = 100$. The trends of the two asymptotes, at zero and infinity, discussed in section 3.5.2 apply to this case also: the asymptote to the curve at zero embraces the numerical noise whereas the asymptote to the curve at infinity corresponds to the most energetic shear layers.

Figure 4.11 shows the λ_2 structures at the specified positions (a, b, c, d, e) marked in Figure 4.10. As for Figure 3.7, at small λ_2 levels numerical noise is dominating (Figure 4.11(a)) while at high levels merely the shear layers are being captured (Figure 4.11(e)). The range $0.05 \leq |\lambda_2| \leq 0.6$ can be detected as the appropriate for the optimal representation of the vortical structures in the wake of body B at Reynolds number of 100. The wake topology shows the vortex cores being no longer parallel to the cylinder axis as the shear layers are not rolling up uniformly along the span.

Since this case involves a sheared velocity profile and a wall, the difference be-

tween this cut-off analysis of the coherent structures' identification criterion and the vorticity magnitude criterion can be highlighted. A normalized enstrophy isocontour is shown in Figure 4.11(f) demonstrating how the non-rotational shear features related to vorticity at the wall are also captured together with the coherent structures.

Figure 4.12 shows pressure contours at planes normal to the cylinder axis at $S/d = 6$, $S/d = 10$, $S/d = 14.5$. Unlike the flow past body A, the extraction of pressure contours at these planes demonstrates lack of correlation along the span of this geometry.

The variation of sectional C_{Fx} for slices normal to the cylinder axis at different locations of the span is depicted in Figure 4.13(a). The top of the cylinder is at $S/d = 0$ and the two-diameter vertical addition extends down to $S/d = 2$ from where the curved part of the structure originates. Figure 4.13(b) shows a schematic of the arc length definition used for Figure 4.13(a). An arc length of $S/d = 15.6$ corresponds to a section inclined approximately 63° from the horizontal after which the artificial blending was applied.

The sectional forces in Figure 4.13(a) are not correlated; at a specific time there is a variation of the sign of sectional C_{Fx} along the span and these forces are distinctly different from those in Figure 4.6. A simple count of the number of like-signed bands indicates that the top of the geometry is shedding at a higher frequency than the bottom, consistent with the observations for Figure 4.11(c) where the cores are detached from the shear layers at a later stage as the curved cylinder approaches the seabed. An oblique front is established towards the top of the cylinder. At times from $\frac{tU_{\infty T}}{d} \approx 310$ to $\frac{tU_{\infty T}}{d} \approx 330$ and from $\frac{tU_{\infty T}}{d} \approx 370$ to $\frac{tU_{\infty T}}{d} \approx 390$ in a periodic manner, a "fork" type structure in the distribution of sectional C_{Fx} can be observed from Figure 4.13(a). A vortex dislocation is often associated with this feature as a result of the variation of frequency along the span, as described in section 2.2.4. Finally, in the region of $S/d = 8$, which corresponds to a section inclined approximately 28° to the horizontal, the sectional forces show a more organized time pattern.

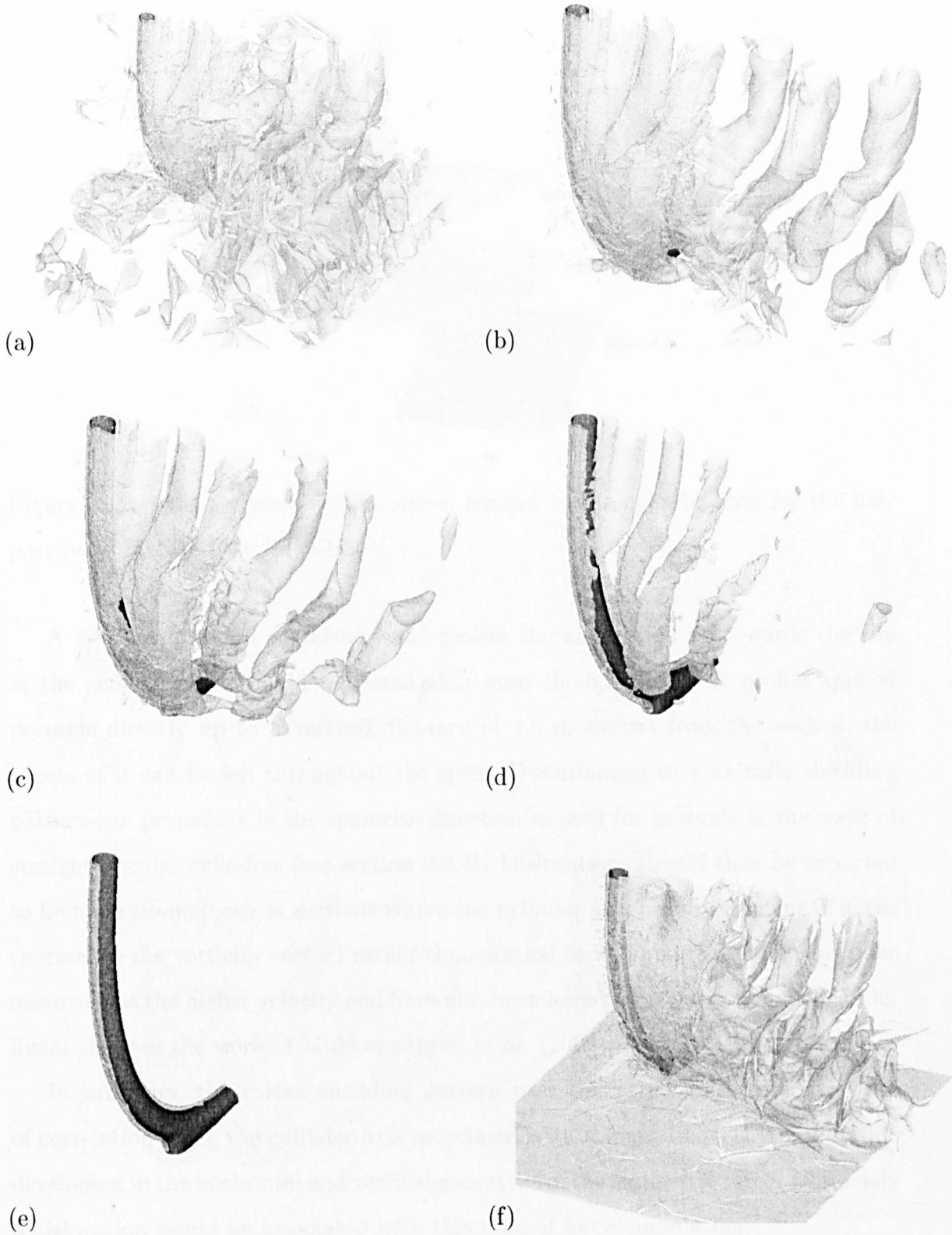


Figure 4.11: Isocontours of λ_2 at: (a) λ_2 = -0.001, (b) λ_2 = -0.03, (c) λ_2 = -0.1, (d) λ_2 = -0.3, (e) λ_2 = -1.5. Normalized enstrophy isocontour at the average value, 0.363, of the flow in the domain (f).

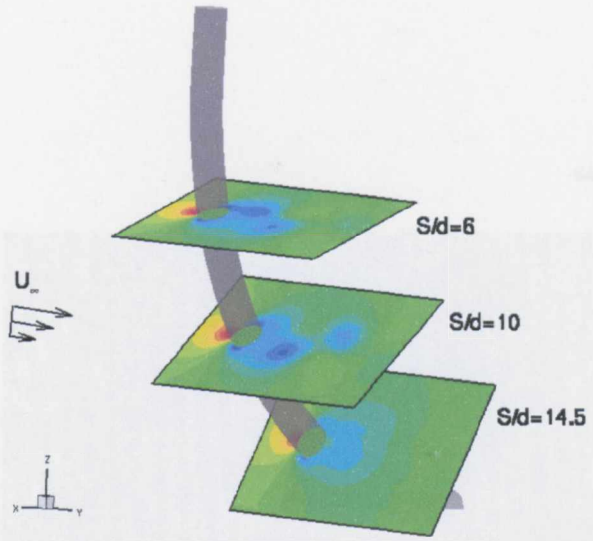
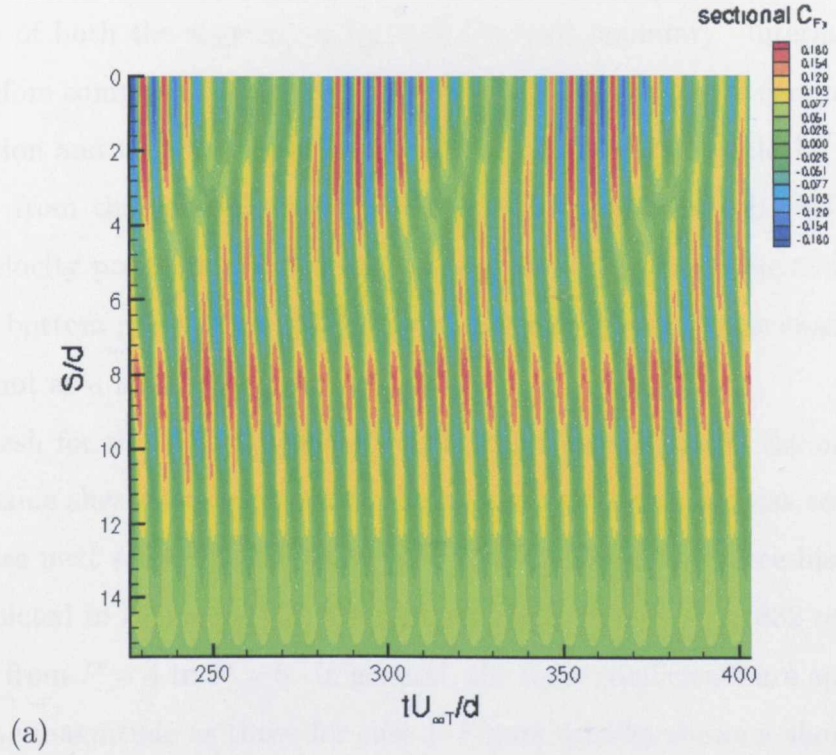


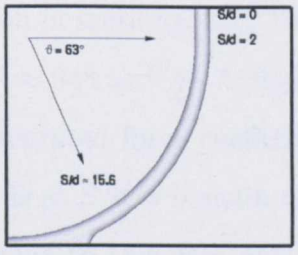
Figure 4.12: Pressure contours on planes normal to the cylinder axis for the flow past body B, case I, at $Re = 100$

A relevant question would be what pushes the dislocation up towards the top of the geometry. It should be noted that even though the shear profile applied pertains directly up to a vertical distance of 4.6 diameters from the seabed, the effects of it can be felt throughout the span. Disturbances to a uniform shedding pattern can propagate in the spanwise direction as seen for example in the wake of straight circular cylinders (see section 2.2.4). Dislocations should then be expected to be more pronounced at sections where the cylinder axis lies in the plane of shear (normal to the vorticity vector) rather than normal to it. Furthermore, dislocations occurring at the higher velocity end have also been found for straight cylinders under linear shear in the work of Mukhopadhyay *et al.* (2002).

In summary, the vortex shedding pattern past this structure exhibited a lack of correlation along the cylinder axis associated with a lower frequency modulation developing in the horizontal and vertical directions of the transverse force. Physically a dislocation would be associated with this type of force modulation.



(a)



(b)

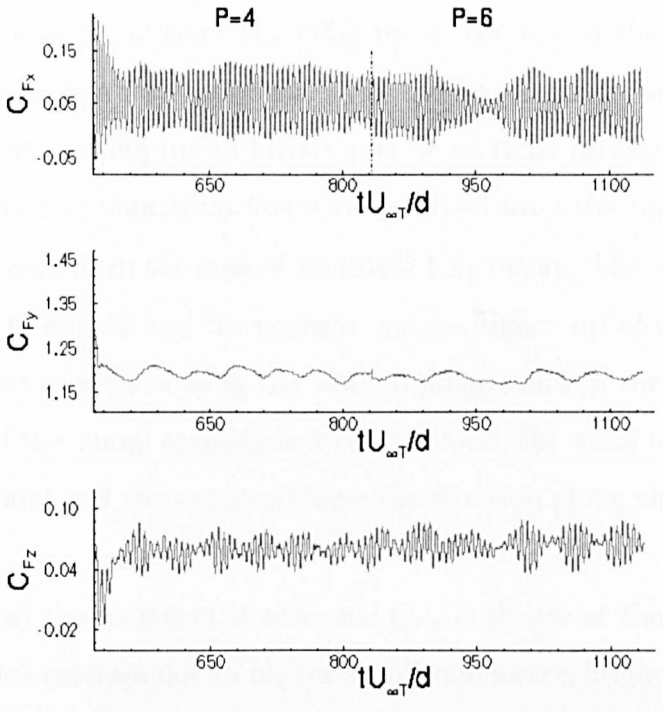
Figure 4.13: (a) Variation of sectional C_{Fx} along the length of Body B, case I, at $Re = 100$; (b) Arc length definition followed in describing the sectional forces for body B

4.1.3 Flow past body B with a slip wall and a sheared velocity profile (case II)

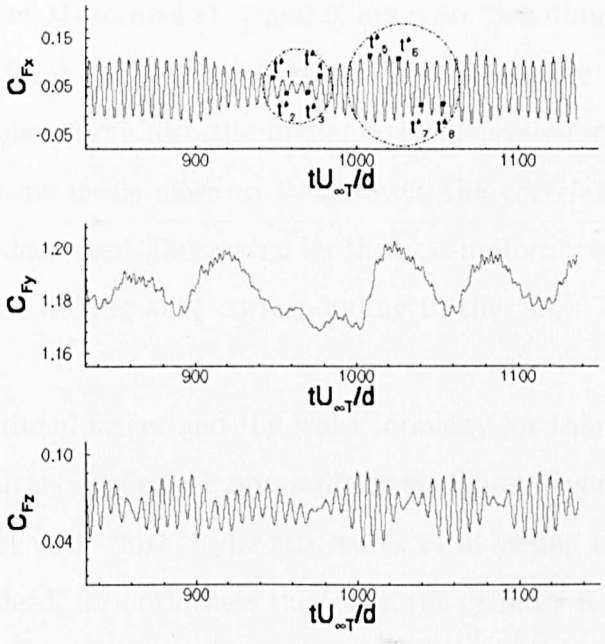
A direct comparison between the cases presented in section 4.1.1 and 4.1.2 involves the effects of both the sheared profile and the wall boundary. Intermediate cases were therefore computed whereby the bottom wall was assigned a symmetry boundary condition and thus the effect of the sheared profile alone could be investigated separately from that of the no-slip wall. The flow past body B under the same sheared velocity profile but with a slip wall boundary is thus presented in this section. The bottom plane is therefore now acting merely as a plane constraining the flow, but not as a no-slip boundary.

The mesh for this computational case is exactly the same as the one for case I with the same sheared velocity profile being applied. This case was restarted from case III (see next section), at $\frac{tU_{\infty T}}{d} \approx 518$, $P = 4$. The entire force history for this case is depicted in Figure 4.14(a). Non-dimensional time $\frac{tU_{\infty T}}{d} \approx 832$ represents the transition from $P = 4$ to $P = 6$. In general, the force coefficients are approximately of the same magnitude as those for case I. Figure 4.14(b) shows a shorter range of the force history, at $P = 6$, highlighting two sectors that will be discussed below in terms of the wake dynamics developed and the sectional forces.

In Figure 4.15(a) the variation of sectional C_{Fx} for slices normal to the cylinder axis is shown at times from $\frac{tU_{\infty T}}{d} \approx 943$ to $\frac{tU_{\infty T}}{d} \approx 984$. This corresponds to the first region marked in the plot of integrated force coefficients, Figure 4.14(b). The top of the cylinder in Figure 4.15(a) is at $S/d = 0$ again and Figure 4.13(b) corresponds to the arc length definition applied to this case also. The evolution of the vortex dynamics in this sector can be discussed with the sectional forces in conjunction with the wake structures depicted in Figure 4.15(b) at a λ_2 value of -0.1. The wake topology for this part is highly three-dimensional, especially at times $t_1^* \approx 949$, $t_2^* \approx 957$, and $t_3^* \approx 970$, where the shed vortices are not parallel to the cylinder axis and vortex linking is also shown to occur. Note that this sector corresponds to minimum amplitude force coefficients in the entire force history, as shown in Figure 4.14(a). The strongly out of phase shedding along the span with the highly three-



(a)



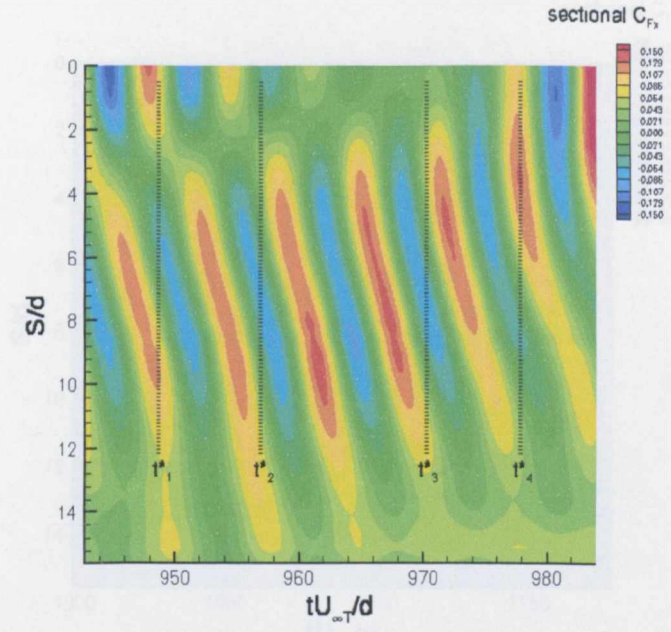
(b)

Figure 4.14: (a) Force history for the flow past body B at $Re = 100$, case II, x- and z- are the horizontal and vertical component of the transverse force respectively, y- is the direction of the drag; (b) A shorter section of the force history marking the sectors that correspond to Figures 4.15 and 4.16

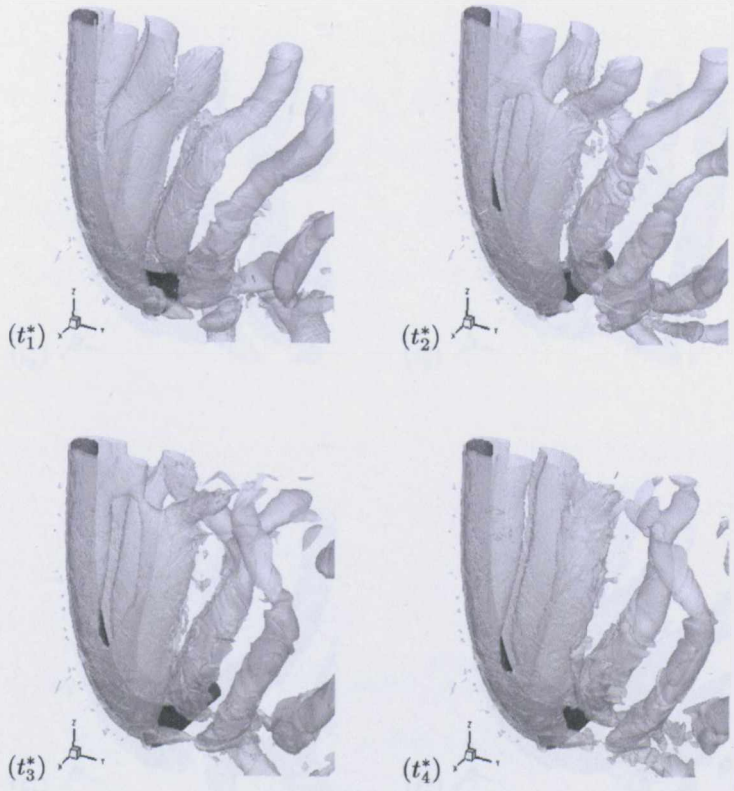
dimensional vortex structures at these time levels minimizes the force fluctuations. At time t_1^* the bottom shear layer is rolling up at the top of the geometry hence resulting in a positive sign for sectional C_{Fx} in the first cross-sections. However, as this shear layer is not rolling up uniformly and at sections further down along the span is connected to the counterclockwise vortex shed from the top in the previous shedding cycle, variations in the sign of sectional C_{Fx} occur. This linking continues to occur at times t_2^* and t_3^* and its position moves higher up along the geometry (smaller S/d values) as seen both in the wake topology and in the sectional forces. At t_4^*, at the end of this small amplitude force envelope, the wake topology becomes less three-dimensional and the sectional force distribution along the span relatively more uniform.

In Figure 4.16(a) the variation of sectional C_{Fx} is shown at the second sector of Figure 4.14(b) which corresponds to higher amplitude forces. Figure 4.16(b) depicts the wake topology at the corresponding times of $t_5^* \approx 1009$, $t_6^* \approx 1027$, $t_7^* \approx 1040$, and $t_8^* \approx 1054$. The vortex structures at t_5^* and t_6^* are more two-dimensional. The higher amplitudes in the force coefficients represent indeed a more correlated shedding process along the span (note also the higher contour levels for the sectional forces of this part). By time levels close to t_7^* however, the correlation in the shedding along the span has decreased, illustrated by the non-uniform rolling up of the shear layers and the vortex linking at t_8^* corresponding to the "fork" type distribution in the sectional forces.

Overall, the sectional forces and the wake topology for this case have exhibited similar patterns with those of case I: non-uniform shedding of vortices along the span, and an oblique front with "fork" type structures establishing in the distribution of sectional forces. Indeed, for both cases the top of the cylinder is shedding at a higher rate compared to the bottom, being affected by the exponentially decaying shear profile. However, the presence of a no-slip boundary resulted in more organized wake patterns towards the bottom of the structure (note the alignment of the sectional forces at $S/d = 8$) confining the oblique front. For the case of the slip wall boundary on the other hand, the oblique front is allowed to extend until further down along the span.

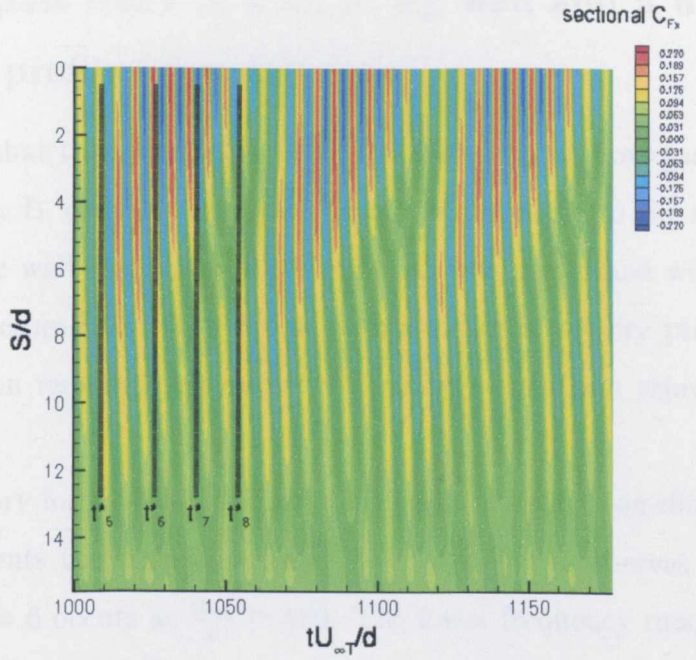


(a)

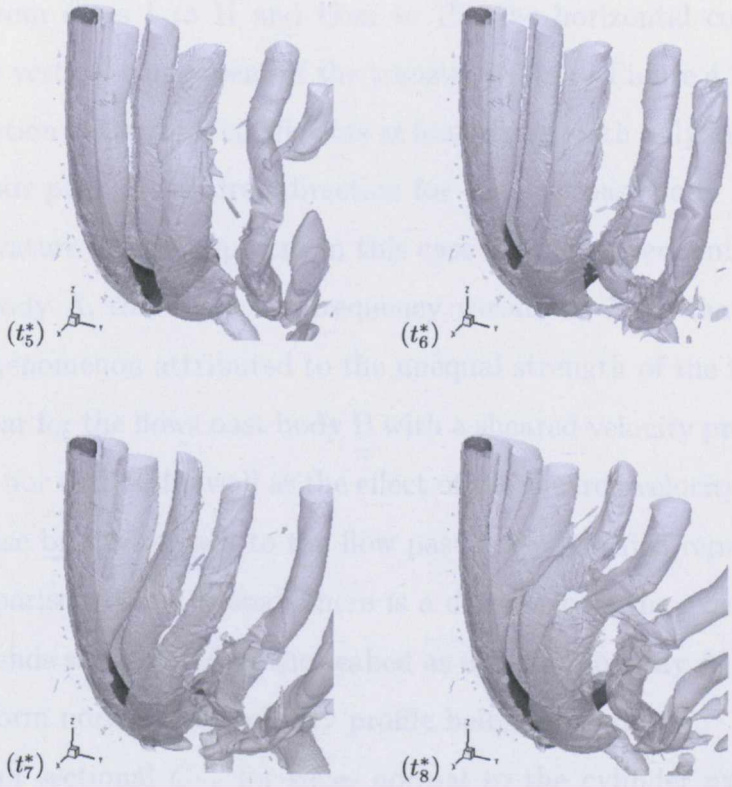


(b)

Figure 4.15: (a) Variation of sectional C_{Fx} for body B, case II, at $Re = 100$ from $\frac{tU_\infty T}{d} \approx 943$ to $\frac{tU_\infty T}{d} \approx 984$; (b) Wake topology extracted at the specified times $t_1^* \approx 949$, $t_2^* \approx 957$, $t_3^* \approx 970$, and $t_4^* \approx 978$, $\lambda_2 = -0.1$



(a)



(b)

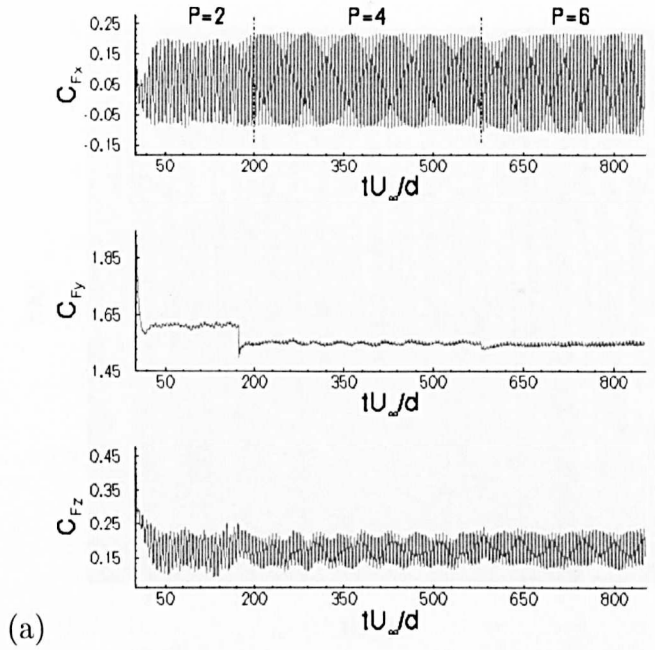
Figure 4.16: (a) Variation of sectional C_{Fx} for body B, case II, at $Re = 100$ from $\frac{tU_\infty T}{d} \approx 999$ to $\frac{tU_\infty T}{d} \approx 1178$; (b) Wake topology extracted at the specified times $t^*_5 \approx 1009$, $t^*_6 \approx 1027$, $t^*_7 \approx 1040$, and $t^*_8 \approx 1054$, $\lambda_2 = -0.1$

4.1.4 Flow past body B with a slip wall and a uniform velocity profile (case III)

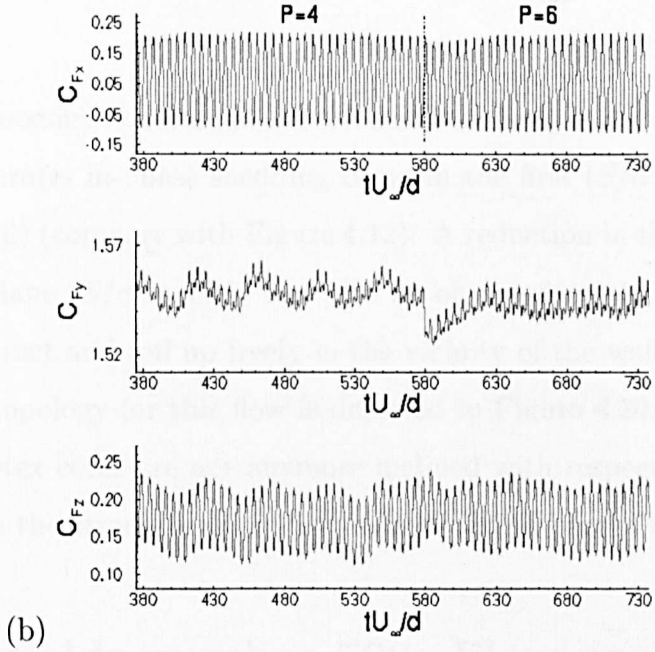
In order to show that the significant differences between the flow past body A and the flow past body B, case I, can indeed be attributed more to the sheared profile rather than to the wall boundary, a computation was performed with exactly the same mesh as for cases I and II, but now with a uniform velocity profile. The wall boundary condition remained a symmetry boundary condition representing a slip wall.

The force history for this case is shown in Figure 4.17(a). Non-dimensional time $\frac{tU_\infty}{d} = 200$ represents the transition from $P = 2$ to $P = 4$ whereas the transition from $P = 4$ to $P = 6$ occurs at $\frac{tU_\infty}{d} \approx 580$. The lower frequency modulation in the horizontal direction of the transverse force has now principally vanished. Overall, therefore, going from cases I to II and then to III, the horizontal component is affected before the vertical component of the transverse force. Figure 4.17(b) shows a more detailed section of the force coefficients at fourth and sixth polynomial orders. The lower amplitude peak in the drag direction for the flow past body A discussed as an effect of curvature is now apparent in this case too. However, unlike the case of the flow past body A, there is a low frequency variation. Note that this lower amplitude peak phenomenon attributed to the unequal strength of the two vortices did not become clear for the flows past body B with a sheared velocity profile neither with a no-slip wall nor with a slip wall as the effect of the sheared velocity profile was dominant. This case brings us back to the flow past body A which represented the base case for comparison. Even though there is a difference in the exact geometry studied (this case ends semi-buried at the seabed as opposed to body A), both cases had the same uniform normal flow velocity profile being applied.

The variation of sectional C_{Fx} for slices normal to the cylinder axis is shown in Figure 4.18. The sectional forces for this case demonstrate regular vortex shedding along most of the body's span, highlighted by the strong periodic fluctuations. However, after approximately $S/d = 10$, the sectional forces start decreasing in magnitude. The strength of the vortices decreases approaching the wall boundary.



(a)



(b)

Figure 4.17: (a) Force history for the flow past body B, case III, at $Re = 100$, x- and z- are the horizontal and vertical component of the transverse force respectively, y- is the direction of the drag; (b) A more detailed section of the force history from $\frac{tU_\infty}{d} = 375$ to $\frac{tU_\infty}{d} = 738$

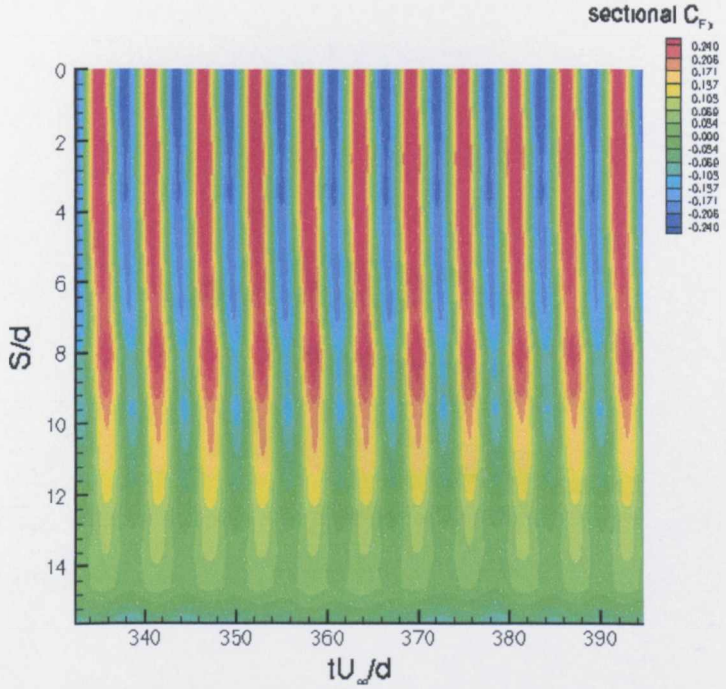


Figure 4.18: Variation of sectional C_{Fx} along the length of Body B, case III, at $Re = 100$

Extraction of pressure contours at slices normal to the cylinder axis, shown in Figure 4.19, also illustrates in-phase shedding between the first ($S/d = 6$) and the second plane ($S/d = 10$) (compare with Figure 4.12). A reduction in the pressure minimum by the third plane ($S/d = 14.5$) can also be observed as the shear layers are not allowed to interact and roll up freely in the vicinity of the wall.

The wake topology for this flow is depicted in Figure 4.20. Contrary to cases I and II, the vortex cores are not anymore inclined with respect to the cylinder axis consistent with the strong periodic fluctuations in the plot of the sectional forces.

4.2 Reynolds number 500: Flow past body A

The flow past body A has also been studied at a higher Reynolds number, that of 500. The computation was restarted from the flow field of the Reynolds number 100 case, presented in section 4.1.1, at fourth polynomial order.

Figure 4.21(a) shows the force history for this case starting from the flow field of the Reynolds number 100 case at $\frac{tU_\infty}{d} \approx 364$. Non-dimensional time $\frac{tU_\infty}{d} \approx 618$

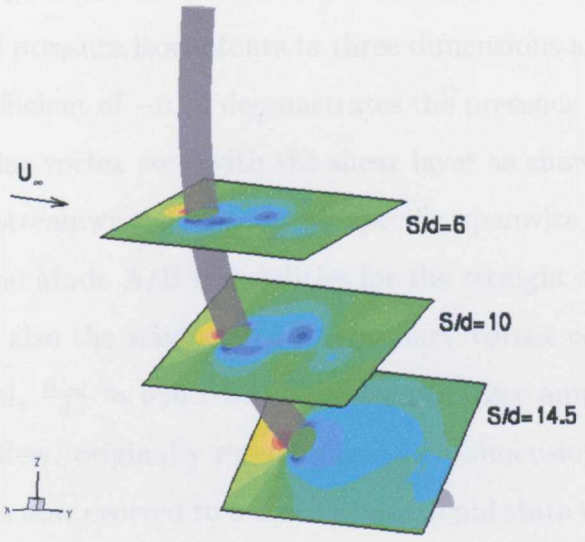


Figure 4.19: Pressure contours at planes normal to the axis of body B, case III, at $Re = 100$, $\frac{tU_\infty}{d} \approx 756$ (C_{Fx} maximum)

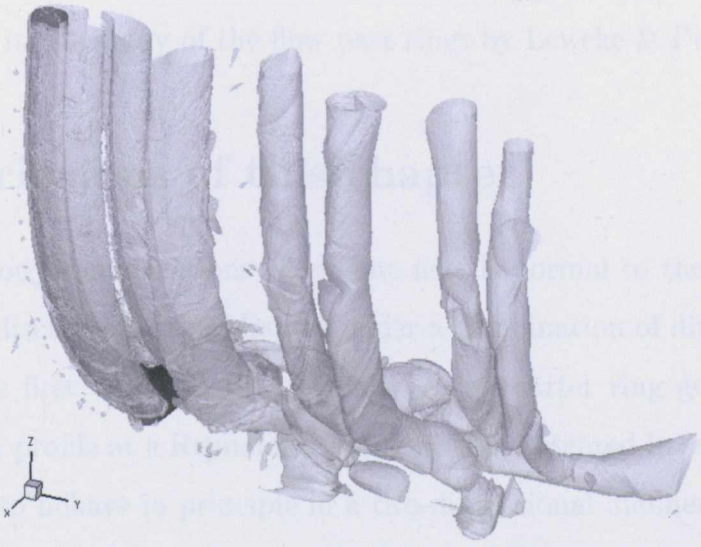


Figure 4.20: Vortex cores in the wake of body B, case III, at $Re = 100$, $\lambda_2 = -0.1$, $\frac{tU_\infty}{d} \approx 756$ (C_{Fx} maximum)

corresponds to the transition from fourth to sixth polynomial order. Figure 4.21(b) depicts a shorter range of the integrated force coefficients at $P = 6$.

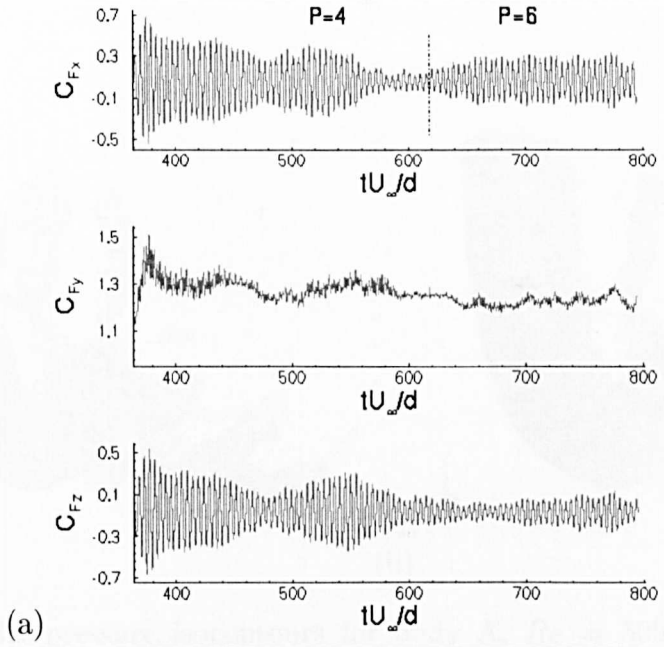
The extraction of pressure isocontours in three dimensions at a level corresponding to a pressure coefficient of -0.74 demonstrates the presence of braids connecting the first shed spanwise vortex core with the shear layer as shown in Figure 4.22(a), $\frac{tU_\infty}{d} \approx 627$. These streamwise structures at specific spanwise wavelengths appear similar to those of the Mode A/B instabilities for the straight circular cylinder (see section 2.2.3). Note also the waviness of the primary vortex cores, Figure 4.22(b), at another time level, $\frac{tU_\infty}{d} \approx 656$ corresponding to larger amplitude forces in the force history. This flow, originally resembling a two-dimensional flow past an axisymmetric body, has now evolved to a three-dimensional state with lack of spanwise correlation.

This is also demonstrated by the sectional forces for this case, shown in Figure 4.23, exhibiting intermittent fluctuations and no regularity, as opposed to the periodicity with the straight bands of alternating sign found at Reynolds number of 100 (Figure 4.6).

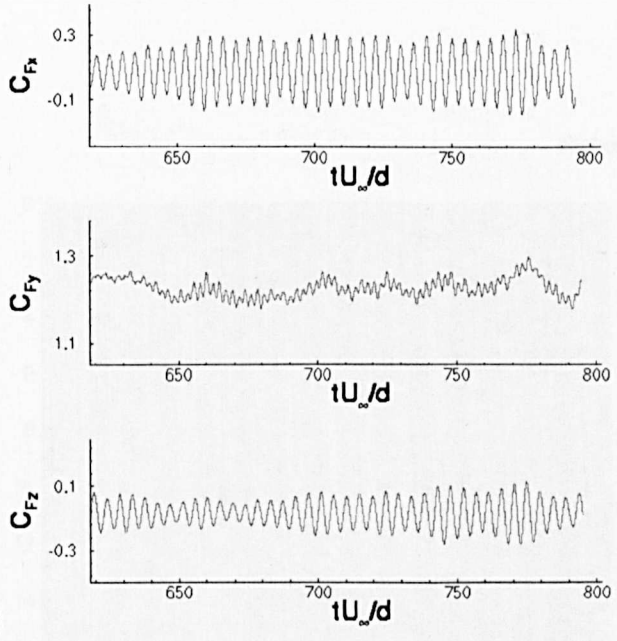
Finally, similarities with the Mode A/B transition for straight circular cylinders were also found in the study of the flow past rings by Leweke & Provansal (1995).

4.3 Conclusions of this chapter

Two separate body configurations where the flow is normal to the plane of curvature have been discussed in this chapter under a combination of different boundary conditions. The first case was that of body A, a quarter ring geometry under a uniform velocity profile at a Reynolds number of 100 presented in section 4.1.1. The flow was found to behave in principle in a two-dimensional manner with respect to cross-sections normal to the cylinder axis. In-phase shedding was shown along the span with vortex rings shed periodically, parallel to the body, in agreement with findings of past literature (Leweke & Provansal 1995). Even though this would appear to allow for a valid usage of a 2D sectional approach, features such as the unequal strength of the inner and outer vortices would not be accounted for by such

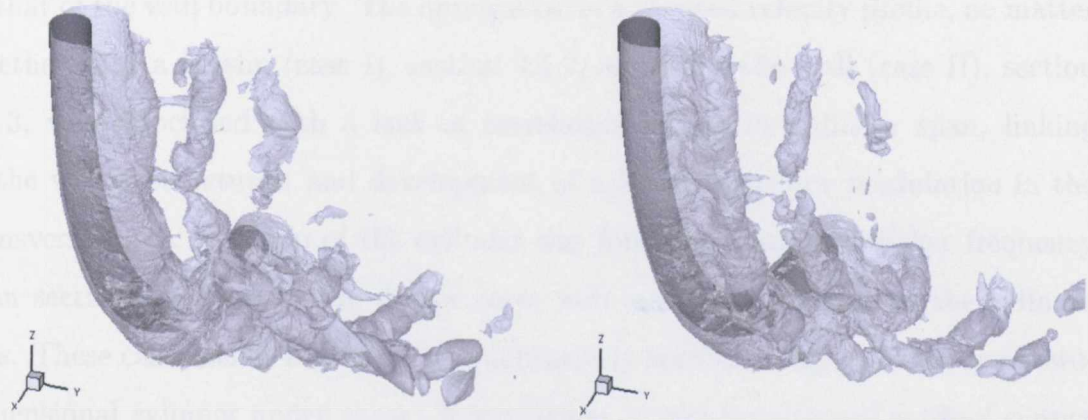


(a)



(b)

Figure 4.21: (a) Force history for the flow past Body A at $Re = 500$, x- and z- are the horizontal and vertical component of the transverse force respectively, y- is the direction of the drag; (b) A more detailed section of the integrated force coefficients at sixth polynomial order



(a) (b)

Figure 4.22: 3D pressure isocontours for body A, $Re = 500$, $C_p = -0.74$: (a) $\frac{tU_\infty}{d} \approx 627$, (b) $\frac{tU_\infty}{d} \approx 656$

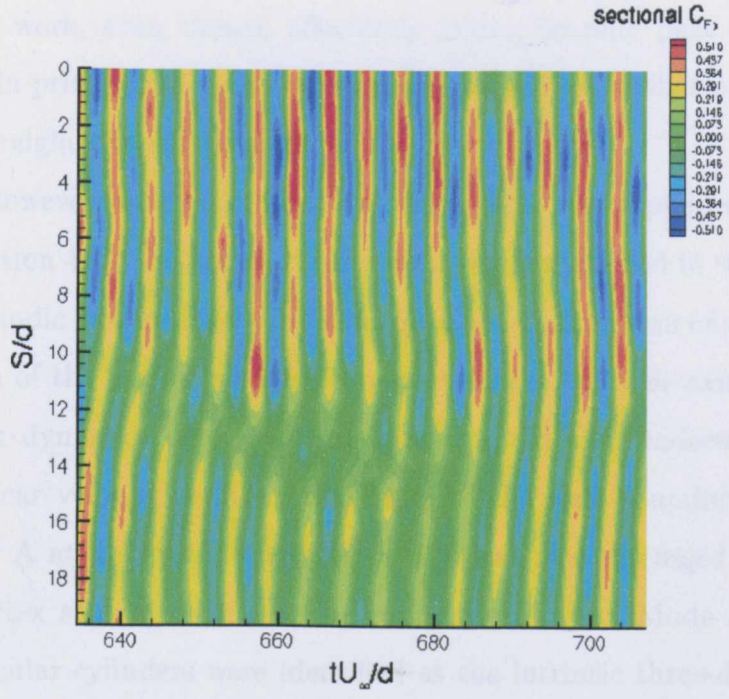


Figure 4.23: Variation of sectional C_{Fx} along the length of Body A, $Re = 500$

a two-dimensional method.

For the second body configuration which ends semi-buried in the ground, body B, the effect of the sheared profile has been found to be more significant when compared to that of the wall boundary. The application of a sheared velocity profile, no matter whether with a no-slip (case I), section 4.1.2, or with a slip wall (case II), section 4.1.3, was associated with a lack of correlation along the cylinder span, linking of the vortex structures, and development of a lower frequency modulation in the transverse force. The top of the cylinder was found to shed at a higher frequency than sections below, and the vortex cores were no longer parallel to the cylinder axis. These cases hence behaved in a qualitatively similar manner to a straight two-dimensional cylinder under shear. Nevertheless, a two-dimensional method cannot identify the three-dimensional wake features.

An oblique front with "fork" type structures was also established in the sectional forces as a result of this frequency variation along the span. Vortex dislocations were encountered in previous research of shear flows past straight circular cylinders (Mukhopadhyay *et al.* 2002). Interestingly, the exponentially decaying shear profile applied in this work, even though effectively acting on only part of the cylinder span, resulted in principle in similar qualitative behaviour to that of a linear shear applied on a straight circular cylinder.

In case III however, where a uniform velocity profile was applied with a slip wall, discussed in section 4.1.4 the vortex cores were no longer inclined to the cylinder axis and regular periodic fluctuations were restored in the distribution of sectional forces. The inclination of the vortex cores with respect to the cylinder axis and the more complex vortex dynamics described previously should thus indeed be attributed more to the shear velocity profile rather than to the wall boundary. Finally, the flow past body A at a Reynolds number of 500 was also discussed in section 4.2. Streamwise vortex structures resembling in nature those of Mode A/B transition for straight circular cylinders were identified as the intrinsic three-dimensionalities have become apparent at this Reynolds number for what was a formally 2D flow at $Re = 100$.

Chapter 5

Three-dimensional computations with the flow parallel to the plane of curvature

This chapter investigates the vortex shedding patterns past curved cylinders under uniform flow in the plane of curvature. The results of the fully three-dimensional computations are compared with experimental flow visualizations and the importance of the three-dimensional method over a sectional approach is considered.

As discussed in section 1.3, two body configurations (body C and body D) have been studied when the free-stream velocity vector is in the plane of curvature. In section 5.1.1 the computational results for the flow past body C at a Reynolds number of 100 are presented. The flow visualization procedure is also outlined and comparison is drawn between the towing tank flow visualizations and the computational findings. Section 5.1.2 presents the flow past body D at a Reynolds number of 100. The flow past body D with a vertical addition of six diameters at a Reynolds number of 100 is also investigated and discussed in section 5.1.3. All three cases have also been computed at a higher Reynolds number of 500 and compared with the experimental flow visualizations. Section 5.2.1 includes the results for the flow past body C at a Reynolds number of 500. Section 5.2.2 presents the flow past body D at a Reynolds number of 500 while the flow past body D with a six-diameter

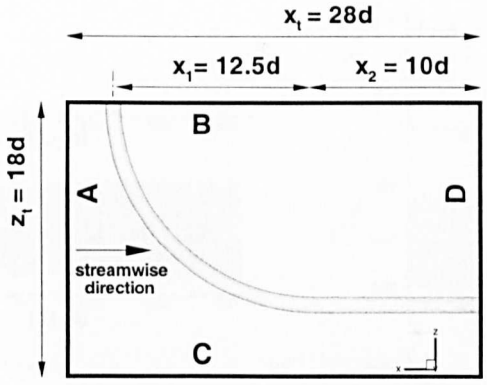


Figure 5.1: Computational boundaries (not to scale) for body C in a plane including the free-stream vector

vertical addition at a Reynolds number of 500 is discussed in section 5.2.3.

5.1 Reynolds number 100: Results and discussion

5.1.1 Flow past body C

The flow past body C, shown in Figure 1.3(a), at a Reynolds number of 100 is discussed in this section. As mentioned in section 1.3 this body consists of a quarter ring, of 12.5 non-dimensional radius of curvature, with a horizontal addition of ten diameters.

Figure 5.1 depicts a cut in the computational domain at a plane including the cylinder axis and the free-stream vector. The flow is in the negative x-direction, from left to right as shown. Boundary B includes an intersection with the curved cylinder and so a symmetry boundary condition was imposed. Boundary D corresponds to the outflow plane and boundaries A and C correspond to free-stream boundaries where the uniform velocity condition, U_∞=[-1 0 0], was imposed. The computational boundaries in the y-direction were at a distance of 5 diameters from the cylinder axis and a uniform free-stream condition was imposed also on these planes.

The mesh comprised 10250 elements, out of which 1184 were the prismatic surface elements. The computation was initially performed using second order polynomials

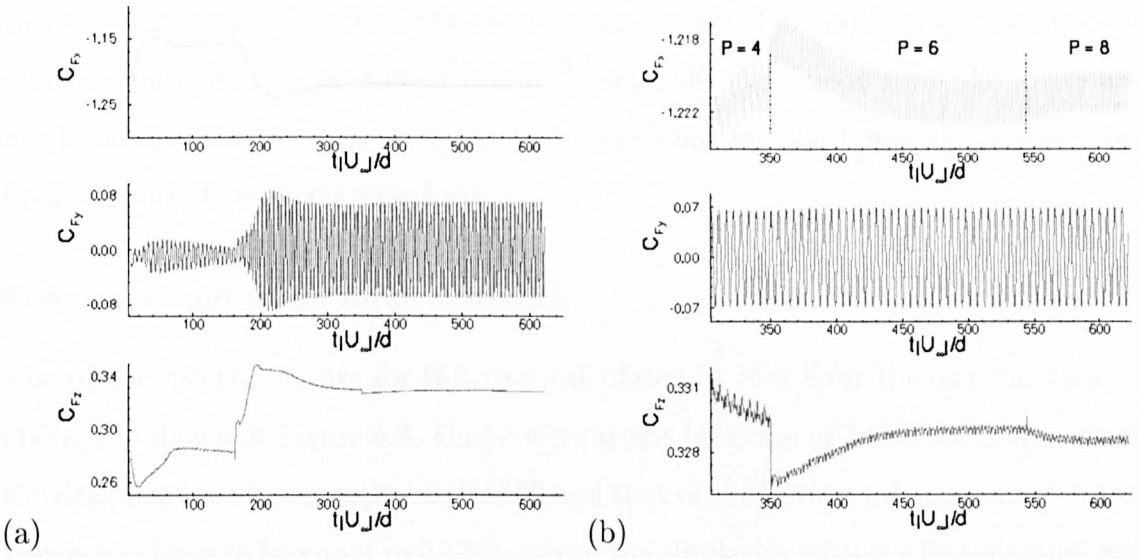


Figure 5.2: (a) Integrated force coefficients for the flow past Body C at $Re = 100$, x- is the direction of the drag, y- is the horizontal component of the transverse force and z- is the vertical one; (b) Snapshot in time for the integrated force coefficients from $\frac{t|U_\infty|}{d} = 305$ to $\frac{t|U_\infty|}{d} = 625$, part of $P = 4$ to $P = 8$

and then restarted with polynomials of fourth, sixth and eighth order. This type of refinement is equivalent to a hierarchical mesh convergence study. As mentioned in section 3.4, at $P = 6$, this mesh had $993,608$ local degrees of freedom per variable. When the solution was computed at $P = 8$ a total of $1,975,410$ local degrees of freedom were accounted for. Blockage for these computational cases was 7.2%.

Figure 5.2 depicts the integrated force coefficients in the x-, y-, and z- directions. The x-direction is the direction of the drag and the y- and z- directions represent the horizontal and vertical component of the transverse force respectively. Figure 5.2(a) shows the entire force history whereas Figure 5.2(b) shows a shorter range of the force history including only part of the fourth and up to the eighth polynomial order. The transition from $P = 2$ to $P = 4$ occurs at a non-dimensional time $\frac{t|U_\infty|}{d} = 162$, from $P = 4$ to $P = 6$ takes place at $\frac{t|U_\infty|}{d} \approx 350$ and the transition from order 6 to 8 at $\frac{t|U_\infty|}{d} = 543$.

Note that the range in the axes of the x- and z- directions is significantly smaller compared to that in the y-direction. Overall, the force coefficients produced for

this case exhibit similarities with those of the standard example of a straight two-dimensional cylinder. As Figure 5.2(b) depicts, the deviations from the mean are much smaller for the drag force (x-direction) than for the horizontal component (y-direction) of the transverse force.

Frequency and mean force statistics

The power spectra density for this case calculated at $P = 8$ for the last ten periods of C_{Fy} are shown in Figure 5.3. Under the current blockage of 7.2%, the frequency of the drag was found to be equal to 0.3522 and that of the horizontal component of the transverse force to be equal to 0.1761; hence the similarity with the two-dimensional cylinder which exhibits a drag force with a frequency equal to twice that of the lift force.

- First order time integration, $P = 8$

  Table 5.1 shows the frequencies, and the mean and rms values of the integrated forces in the three Cartesian directions determined with first order time integration at $P = 8$. To highlight the force convergence four decimal places will be employed in this section.

- First order time integration, $P = 6$, time step variation

  Table 5.2 depicts the frequencies along with the mean and rms values of the integrated force coefficients computed with first order time integration at different time steps, Δt, at $P = 6$. The original time step, $\Delta t = 0.0025$, has been reduced in steps of 1/4 up to $\frac{\Delta t}{2}$.

  The frequencies obtained for the different time steps at first order time integration have at most a discrepancy of 0.1% whereas the mean values for the integrated force coefficients have a maximum discrepancy of 0.09%. Similarly the agreement in the frequencies and mean values for the force coefficients between $P = 6$ and $P = 8$ is very good. These discrepancies can be considered negligible hence overall force convergence has been achieved.

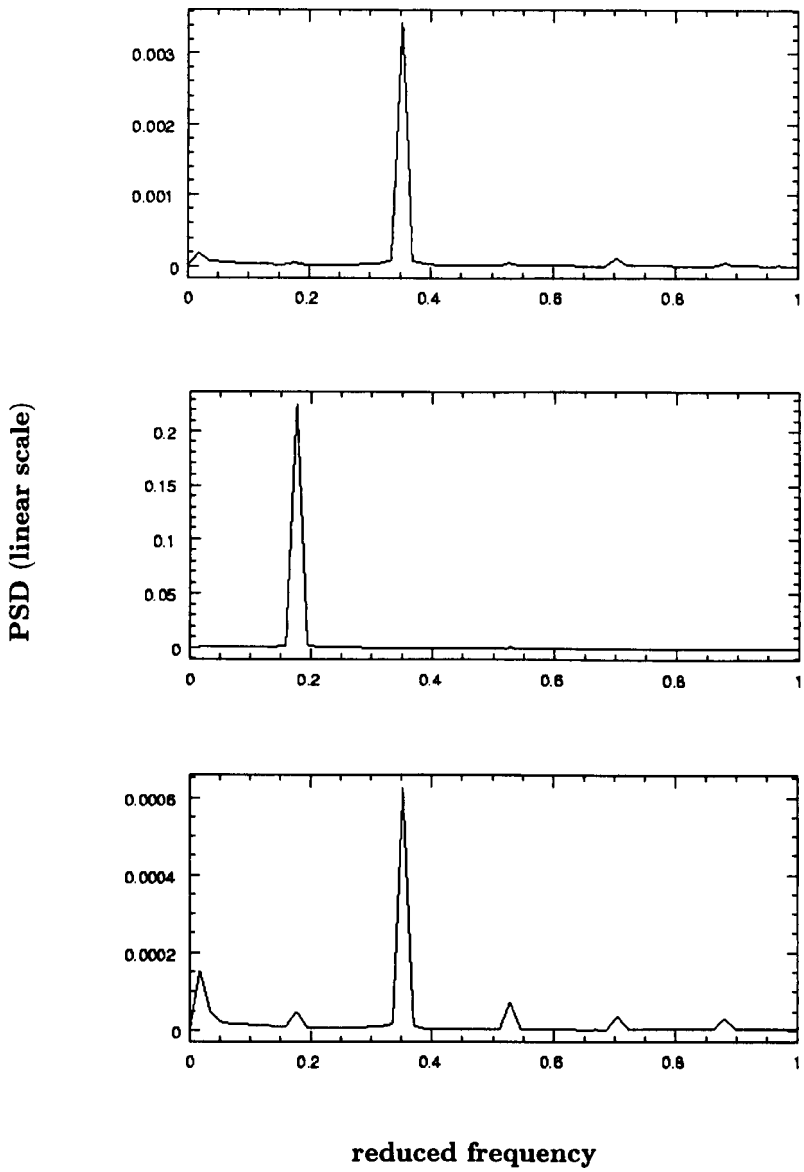


Figure 5.3: Power spectra density of the integrated forces in the x-, y- and z-directions for the flow past body C at $Re = 100$

	P=8
St_{Fx}	0.3522
St_{Fy}	0.1761
St_{Fz}	0.3522
$C_{Fx_{mean}}$	-1.2209
$C_{Fx_{rms}}$	0.0008
$C_{Fy_{mean}}$	0.0
$C_{Fy_{rms}}$	0.0490
$C_{Fz_{mean}}$	0.3286
$C_{Fz_{rms}}$	0.0001

Table 5.1: Frequencies along with mean and rms values for the integrated force coefficients for the flow past body C at $Re = 100$ computed at $P = 8$ with first order time integration

The simulations were also computed with second order time integration and the agreement was in the order of 10^{-3}.

Flow features

The qualitative features of the flow past body C at $Re = 100$ are discussed in this section.

Figure 5.4 depicts a 3D view of the wake topology obtained by the Jeong & Hussain (1995) criterion discussed in section 3.5.1. A λ_2 value of -0.1, which belongs to the appropriate cut-off range based on the enstrophy analysis presented in section 3.5.2, has been chosen for the vortex core extraction. Figure 5.4(a) shows the wake topology extracted at $\frac{t|U_\infty|}{d} \approx 524$ with the top shear layer rolling up, hence corresponding to more suction in the negative y-direction. Indeed, this non-dimensional time corresponds to a minimum in the integrated C_{Fy}. Figure 5.4(b) shows the wake topology extracted at $\frac{t|U_\infty|}{d} \approx 532$, representing the maximum in the integrated C_{Fy}. At this non-dimensional time the bottom shear layer is rolling up, creating more suction in the positive y-direction. As a result a positive value for C_{Fy}

P = 6			
	$\Delta t = 0.0025$	$\Delta t = 0.001875$	$\Delta t = 0.00125$
St_{Fx}	0.3524	0.3522	0.3520
St_{Fy}	0.1762	0.1761	0.1760
St_{Fz}	0.3522	0.3522	0.3520
$C_{Fx_{mean}}$	-1.2214	-1.2211	-1.2209
$C_{Fx_{rms}}$	0.0009	0.0008	0.0008
$C_{Fy_{mean}}$	0.0001	0.0001	0.0001
$C_{Fy_{rms}}$	0.0492	0.0491	0.0490
$C_{Fz_{mean}}$	0.3289	0.3288	0.3286
$C_{Fz_{rms}}$	0.0001	0.0001	0.0001

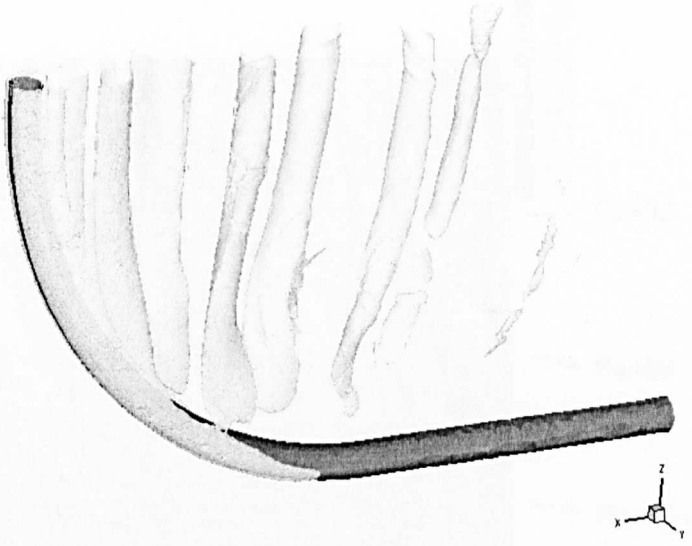
Table 5.2: Statistics for the flow past body C at $Re = 100$ computed with first order time integration at $P = 6$ for three different time steps

is obtained. Figure 5.4(c) depicts a projection of the vortex cores on the xy-plane, i.e. viewed from the top, showing the anti-symmetric wake with a staggered array of vortices at the time of the C_{Fy} minimum, $\frac{t|U_\infty|}{d} \approx 524$.

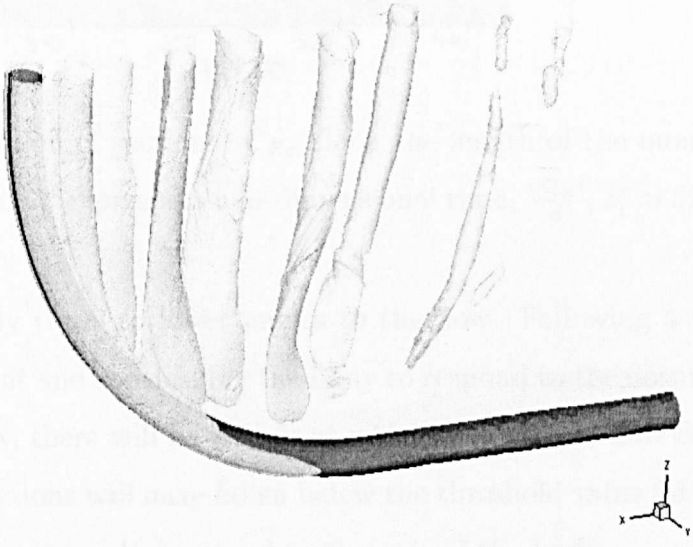
Overall, Figure 5.4 suggests that close to the body the vortex cores are straight, with their axes normal to the free-stream, but start to distort further downstream in the near wake.

The variation of sectional C_{Fy}, computed at slices normal to the cylinder axis at different locations of the span for this structure is depicted in Figure 5.5. With S denoting the arc length measured from the top, the top of the cylinder is at $S/d = 0$ whereas the vertical slice at the end of the quarter ring corresponds to a non-dimensional arc length of $S/d = 19.6$.

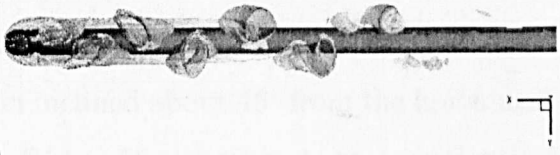
It should be emphasized that even though the velocity profile at the inlet is uniform, there is an effective reduction in the local normal Reynolds number along the span as the free-stream velocity vector is not normal to the centreline of the body at all sections. Therefore, the component of the incoming flow vector in the sectional planes, and hence the local normal Reynolds number, becomes increasingly



(a)



(b)



(c)

Figure 5.4: Vortex cores in the wake of body C at $Re = 100$, $\lambda_2 = -0.1$: (a) 3D view extracted at a minimum of the integrated C_{Fy}, $\frac{t|U_\infty|}{d} \approx 524$, (b) 3D view extracted at a maximum of the integrated C_{Fy}, $\frac{t|U_\infty|}{d} \approx 532$, (c) View from the top

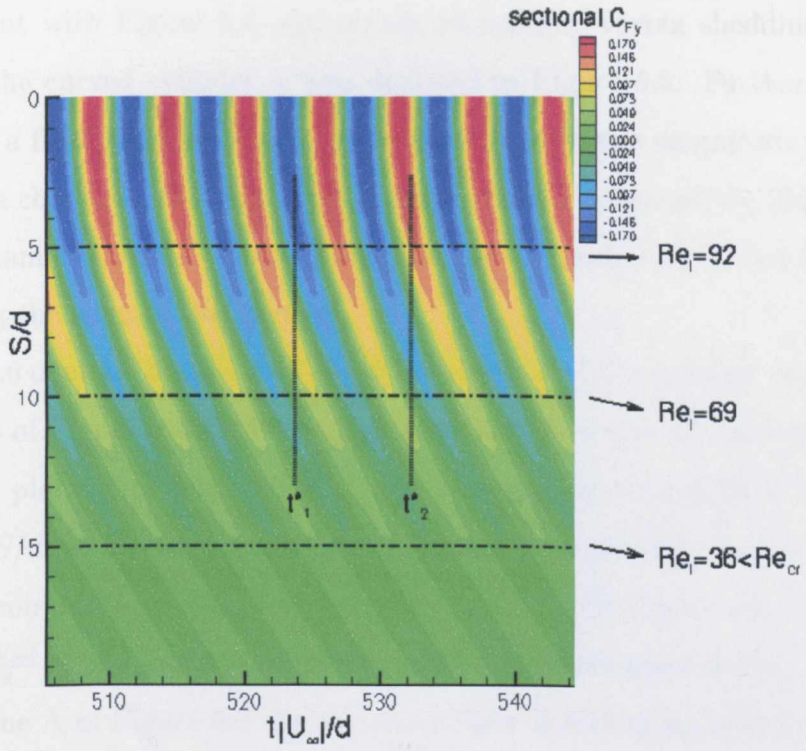


Figure 5.5: Variation of sectional C_{Fy} along the length of the quarter ring part of body C, $Re = 100$ (t^* represents non-dimensional time, $\frac{t|U_\infty|}{d}$; $t_1^* \approx 524$ and $t_2^* \approx 532$)

small as the body turns to lower angles to the flow. Following a two-dimensional sectional argument and considering the body to respond to the normal component of incident flow only, there will be a limit at which: the normal flow Reynolds number in some of the sections will have fallen below the threshold value for vortex shedding and vortices will not be shed normal to the axis of the body.

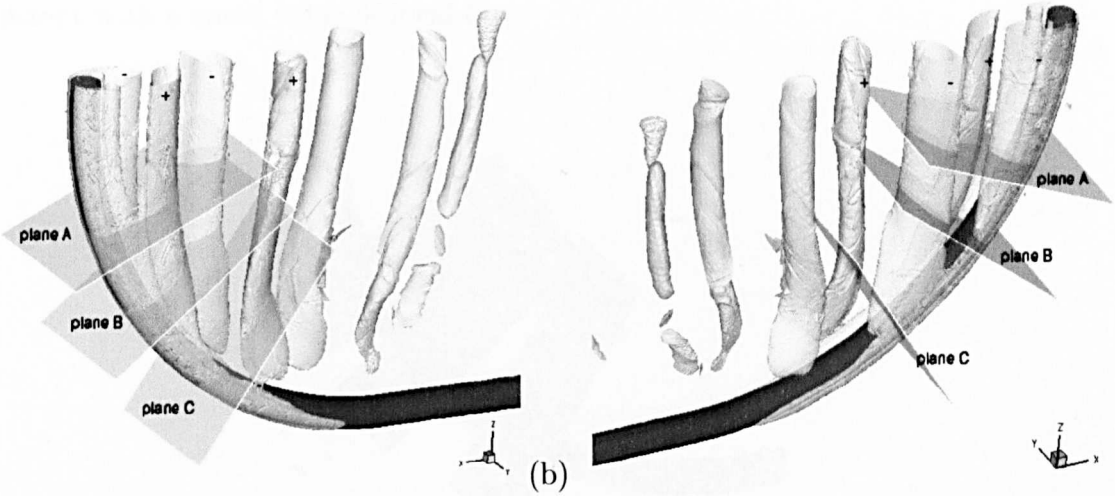
In Figure 5.5 a non-dimensional arc length of $S/d = 5$ corresponds to a section inclined at approximately 23° from the horizontal and a local Reynolds number, Re_l, of approximately 92. Similarly, a non-dimensional arc length of $S/d = 10$ corresponds to a section inclined about 46° from the horizontal and a local Reynolds number of 69 whereas $S/d = 15$ corresponds to a section inclined about 69° from the horizontal where Re_l is approximately 36. This local sectional Reynolds number is lower than the critical Reynolds number of $47 - 49$ where the onset of vortex shedding for a circular straight cylinder occurs. A Reynolds number of 50 would correspond to a non-dimensional arc length of approximately 13.

Consistent with Figure 5.4, the strong alternating vortex shedding pattern at the top of the curved cylinder is also depicted in Figure 5.5. Further down along the span at a fixed time level we observe a decrease in the magnitude of the forces and finally a change in the sign. This gradual phase change will be illustrated with a specific example in time (at a minimum in the integrated C_{Fy}), considering three planes along the span of the cylinder.

Figure 5.6 depicts three planes normal to the axis of the cylinder intersecting the vortex cores of Figure 5.4(a). Plane A corresponds to a non-dimensional arc length of $S/d = 5$, plane B corresponds to a non-dimensional arc length of $S/d = 8$ and plane C to $S/d = 12$. The intersection of these planes through the vortex cores can be directly compared with the values for sectional C_{Fy} in Figure 5.5. As mentioned before, at $\frac{t|U_\infty|}{d} \approx 524$ the integrated forces indicate a minimum in C_{Fy}. At this time level, at plane A of Figure 5.6 the top shear layer is rolling up hence resulting in a negative value for the local C_{Fy} as shown in Figure 5.5. At $\frac{t|U_\infty|}{d} \approx 524$ for $S/d = 5$, sectional $C_{Fy} = -0.131$. Further down along the span, at plane B however, the first shed anti-clockwise vortex is now closest to the body hence being responsible for a positive value of local C_{Fy}. Indeed, in Figure 5.5 a non-dimensional arc length of $S/d = 8$ corresponds to sectional $C_{Fy} = 0.102$ at $\frac{t|U_\infty|}{d} \approx 524$. At plane C though, further down along the span, the reverse happens as can be better seen in the second view of Figure 5.6. This indeed results in negative values again for local C_{Fy}, however now of a smaller magnitude. In Figure 5.5 at $\frac{t|U_\infty|}{d} \approx 524$, sectional $C_{Fy} = -0.032$ for $S/d = 12$.

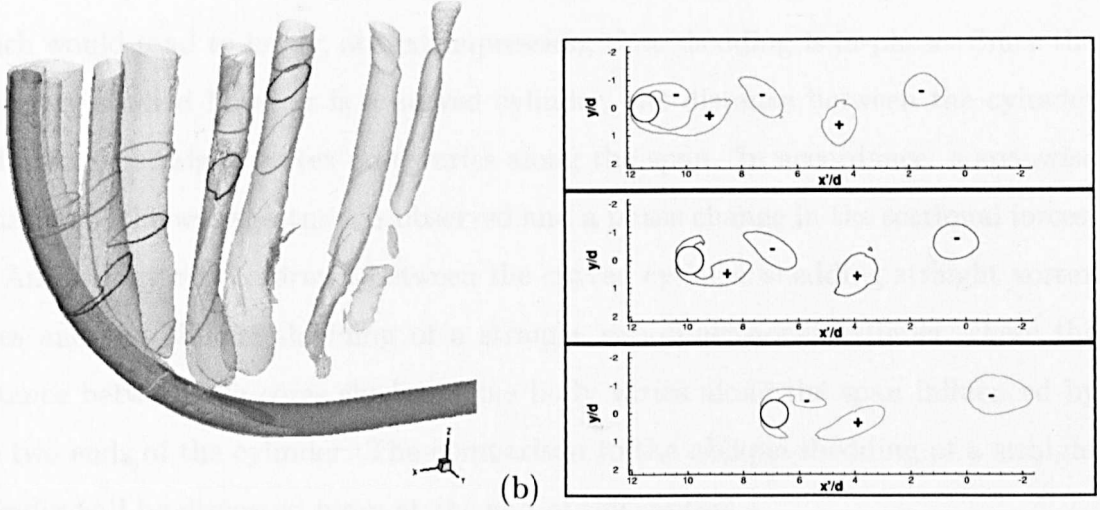
The intersections of these planes with the vortex cores are highlighted in a 3D view in Figure 5.7(a). In Figure 5.7(b) these cross-sections are shown in a 2D view where the influence of the developing shear layers and the first shed vortices on the sign of the local C_{Fy} can be seen more clearly (x' is the x-direction in the new coordinate system in the local planes).

Figure 5.8 shows the ω_z vorticity component in the three planes normal to the axis of the curved cylinder at the time of the C_{Fy} minimum. The spanwise variation of ω_z is consistent with the wake topology and the sectional forces for this case. At the first plane the positive shear layer cuts the supply of vorticity of the negative



(a) (b)

Figure 5.6: Three planes normal to the axis of body C intersecting the wake structures extracted at the time of a C_{Fy} minimum, $\frac{t|U_\infty|}{d} \approx 524$; two different views



(a) (b)

Figure 5.7: (a) A 3D view of the vortex core intersections at the three planes A, B, C; (b) Planar views of these cross-sections

shear layer consistent with a negative local C_{Fy} whereas at the second plane the reverse happens. Finally, at the third plane shear layers do not interact strongly consistent with a small value of local C_{Fy}.

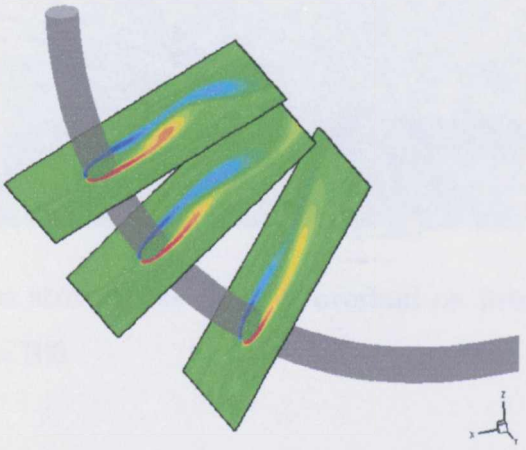


Figure 5.8: Spanwise vorticity component at the A, B, C planes extracted at the time of a C_{Fy} minimum, $\frac{t|U_\infty|}{d} \approx 524$

Overall from the previous figures, it is concluded that the shedding of vortices is out of phase along the span of body C at Reynolds number of 100. This is not contradictory with the fact that the vortex cores are straight close to the body which would tend to imply, at first impression, that shedding is in-phase. Since the geometry studied however is a curved cylinder, the distance between the cylinder and a single straight vortex core varies along the span. In accordance, a spanwise variation of the wake features is observed and a phase change in the sectional forces.

An analogy can be drawn between the curved cylinder shedding straight vortex cores and the oblique shedding of a straight two-dimensional cylinder where the distance between the cores shed and the body varies along the span influenced by the two ends of the cylinder. The comparison to the oblique shedding of a straight cylinder will be discussed more at the end of this section.

In the discussion of the sectional forces, Figure 5.5, the variation of the local normal Reynolds number was considered with respect to a two-dimensional argument. A sectional two-dimensional argument would predict variation of the local normal Reynolds number which would thus result in variation of the Strouhal fre-

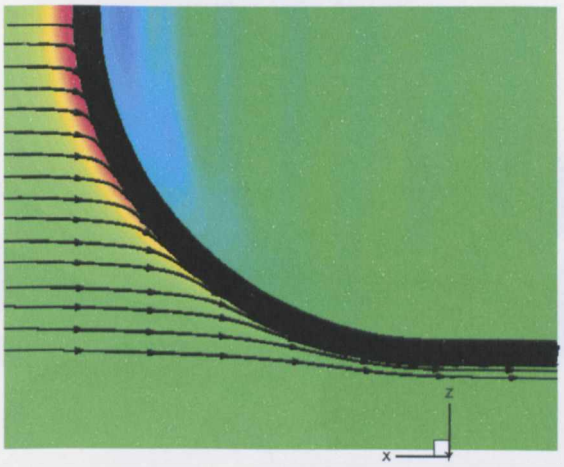
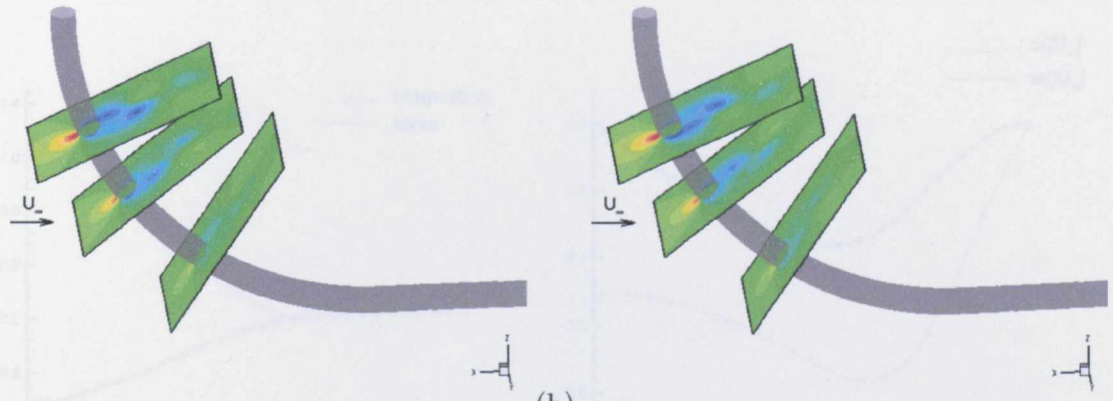


Figure 5.9: Centreplane streamlines ($y = 0$) overlaid on pressure contours for the flow past body C, $Re = 100$

quency along the span of body C. This would possibly suggest cellular flow patterns. However, the results of this study show that the flow behaves in a three-dimensional manner, with the upper cylinder shedding driving the lower end and no frequency variation in time occurring along the span. In accordance, the power spectra density showed only one dominant frequency in the C_{Fy} direction. Overall, as a result of the geometry, along the span the shedding is out of phase, but in time the top of the cylinder is shedding at the same frequency with the sections below.

From a three-dimensional perspective, the decrease in the local Reynolds number can be discussed in terms of the flow along the length of the curved cylinder. Figure 5.9 shows centreplane ($y = 0$) streamlines upstream of the body superimposed on pressure contours. The streamlines show motion along the length of the curved cylinder towards the bottom of the geometry dictated by the shape of the stagnation face which tends to deflect the flow away from the curved cylinder.

The increasingly dominant axial flow along the length of the curved cylinder converts the flow from "bluff" to "slender". In accordance, along the lower part of the curved cylinder as it bends to become aligned with the free-stream, vortex shedding in the near wake becomes less vigorous. This is associated with the reduction of the pressure minimum in the sectional planes shown at a minimum and maximum in the integrated C_{Fy} in Figures 5.10(a) and (b) respectively.



(a) (b)

Figure 5.10: Pressure contours on planes normal to the cylinder axis for the flow past body C at $Re = 100$ at: (a) a minimum in the integrated C_{Fy}, $\frac{t|U_\infty|}{d} \approx 524$, (b) a maximum in the integrated C_{Fy}, $\frac{t|U_\infty|}{d} \approx 532$

Figure 5.11(a) depicts the variation of pressure on the stagnation line and the base pressure. The variation of the u and w velocity components (Cartesian axes), extracted 0.3 diameters upstream of the curved cylinder, is shown in Figure 5.11(b) to highlight the three-dimensionality of this type of flow. As pressure decreases along the stagnation line (Figure 5.11(a)), the magnitude of the w velocity component increases along the span (up to approximately midspan) and reaches a maximum of 36% of the free-stream magnitude. At a non-dimensional arc length of $S/d = 10.6$, which corresponds to a section inclined 48.3° from the horizontal, $w/|U_\infty| = -0.36$. The local coordinates at each section are then considered and in Figure 5.11(c) the normal and axial flow components along the body are plotted from the three-dimensional computations. With θ denoting the angle that each section traces with respect to the horizontal (from the centre of curvature), the normal component is equal to $(u\cos\theta - w\sin\theta)/|U_\infty|$ whereas the axial component corresponds to $(w\cos\theta + u\sin\theta)/|U_\infty|$. Therefore, both the normal and the axial components have contributions from both u and w. A two-dimensional argument on the other hand considers only the normal direction which is equal to $u\cos\theta$.

Figure 5.12 shows the ω_x vorticity component on vertical planes at the time of

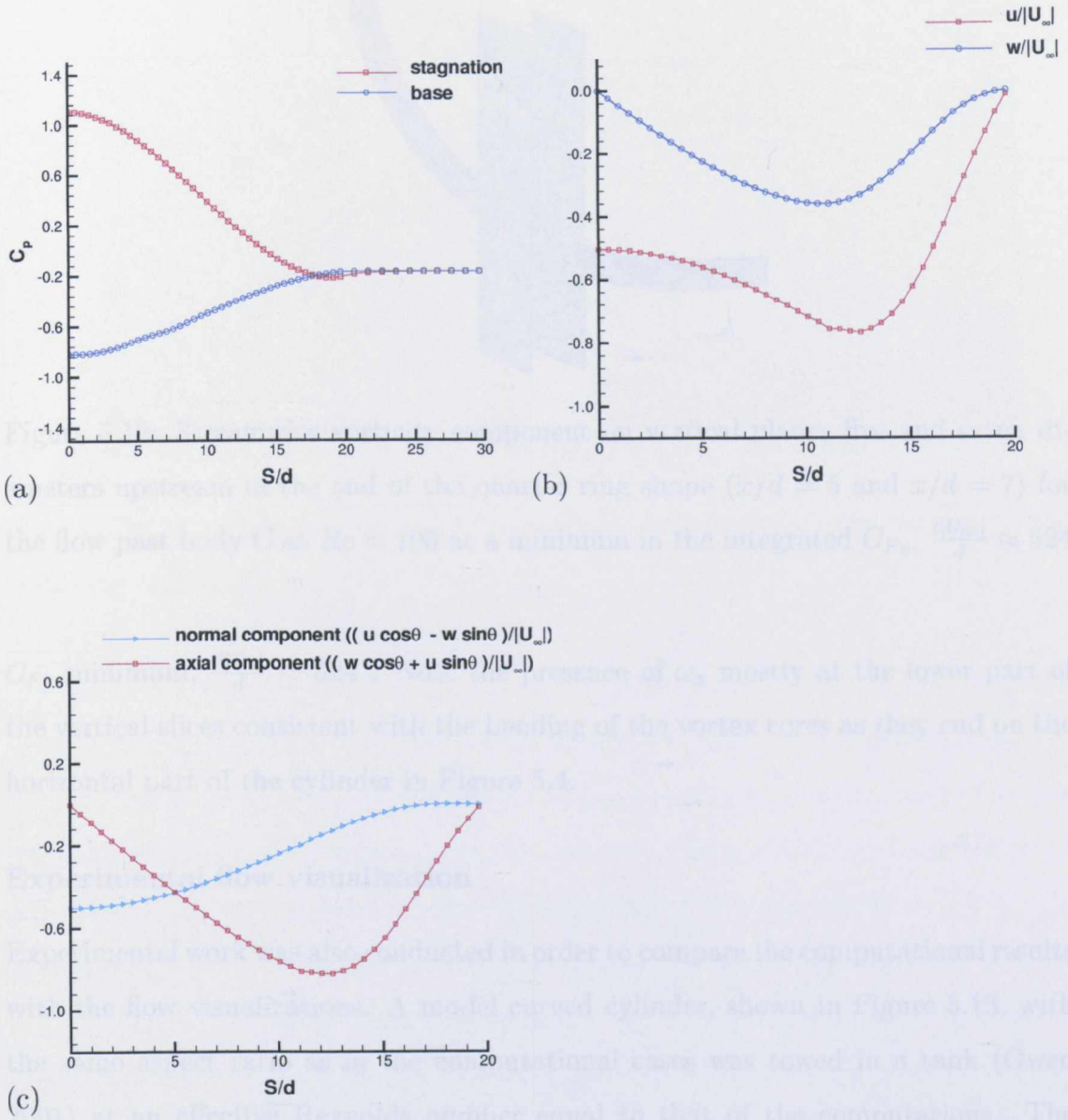


Figure 5.11: Variation of pressure and velocity along the span of body C, $Re = 100$, $\frac{t|U_\infty|}{d} \approx 524$: (a) Base pressure and stagnation pressure, (b) u and w velocity components extracted 0.3 diameters upstream of the curved cylinder, (c) Normal $((u\cos\theta - w\sin\theta)/|U_\infty|)$ and axial $((w\cos\theta + u\sin\theta)/|U_\infty|)$ components computed from the 3D simulation 0.3 diameters upstream of the curved cylinder

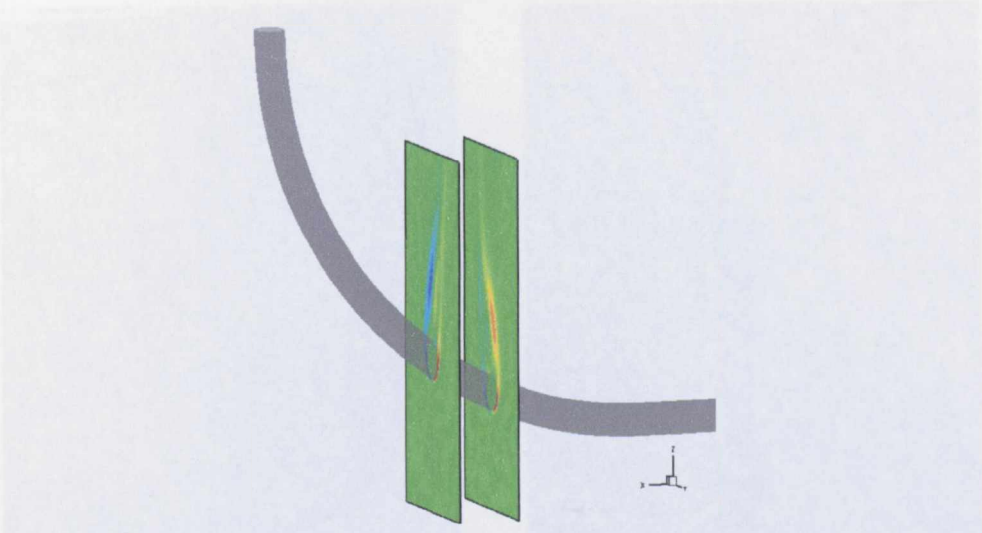


Figure 5.12: Streamwise vorticity component on vertical planes five and seven diameters upstream of the end of the quarter ring shape ($x/d = 5$ and $x/d = 7$) for the flow past body C at $Re = 100$ at a minimum in the integrated C_{Fy}, $\frac{t|U_\infty|}{d} \approx 524$

C_{Fy} minimum, $\frac{t|U_\infty|}{d} \approx 524$. Note the presence of ω_x mostly at the lower part of the vertical slices consistent with the bending of the vortex cores as they end on the horizontal part of the cylinder in Figure 5.4.

Experimental flow visualization

Experimental work was also conducted in order to compare the computational results with the flow visualizations. A model curved cylinder, shown in Figure 5.13, with the same aspect ratio as in the computational cases was towed in a tank (Owen 2001) at an effective Reynolds number equal to that of the computations. The flow visualization technique employed was laser induced fluorescence. The dye was adhered on the stagnation line of the curved cylinder, in two slots symmetrically offset slightly from the centre. The red and green colours in the towing tank flow visualization images are attributed to sulfuro rhodamine and sodium fluorescein dye respectively (Lear 2003). A Class IV laser was used to illuminate the dye diffusing from the stagnation line of the curved cylinder and the wake patterns formed. Further details about the experimental setup and this flow visualization technique can be found in Owen (2001) and Lear (2003).

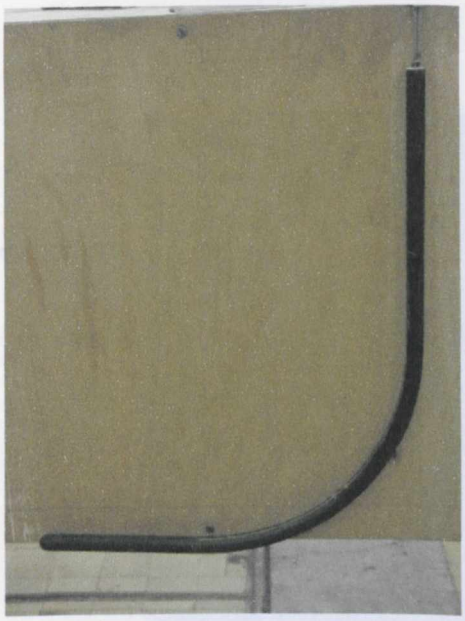
(a)  (b) 

Figure 5.13: Two different views of the curved cylinder model used for the towing tank flow visualizations

The flow visualization images have shown good qualitative agreement with the numerical investigations. The flow visualization obtained for this case is shown in Figure 5.14. Note that as the camera in the experiments was positioned lower than the water free surface, a reflection was introduced. The picture thus includes in the top part the mirror image of the flow visualization in the water surface.

Figure 5.14 can be compared with Figure 5.4. The slight bowing of the vortices towards the top cylinder end in experiments where a straight circular cylinder is towed through a water surface has been observed before and discussed in Slaouti & Gerrard (1981). Furthermore, the bending of the vortices further downstream in the wake is more apparent in the experiments than in the computations where the mesh is less refined away from the curved cylinder.

In all of the previous section, the wake topology was extracted at a $\lambda_2 = -0.1$. A second value of $\lambda_2 = -0.03$, which is within the appropriate cut-off range based on the analysis of section 3.5.2, can also be chosen (Figure 5.15) to compare with Figure 5.14.

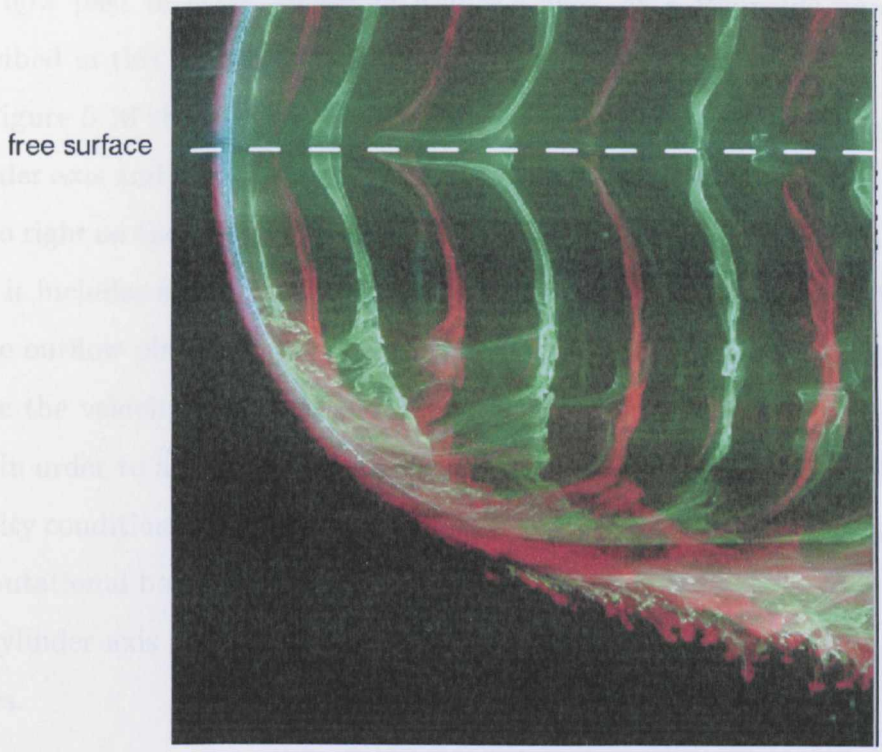


Figure 5.14: Towing tank flow visualization for body C, $Re = 100$

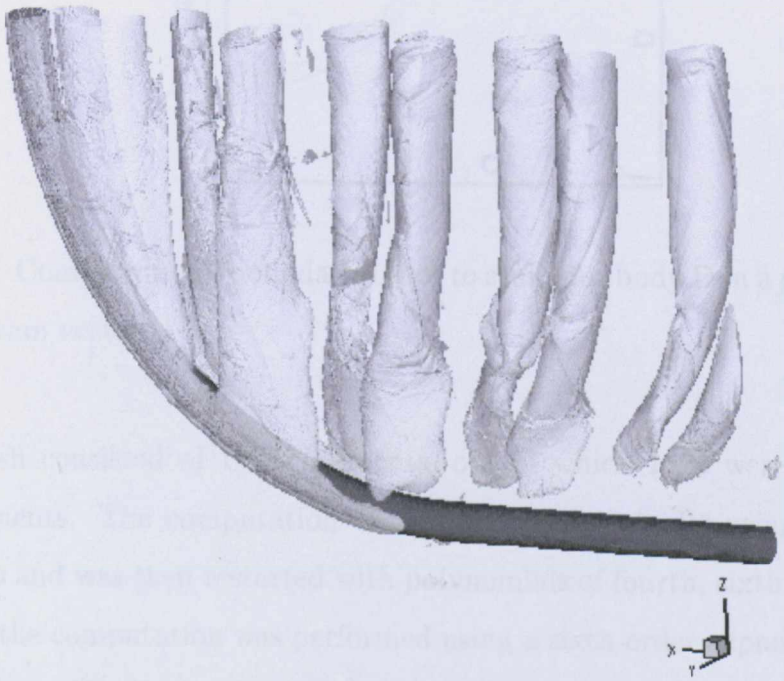


Figure 5.15: Wake topology for the flow past body C at $Re = 100$, $\lambda_2 = -0.03$

5.1.2 Flow past body D

The flow past body D, shown in Figure 1.3(b), at a Reynolds number of 100 is described in this section.

Figure 5.16 shows a cut in the computational domain at a plane including the cylinder axis and the free-stream vector. The flow is in the positive x-direction from left to right on the page. A symmetry boundary condition was imposed on boundary B as it includes an intersection with the curved cylinder. Boundary D corresponds to the outflow plane and boundaries A and C correspond to free-stream boundaries where the velocity condition, U_∞=[1 0 0] was imposed away from the body. Note that in order to accommodate the solid boundary intersecting the inflow plane, the velocity condition imposed actually involved a boundary layer thickness of 10%. The computational boundaries in the y-direction were at a distance of 8 diameters from the cylinder axis and a uniform free-stream condition was prescribed also on these planes.

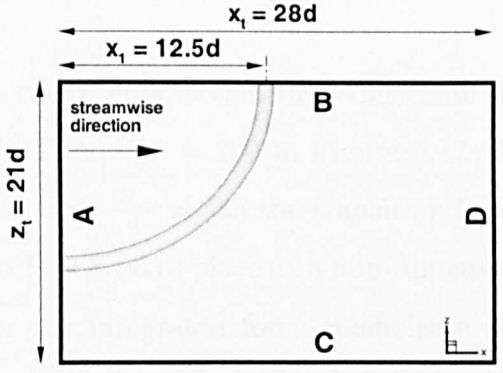


Figure 5.16: Computational boundaries (not to scale) for body D in a plane including the free-stream vector

The mesh consisted of 14847 elements, out of which 1574 were the prismatic surface elements. The computation was carried out originally using second order polynomials and was then restarted with polynomials of fourth, sixth and eighth order. When the computation was performed using a sixth order expansion, the mesh accounted for 1,423,436 local degrees of freedom per variable whereas 2,827,515 local degrees of freedom were allowed for at $P = 8$. Blockage for these computational

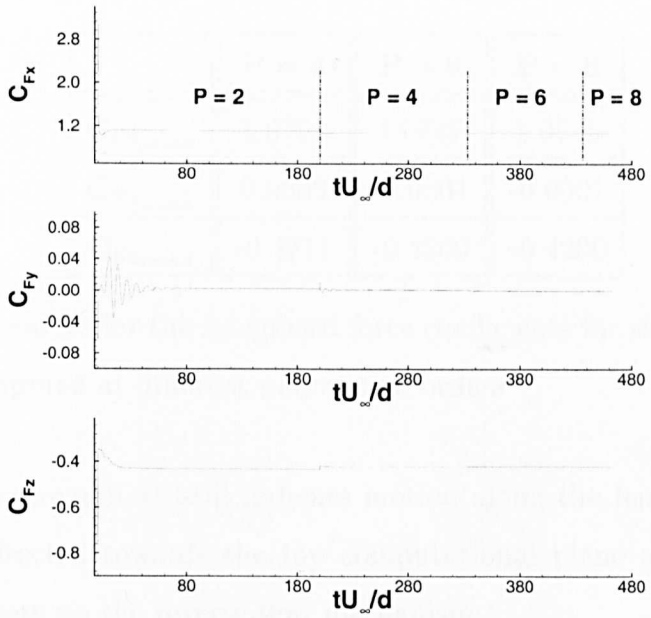


Figure 5.17: Force history for the flow past body D at $Re = 100$, x- is the direction of the drag, y- is the horizontal component of the transverse force and z- is the vertical one

cases was 3.9%.

The integrated force coefficients in the three Cartesian directions are shown for this case in Figure 5.17. Time $\frac{tU_\infty}{d} = 200$ in Figure 5.17 represents the transition from $P = 2$ to $P = 4$ and time $\frac{tU_\infty}{d} = 333$ the transition from $P = 4$ to $P = 6$. The transition from $P = 6$ to $P = 8$ takes place at a non-dimensional time of $\frac{tU_\infty}{d} \approx 436$.

The mean values for the integrated force coefficients are shown in Table 5.3. A reduction of merely 0.1% in the magnitude of C_{Fx} is observed as the polynomial order is increased from four to six and a reduction of merely 0.02% as the polynomial order is increased from six to eight.

Contrary to the flow past body C, this configuration surprisingly does not exhibit vortex shedding features. As Figure 5.17 shows, the forces are steady. Furthermore, the magnitude of the force coefficient in the x-direction is smaller by 12% compared to the previous case when both solutions have been approximated by eighth order polynomials.

Centreplane streamlines ($y = 0$) upstream of the curved cylinder superimposed on pressure contours are shown in Figure 5.18, which can be directly compared with

	P = 4	P = 6	P = 8
$C_{Fx_{mean}}$	1.0758	1.0747	1.0745
$C_{Fy_{mean}}$	0.0009	-0.0001	-0.0001
$C_{Fz_{mean}}$	-0.4211	-0.4200	-0.4200

Table 5.3: Mean values for the integrated force coefficients for the flow past body D at $Re = 100$ computed at different polynomial orders

Figure 5.9. The streamlines still indicate motion along the length of the cylinder but it is now directed towards the top computational plane as the shape of the stagnation face sets up the reverse flow mechanism.

Figure 5.18 also depicts the u velocity contours in the vicinity of the cylinder at four different horizontal planes located at: the top surface, two, five and eight diameters vertically below. These velocity contours are consistent with the force plots indicating that periodic vortex shedding does not occur as they show symmetric wakes.

Moreover, a variation in the wake width along the span can be observed from these slices. The top slice exhibits the widest wake and the bottom one the narrowest. Qualitatively similar results were obtained in the computational work of Darekar & Sherwin (2001b), Darekar (2001) and the experimental one of Bearman & Owen (1998a, 1998b), Owen (2001) on wavy cylinders where a sinusoidal deformation was applied to the stagnation face. Leading edge cross-flow was found to be associated with streamwise vorticity which can result in the breakdown of the vortex street and hence significant drag reductions. In addition, variation of the wake width was observed both in the computational and in the experimental study. The widest wake along the span of the wavy cylinder was found to be at the geometrical minimum, or "valley" (Darekar & Sherwin 2001b), defined as the most downstream cross-section. In the case of the curved cylinder of this study, the "geometrical minimum" in Figure 5.18 is the top computational plane, $z = 0$, which indeed exhibits the widest wake.

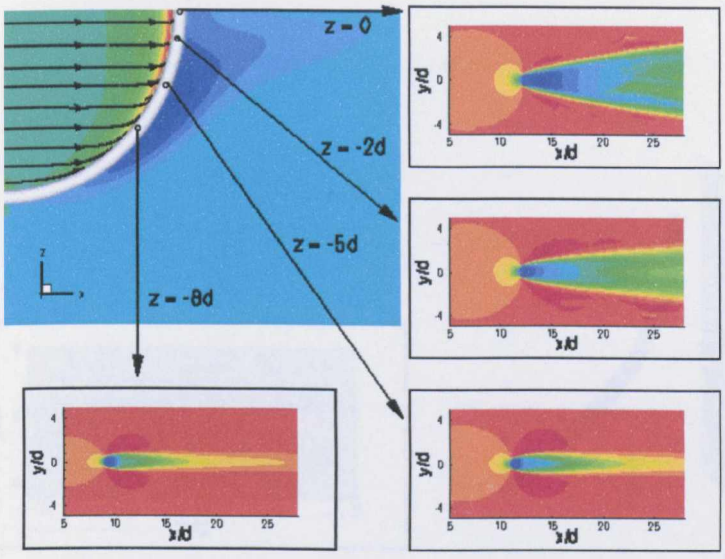
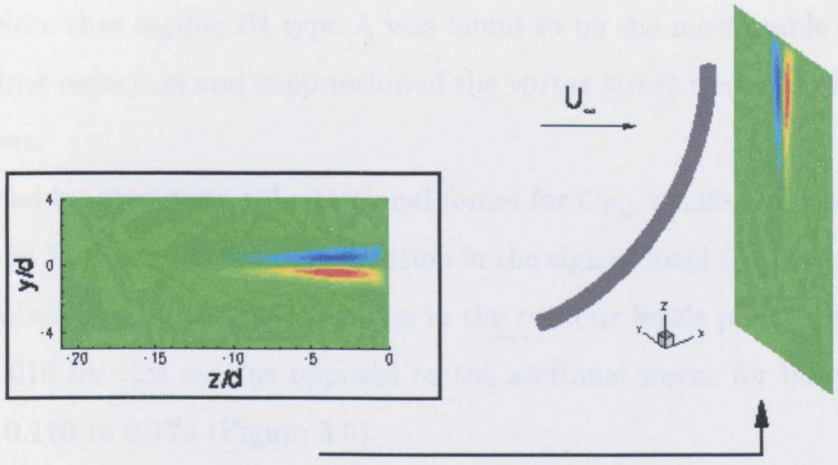


Figure 5.18: Centreplane streamlines ($y = 0$) overlaid on pressure contours for the flow past body D at $Re = 100$. The insets show u velocity contours at horizontal slices which are located at the top plane, and two, five and eight diameters vertically below.

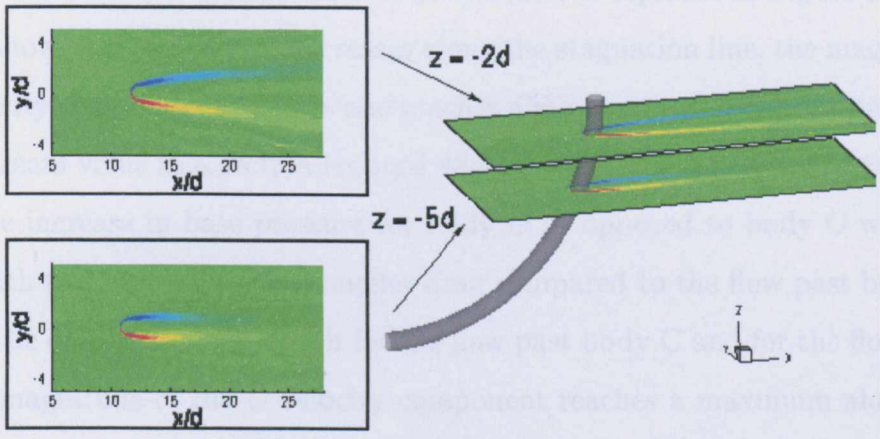
The horizontal component of vorticity, ω_x, in a vertical plane in the wake five diameters downstream of the curved cylinder is shown in Figure 5.19(a). Variation of the strength of ω_x along this plane can also be observed. Figure 5.19(b) depicts ω_z, the spanwise vorticity in two horizontal planes located at two and five diameters vertically below the top surface. The shear layers are not interacting and the variation in the wake width can be observed again.

Figure 5.19(a) can be compared with Figure 5.12. As a result of the geometry's curvature, both configurations account for streamwise vorticity in the wake in addition to the two-dimensional component. However, in the case of the flow past body C the streamwise vorticity appears towards the bottom part of the curved cylinder and is associated with the bending of the vortices as they approach the horizontal extension of body C. On the other hand, for this case the streamwise vorticity in a vertical plane in the wake occurs towards the top of the body which would otherwise be expected to be the part associated with 2D shedding.

The wake topology for this case is depicted in two views in Figure 5.20 which



(a)



(b)

Figure 5.19: (a) Streamwise vorticity on a vertical plane five diameters downstream of body D, $Re = 100$; (b) Spanwise vorticity on horizontal planes two and five diameters vertically below the top surface for body D, $Re = 100$

illustrates just the shear layers separating from the body but not interacting. Similarly, for regime III type A of the wavy cylinders at a Reynolds number of 100, Darekar & Sherwin (2001b) found a symmetric wake topology with respect to the centreline. Note that regime III type A was found to be the most stable one where the largest drag reduction and suppression of the vortex street were observed for the wavy cylinders.

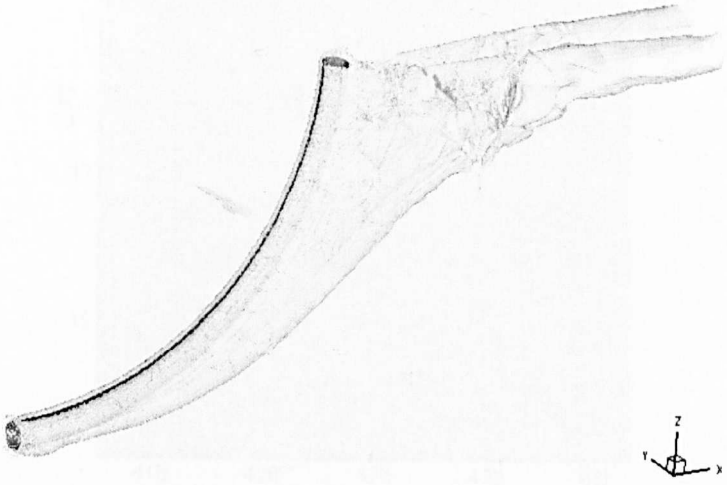
We proceed by considering the sectional forces for C_{Fy}, which are indeed shown to be steady in Figure 5.21. A small variation in the sign of local C_{Fy} along the span can also be observed. Note that the range in the contour levels plotted varies from -0.016 to 0.016 for this case as opposed to the sectional forces for body C which vary from -0.170 to 0.170 (Figure 5.5).

Figure 5.22 depicts the variation of pressure and velocity components along the span of body D. Specifically, Figure 5.22(a) shows the variation of pressure on the stagnation line and base pressure. The variation of u and w velocity components, extracted 0.3 diameters upstream of the curved cylinder, is depicted in Figure 5.22(b). These plots show that as pressure decreases along the stagnation line, the magnitude of the w velocity component increases and reaches a maximum of approximately 28% of the free-stream value at a section inclined 48.3° from the horizontal ($S/d = 10.6$). Also note the increase in base pressure for body D as opposed to body C which is consistent with this case exhibiting smaller drag compared to the flow past body C.

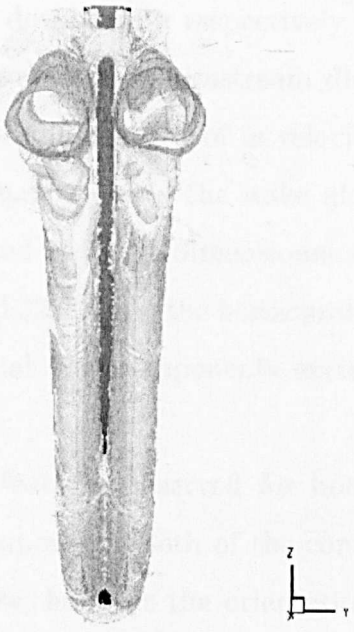
It should be emphasized that both for the flow past body C and for the flow past body D the magnitude of the w velocity component reaches a maximum along the span at exactly the same location, 48.3° from the horizontal, suggesting a strong influence of the geometry.

Moreover, even though pressure is higher at the top of body D and decreases along the span, the flow along the length of body D is directed against the pressure gradient. The maximum w velocity component (28% of the free-stream) for body D is smaller in magnitude than the maximum value of w (36% of the free-stream) reached for the flow past body C, but is still a strong component directed towards the top computational plane.

Figure 5.22(c) shows the variation of w velocity component at the rear of the



(a)



(b)

Figure 5.20: Two different views of the wake topology for the flow past body D at $Re = 100$, $\lambda_2 = -0.01$

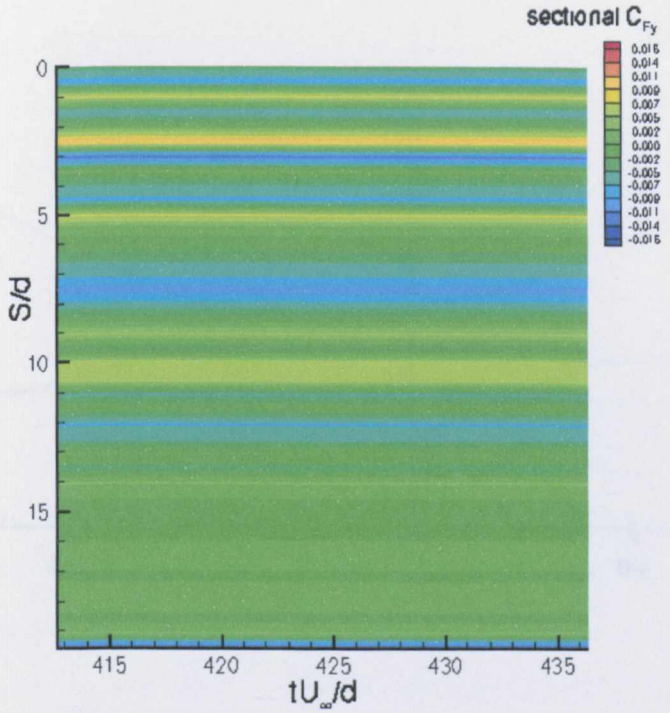


Figure 5.21: Sectional C_{Fy} along the length of body D, $Re = 100$

cylinder 0.3, 0.6 and 1.5 diameters downstream respectively. The magnitude of w velocity component is found to increase with downstream distance until a line 1.5 diameters downstream. Note that the magnitude of w velocity component reaches a maximum of 66% of the free-stream value in the wake along a line located 1.5 diameters downstream of body D and at a non-dimensional arc length of $S/d = 7$. This corresponds to a section located 32.2° from the horizontal. Furthermore, Figure 5.22(d) depicts the normal and axial flow components extracted from the three-dimensional simulations.

The completely different wake features observed for bodies C and D can be related to the strong w velocity component. Both of the configurations generate a w velocity component and axial flow; however the orientation of the leading edge affects the direction of this velocity component. For body C the flow is directed away from the part of the cylinder normal to the flow, whereas for body D it is directed towards the top of the cylinder which would normally be likely to account for regular periodic vortex shedding. The strong axial flow component, even at the rear of the cylinder, heading towards the top of the geometry and the production of

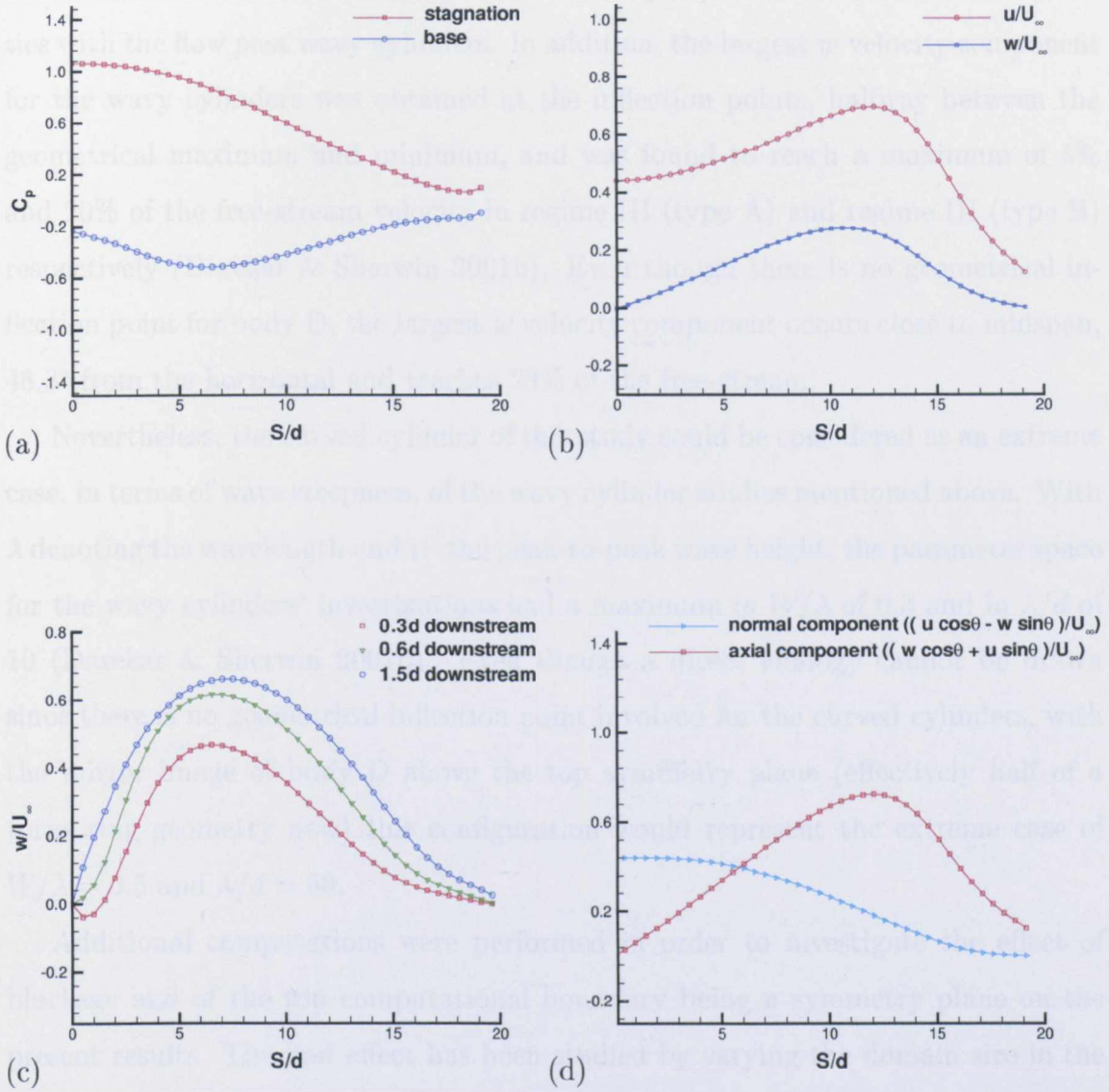


Figure 5.22: Variation of pressure and velocity along the span of body D, $Re = 100$: (a) Base pressure and stagnation pressure, (b) u and w velocity components extracted 0.3 diameters upstream of the curved cylinder, (c) w velocity component extracted 0.3, 0.6 and 1.5 diameters downstream of the curved cylinder, (d) Normal $((u\cos\theta - w\sin\theta)/U_\infty)$ and axial $((w\cos\theta + u\sin\theta)/U_\infty)$ components computed from the 3D simulation 0.3 diameters upstream of body D

streamwise vorticity are acting as the stabilizing mechanism setting the suppression of periodic vortex shedding.

As mentioned before, the flow features for body D presented here exhibit similarities with the flow past wavy cylinders. In addition, the largest w velocity component for the wavy cylinders was obtained at the inflection points, halfway between the geometrical maximum and minimum, and was found to reach a maximum of 5% and 20% of the free-stream velocity in regime III (type A) and regime III (type B) respectively (Darekar & Sherwin 2001b). Even though there is no geometrical inflection point for body D, the largest w velocity component occurs close to midspan, 48.3° from the horizontal and reaches 28% of the free-stream.

Nevertheless, the curved cylinder of this study could be considered as an extreme case, in terms of wave steepness, of the wavy cylinder studies mentioned above. With λ denoting the wavelength and W the peak-to-peak wave height, the parameter space for the wavy cylinders' investigations had a maximum in W/λ of 0.3 and in λ/d of 10 (Darekar & Sherwin 2001b). Even though a direct analogy cannot be drawn since there is no geometrical inflection point involved for the curved cylinders, with the mirror image of body D above the top symmetry plane (effectively half of a torus ring geometry now) this configuration would represent the extreme case of $W/\lambda = 0.5$ and $\lambda/d = 50$.

Additional computations were performed in order to investigate the effect of blockage and of the top computational boundary being a symmetry plane on the present results. The first effect has been studied by varying the domain size in the y-direction and the results presented in this section were found to be qualitatively free from the effects of blockage. The second effect has been studied by adding a six-diameter straight cylinder vertical extension on top of the main body. The effect of the vertical addition of a straight cylinder is presented for Reynolds number of 100 in the next section and for Reynolds number of 500 in section 5.2.3.

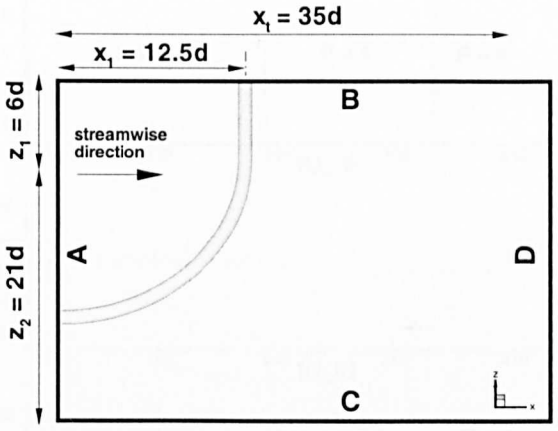


Figure 5.23: Computational boundaries (not to scale) in a plane including the free-stream vector for body D with a straight cylinder addition of six diameters vertically

5.1.3 Flow past body D with a six-diameter straight cylinder vertical addition

A vertical extension of a straight cylinder six diameters long was added to body D shown in Figure 1.3(b). Along with investigating the effect of the top computational symmetry plane, this case was intended to show the extent to which the steady wake features obtained for body D would persist with the straight cylinder extension on top. The six-diameter straight cylinder addition represents a substantial addition of almost 50% of the height of body D.

Figure 5.23 depicts the computational domain size in a plane including the cylinder axis and the free-stream vector for this configuration. The flow is in the positive x-direction, from left to right in the page. The same boundary conditions on the corresponding planes were assigned as for body D. The computational boundaries in the y-direction were at a distance of 8 diameters from the cylinder axis. A uniform free-stream condition was imposed on these planes.

This mesh consisted of 19381 elements, out of which 2034 were the prismatic elements on the surface of the body. As for the previous cases, the computation was performed originally using second order polynomial expansions and was then restarted at $P = 4$ and $P = 6$. When the solution was computed with sixth

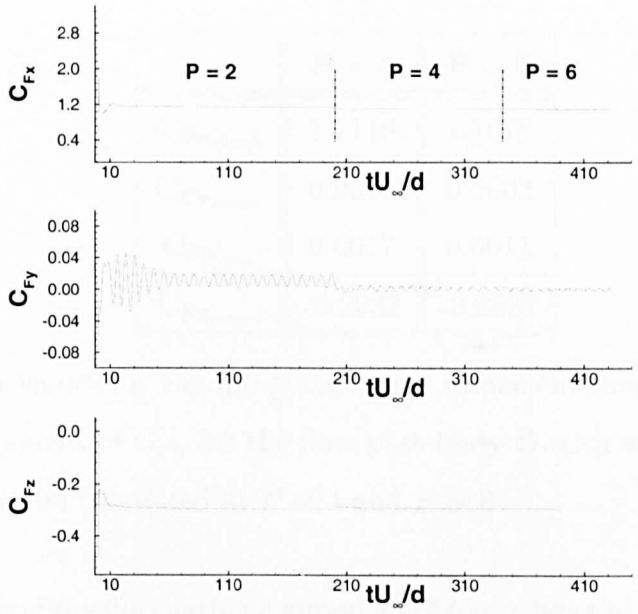


Figure 5.24: Integrated forces for the flow past body D with six diameters vertical addition at $Re = 100$, x- is the direction of the drag, y- is the horizontal component of the transverse force and z- is the vertical one

order polynomials, this mesh accounted for $1,855,812$ local degrees of freedom per variable. Blockage for these computational cases was 4.4%.

The integrated force coefficients for this case are shown in Figure 5.24. Time $\frac{tU_\infty}{d} = 200$ in Figure 5.24 represents the transition from $P = 2$ to $P = 4$ whereas the transition from $P = 4$ to $P = 6$ occurs at a non-dimensional time of $\frac{tU_\infty}{d} = 342$.

The forces in the y-direction exhibit periodic fluctuations whose magnitude, however, is much smaller than that for the flow past body C at the same Reynolds number. The mean values of the force coefficients in the three Cartesian directions (and the rms value of the fluctuating component of C_{Fy}) are shown in Table 5.4.

The Strouhal frequency corresponding to the periodic fluctuations in C_{Fy} was found to be 0.1142 at $P = 4$ and 0.1123 at $P = 6$. This frequency is smaller than the Strouhal frequency for body C (Table 5.2) by approximately 36%.

We note that there is a reduction of merely 0.3% in the magnitude of C_{Fx} as the polynomial order is increased from four to six. Moreover, there is a 3% increase from the magnitude of C_{Fx} for body D but this still corresponds to a reduction of 9% from the magnitude of C_{Fx} for body C.

	P = 4	P = 6
$C_{Fx_{mean}}$	1.1116	1.1078
$C_{Fy_{mean}}$	0.0010	0.0002
$C_{Fy_{rms}}$	0.0017	0.0011
$C_{Fz_{mean}}$	-0.2932	-0.2937

Table 5.4: Mean values for the integrated force coefficients and rms values for the fluctuating component of C_{Fy} for the flow past body D with six diameters vertical addition at $Re = 100$ computed at $P = 4$ and $P = 6$

The rms value of the fluctuating component of C_{Fy} when the solution is computed at $P = 6$ is equal to 0.0011 and this can be compared with the $C_{Fy_{rms}}$ for the flow past body C which is of the order of 0.0491 ± 0.0001 (Table 5.2).

Figure 5.25 depicts centreplane streamlines ($y = 0$) upstream of the geometry superimposed on pressure contours and u velocity contours at horizontal planes. The streamlines show that the motion along the length of the curved cylinder is towards the top boundary even with the six-diameter vertical extension. The u velocity contours now demonstrate unsteadiness at the top plane, which is located at the end of the six-diameter straight cylinder extension, and at midspan of the straight cylinder addition. At $z = 0$ however, which represents the end of the curved cylinder part (top of body D), the wake is narrow and nearly symmetric. Note that the wake at this plane appears narrower than the corresponding one for body D at $z = 0$ in Figure 5.18. The region at the rear of the cylinder that has the most negative pressure coefficients has now moved higher up in the z-direction up to the $z = 0$ level compared to the $z \approx -3.6d$ level for the flow past body D.

Figure 5.26(a) depicts the wake topology extracted at $\frac{tU_\infty}{d} = 414$ corresponding to a C_{Fy} maximum in the integrated forces where indeed the top shear layer is rolling up. In Figure 5.26(b) the wake topology is shown for $\frac{tU_\infty}{d} \approx 427$ corresponding to a C_{Fy} minimum where the bottom shear layer is influencing the sign of the forces.

The variation of sectional C_{Fy} is shown in Figure 5.27(a). Note that the range

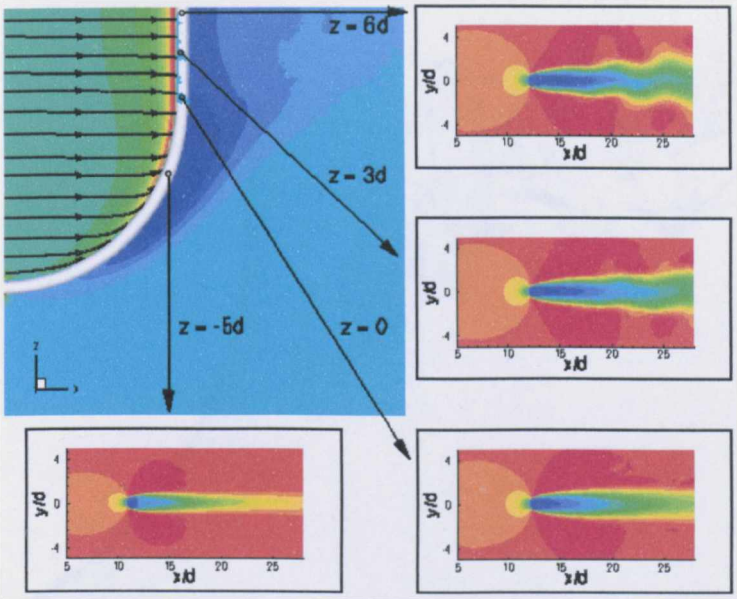
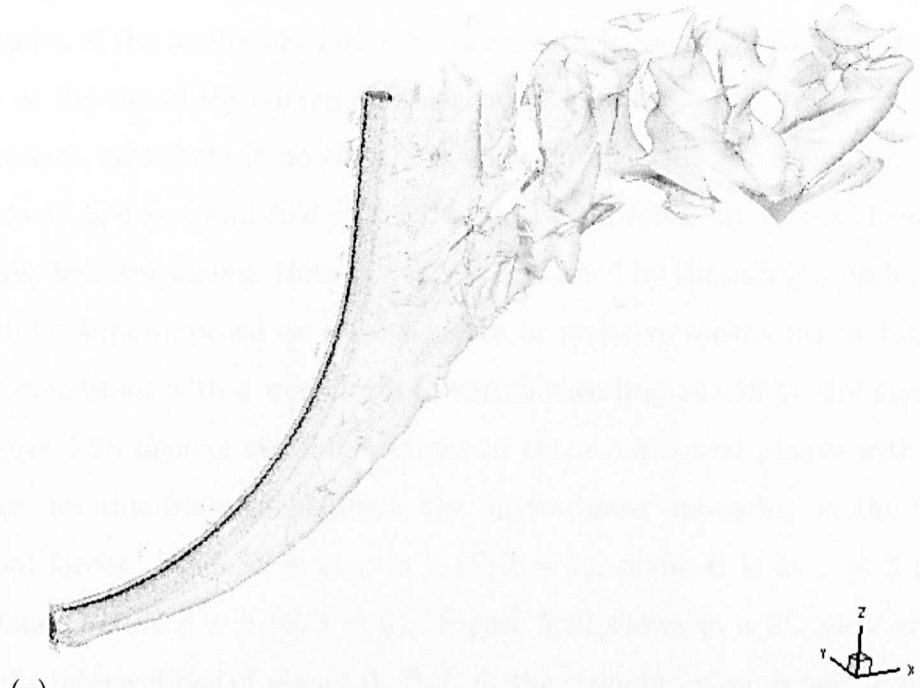


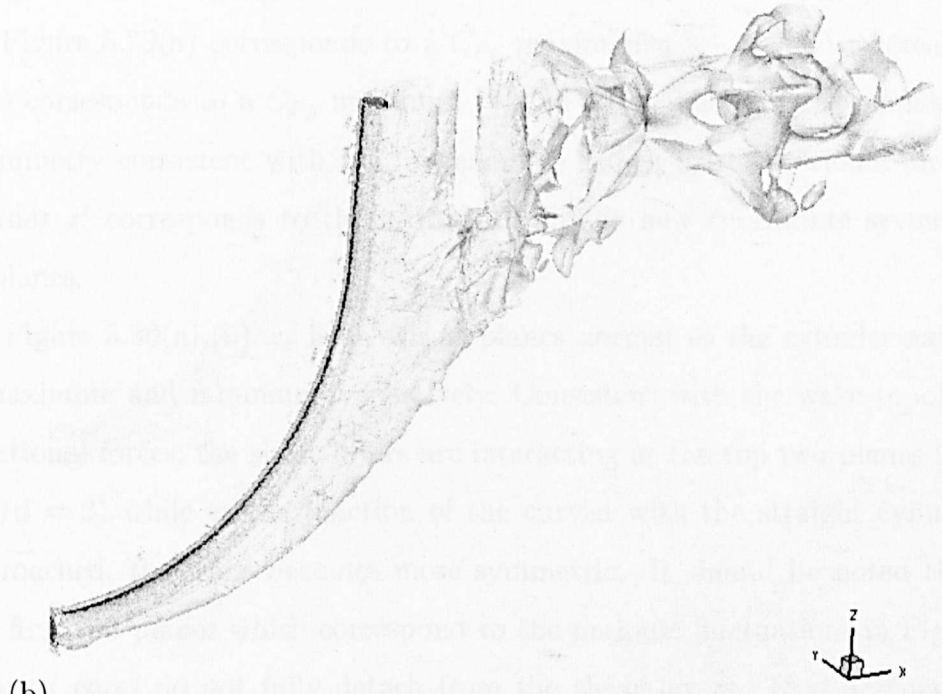
Figure 5.25: Centreplane streamlines ($y = 0$) overlaid on pressure contours for the flow past body D with a vertical extension of six diameters, $Re = 100$, $\frac{tU_\infty}{d} = 414$ (C_{Fy} maximum). The insets depict u velocity contours at four horizontal slices along the span.

in the contour levels plotted is now between -0.025 and 0.025, slightly higher than the range for body D (-0.016 to 0.016, Figure 5.21) but still an order of magnitude smaller than that for body C (-0.170 to 0.170, Figure 5.5). The fluctuations in the integrated C_{Fy} in Figure 5.24 can hence be attributed to the unsteady features in the six-diameter straight cylinder addition in Figure 5.27. The frequencies and the maxima and minima of these sectional forces are consistent with the corresponding ones for the integrated forces.

The oscillations with respect to the mean at three locations of $S/d = 1$, $S/d = 3$ and $S/d = 6$ can be seen more clearly in Figure 5.27(b). At $S/d = 1$ the sectional C_{Fy} has a mean of -0.0175 and as the amplitude of the oscillatory force is not large enough to bring the local C_{Fy} up to a positive value, the sectional forces at this S/d level are negative ranging from -0.011 to -0.024. Further down along the span at $S/d = 3$ the sectional C_{Fy} has a mean of 0.0037 and the sectional forces range from 0.0002 to 0.0071. Finally, at $S/d = 6$ which corresponds to the end of the



(a)



(b)

Figure 5.26: Wake topology for body D with a six-diameter vertical extension at $Re = 100$, $\lambda_2 = -0.01$: (a) extracted at a C_{Fy} maximum, $\frac{tU_\infty}{d} = 414$, (b) extracted at a C_{Fy} minimum, $\frac{tU_\infty}{d} \approx 427$

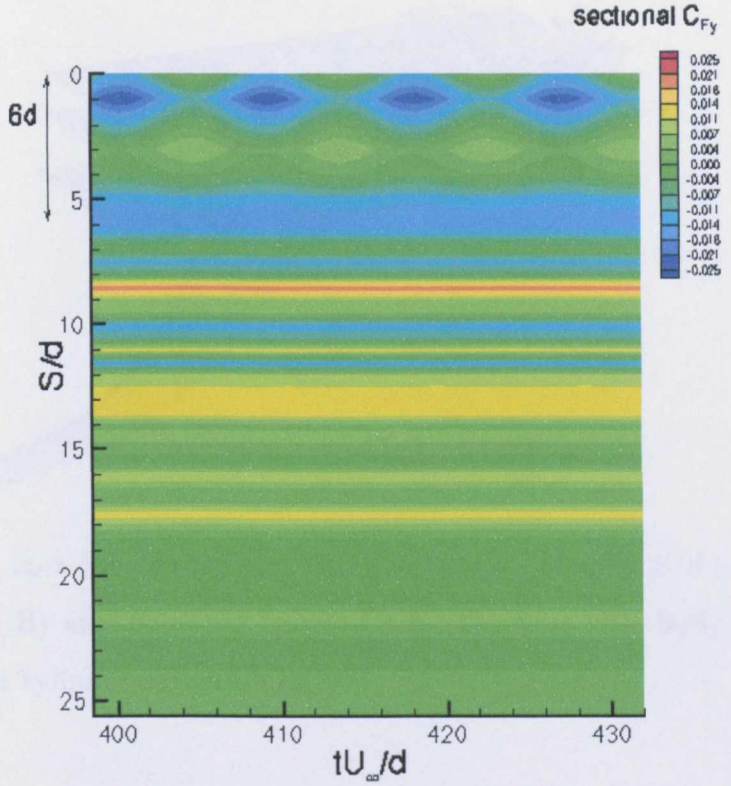
straight cylinder extension, the sectional forces are steady at a value of -0.017. The amplitudes of the oscillatory forces decrease with increasing S/d until they become steady at the top of the curved cylinder part ($S/d = 6$).

The fact that there is no change in the sign of local C_{Fy} at the top levels, for example at $S/d = 1$ and $S/d = 3$, as would be expected for vortex shedding, may originally look surprising. However, this is explained by the oscillations having small amplitudes superimposed on local positive or negative means (as in Figure 5.21). This is consistent with a weak form of vortex shedding as will be discussed below.

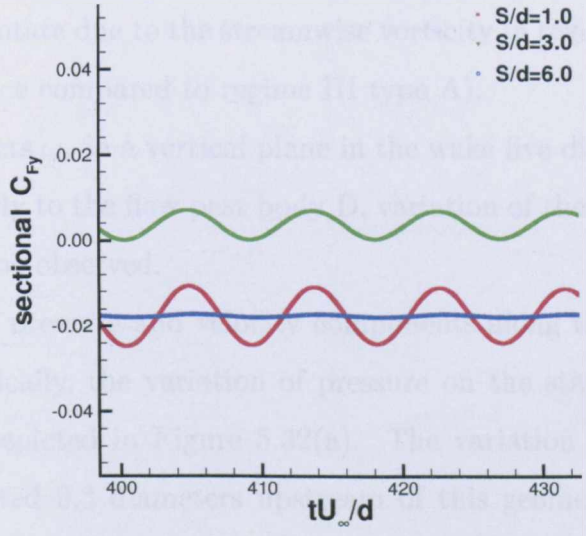
Figure 5.28 depicts the intersections of three horizontal planes with the wake topology for this body to highlight the unsteadiness appearing at the top in the sectional forces. Plane A is at $z = 5$ ($S/d = 1$), plane B is at $z = 3$ ($S/d = 3$) and plane C is at $z = 0$ ($S/d = 6$). Figure 5.29 shows in a 2D view at two time levels the intersections of planes A, B, C at the straight cylinder part with the wake topology along with planes at $S/d = 8.5$, $S/d = 10$, $S/d = 13.5$ in the curved part. Figure 5.29(a) corresponds to a C_{Fy} maximum ($\frac{tU_\infty}{d} = 414$) whereas Figure 5.29(b) corresponds to a C_{Fy} minimum ($\frac{tU_\infty}{d} \approx 427$). The first two planes exhibit antisymmetry consistent with the unsteadiness shown in the sectional forces plot. Note that x' corresponds to the x-direction in the new coordinate system in the local planes.

In Figure 5.30(a),(b) ω_z is shown at planes normal to the cylinder axis at the C_{Fy} maximum and minimum respectively. Consistent with the wake topology and the sectional forces, the shear layers are interacting at the top two planes ($S/d = 1$ and $S/d = 3$) while as the junction of the curved with the straight cylinder part is approached, the wake becomes more symmetric. It should be noted that even at the first two planes which correspond to the periodic fluctuations in Figure 5.27 the vortex cores do not fully detach from the shear layers. It is postulated that the strength of the growing vortex is not large enough to fully draw the opposite shear layer across the wake and subsequently be shed, as would be expected for a regular vortex shedding process. Moreover, the longer formation regions are indeed associated with lower shedding frequencies.

This weak form of shedding is consistent with the wake topology depicted in



(a)



(b)

Figure 5.27: (a) Variation of sectional C_{Fy} for body D with a six-diameter straight cylinder extension vertically, $Re = 100$; (b) Variation of C_{Fy} with time at the specified locations of $S/d = 1$, $S/d = 3$, and $S/d = 6$

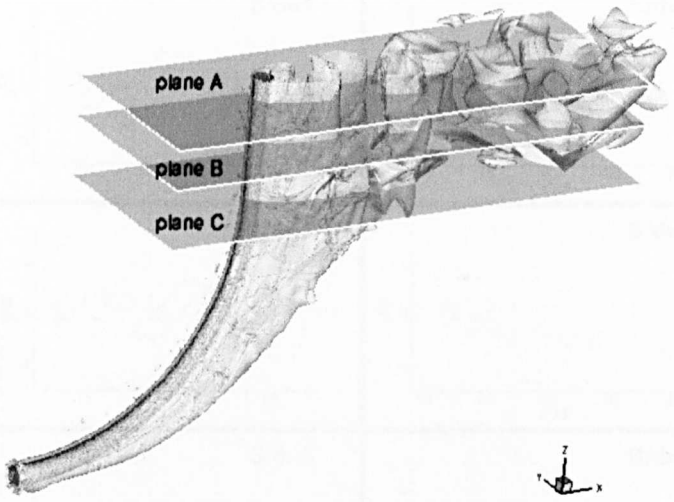


Figure 5.28: Vortex core intersections at three horizontal planes: $S/d = 1$ (plane A), $S/d = 3$ (plane B) and $S/d = 6$ (plane C) for the flow past body D with a six-diameter straight cylinder extension on top

Figure 5.26 where the structures connect away from the body. In the case of the wavy cylinders, a similar phenomenon was observed where the spanwise vortex structures were found to reorientate due to the streamwise vorticity in regime II type A (milder geometric disturbance compared to regime III type A).

Figure 5.31 depicts ω_x in a vertical plane in the wake five diameters downstream of the body. Similarly to the flow past body D, variation of the strength of ω_x along this plane can also be observed.

The variation of pressure and velocity components along this body is shown in Figure 5.32. Specifically, the variation of pressure on the stagnation line and the base pressure are depicted in Figure 5.32(a). The variation of u and w velocity components, extracted 0.3 diameters upstream of this geometry is shown in Figure 5.32(b). The magnitude of w velocity component increases along the span and reaches a maximum of 28% of the free-stream magnitude at $S/d = 16.6$. This non-dimensional arc length corresponds to a section inclined approximately 48.3° from the horizontal. Hence the maximum w velocity component occurs at exactly the same location for this configuration as for bodies C and D. Therefore, the verti-

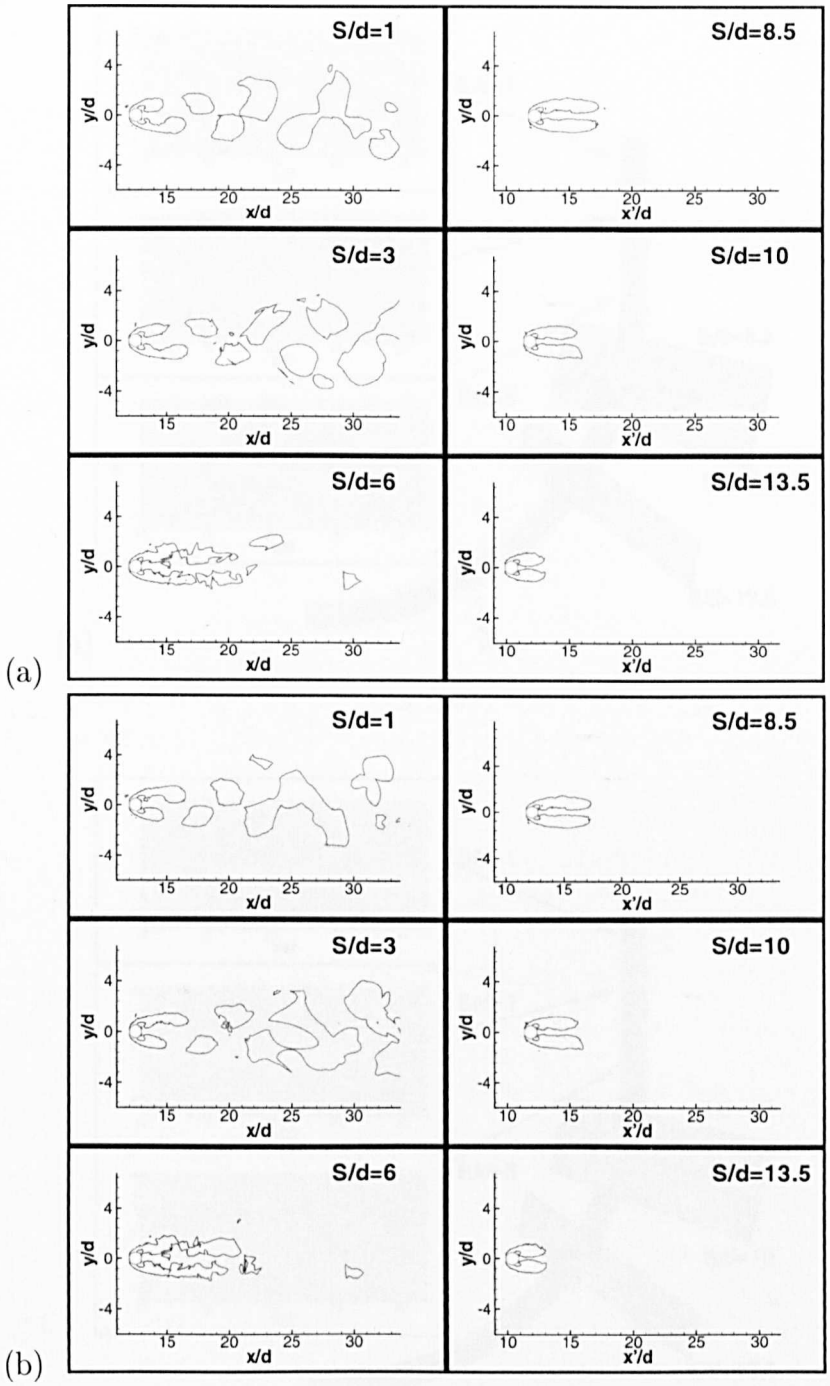
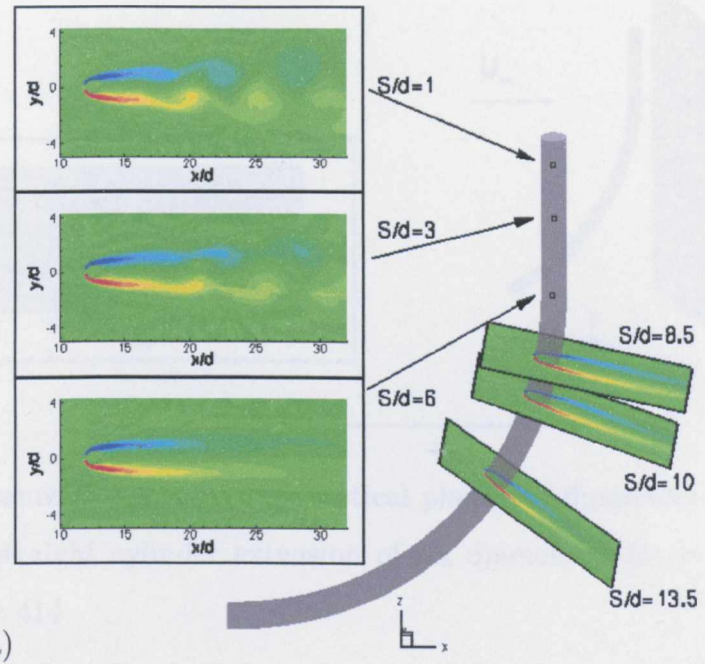
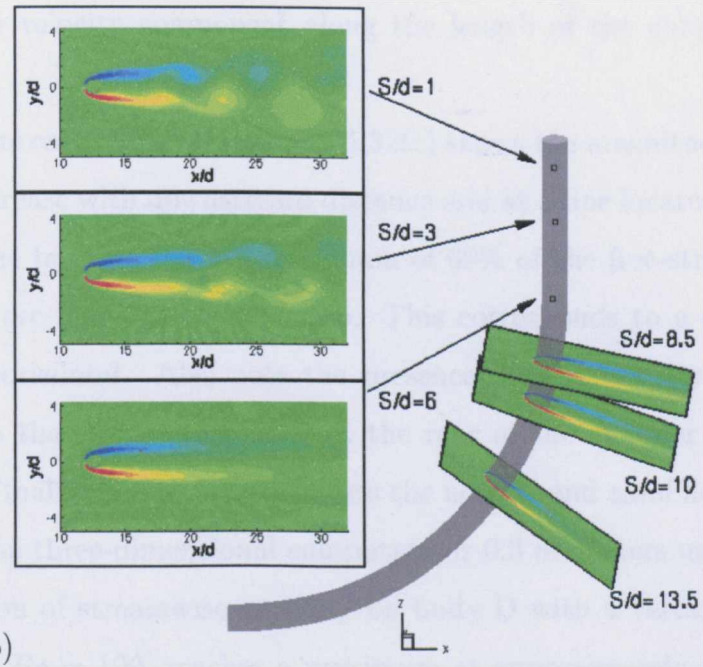


Figure 5.29: Vortex core intersections at six planes for the flow past body D with a vertical extension of six diameters, $Re = 100$: (a) $\frac{tU_\infty}{d} = 414$, C_{Fy} maximum, (b) $\frac{tU_\infty}{d} \approx 427$, C_{Fy} minimum



(a)



(b)

Figure 5.30: Spanwise vorticity contours for body D with a straight cylinder extension of six diameters at $Re = 100$: (a) $\frac{tU_\infty}{d} = 414$, C_{Fy} maximum, (b) $\frac{tU_\infty}{d} \approx 427$, C_{Fy} minimum

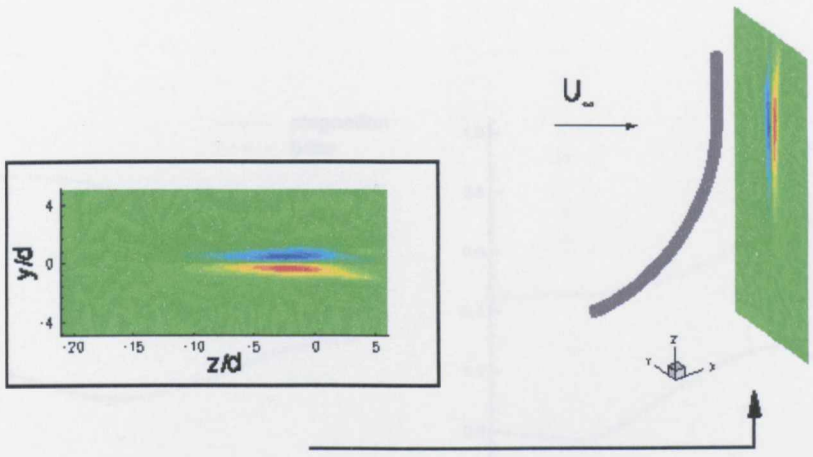


Figure 5.31: Streamwise vorticity on a vertical plane five diameters downstream of body D with a straight cylinder extension of six diameters, $Re = 100$, at a C_{Fy} maximum, $\frac{tU_\infty}{d} = 414$

cal addition of a straight cylinder six diameters long on top has not affected the distribution of w velocity component along the length of the curved part of the body.

Similarly to the case of body D, Figure 5.32(c) shows the magnitude of w velocity component to increase with downstream distance and at a line located 1.5 diameters downstream of the body to reach a maximum of 69% of the free-stream value at a non-dimensional arc length of $S/d = 12.5$. This corresponds to a section located 29.9° from the horizontal. Also note the presence of a w velocity component of the order of 20% the free-stream value at the rear of the cylinder in the vertical extension part. Finally, Figure 5.32(d) shows the normal and axial flow components extracted from the three-dimensional computations 0.3 diameters upstream.

The production of streamwise vorticity on body D with a vertical extension of six diameters, at $Re = 100$, reaches a maximum at approximately midspan of the curved part of the body as Figure 5.33 shows. Note that this was also found to be the case for the wavy cylinders where the streamwise vorticity component was emerging strongly at the geometric inflection points (Darekar & Sherwin 2001b).

As mentioned at the beginning of this section this case was proposed to show the extent to which the steady features found for the flow past body D would

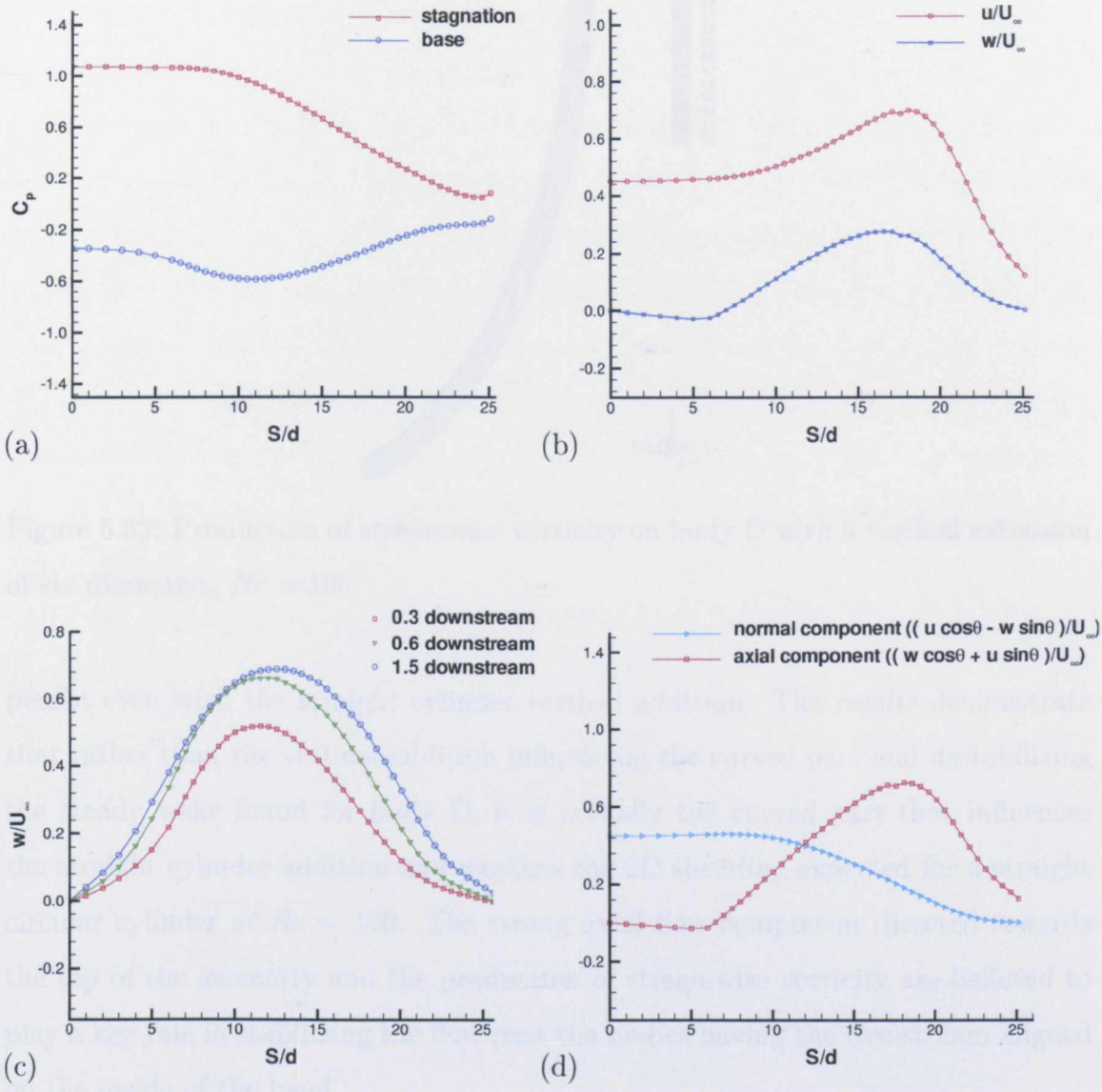


Figure 5.32: Variation of pressure and velocity along the span of body D with a six-diameter straight cylinder extension, $Re = 100$: (a) Base pressure and stagnation pressure, (b) u and w velocity components extracted 0.3 diameters upstream of the curved cylinder, (c) w velocity component extracted 0.3, 0.6 and 1.5 diameters downstream of the curved cylinder, (d) Normal $((u\cos\theta - w\sin\theta)/U_\infty)$ and axial $((w\cos\theta + u\sin\theta)/U_\infty)$ components computed from the 3D simulation 0.3 diameters upstream of the geometry

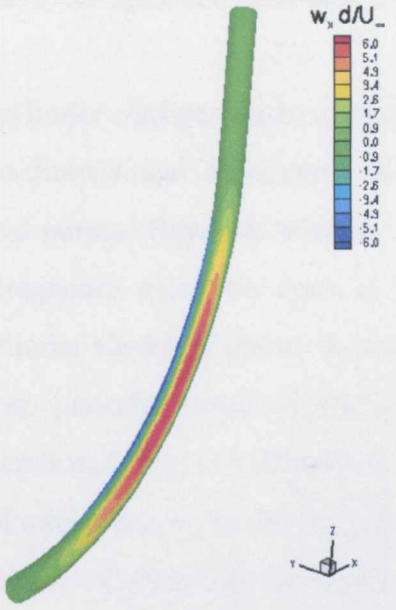


Figure 5.33: Production of streamwise vorticity on body D with a vertical extension of six diameters, $Re = 100$

persist even with the straight cylinder vertical addition. The results demonstrate that rather than the vertical addition influencing the curved part and destabilizing the steady wake found for body D, it is actually the curved part that influences the straight cylinder addition and weakens the 2D shedding expected for a straight circular cylinder at $Re = 100$. The strong axial flow component directed towards the top of the geometry and the production of streamwise vorticity are believed to play a key role in stabilizing the flow past the bodies having the free-stream aligned on the inside of the bend.

Relation to other cylinder shapes and summary of cases at Reynolds number of 100

The results for these curved cylinder configurations can be discussed in conjunction with other cylinder shapes studied in the bluff body flow community. As described in section 2.5, Gaster (1969, 1971) found the vortex shedding past tapered cylinders to occur in spanwise cells of constant frequency each, with jumps in frequency between cells. Following, Piccirillo & Van Atta (1993) studied the details of the dislocations

produced at the boundaries of the spanwise cells and the corresponding modulation frequency.

For none of the curved cylinder configurations of this work was cellular behaviour observed. A sectional two-dimensional argument, as discussed previously would predict variation of the local normal Reynolds number which would hence result in variation of the Strouhal frequency along the span of body C. However, as shown in Figure 5.5, the upper cylinder shedding drives the lower end. For body D steady forces were detected and no periodic vortex shedding. Therefore no similarities can be found between tapered and curved cylinders in terms of the wake patterns observed. The variation of sweep angle for curved cylinders seems to set different mechanisms than the variation of diameter for tapered cylinders. In analogy to tapered cylinders, uniform straight cylinders under shear flow, as discussed in section 2.3, exhibit cellular behaviour.

A comparison can be drawn between the shedding patterns of the curved cylinders of this study and those of the oblique cylinders described in section 2.4. Similarly to the Independence Principle (cosine law) failing to predict the flow past a stationary oblique circular cylinder (Ramberg 1983), the curved cylinders behave in a three-dimensional manner not following the variations in the normal flow component and Reynolds number.

Finally, as discussed in section 2.2, straight uniform circular cylinders can shed in an oblique mode biased by the end effects. For oblique shedding of a straight cylinder, a Reynolds number of 92 would correspond to a Strouhal frequency of approximately 0.157, whereas a Reynolds number of 69 to approximately 0.138 (data extracted from Williamson (1996), and Williamson (1989)). Body C accounts for a local normal Reynolds number of 92 at $S/d = 5$ and a local Reynolds number of 69 at $S/d = 10$. However, as body C sheds at one frequency with the top end driving the bottom, rather than adjusting to local frequencies determined by the local Reynolds number, such an analogy cannot be drawn. Furthermore, if we consider the top Reynolds number of 100, oblique shedding for a straight cylinder at this Reynolds number would suggest a shedding angle of $12 - 12.2°$ with a Strouhal frequency of approximately 0.16. However, under the current blockage conditions, the Strouhal

frequency found in this work for body C is larger.

Overall, these computations have shown that more insight can be gained with a three-dimensional approach. For the flows past body D and past body D with a vertical extension of six diameters, a sectional argument considering the normal component of the free-stream would predict shedding even at the curved part of the body. Nevertheless, as discussed above, the axial flow component and its direction towards the top of the geometry was the key factor in stabilizing these flows; and this is exactly the component not modelled by the two-dimensional methods.

5.2 Reynolds number 500: Results and discussion

5.2.1 Flow past body C

The flow past body C has also been computed at a higher Reynolds number, that of 500, to see the effects of introducing three dimensional instability in the wake, following the straight 2D cylinder behaviour. Moreover, the higher Reynolds number should tend to preserve shedding to a lower angle at the bottom following the local normal velocity analogy. The computation was restarted from the flow field of the Reynolds number 100 case, presented in section 5.1.1 using a fourth order polynomial expansion.

Figure 5.34(a) shows the force history for this case starting at $\frac{t|U_\infty|}{d} \approx 309$ from the flow field of the Reynolds number 100 case. Figure 5.34(b) shows in detail a section of the integrated force coefficients in the x-,y-, and z- directions for part of the simulation computed at sixth polynomial order. The x- direction is the direction of the drag and the y- and z- directions represent the horizontal and vertical component of the transverse force respectively. Non-dimensional time $\frac{t|U_\infty|}{d} \approx 631$ corresponds to the transition from fourth to sixth order polynomials.

To investigate whether the features of the enstrophy analysis presented in section 3.5.2 for Reynolds number 100 would persist at 500 also, the amount of enstrophy captured in the coherent structures at each λ_2 level was computed. Figure 5.35(a) depicts the enstrophy Z, captured at each λ_2 level, normalized by the total enstrophy,

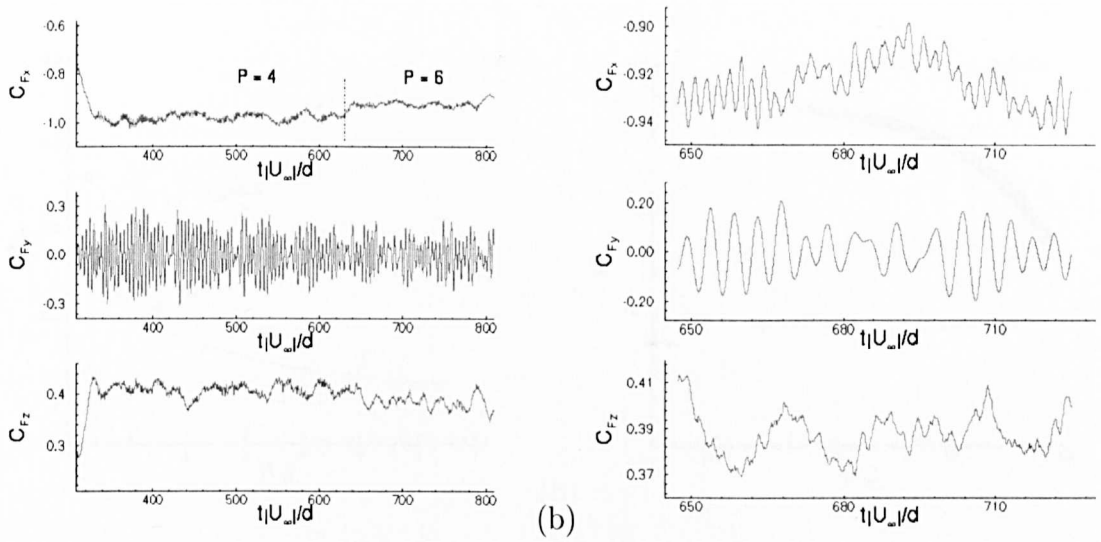


Figure 5.34: (a) Force history for Body C at Reynolds number of 500; (b) A more detailed section of the integrated force coefficients at sixth polynomial order

Z_{tot}, as a function of the cut-off value for the flow past body C at $Re = 500$. This curve is shown in a log-log axis in Figure 5.35(b).

Comparing with Figure 3.6, the asymptote for this case at $Re = 500$ is reached at a higher λ_2 value corresponding to the vortex cores being more energetic and of higher strength at the higher Reynolds number. Overall, the trends of the two asymptotes at zero and at infinity, discussed in section 3.5.2, can be discerned for this case also.

Figure 5.36 depicts the λ_2 structures at the specified positions (a, b, c, d, e, f) marked in Figure 5.35(a). Similarly to Figure 3.7, at small λ_2 levels numerical noise is dominating (Figure 5.36(a)). At high levels, however, it is mostly the shear layers being identified while the wake dynamics are not captured (Figure 5.36(f)). Hence an appropriate cut-off range can be recognized as $0.5 \leq |\lambda_2| \leq 1.5$ for the optimal representation of the vortical structures in the wake of body C at Reynolds number of 500. This range is also shown in Figure 5.35(b). Even though it may look as if this appropriate cut-off range is shorter than that of Figure 3.6(b), note that the range of the x-axis is longer in this case.

The variation of sectional C_{Fy} computed at slices normal to the cylinder axis

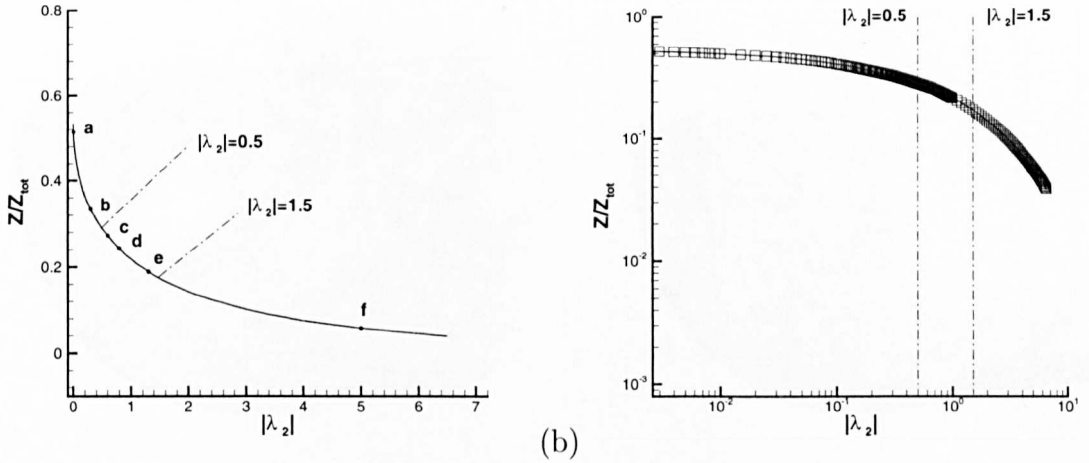


Figure 5.35: (a) Normalized enstrophy, Z/Z_{tot}, versus λ_2 for the flow past Body C at $Re = 500$, (b) log-log axis

at different locations of the span for body C at $Re = 500$ is depicted in Figure 5.37. As in Figure 5.5, the top of the cylinder is at $S/d = 0$ whereas $S/d = 19.6$ corresponds to the end of the quarter turn. A non-dimensional arc length of $S/d = 5$ corresponds to a section inclined approximately 23° from the horizontal and a local Reynolds number of 460 whereas an arc length of $S/d = 15$ corresponds to a section inclined 69° from the horizontal and a local Reynolds number of nearly 180. This sectional local Reynolds number is now higher than the critical Reynolds number for the vortex shedding of a circular straight cylinder.

The contour levels are now higher than those for $Re = 100$ while the forces persist until lower angles at the bottom (higher S/d levels). The periodicity in the sectional forces observed in Figure 5.5 is not apparent at this higher Reynolds number case. For a straight 2D cylinder, the Reynolds number of 500 is above the transition stage to three-dimensionality.

Figure 5.38(a) depicts the wake topology in a 3D perspective whereas Figure 5.38(b) shows a view from the top at $\frac{t|U_\infty|}{d} \approx 652$, $\lambda_2 = -0.8$. Both the 3D and the top view show vertical rollers and braids inbetween. This sort of flow structures are commonly attributed to Mode A and B transition for a straight cylinder. The region where the vortices curl towards the horizontal part of the body becomes more

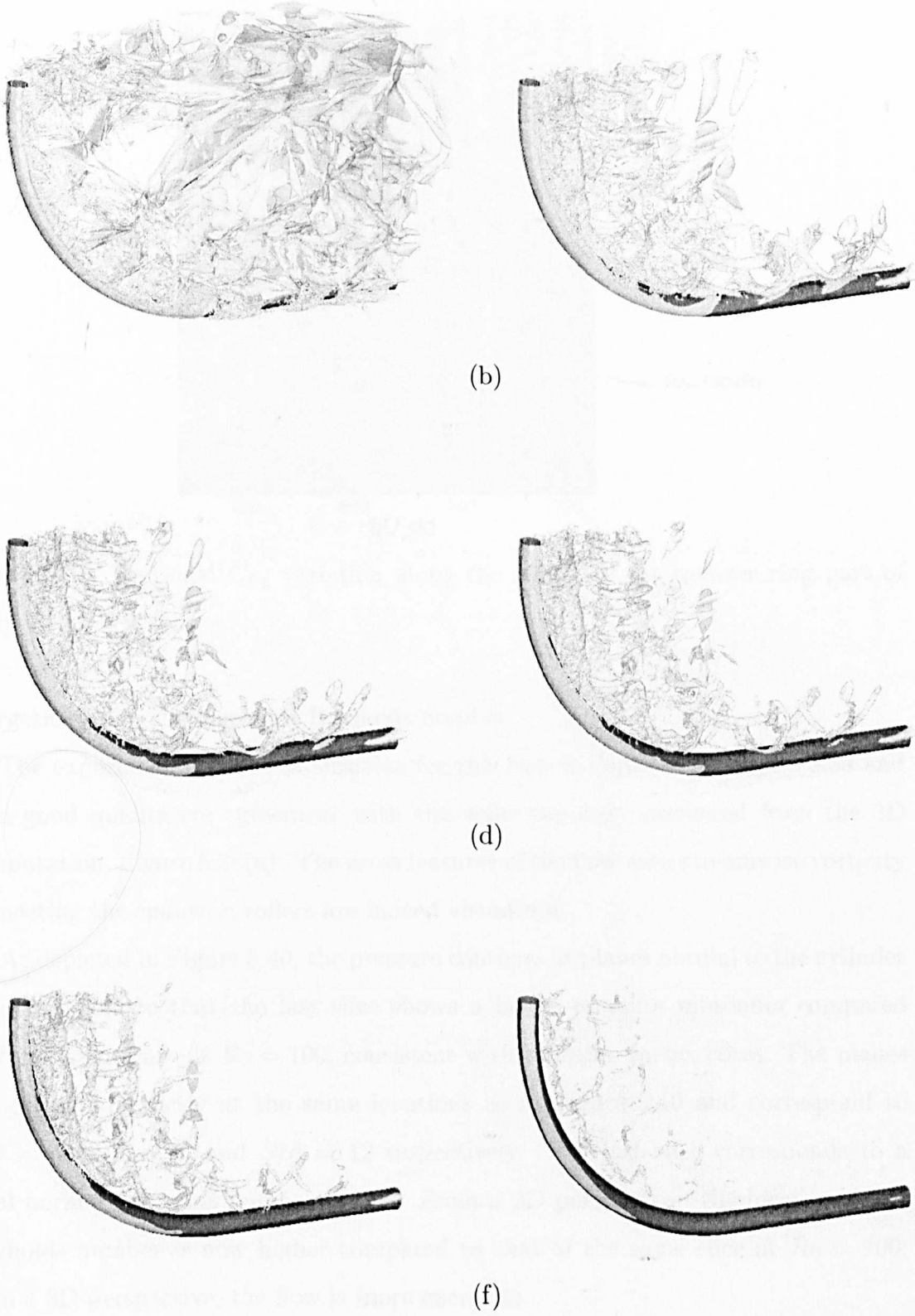


Figure 5.36: Isocontours of λ_2 at: (a) λ_2 = -0.005, (b) λ_2 = -0.3, (c) λ_2 = -0.6, (d) λ_2 = -0.8, (e) λ_2 = -1.3, (f) λ_2= -5.0

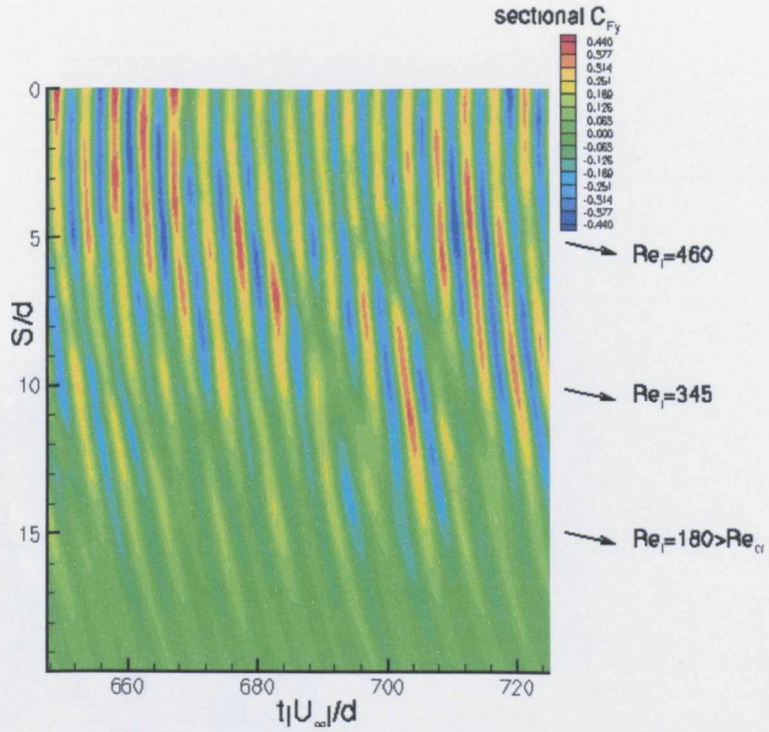


Figure 5.37: Sectional C_{Fy} variation along the length of the quarter ring part of body C, $Re = 500$

energetic due to the increased Reynolds number.

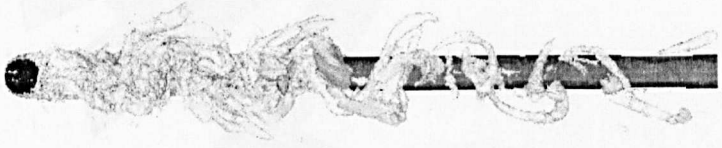
The experimental flow visualization for this case is depicted in Figure 5.39 and is in good qualitative agreement with the wake topology extracted from the 3D computation, Figure 5.38(a). The gross features of the flow with streamwise vorticity connecting the spanwise rollers are indeed visualized.

As depicted in Figure 5.40, the pressure contours at planes normal to the cylinder axis demonstrate that the last slice shows a larger pressure minimum compared with the same case at $Re = 100$, consistent with stronger vortex cores. The planes are extracted exactly at the same locations as in Figure 5.10 and correspond to $S/d = 5$, $S/d = 8$, and $S/d = 12$ respectively. The last slice corresponds to a local normal Reynolds number of 284. From a 2D perspective, the local sectional Reynolds number is now higher compared to that of the same slice at $Re = 100$; from a 3D perspective, the flow is more energetic.

The variation of pressure on the stagnation line and the base pressure for body C at $Re = 500$ are shown in Figure 5.41(a). This is the case with the smallest



(a)



(b)

Figure 5.38: Vortex cores in the wake of body C at $Re = 500$, $\lambda_2 = -0.8$, $\frac{t|U_\infty|}{d} \approx 652$: (a) 3D view, (b) View from the top

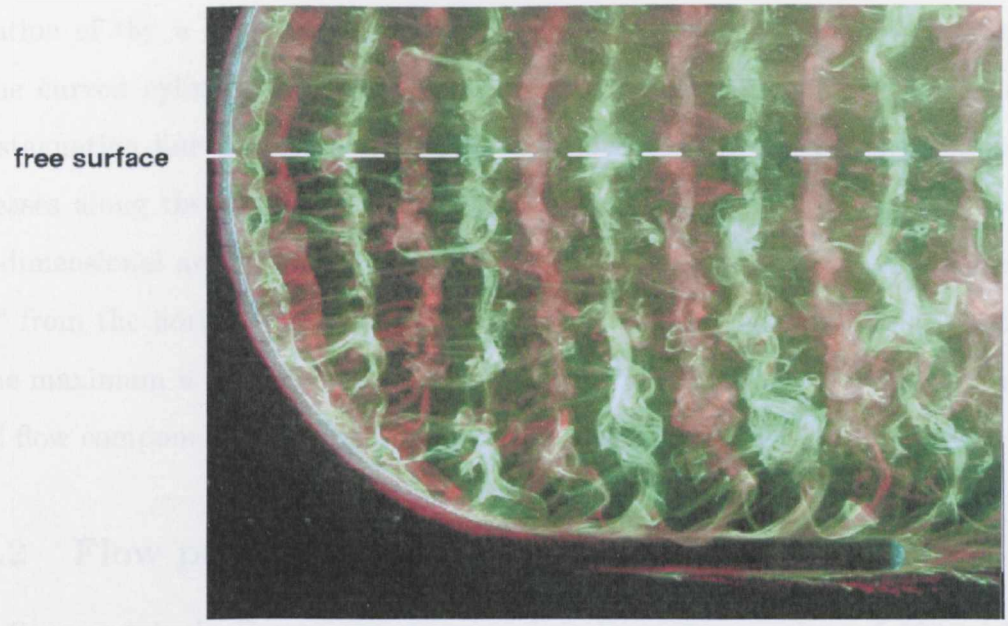


Figure 5.39: Towing tank flow visualization for body C, $Re = 500$

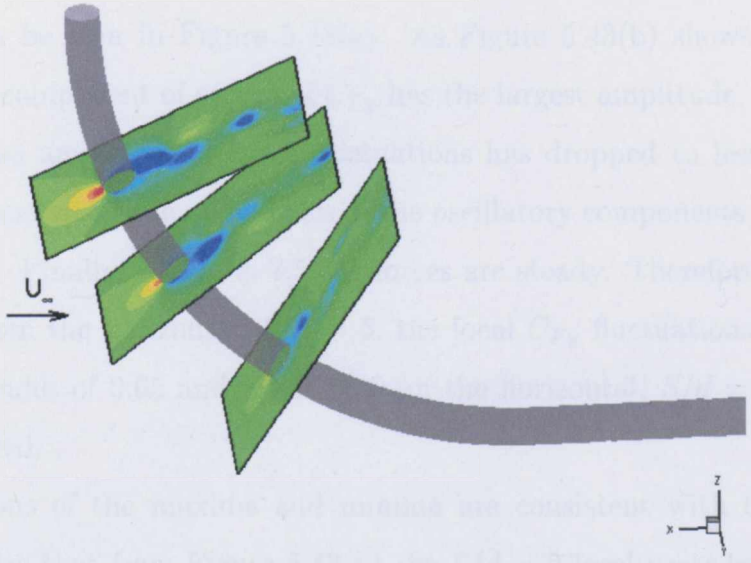


Figure 5.40: Pressure contours on planes normal to the cylinder axis for the flow past body C at $Re = 500$, $\frac{t|U_\infty|}{d} \approx 652$

pressure coefficients consistent with this case being the strongest shedding one. The variation of the u and w velocity components, extracted 0.3 diameters upstream of the curved cylinder, is shown in Figure 5.41(b). As pressure decreases along the stagnation line (Figure 5.41(a)), the magnitude of the w velocity component increases along the span and reaches a maximum of 33% of the free-stream at a non-dimensional arc length of $S/d = 12$, which corresponds to a section inclined 55.4° from the horizontal. The higher Reynolds number has brought the location of the maximum w further down along the span. In Figure 5.41(c) the normal and axial flow components are plotted from the three-dimensional computations.

5.2.2 Flow past body D

The flow past body D was also computed at Reynolds number of 500 with the outflow plane now extending 35 diameters downstream rather than 28.

The integrated force coefficients for the flow past body D at $Re = 500$ are shown in Figure 5.42. Non-dimensional time $\frac{tU_\infty}{d} = 200$ represents the transition from $P = 2$ to $P = 4$ whereas $\frac{tU_\infty}{d} \approx 433$ the transition from $P = 4$ to $P = 6$.

The fluctuations in the integrated C_{Fy} can be attributed to the top part of body D as can be seen in Figure 5.43(a). As Figure 5.43(b) shows, at $S/d = 2$ the oscillatory component of sectional C_{Fy} has the largest amplitude, equal to 0.25. By $S/d = 4$ the amplitude of these fluctuations has dropped to less than a half, equal to 0.10, and so on the amplitudes of the oscillatory components decrease with increasing S/d. Finally, at $S/d = 7.5$ the forces are steady. Therefore for a section inclined 23° from the horizontal, $S/d = 5$, the local C_{Fy} fluctuations already have smaller amplitudes of 0.05 and by 34.6° from the horizontal, $S/d = 7.5$, a steady wake is recovered.

The locations of the maxima and minima are consistent with the integrated forces. Note also that from Figure 5.43(b) the $S/d = 2$ level precedes the $S/d = 4$ and so on, consistent with the slight obliqueness in the contours of the sectional forces.

The spanwise vorticity component at three planes normal to the cylinder axis at

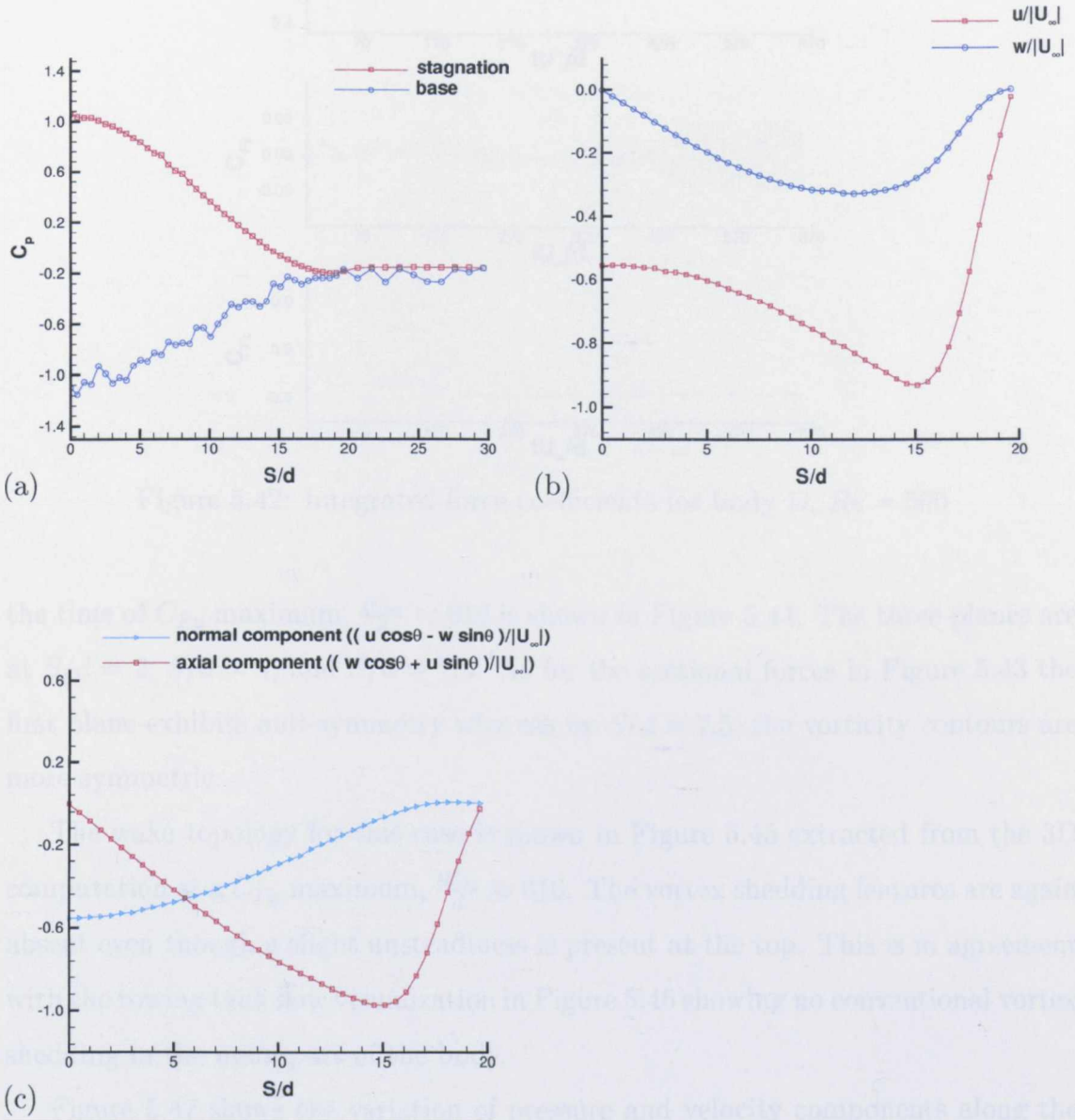


Figure 5.41: Variation of pressure and velocity along the span of body C, $Re = 500$: (a) Base pressure and stagnation pressure, (b) u and w velocity components extracted 0.3 diameters upstream of the curved cylinder, (c) Normal $(u\cos\theta - w\sin\theta/|U_\infty|)$ and axial $(w\cos\theta + u\sin\theta/|U_\infty|)$ components computed from the 3D simulation 0.3 diameters upstream of the curved cylinder

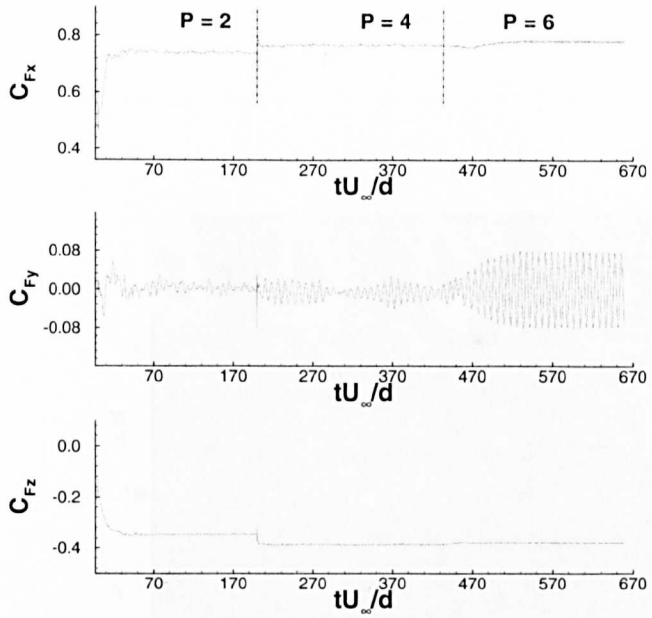
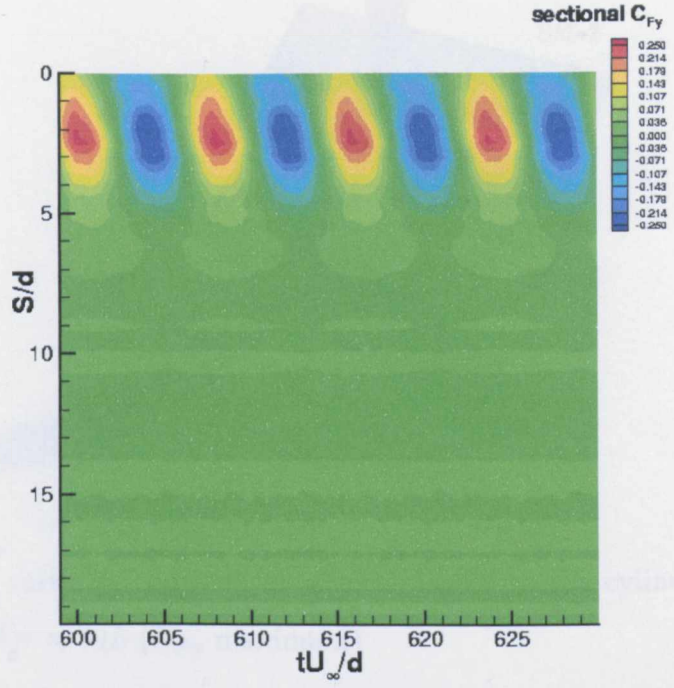


Figure 5.42: Integrated force coefficients for body D, $Re = 500$

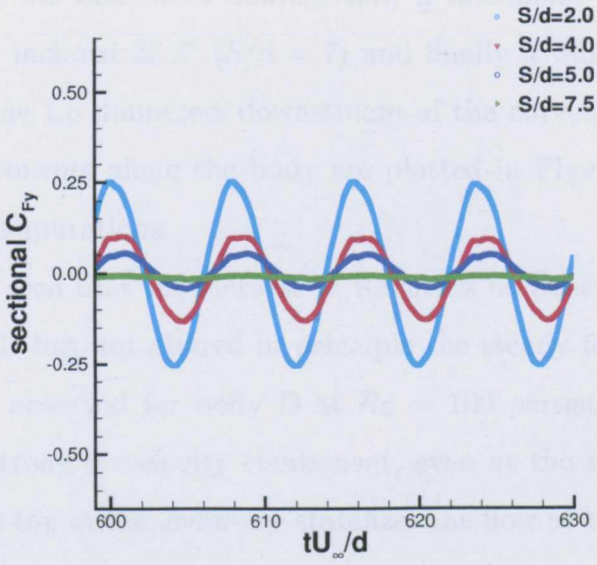
the time of C_{Fy} maximum, $\frac{tU_\infty}{d} \approx 616$ is shown in Figure 5.44. The three planes are at $S/d = 2$, $S/d = 4$, and $S/d = 7.5$. As for the sectional forces in Figure 5.43 the first plane exhibits anti-symmetry whereas by $S/d = 7.5$, the vorticity contours are more symmetric.

The wake topology for this case is shown in Figure 5.45 extracted from the 3D computation at a C_{Fy} maximum, $\frac{tU_\infty}{d} \approx 616$. The vortex shedding features are again absent even though a slight unsteadiness is present at the top. This is in agreement with the towing tank flow visualization in Figure 5.46 showing no conventional vortex shedding in the main part of the body.

Figure 5.47 shows the variation of pressure and velocity components along the span of body D at a Reynolds number of 500. Specifically, Figure 5.47(a) shows the variation of pressure along the stagnation line and base pressure. The variation of u and w velocity components, extracted 0.3 diameters upstream of the curved cylinder, is depicted in Figure 5.47(b) where the magnitude of the w velocity component reaches a maximum of 26% of the free-stream value at a section inclined 57.7° from the horizontal ($S/d = 12.6$). Note that, as Figure 5.47(c) depicts, the magnitude of the w velocity component at a line 0.3 diameters downstream of the body reaches the free-stream magnitude at a section inclined 27.6° from the horizontal ($S/d = 6$).



(a)



(b)

Figure 5.43: (a) Variation of sectional C_{Fy} along the length of body D, $Re = 500$; (b) Variation of C_{Fy} with time at the specified locations of $S/d = 2$, $S/d = 4$, $S/d = 5$, and $S/d = 7.5$

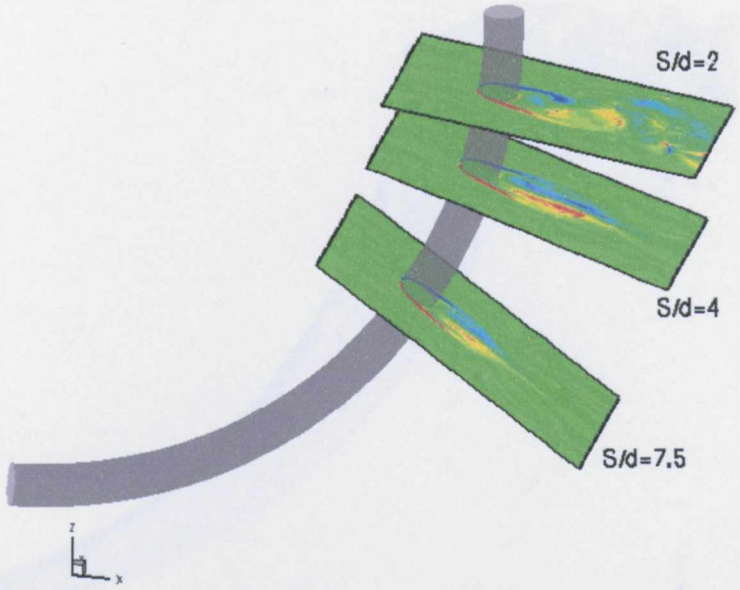


Figure 5.44: Spanwise vorticity contours at planes normal to the cylinder axis for body D at $Re = 500$, $\frac{tU_\infty}{d} \approx 616$ (C_{Fy} maximum)

Moreover, on a line 0.6 diameters downstream, a maximum value of $1.08U_\infty$ is reached at a section inclined 32.2° ($S/d = 7$) and finally a value of $1.13U_\infty$ at the same section on a line 1.5 diameters downstream of the curved body. The normal and axial flow components along the body are plotted in Figure 5.47(d) from the three-dimensional computations.

Overall, we have seen that the increase in Reynolds number from 100 to 500 for the flow past body D has not altered in principle the steady features of this flow. The flow structures observed for body D at $Re = 100$ persist at $Re = 500$ also. The presence of a strong w velocity component, even at the rear of the cylinder, directed towards the top of the geometry stabilizes the flow at this higher Reynolds number also where the wake of a straight 2D cylinder would have already undergone transition to three-dimensionality.

Darekar & Sherwin (2001a) also computed the flow past the wavy cylinders at $Re = 500$ and found substantial drag reductions compared to the straight cylinder at this Reynolds number. The three-dimensional wake structure behind a wavy cylinder was also presented recently by Lam *et al.* (2002). In the experimental

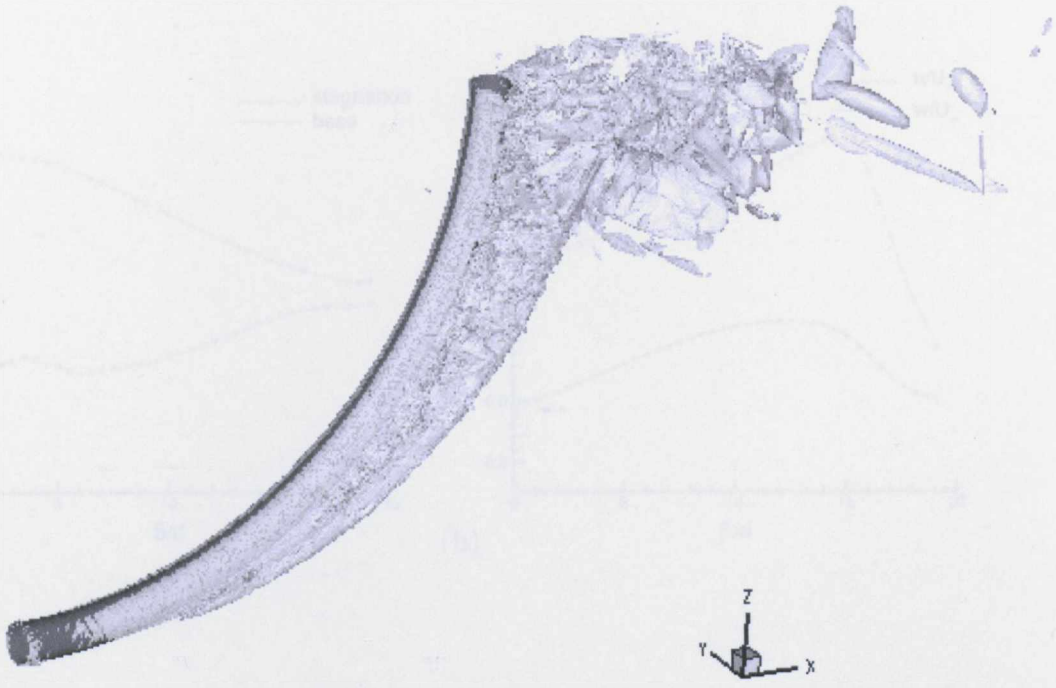


Figure 5.45: Wake topology for body D at $Re = 500$, $\lambda_2 = -0.4$, $\frac{tU_\infty}{d} \approx 616$ (C_{Fy} maximum)

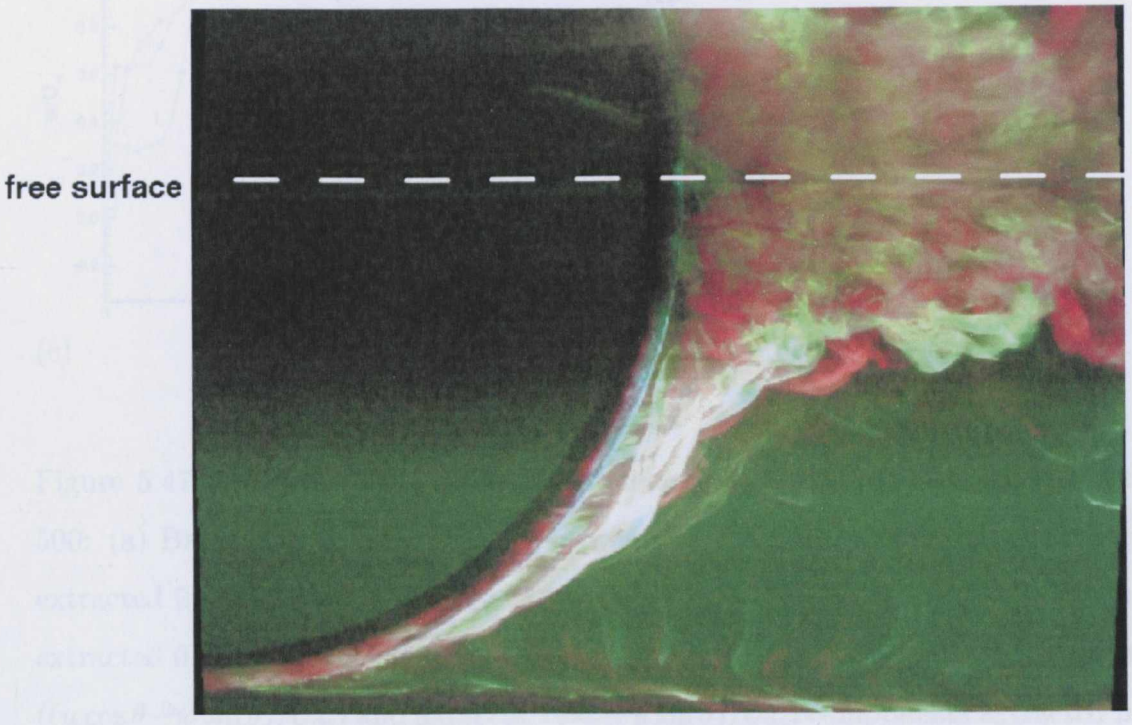


Figure 5.46: Towing tank flow visualization for body D, $Re = 500$

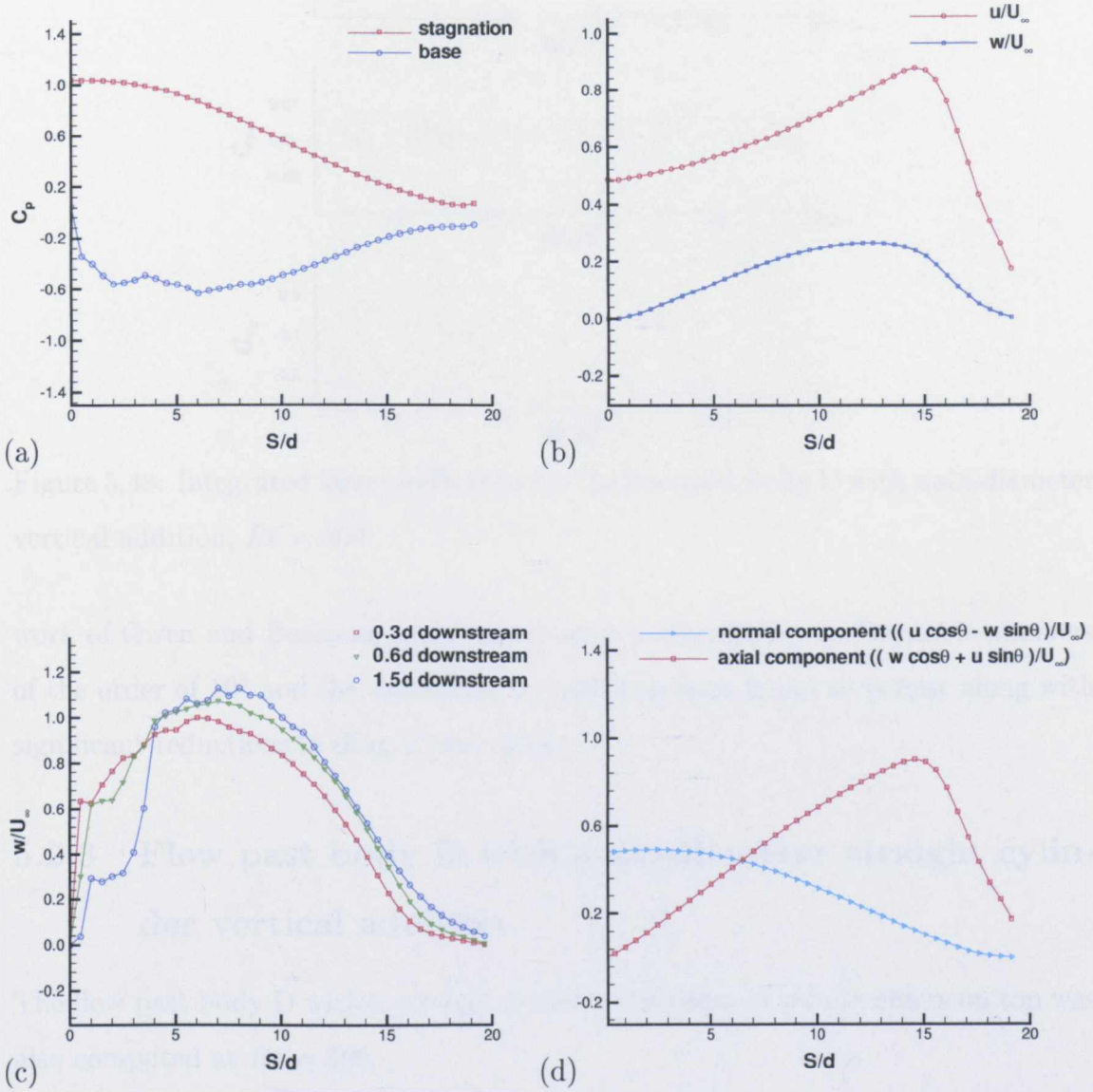


Figure 5.47: Variation of pressure and velocity along the span of body D, Re = 500: (a) Base pressure and stagnation pressure, (b) u and w velocity components extracted 0.3 diameters upstream of the curved cylinder, (c) w velocity component extracted 0.3, 0.6 and 1.5 diameters downstream of the curved cylinder, (d) Normal $((u\cos\theta - w\sin\theta)/U_\infty)$ and axial $((w\cos\theta + u\sin\theta)/U_\infty)$ components extracted from the 3D computation 0.3 diameters upstream of the curved cylinder

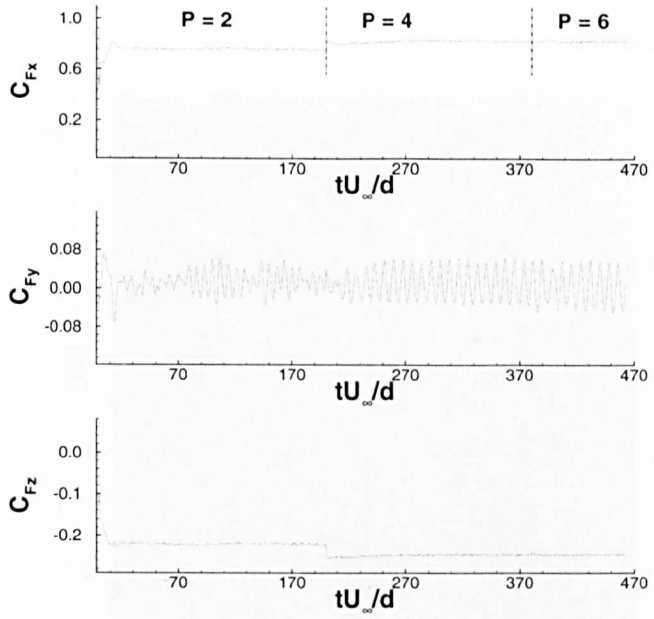


Figure 5.48: Integrated force coefficients for the flow past body D with a six-diameter vertical addition, $Re = 500$

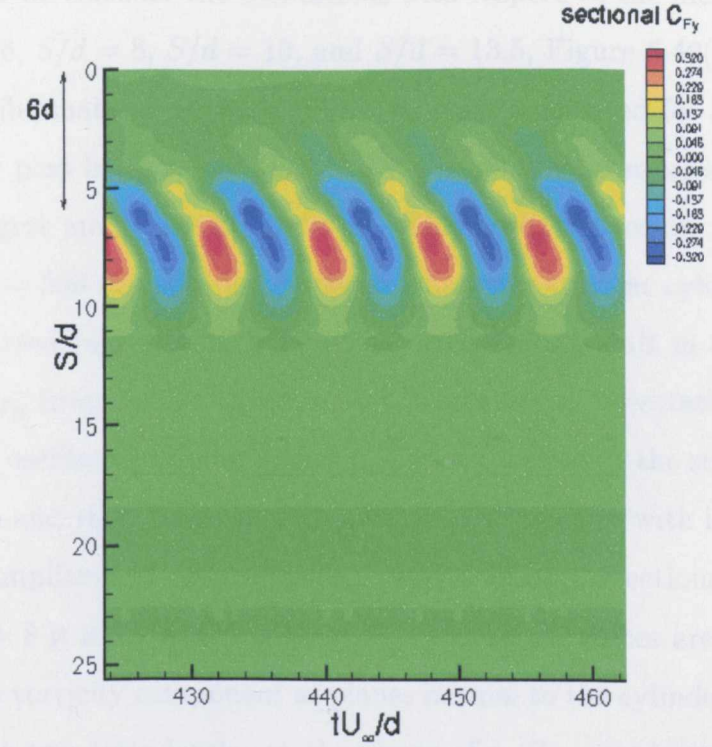
work of Owen and Bearman experiments were performed up to Reynolds numbers of the order of 10^5 and the stabilizing mechanisms were found to persist along with significant reductions in drag (Owen 2001).

5.2.3 Flow past body D with a six-diameter straight cylinder vertical addition

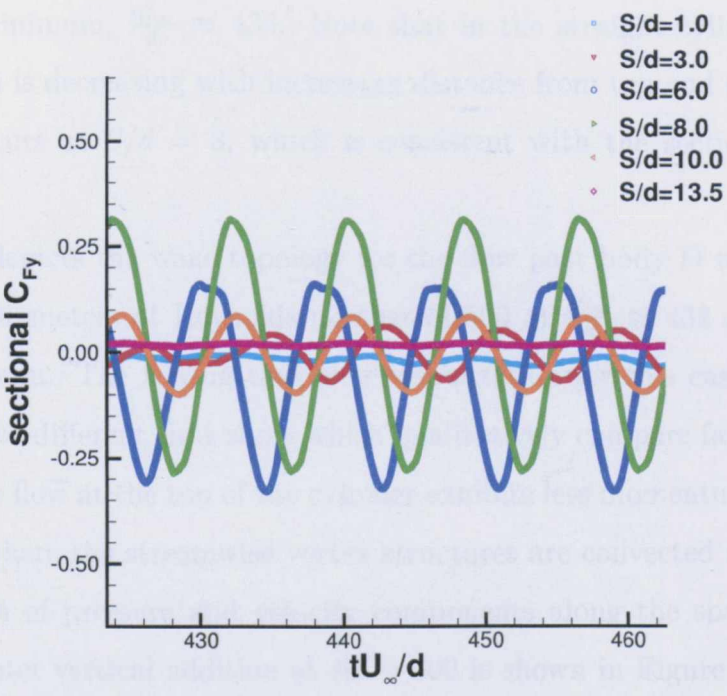
The flow past body D with a straight cylinder extension of six diameters on top was also computed at $Re = 500$.

Figure 5.48 depicts the integrated force coefficients for this case, with x- representing the direction of the drag, y- the horizontal component of the transverse force and z- the vertical one. Non-dimensional time $\frac{tU_\infty}{d} = 200$ represents the transition from $P = 2$ to $P = 4$ whereas $\frac{tU_\infty}{d} \approx 380$ the transition from $P = 4$ to $P = 6$.

In order to determine which part of the body were these fluctuations in integrated C_{Fy} mostly attributed to, the sectional forces for this geometry are shown in Figure 5.49(a). What comes as a surprise therefore, is that it is not the straight cylinder extension on the top of the curved body that is contributing the most to the unsteadiness, but is rather the sections further down along the span.



(a)



(b)

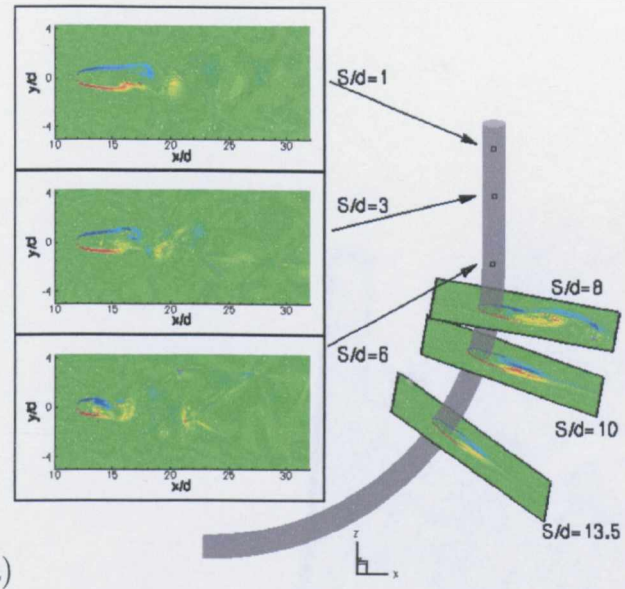
Figure 5.49: (a) Variation of sectional C_{Fy} for body D with a six-diameter straight cylinder extension vertically, $Re = 500$; (b) Variation of C_{Fy} with time at the specified locations of $S/d = 1$, $S/d = 3$, $S/d = 6$, $S/d = 8$, $S/d = 10$, and $S/d = 13.5$

Specifically, if we consider the oscillations with respect to the mean at $S/d = 1$, $S/d = 3$, $S/d = 6$, $S/d = 8$, $S/d = 10$, and $S/d = 13.5$, Figure 5.49(b), we observe that the largest fluctuations in the sectional forces are detected for $S/d = 8$. Note that for the flow past body D at $Re = 500$ the oscillatory component of sectional C_{Fy} had the largest amplitude at $S/d = 2$. Therefore, the results of this section show that at $Re = 500$ the addition of the six-diameter straight cylinder extension on top of the curved body brought about a corresponding shift in the location of the maximum C_{Fy} from $S/d = 2$ to $S/d = 8$. Contrary to expectations hence, the amplitude of the oscillatory component of C_{Fy} is not largest at the straight cylinder extension on top and then starting to decrease monotonically with increasing S/d. At $S/d = 3$ the amplitude of the oscillatory component of the sectional forces is 0.06 whereas at $S/d = 8$ it is 0.3 and finally, by $S/d = 13.5$ the forces are steady.

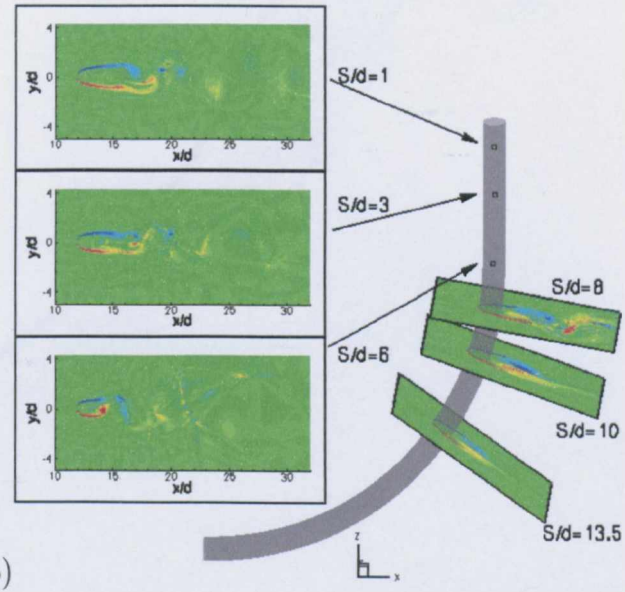
The spanwise vorticity component at planes normal to the cylinder axis is shown in Figure 5.50 at two time levels, at the times of a C_{Fy} maximum, $\frac{tU_\infty}{d} \approx 432$, and of a C_{Fy} minimum, $\frac{tU_\infty}{d} \approx 436$. Note that in the straight cylinder part the formation length is decreasing with increasing distance from top and the maximum unsteadiness occurs at $S/d = 8$, which is consistent with the sectional forces in Figure 5.49.

Figure 5.51 depicts the wake topology for the flow past body D with a vertical addition of six diameters at Reynolds number of 500 at $\frac{tU_\infty}{d} \approx 432$ corresponding to a C_{Fy} maximum. The towing tank flow visualization for this case is shown in Figure 5.52 at two different time shots which qualitatively compare favourably with Figure 5.51. The flow at the top of the cylinder exhibits less momentum than at the sections below where the streamwise vortex structures are convected downstream.

The variation of pressure and velocity components along the span of body D with a six-diameter vertical addition at $Re = 500$ is shown in Figure 5.53. Specifically, Figure 5.53(a) shows the variation of pressure on the stagnation line and base pressure. The variation of u and w velocity components, extracted 0.3 diameters upstream of the curved cylinder, is depicted in Figure 5.53(b). The magnitude of w velocity component is shown to increase until reaching a maximum of 27% of the free-stream value at a section inclined 55.4° from the horizontal ($S/d = 18$).



(a)



(b)

Figure 5.50: Spanwise vorticity contours for body D with a vertical addition of a six-diameter long cylinder, $Re = 500$: (a) $\frac{tU_\infty}{d} \approx 432$, C_{Fy} maximum, (b) $\frac{tU_\infty}{d} \approx 436$, C_{Fy} minimum

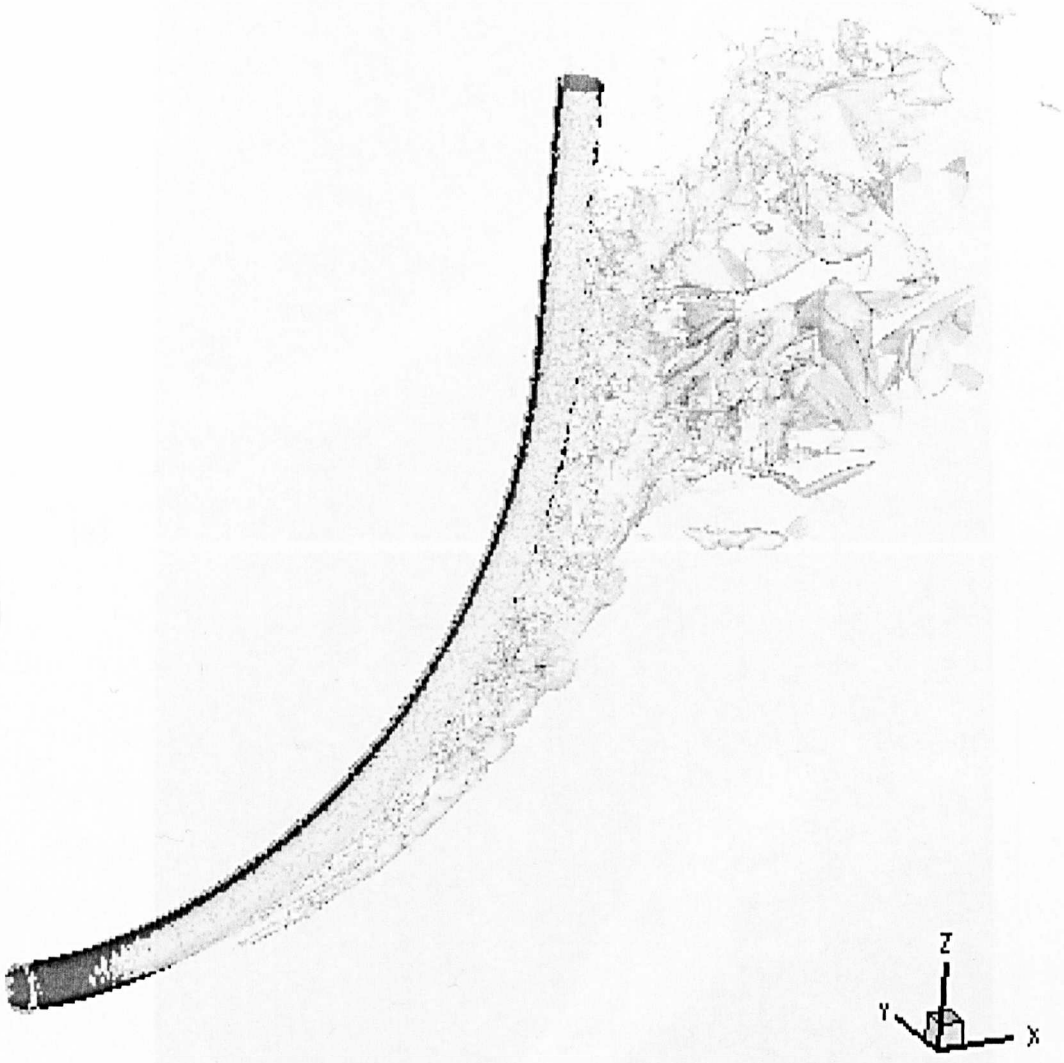
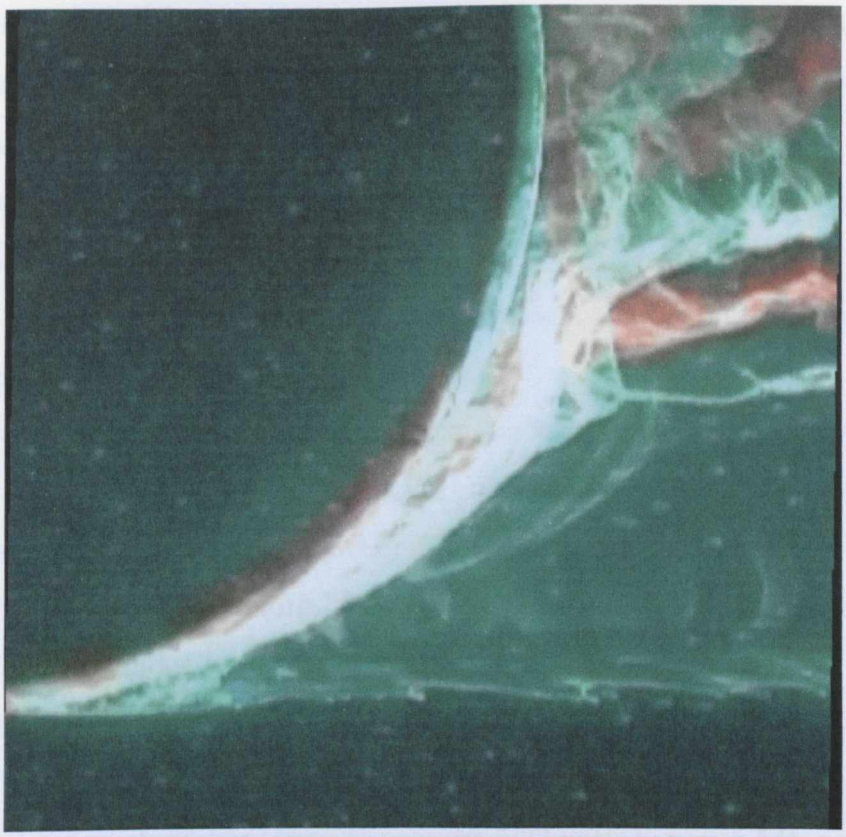


Figure 5.51: Wake topology for body D with a six-diameter straight cylinder extension vertically at $Re = 500$, $\lambda_2 = -0.6$, $\frac{tU_\infty}{d} \approx 432$, C_{Fy} maximum

(a)



(b)

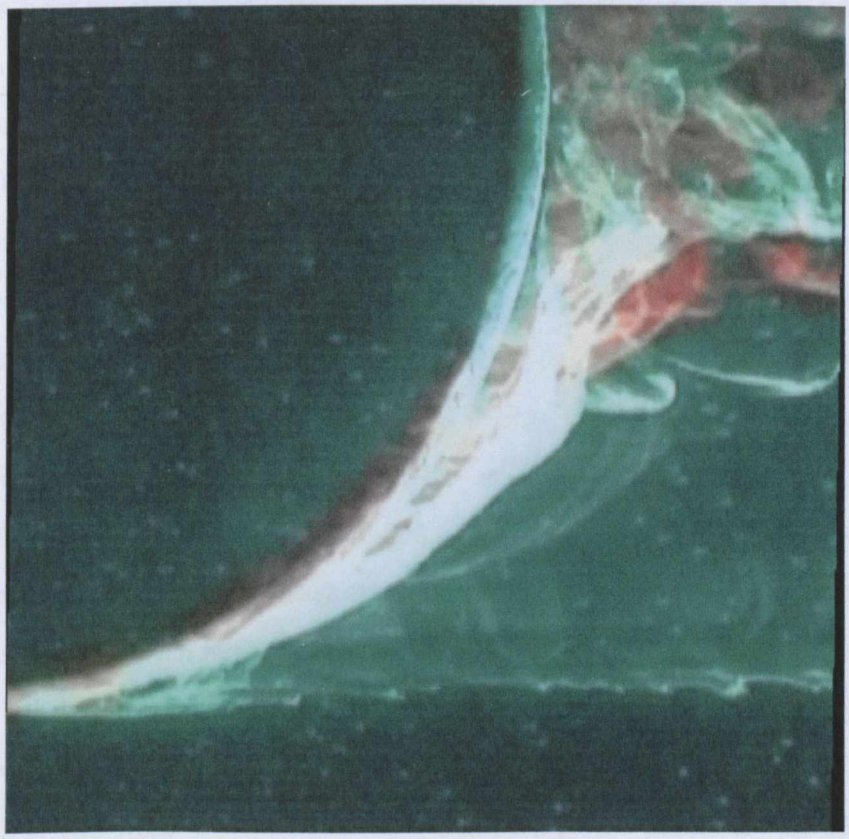


Figure 5.52: Towing tank flow visualization at two different time instants for body D with a vertical addition of 6 diameters, $Re = 500$

Moreover, as Figure 5.53(c) depicts, the magnitude of the w velocity component at a line 0.3 diameters downstream of the body reaches the value of the free-stream at a section inclined 29.9° from the horizontal ($S/d = 12.5$). Furthermore, a value of $1.10U_\infty$ is reached at a section inclined 27.6° ($S/d = 12$) on a line 0.6 diameters downstream and a value of $1.12U_\infty$ at a section inclined 34.5° ($S/d = 13.6$) on a line 1.5 diameters downstream of the curved body. Finally, the computed normal and axial flow components are shown in Figure 5.53(d).

Figure 5.54 shows the production of streamwise vorticity on the body to occur at the curved part of the geometry, reaching a maximum approximately at midspan for this higher Reynolds number also as for Figure 5.33.

The pertinent question therefore is: how is the attenuation of vortex shedding at the top straight cylinder part achieved? As for the flow past the same body at $Re = 100$, a strong w velocity component is present even in the straight cylinder part at the rear of the geometry. The magnitude of the produced streamwise vorticity on the body is now much higher (compare Figure 5.33 with Figure 5.54), and the w velocity components in the wake reach much higher values. The direction of this w velocity component towards the straight cylinder part and the reorientation in the x-direction can be acting as a similar mechanism to base bleed. The streamlines in 3D at the rear of the cylinder are shown in Figure 5.55(a) for part of the cylinder length (and in a zoomed view in Figure 5.55(b)). The complex three-dimensional flow patterns are depicted. Furthermore, recall the longer formation regions encountered at the top of the straight cylinder extension in Figure 5.50 consistent with findings about base bleed in past literature.

Bearman (1967a) investigated the effects of base bleed on the flow past a two-dimensional model with a blunt trailing edge. He found the regular vortex street pattern to break down with sufficiently large bleed quantities. Base bleed is among others one of the ways to weaken the interaction between the two shear layers and stabilize the wake of a bluff body.

We note that the weak form of shedding found for this geometry at $Re = 100$ can be associated with the same mechanism also (recall the long formation regions mentioned for Figure 5.30). At $Re = 500$ though, the increased Reynolds number

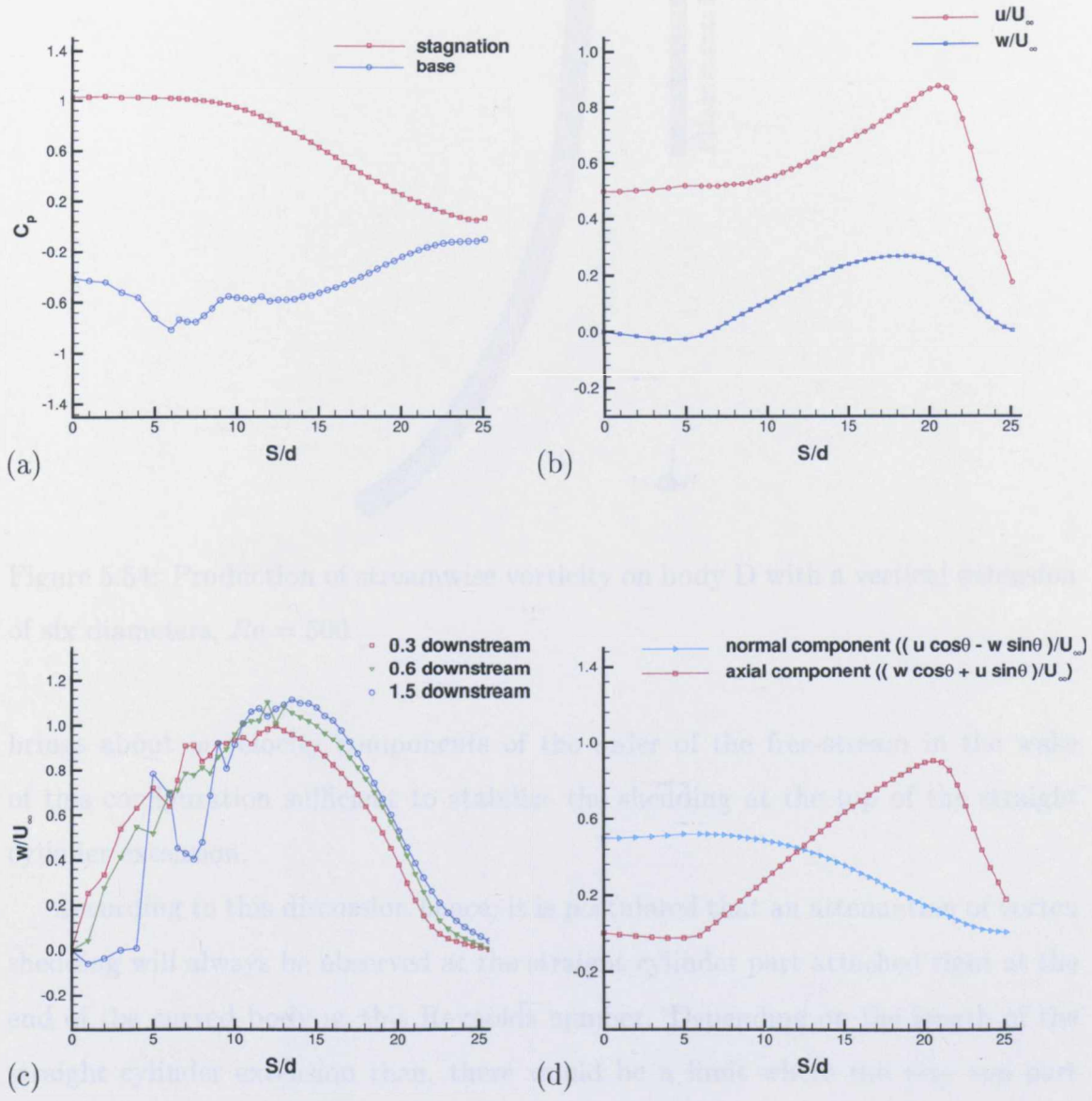


Figure 5.53: Variation of pressure and velocity along the span of body D with a six-diameter straight cylinder extension, $Re = 500$: (a) Base pressure and stagnation pressure, (b) u and w velocity components extracted 0.3 diameters upstream of the curved cylinder, (c) w velocity component extracted 0.3, 0.6 and 1.5 diameters downstream, (d) Normal $((u\cos\theta - w\sin\theta)/U_\infty)$ and axial $((w\cos\theta + u\sin\theta)/U_\infty)$ components computed from the 3D simulation 0.3 diameters upstream of the curved cylinder

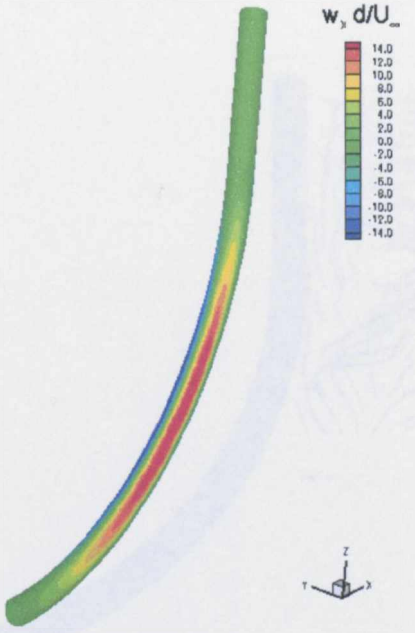


Figure 5.54: Production of streamwise vorticity on body D with a vertical extension of six diameters, $Re = 500$

brings about w velocity components of the order of the free-stream in the wake of this configuration sufficient to stabilize the shedding at the top of the straight cylinder extension.

According to this discussion hence, it is postulated that an attenuation of vortex shedding will always be observed at the straight cylinder part attached right at the end of the curved body at this Reynolds number. Depending on the length of the straight cylinder extension then, there would be a limit where the very top part of the cylinder would start to shed, followed by a part of the straight cylinder not shedding as the axial flow originating from the curved part of the body would disrupt the conventional shedding process and stabilize the wake. A schematic diagram of the different regimes expected in the wake of body D with a long straight cylinder extension on top at this Reynolds number is shown in Figure 5.56.

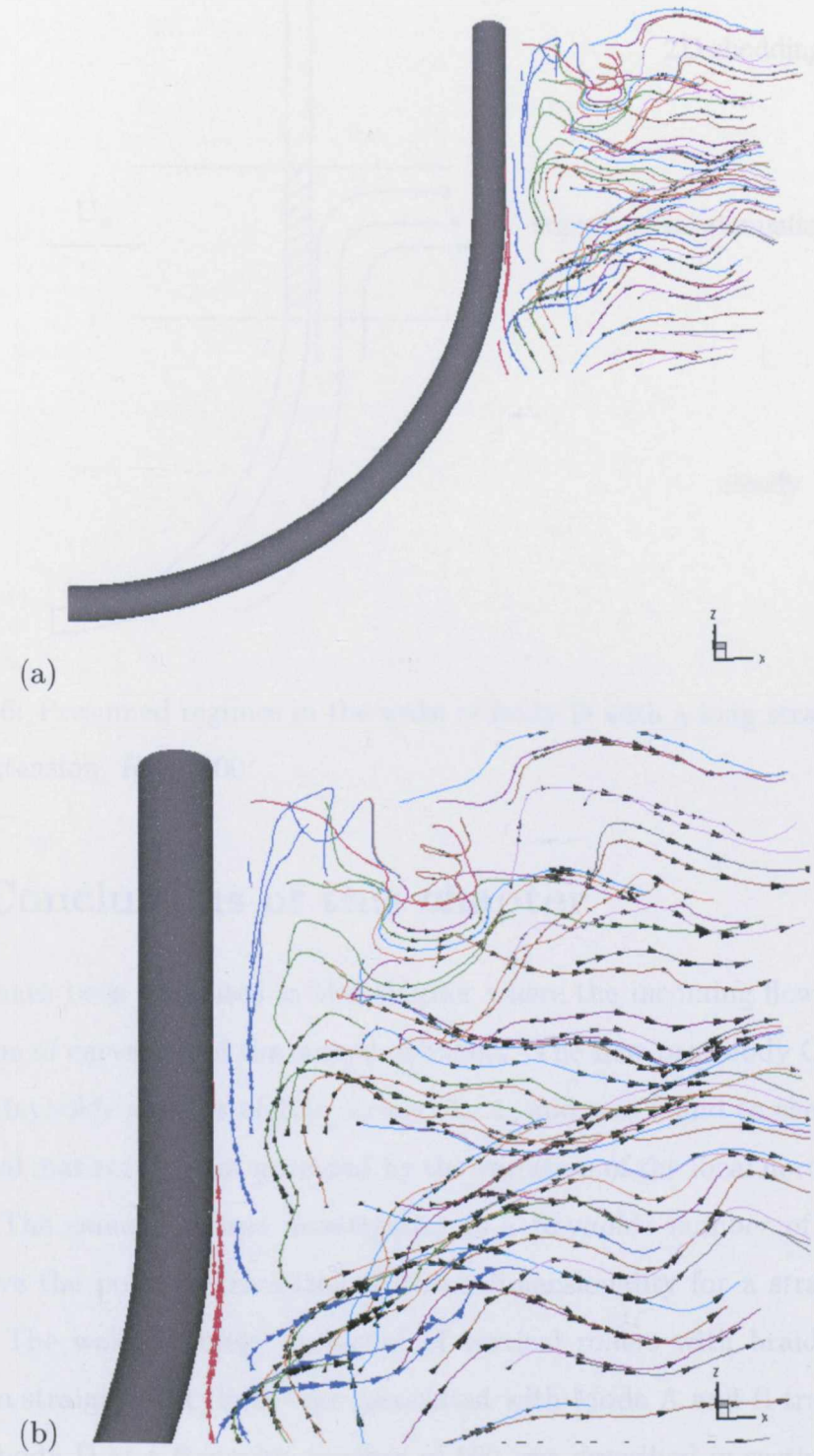


Figure 5.55: (a) Streamlines in 3D at the rear of body D with a vertical extension of six diameters, $Re = 500$, (b) Enlarged view

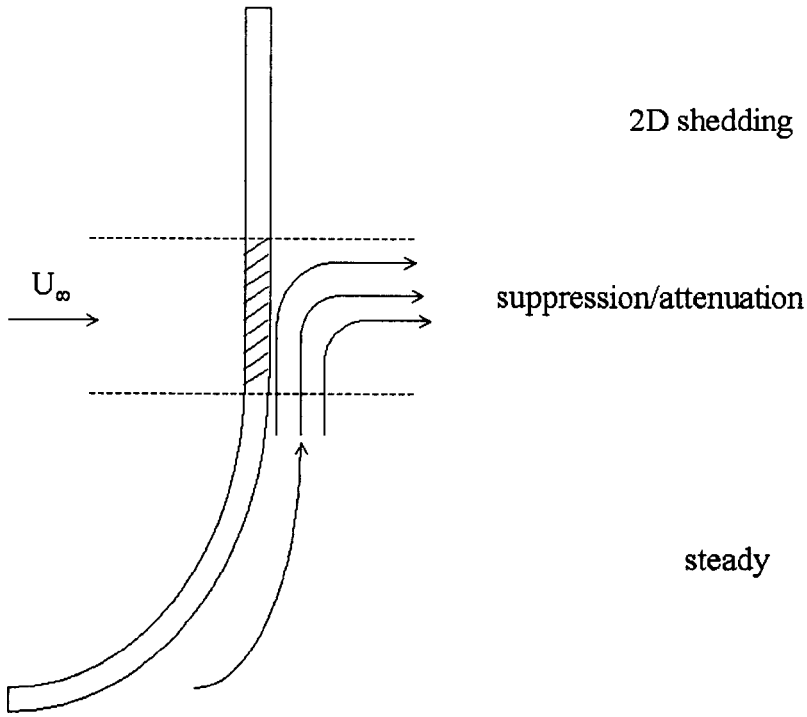


Figure 5.56: Presumed regimes in the wake of body D with a long straight cylinder vertical extension, $Re = 500$

5.3 Conclusions of this chapter

Six cases have been presented in this chapter where the incoming flow was parallel to the plane of curvature of the curved cylinders. The flow past body C was studied first at a Reynolds number of 100, section 5.1.1, and was found to shed in a three-dimensional manner and not governed by the variation of the local normal Reynolds number. The same case was investigated at a Reynolds number of 500, section 5.2.1, above the point of transition to three-dimensionality for a straight circular cylinder. The wake topology consisted of vertical rollers with braids inbetween, which for a straight 2D cylinder are associated with Mode A and B transition. The flow past body D at a Reynolds number of 100 was described in section 5.1.2. The axial flow being directed towards the top computational plane and the production of streamwise vorticity were found to result in the suppression of vortex shedding. Table 5.5 summarizes the location and the magnitude of the maximum w velocity component upstream and downstream of the body for the different cases. The

	upstream(0.3d)	downstream(1.5d)
body C, $Re = 100$	$0.36U_\infty$ at 48.3°	
body D, $Re = 100$	$0.28U_\infty$ at 48.3°	$0.66U_\infty$ at 32.2°
body D with 6 diameters, $Re = 100$	$0.28U_\infty$ at 48.3°	$0.69U_\infty$ at 29.9°
body C, $Re = 500$	$0.33U_\infty$ at 55.4°	
body D, $Re = 500$	$0.26U_\infty$ at 57.7°	$1.13U_\infty$ at 32.2°
body D with 6 diameters, $Re = 500$	$0.27U_\infty$ at 55.4°	$1.12U_\infty$ at 34.5°

Table 5.5: Location and magnitude of the maximum w velocity component upstream and downstream of the curved bodies for the different cases

same case was computed at Reynolds number of 500 where the conventional vortex shedding features were still absent even though unsteadiness was encountered at the top of the geometry. To investigate the effect of the top computational boundary and the extent to which the stabilizing mechanism for the flow past body D persists even with a straight cylinder addition on top, the flow past body D with a six-diameter straight cylinder extension was studied first at a Reynolds number of 100 (section 5.1.3) and then at $Re = 500$ (section 5.2.3). At a Reynolds number of 100 a weak form of shedding was encountered at the top of the geometry with the vortices not fully detaching from the corresponding shear layers. The novelty in the flow patterns past the geometry with the six-diameter straight cylinder addition was related to the location of the unsteadiness at $Re = 500$. Rather than this configuration shedding at the top of the geometry at the straight cylinder part, unsteadiness was detected at the top of the curved part, at the same location respectively as for the flow past body D at $Re = 500$. It is believed that the feeding of the strong axial flow, which originates from the curved part of the body, into the wake of the straight cylinder part acts as a similar mechanism to base bleed and hence stabilizes the wake of the straight cylinder extension. As part of further work, it would be of great interest to perform a study on gradually increasing the length of the straight cylinder addition in order to investigate the threshold where the very top of the straight cylinder

would start to shed following the drawing in Figure 5.56.

Furthermore, the computational results were in qualitative agreement with experimental flow visualizations obtained with the laser induced fluorescence technique for a model cylinder towed in a water tank.

It should be emphasized that in none of the cases where the flow is directed on the inside of the bend was there a conventional shedding pattern observed. Moreover, the results for all the cases of this chapter have highlighted the importance of approaching the curved cylinder problem with a fully three-dimensional rather than with a 2D sectional method.

Chapter 6

Conclusions and further work

6.1 Conclusions

Three-dimensional computations of the flow past curved cylinders at Reynolds numbers of 100 and 500 have been performed with $\mathcal{N}\varepsilon\kappa\mathcal{T}\alpha r$, a Navier-Stokes algorithm based on the spectral/*hp* element method. Different body configurations were investigated, all built on the basic shape of a quarter ring geometry with a non-dimensional radius of curvature of 12.5. The first part of this study consisted of computations where the flow was normal to the plane of curvature, whereas the second part comprised computations where the flow was parallel to the plane of curvature.

6.1.1 Flow normal to the plane of curvature

Starting from a quarter of the ring geometry, to represent a generic shape of a curved cylinder, different cases were built up aiming to investigate the effects of curvature, of a sheared velocity profile and of a wall boundary. The axisymmetric geometry of the quarter ring, body A, under a uniform velocity profile in the normal direction constitutes a quasi two-dimensional case at $Re = 100$. Indeed, in-phase shedding along the span was detected from the three-dimensional computations while vortex rings were found to be shed periodically in the wake of this geometry. At a Reynolds number of 100, the straight circular cylinder would also be expected to shed in-phase

suggesting that a two-dimensional sectional approach might still be suitable for these flow conditions. However, the effect of curvature in introducing unequal strengths between the inner and outer vortices, for example, would not be accounted for by such a two-dimensional method unless the difference in circulation shed each way of the wake centreline were negligible.

A second geometry was then considered with a marine industry motivation, where a deformed curved cylinder ended semi-buried in the ground (body B). This geometry was studied under a combination of different boundary conditions including a no-slip or a slip wall, and a sheared or a uniform velocity profile. The effect of the shear profile was found to be dominant compared to that of the wall boundary. As long as a sheared velocity profile was applied (in this case an exponentially decaying shear profile was chosen), lack of correlation was observed along the span of the body with strongly three-dimensional wake topology. A modulation frequency was established in the transverse force and linking was observed in the vortex structures. Vortex dislocations are similarly expected in the wake of straight circular cylinders under shear. Once a uniform profile was applied, even for this deformed curved cylinder geometry, the vortex cores were no longer inclined to the cylinder axis and the sectional forces demonstrated correlated shedding along the major part of the cylinder span. Note that a weakening of the strength of the vortices was observed as the wall boundary was approached, depicted also in the variation of sectional forcing along the cylinder length. The more complex 3D wake dynamics were thus indeed attributed primarily to the sheared profile rather than to the wall boundary. Finally, at a higher Reynolds number of 500, the intrinsic three-dimensionalities had developed in the wake of the quarter ring geometry; vortex structures similar to those of Mode A/B transition for the straight circular cylinder were found along with intermittent fluctuations and no regularity in the sectional forces.

Overall, therefore, this first part of the study, where the flow was normal to the plane of curvature, has shown a qualitative behaviour in general similar to that expected for a straight two-dimensional cylinder. The three-dimensional computations have still proven insightful in capturing the three-dimensional vortex shedding features, something that, as should be emphasized, a two-dimensional sectional method

could not allow for.

6.1.2 Flow parallel to the plane of curvature

The focus was then placed on computations where the upstream flow was parallel to the plane of curvature. These cases are of fundamental interest as the free-stream velocity vector is not included in each cross-sectional plane, hence highlighting the potential shortcomings of a sectional method and the benefits of a fully three-dimensional approach. A uniform velocity profile was specified in all the cases of this set, but different configurations were investigated in terms of whether the upstream flow was directed onto the outside (body C) or the inside (body D) of the bend.

Shedding was found to be out of phase along the span of body C with a spanwise variation of the wake features. Axial flow (flow along the length of the cylinder) was observed, directed towards the bottom of the geometry. No frequency variation was shown to occur along the span as the flow responds in a three-dimensional manner, with the upper cylinder shedding driving the lower end. A sectional two-dimensional argument, however, would predict variation of the local normal Reynolds number which would hence result in variation of the Strouhal frequency along the span of body C. For body D, however, no antisymmetric shedding features were detected. The integrated forces were steady and the magnitude of the drag force coefficient was smaller by 12% compared to that for body C. Axial flow was observed for this case also, but was now directed towards the top computational plane. Symmetric wakes were shown for 2D planes extracted at different spanwise locations and a variation of the wake width was observed along the span. Similarities were drawn with the wakes of wavy cylinders (sinusoidal deformation on the stagnation face). Moreover, the wake topology showed the shear layers not interacting. To examine the effect of the top computational plane and investigate the extent to which the steady features in the wake of body D would persist, a straight cylinder extension of six diameters (almost 50% of the curved geometry's height) was added on top of body D. Weak periodic fluctuations, originating from the straight cylinder part,

were observed in the horizontal component of the transverse force at a frequency smaller than that for body C by approximately 36%. The rms of the fluctuating component of C_{Fy} was equal to 0.0011 compared to a corresponding value of 0.0491 for body C. The drag coefficient exhibited an increase of 3% compared to that for body D, still corresponding to a drag reduction of 9% from that for body C. Longer formation regions were shown at planes in the straight cylinder part corresponding to the weak periodic fluctuations in the horizontal component of the transverse force. Overall, the vertical addition of a straight cylinder extension did not affect the steady wake features of body D. Interestingly to note, the magnitude of the w velocity component 0.3 diameters upstream of the curved body reached a maximum at a section inclined approximately 48.3° from the horizontal for all three cases (body C, body D, and body D with a vertical addition of six diameters), hence suggesting a strong influence of the geometry. Furthermore, maximum w velocity components in the order of 66% to 69% of the free-stream were detected in the wake for both body D and body D with a straight cylinder extension. Note that for the latter geometry, a w component equal to 20% of the free-stream value was present in the straight cylinder part associated with the longer formation regions and the weakening of the vortex shedding process. Overall, therefore, these cases have demonstrated that:

- the direction of the flow towards the top of the geometry, which would normally account for regular periodic vortex shedding, and the production of streamwise vorticity play a key role in stabilizing the wakes of bodies having the free-stream aligned on the inside of the bend; the variation of the wake width is associated with this suppression mechanism.

- the addition of a six-diameter long straight cylinder on top of the curved geometry did not destabilize the steady wake features of the curved part; on the contrary, it was the curved part that weakened the strong 2D shedding expected from a straight cylinder at a Reynolds number of 100.

All these three cases were then computed at a higher Reynolds number of 500 to examine the effects of introducing three-dimensional instability in the wake, according to the straight cylinder behaviour. Vortex shedding became more vigorous

even at lower angles to the bottom for body C at $Re = 500$ with the intrinsic three-dimensionalities becoming apparent. Streamwise vorticity, through braids, was shown to connect the spanwise rollers in the wake of this geometry. The steady wake features for body D persisted even at this higher Reynolds number; slight unsteadiness was observed at the top of the geometry (the oscillatory component of sectional C_{Fy} had the largest amplitude at a non-dimensional arc length of $S/d = 2$) while the conventional vortex shedding features were absent in the main part of the body. When the straight cylinder extension was added at the top of body D, no vigorous vortex shedding was observed. Fluctuations were exhibited in the integrated C_{Fy}; however, the sectional forces demonstrated that rather than the straight cylinder top, it was the sections further down along the span that contributed the most to the unsteadiness. Note that the largest fluctuations in the sectional forces were now detected at $S/d = 8$, corresponding to a shift by six diameters. Consistently, the formation length was shown to decrease with increasing distance from the top and the maximum unsteadiness also occurred at $S/d = 8$. In the wake of both body D and body D with a vertical extension, w velocity components of the order of the free-stream were detected at $Re = 500$. A new feature which has become apparent from these results is the fact that the flow at the top of the cylinder, expected to be the more energetic part following the canonical case of a straight 2D cylinder especially at $Re = 500$, was shown to exhibit less momentum than the sections below. Similarities to a base bleed mechanism, consistent with the longer formation lengths, where the axial flow originated in the curved part is feeding the straight cylinder part and disrupting its shedding process were considered.

Finally, experimental flow visualization work was conducted in the towing tank facilities of the Department of Aeronautics in order to compare and validate the computational findings. A laser induced fluorescence technique was employed on a model curved cylinder of the same non-dimensional radius of curvature. The flow visualization images of the wake patterns formed by the diffusion of the dye, that was originally adhered to the stagnation line of the curved cylinder, have shown close qualitative agreement with the wake topologies extracted from the corresponding computations.

The results for all the cases of this set of computations have illustrated the necessity of approaching the curved cylinder problem with a fully three-dimensional method compared to the limitations of a sectional approach. Even for body C which was found to shed regularly, a two-dimensional approach would not have predicted the body's adapting at just one frequency along the span. More importantly though, the unforeseen results for body D, with and without the straight cylinder extension, have highlighted the three-dimensional nature of this flow. While the sectional methods would predict shedding at least at large regions of these geometries, no conventional shedding was detected in any of these cases. The axial flow component was found to be the key factor in stabilizing these flows and this is exactly the component that is not modelled by the two-dimensional methods. Overall, therefore, the greater challenge posed by employing the fully three-dimensional version of *NεκTαr*, in what constituted the first extensive study of a bluff body flow past a 3D geometry, compared to the Fourier version of the code previously applied to 3D flows past 2D geometries, has been substantiated.

6.2 Further work

Given the findings of this study, a number of suggestions can be placed for future investigations.

In the normal flow direction, different shear profiles could be investigated, including the standard one of a linear shear profile, although it is envisaged that qualitatively no radical effects will probably be observed. In the parallel flow direction, however, a further investigation on gradually increasing the length of the straight cylinder extension for the flow described in section 5.1.3 would be of paramount importance. It is expected that by doing so, a threshold will be reached whereby the top of the straight cylinder extension would start to shed in accordance to the presumed regimes of Figure 5.56. Furthermore, a stability analysis on 2D planes normal to the cylinder axis for the flows past body D and body D with a straight cylinder extension would provide additional insight into the stabilizing mechanisms observed in the wakes of these configurations.

In addition, different curvatures and higher Reynolds numbers can be investigated as part of a further study. This work has constituted a fundamental study of the vortex shedding mechanisms of curved cylinders and the first of its kind with a fully three-dimensional approach; hence relatively low Reynolds numbers were chosen to make the problem more tractable. Now that the different wake patterns developed for the various cases have been established, investigating the effect of increasing the Reynolds number, especially on the wakes of body D and body D with the straight cylinder extension, could complement this study.

Furthermore, changing direction from a fundamental study to the offshore applications, a number of recommendations for further work could be put forward in relevance to the marine industry motivation. Forced oscillations (fixed mesh) would be the first step in building up on the stationary curved cylinder findings. Whether the steady wake features for body D would persist at higher Reynolds numbers and under forced oscillations would be of great interest to investigate. Moreover, sinusoidal cylinder motions prescribed along the cylinder axis could be studied with an ALE (Arbitrary-Lagrangian-Eulerian) formulation in what would be a much closer representation of the actual marine problem with the riser pipe touching the ground. This would constitute potentially the final stage of this work with quite a severe computational expense and challenge however. Comparisons with real field data from offshore industries could then be drawn. To complete the actual marine problem, an investigation of the effect of the horizontal part of the pipe lying in a trenched ground, for example, could be conducted with the Fourier version of *NεκTar* alongside the previous studies.

Bibliography

Barkley, D. & Henderson, R. D. (1996). Three-dimensional Floquet stability analysis of the wake of a circular cylinder. *Journal of Fluid Mechanics 322*, 215–241.

Barkley, D., Tuckerman, L. S., & Golubitsky, M. (2000). Bifurcation theory for three-dimensional flow in the wake of a circular cylinder. *Physical Review E 61*, 5247–5252.

Bearman, P. W. (1967a). The effect of base bleed on the flow behind a two-dimensional model with a blunt trailing edge. *The Aeronautical Quarterly 18*, 207–224.

Bearman, P. W. (1967b). On vortex street wakes. *Journal of Fluid Mechanics 28*, 625–641.

Bearman, P. W. (1997). Near wake flows behind two- and three-dimensional bluff bodies. *Journal of Wind Engineering and Industrial Aerodynamics 69-71*, 33–54.

Bearman, P. W. (1998). Developments in the understanding of bluff body flows. *JMSE International Journal Vol.41*, Series B, No.1.

Bearman, P. W. & Owen, J. C. (1998a). Special Brief Note: Reduction of bluff-body drag and suppression of vortex shedding by the introduction of wavy separation lines. *Journal of Fluids and Structures 12*, 123–130.

Bearman, P. W. & Owen, J. C. (1998b). Suppressing vortex shedding from bluff bodies by the introduction of wavy separation lines. In *1998 Conference on Bluff Body Wakes and Vortex-Induced Vibration, ASME Fluids Engineering Division (Annual Summer Meeting), Washington, D.C.*

Bearman, P. W. & Takamoto, M. (1988). Vortex shedding behind rings and discs. *Fluid Dynamics Research 3*, 214–218.

Bearman, P. W. & Zdravkovich, M. M. (1978). Flow around a circular cylinder near a plane boundary. *Journal of Fluid Mechanics 89*, 33–47.

Berger, E. & Wille, R. (1972). Periodic flow phenomena. *Annual Review of Fluid Mechanics 4*, 313–340.

Brede, M., Eckelmann, H., & Rockwell, D. (1996). On secondary vortices in the cylinder wake. *Physics of Fluids 8*, 2117–2124.

Creusé, E. & Mortazavi, I. (2001). Vortex dynamics over a dihedral plane in a transitional slightly compressible flow: a computational study. *European Journal of Mechanics-B/Fluids 20*, 603–626.

Darekar, R. M. (2001). *Drag Reduction on Bluff Bodies by the Introduction of a Wavy Stagnation Face.* Ph. D. thesis, University of London.

Darekar, R. M. & Sherwin, S. J. (2001a). Flow past a bluff body with a wavy stagnation face. *Journal of Fluids and Structures 15*, 587–596.

Darekar, R. M. & Sherwin, S. J. (2001b). Flow past a square-section cylinder with a wavy stagnation face. *Journal of Fluid Mechanics 426*, 263–295.

Eisenlohr, H. & Eckelmann, H. (1989). Vortex splitting and its consequences in the vortex street wake of cylinders at low Reynolds number. *Physics of Fluids A1*, 189–192.

Gaster, M. (1969). Vortex shedding from slender cones at low Reynolds numbers. *Journal of Fluid Mechanics 38*, 565–576.

Gaster, M. (1971). Vortex shedding from circular cylinders at low Reynolds numbers. *Journal of Fluid Mechanics 46*, 749–756.

Gerich, D. & Eckelmann, H. (1982). Influence of end plates and free ends on the shedding frequency of circular cylinders. *Journal of Fluid Mechanics 122*, 109–121.

Gerrard, J. H. (1966). The mechanics of the formation region of vortices behind bluff bodies. *Journal of Fluid Mechanics 25*, 401–413.

Graham, J. M. R. (1992). Comparing computation of flow past circular cylinders with experimental data. In *IUTAM Symposium Bluff-Body Wakes, Dynamics and Instabilities*, pp. 317–323. Springer-Verlag.

Griffin, O. M. (1985). Vortex shedding from bluff bodies in a shear flow: A review. *ASME Journal of Fluids Engineering 107*, 298–306.

Hammache, M. & Gharib, M. (1989). A novel method to promote parallel vortex shedding in the wake of circular cylinders. *Physics of Fluids A1*, 1611–1614.

Hammache, M. & Gharib, M. (1991). An experimental study of the parallel and oblique vortex shedding from circular cylinders. *Journal of Fluid Mechanics 232*, 567–590.

Hansen, E. A., Mayer, S., Bryndum, M. B., Sortland, L., Verley, R., & Nes, H. (1999). Numerical modelling of pipeline free span vibrations. In T. Kvamsdal, I. Enevoldsen, K. Herfjord, C. Jenssen, K. Mehr, & S. P. Norsett (Eds.), *Computational Methods for Fluid-Structure Interaction*, pp. 325–336. TAPIR Publishers.

Henderson, R. D. (1994). *Unstructured Spectral Element Methods: Parallel Algorithms and Simulations.* Ph. D. thesis, Princeton University.

Henderson, R. D. (1995). Details of the drag curve near the onset of vortex shedding. *Physics of Fluids 7*, 2102–2104.

Henderson, R. D. (1998). Turbulent wake transition. In *1998 Conference on Bluff Body Wakes and Vortex-Induced Vibration, ASME Fluids Engineering Division (Annual Summer Meeting), Washington, D.C.*

Henderson, R. D. & Barkley, D. (1996). Secondary instability in the wake of a circular cylinder. *Physics of Fluids 8*, 1683–1685.

Huse, E. & Kleiven, G. (2000). Impulse and energy in deepsea riser collisions owing to wake interference. In *2000 Offshore Technology Conference, Houston, Texas.*

Jensen, B. L., Sumer, B. M., Jensen, H. R., & Fredsoe, J. (1990). Flow around and forces on a pipeline near a scoured bed in steady current. *ASME Journal of Offshore Mechanics and Arctic Engineering 112*, 206–213.

Jeong, J. & Hussain, F. (1995). On the identification of a vortex. *Journal of Fluid Mechanics 285*, 69–94.

Karniadakis, G. E., Israeli, M., & Orszag, S. A. (1991). High-order splitting methods for the incompressible Navier-Stokes equations. *Journal of Computational Physics 97*, 414–443.

Karniadakis, G. E. & Sherwin, S. J. (1999). *Spectral/hp Element Methods for CFD.* Oxford University Press.

Karniadakis, G. E. & Triantafyllou, G. S. (1992). Three-dimensional dynamics and transition to turbulence in the wake of bluff objects. *Journal of Fluid Mechanics 238*, 1–30.

König, M., Eisenlohr, H., & Eckelmann, H. (1990). The fine structure in the Strouhal-Reynolds number relationship of the laminar wake of a circular cylinder. *Physics of Fluids A2*, 1607–1614.

Lam, K., Wang, F. H., & So, R. M. C. (2002). Three-dimensional vortices in the near wake of a wavy cylinder. In *Conference on Bluff Body Wakes and Vortex-Induced Vibrations (BBVIV3)*, pp. 125–128.

Larsen, C. M. (2000). Empirical VIV models. In *Workshop on Vortex-Induced Vibrations of Offshore Structures*, pp. 22–27.

Lear, C. J. (2003). *Controlling the Break-Up distance of Aircraft Trailing Vortices.* Ph. D. thesis, University of London.

Leweke, T. (1994). *Étude expérimentale et modélisation du sillage d'un tore à bas nombre de Reynolds.* Ph. D. thesis, Université de Provence (Aix-Marseille I).

Leweke, T. & Provansal, M. (1995). The flow behind rings: bluff body wakes without end effects. *Journal of Fluid Mechanics 288*, 265–310.

Leweke, T., Provansal, M., & Boyer, L. (1993). Stability of vortex shedding modes in the wake of a ring at low Reynolds numbers. *Physical Review Letters 71*, 3469–3473.

Lucor, D. & Karniadakis, G. E. (2002). Effects of oblique inflow in vortex-induced vibrations. In *IUTAM Symposium Unsteady Separated Flows.*

Mair, W. A. & Stansby, P. K. (1975). Vortex wakes of bluff cylinders in shear flow. *SIAM Journal of Applied Mathematics 28*, 519–540.

Maull, D. J. & Young, R. A. (1973). Vortex shedding from bluff bodies in a shear flow. *Journal of Fluid Mechanics 60*, 401–409.

Miller, G. D. & Williamson, C. H. K. (1994). Control of three-dimensional phase dynamics in a cylinder wake. *Experiments in Fluids 18*, 26–35.

Mukhopadhyay, A., Venugopal, P., & Vanka, S. P. (1999). Numerical study of vortex shedding from a circular cylinder in linear shear flow. *ASME Journal of Fluids Engineering 121*, 460–468.

Mukhopadhyay, A., Venugopal, P., & Vanka, S. P. (2002). Oblique vortex shedding from a circular cylinder in linear shear flow. *Computers and Fluids 31*, 1–24.

Noack, B. R., König, M., & Eckelmann, H. (1993). Three-dimensional stability analysis of the periodic flow around a circular cylinder. *Physics of Fluids A 5*, 1279–1281.

Norberg, C. (1994). An experimental investigation of the flow around a circular cylinder: influence of aspect ratio. *Journal of Fluid Mechanics 258*, 287–316.

Norberg, C. (2003). Fluctuating lift on a circular cylinder: review and new measurements. *Journal of Fluids and Structures 17*, 57–96.

Owen, J. C. (2001). *Passive Control of Vortex Shedding in the Wakes of Bluff Bodies.* Ph. D. thesis, University of London.

Peiró, J., Peraire, J., & Morgan, K. (1994). *Felisa Manual.* Department of Aeronautics, Imperial College of Science, Technology and Medicine.

Peiró, J. & Sayma, A. I. (1995). A 3-D unstructured multigrid Navier-Stokes solver. In K. W. Morton & M. J. Baines (Eds.), *Numerical Methods for Fluid Dynamics, V.* Oxford University Press.

Peraire, J., Peiró, J., & Morgan, K. (1993). Multigrid solution of the 3-D compressible Euler equations on unstructured tetrahedral grids. *International Journal for Numerical Methods in Engineering 36*, 1029–1044.

Piccirillo, P. S. & Van Atta, C. W. (1993). An experimental study of vortex shedding behind linearly tapered cylinders at low Reynolds number. *Journal of Fluid Mechanics 246*, 163–195.

Posdziech, O. & Grundmann, R. (2001). Numerical simulation of the flow around an infinitely long circular cylinder in the transition regime. *Theoretical and Computational Fluid Dynamics 15*, 121–141.

Prasad, A. & Williamson, C. H. K. (1997). Three-dimensional effects in turbulent bluff-body wakes. *Journal of Fluid Mechanics 343*, 235–265.

Ramberg, J. (1983). The effects of yaw and finite length upon the vortex wakes of stationary and vibrating circular cylinders. *Journal of Fluid Mechanics 128*, 81–107.

Roshko, A. (1955). On the wake and drag of bluff bodies. *Journal of the Aeronautical Sciences 124*, 124–132.

Roshko, A. (1993). Perspectives on bluff body aerodynamics. *Journal of Wind Engineering and Industrial Aerodynamics 49*, 79–100.

Sherwin, S. J. (1995). *Triangular and Tetrahedral Spectral/hp Finite Element Methods for Fluid Dynamics.* Ph. D. thesis, Princeton University.

Sherwin, S. J. (2002). A substepping Navier-Stokes splitting scheme for spectral/hp element discretisations. In *Parallel Computational Fluid Dynamics (PCFD).*

Sherwin, S. J. & Casarin, M. (2001). Low-energy basis preconditioning for elliptic substructured solvers based on unstructured spectral/*hp* element discretizations. *Journal of Computational Physics 171*, 394–417.

Sherwin, S. J. & Karniadakis, G. E. (1995). A triangular spectral element method: applications to the incompressible Navier-Stokes equations. *Computer Methods in Applied Mechanics and Engineering 123*, 189–229.

Sherwin, S. J. & Karniadakis, G. E. (1996). Tetrahedral *hp* finite elements: Algorithms and flow solutions. *Journal of Computational Physics 124*, 14–45.

Slaouti, A. & Gerrard, J. H. (1981). An experimental investigation of the end effects on the wake of a circular cylinder towed through water at low Reynolds numbers. *Journal of Fluid Mechanics 112*, 297–314.

Sumer, B. M. & Fredsoe, J. (1999). *Hydrodynamics around Cylindrical Structures.* Advanced Series on Ocean Engineering-Volume 12, World Scientific.

Szabo, B. & Babuska, I. (1991). *Finite Element Analysis.* Wiley.

Szepessy, S. & Bearman, P. W. (1992). Aspect ratio and end plate effects on vortex shedding from a circular cylinder. *Journal of Fluid Mechanics 234*, 191–217.

Takamoto, M. & Izumi, K. (1981). Experimental observation of stable arrangement of vortex rings. *Physics of Fluids 24*, 1582–1583.

Thompson, M. C., Hourigan, K., & Sheridan, J. (1995). Three-dimensional mode development in low Reynolds number flow over a cylinder. In *Australasian Fluid Mechanics Conference, Sydney, Australia.*

Thompson, M. C., Hourigan, K., & Sheridan, J. (1996). Three-dimensional instabilities in the wake of a circular cylinder. *Experimental Thermal and Fluid Science 12*, 190–196.

Thomson, K. D. & Morrison, D. F. (1971). The spacing, position and strength of vortices in the wake of slender cylindrical bodies at large incidence. *Journal of Fluid Mechanics 50*, 751–783.

Tombazis, N. & Bearman, P. W. (1997). A study of three-dimensional aspects of vortex shedding from a bluff body with a mild geometric disturbace. *Journal of Fluid Mechanics 330*, 85–112.

Tritton, D. J. (1959). Experiments on the flow past a circular cylinder at low Reynolds numbers. *Journal of Fluid Mechanics 6*, 547–567.

Van Atta, C. W. (1968). Experiments on vortex shedding from yawed circular cylinders. *AIAA Journal 6*, 931–933.

Warburton, T. C. (1998). *Spectral/hp Methods on Polymorphic Multi-Domains: Algorithms and Applications.* Ph. D. thesis, Brown University.

Weiss, J. (1991). The dynamics of enstrophy transfer in two-dimensional hydrodynamics. *Physica D 48*, 273–294.

Williamson, C. H. K. (1988). The existence of two stages in the transition to three-dimensionality of a cylinder wake. *Physics of Fluids 31*, 3165–3168.

Williamson, C. H. K. (1989). Oblique and parallel modes of vortex shedding in the wake of a circular cylinder at low Reynolds numbers. *Journal of Fluid Mechanics 206*, 579–627.

Williamson, C. H. K. (1992a). The natural and forced formation of spot-like 'vortex dislocations' in the transition of a wake. *Journal of Fluid Mechanics 243*, 393–441.

Williamson, C. H. K. (1992b). Three-dimensional phenomena in bluff body wakes: Part 1: 3-D Phase dynamics, Part 2: Wave interactions in the far wake. In *IUTAM Symposium Bluff-Body Wakes, Dynamics and Instabilities*, pp. 333–336. Springer-Verlag.

Williamson, C. H. K. (1996). Vortex dynamics in the cylinder wake. *Annual Review of Fluid Mechanics 28*, 477–539.

Wu, J., Sheridan, J., Welsh, M. C., Hourigan, K., & Thompson, M. (1994). Longitudinal vortex structures in a cylinder wake. *Physics of Fluids 6*, 2883–2885.

Zdravkovich, M. M. (2003). *Flow Around Circular Cylinders, Vol 2: Applications.* Oxford University Press.